Velocity Selective Preparations in Magnetic Resonance Imaging



James A. Meakin

Lincoln College

University of Oxford

A Thesis Submitted for the Degree of

Doctor of Philosophy

Trinity 2013

Velocity Selective Preparations in Magnetic Resonance Imaging

James A. Meakin
Lincoln College, University of Oxford

A Thesis Submitted for the Degree of Doctor of Philosophy
Trinity 2013

Abstract

Arterial Spin Labeling (ASL) is a Magnetic Resonance Imaging (MRI) technique that is able to non-invasively quantify the rate of delivery of arterial blood to tissue, known as perfusion. In this thesis a method that uses Velocity Selective (VS) preparations to generate contrast between blood and tissue spins is investigated.

The systematic errors associated with performing a VSASL experiment on imperfect hardware is first investigated. It is shown through simulations and experiments that some VS preparations will underestimate perfusion due to static and transmit magnetic field errors, and that eddy currents caused by switching of magnetic gradients lead to an overestimation of perfusion with VSASL by up to a factor 2. A novel VS preparation, BIR-8, is presented which is shown to be the most robust to these imperfections.

The BIR-8 VSASL technique is then applied in brain tumours where it is found that significant VSASL signal can be detected in less than 5 minutes. However, in a comparison with a spatially selective ASL technique it is found that VSASL overestimates perfusion in these tumours, despite agreeing in Grey Matter.

The systematic errors due to physiology are then modelled, and it is shown that both diffusion and bulk motion will systematically bias the VSASL measurement. A diffusion insensitive VSASL technique, VS-TILT, is then developed and it is found that a significant proportion of the VSASL signal originates from diffusion effects. Theoretical models for the shape of the bolus in vascular networks are also derived, and it is shown that an isotropic network of laminar vessels produces the most efficient saturation, but saturation is also achieved with plug flow.

The diffusion insensitive VS preparation is then applied in an attempt to isolate the venous compartment in order to measure Oxygen Extraction Fraction. A kinetic model is derived in order to optimise the acquisition. However, it is found that accurate measurements of OEF would not be produced by this sequence in a clinically realistic time.

Acknowledgements

This thesis would not have been possible without the support, advice and encouragement of a vast number of people.

First of all I would like to thank my supervisor, Peter Jezzard, whose wealth of knowledge, patience, ideas of how to attack the brick walls and advice on how to turn my work into a thesis were invaluable. I am also greatly indebted to Natalie Voets, whose ideas for collaboration during a chance encounter at the pub, incredible patient manner and in-depth discussions rescued this thesis.

It was a pleasure to work at FMRIB for the past four years; it is a fantastic environment both academically and socially and it is a shame to be moving on. There is not enough room to thank everyone here, but a special thanks must go to a few people: firstly to Tom, for the epic tea breaks where most of my ideas were first hammered out; to Way Cherng, for encouraging my cycling and those weekends spent training in the Oxfordshire countryside; to Rob, who became my go-to scan victim once I realised that he couldn't say no to watching the latest 'Storyville' in the scanner (sorry!); to Wilfred, who would never complain about my frequent interruptions with nonsense ideas; to Sean F., for helping to keep a sense of humour down in the bunker; and to Karla, for encouraging me to give lecturing a go. Finally, thank you to all the students and post-docs who I've known along the way who made it such a great place and interesting journey.

This thesis would not have been possible without the funding from Cancer Research UK, the EPSRC, Guarantors of Brain, nor the vast amount of time my colleagues spent volunteering for scans. I'm leaving with fond memories of my time in Oxford, and I'd particularly like to thank Ollie, Shanna, Nicky, Jane, Andrew, Rosa, Dave, Laure and everyone at the Oxford University Cycling Club for all the good times.

Finally, I would like to dedicate this thesis to my Dad, whose support and encouragement over the years made this possible.

Contents

Contents i

List of Figures vi

List of Tables vii

List of Abbreviations ix

List of Publications xi

1 Introduction 1
1.1 Motivation . . . 1
1.2 Thesis Outline . . . 3

2 Background 5
2.1 Cancer . . . 5
2.1.1 Current Methods to Measure Perfusion and Hypoxia . . . 6
2.1.1.1 Measuring Perfusion . . . 6
2.1.1.2 Measuring Hypoxia . . . 8
2.2 Fundamentals of MRI . . . 10
2.2.1 Polarisation and Relaxation . . . 10
2.2.2 Image Formation . . . 12
2.2.2.1 Gradients and Eddy Currents . . . 14
2.2.2.2 Motion Sensitisation . . . 16
2.2.3 RF Pulses . . . 18
2.2.3.1 Adiabatic RF Pulses . . . 18
2.3 Arterial Spin Labeling . . . 25
2.3.1 Spatially Selective Labeling . . . 26
2.3.1.1 Pulsed Labeling . . . 27
2.3.1.2 Continuous Labeling . . . 31
2.3.2 Velocity Selective Labeling . . . 36
2.3.2.1 Velocity Selective RF Pulses . . . 37
2.3.2.2 Velocity Selective ASL Perfusion Experiment . . . 41
2.3.2.3 VSASL Beyond Perfusion . . . 44
2.3.3 Background Suppression . . . 49
2.3.4 ASL Readout . . . 54

2.3.5 Quantification of ASL 55

3 Physical and Hardware Effects in VSASL **59**
3.1 Design of a B_1 and Eddy Current Insensitive VS Pulse 60
3.1.1 Methods 62
3.1.2 Results 65
3.2 VSASL Implementation 69
3.2.1 Methods 70
3.2.2 Results 71
3.2.3 Discussion 72
3.3 Eddy Current Effects in vivo 72
3.3.1 Methods 73
3.3.2 Results 76
3.3.3 Discussion 78
3.4 Further Eddy Current Reduction: symBIR-8 80
3.4.1 Methods 80
3.4.2 Results 82
3.4.3 Discussion 84
3.5 Discussion and Conclusions 84

4 VSASL Applied in Brain Tumours **87**
4.1 Methods 87
4.2 Results 90
4.3 Discussion and Conclusions 97

5 Physiological Effects in VSASL **101**
5.1 Simulation of Motion and Diffusion Effects 101
5.1.1 Theory 102
5.1.2 Methods 105
5.1.3 Results 106
5.1.4 Discussion 108
5.2 Elimination of Diffusion Effects 109
5.2.1 VS-TILT Design 110
5.2.1.1 Theory 110
5.2.1.2 Simulation Methods 114
5.2.1.3 Results 115
5.2.1.4 Discussion 118
5.2.2 Implementation of VS-TILT 120
5.2.2.1 Methods 120
5.2.2.2 Results 122
5.2.2.3 Discussion 124
5.2.3 Diffusion Effects in VSASL 125
5.2.3.1 Methods 125
5.2.3.2 Results 127
5.2.3.3 Discussion 129

5.2.4 Measurement of ADC . . . 131
5.2.4.1 Methods . . . 133
5.2.4.2 Results . . . 135
5.2.4.3 Discussion . . . 136
5.2.5 Discussion: Diffusion in VSASL . . . 138
5.3 What Is the Bolus Shape in VSASL? . . . 139
5.3.1 Theory . . . 139
5.3.2 Discussion . . . 145
5.4 Conclusions . . . 146

6 Measurement of Oxygen Extraction Fraction 147
6.1 TRUST . . . 148
6.1.1 Methods . . . 148
6.1.2 Results . . . 150
6.1.3 Discussion and Conclusions . . . 152
6.2 QUIXOTIC . . . 153
6.2.1 A Kinetic Model for QUIXOTIC . . . 153
6.2.2 The SNR Requirements for QUIXOTIC . . . 157
6.2.2.1 Methods . . . 157
6.2.2.2 Results . . . 158
6.2.2.3 Discussion and Conclusions . . . 160
6.2.3 Implementation of QUIXOTIC-TILT . . . 161
6.2.4 Results . . . 162
6.2.5 Discussion and Conclusions . . . 164

7 Thesis Summary and Future Work 167
7.1 Future Work . . . 168

References 171

List of Figures

2.1 Eddy Currents . . . 15
2.2 Gradient Moments . . . 17
2.3 BIR-4 Trajectory . . . 24
2.4 ASL Labeling Schemes . . . 28
2.5 Velocity Selective Pulses . . . 38
2.6 VSASL Magnetisation Profile . . . 40
2.7 VSASL Pulse Sequence . . . 41
2.8 QUIXOTIC Pulse Sequence . . . 44
2.9 SEEPAGE Pulse Diagram . . . 52
2.10 SEEPAGE Signal in the Internal Iliac . . . 53

3.1 DRHS, BIR-4 and BIR-8 Pulse Diagrams . . . 60
3.2 Applied Eddy Current Compensation . . . 64
3.3 Simulated ΔB_1 Response . . . 66
3.4 Simulated Off-Resonance and Velocity Response . . . 66
3.5 BIR-6 Off-Resonance Simulation . . . 67
3.6 Simulated Spatial Eddy Current Response . . . 68
3.7 Simulated B_0 Eddy Current Response . . . 68
3.8 VSASL Pulse Sequence . . . 69
3.9 Measurement of Saturation Efficiency . . . 71
3.10 BIR-4 and BIR-8 B_1 Calibration . . . 72
3.11 Optimisation of TR and TI . . . 73
3.12 DRHS, BIR-4 and BIR-8 in vivo . . . 77
3.13 Correlation of Apparent Perfusion with G_{MAX} . . . 78
3.14 z Tagging in vivo . . . 79
3.15 Symmetric BIR-8 Pulse Diagram . . . 81
3.16 Application of BIR-4, BIR-8 and symBIR-8 in a Silicone Oil Phantom 83
3.17 Subtraction Errors in a Silicone Oil Phantom . . . 85

4.1 Low Grade Glioma pCASL and VSASL . . . 91
4.2 Grade III Glioma pCASL and VSASL . . . 92
4.3 Grade II Glioma pCASL and VSASL . . . 93
4.4 Glioblastoma Multiforme pCASL and VSASL . . . 94
4.5 VSASL SNR and % Significant Pixels in Tumour . . . 96
4.6 pCASL and VSASL Agreement in Tumour and Grey Matter . . . 97

5.1 The VSASL Pulse Sequence . . . 102
5.2 Simulation of f Overestimation Due to Tissue Diffusion . . . 106
5.3 Simulation of f Overestimation Due to Tissue Motion . . . 107
5.4 BIR-4 VS-TILT Preparations . . . 112
5.5 BIR-8 VS-TILT Preparations . . . 113
5.6 BIR-4 VS-TILT Off Resonance Response . . . 115
5.7 BIR-8 VS-TILT Off Resonance Response . . . 116
5.8 BIR-4 VS-TILT Eddy Current Response . . . 117
5.9 BIR-8 VS-TILT Eddy Current Response . . . 119
5.10 BIR-4 and BIR-8 VS-TILT ΔM Error in a Static Phantom . . . 123
5.11 BIR-8 VS-TILT Saturation Efficiency . . . 124
5.12 VSASL, VSASL-II and VS-TILT Preparations . . . 126
5.13 VSASL, VSASL-II and VS-TILT Perfusion Maps . . . 128
5.14 f measured in the CSF masks . . . 129
5.15 IVIM, VASO-IVIM and FLAIR-IVIM in vivo . . . 135
5.16 Bolus Shape for Anisotropic and Isotropic Distributions of Vessels . . . 141
5.17 Bolus Shape for Mixed and Unmixed Laminar Flow . . . 144

6.1 TRUST Calibration Curves . . . 150
6.2 TRUST Tag, Control and Subtraction . . . 151
6.3 TRUST Measurement When Breathing Air or 100% O_2 . . . 151
6.4 iVASO-QUIXOTIC-TILT Pulse Sequence . . . 153
6.5 QUIXOTIC Signal Model . . . 156
6.6 Precision and Accuracy of QUIXOTIC . . . 159
6.7 iVASO QUIXOTIC TILT Images . . . 162
6.8 QUIXOTIC-TILT Images . . . 163

7.1 accASL-TILT preparations . . . 169

List of Tables

3.1 Mean Perfusion for DRHS, BIR-4 and BIR-8 76
3.2 FMRIB Verio Eddy Current Compensation 80

4.1 Patient Tumour Types 88
4.2 Grey Matter and Tumour pCASL and VSASL quantification 95

5.1 Tissue Properties Used in the Simulations 105
5.2 Diffusion b-values for VSASL, VSASL II and VS-TILT. 127
5.3 Acceleration Moments for VSASL, VSASL-II and VS-TILT 132
5.4 IVIM, VASO-IVIM and FLAIR-IVIM in vivo results 137
5.5 Derived Bolus Shape Equations 142

6.1 iVASO QUIXOTIC Temporal SNR 164

List of Abbreviations

AFP	Adiabatic Full Passage
AHP	Adiabatic Half Passage
ASL	Arterial Spin Labeling
B_0	Static Magnetic Field (longitudinal)
B_1	Radio Frequency Magnetic Field (transverse)
BIR	B_1 Insensitive Rotation
BOLD	Blood Oxygenation Level Dependent
CNR	Contrast to Noise Ratio
CSF	Cerebrospinal Fluid
DCE	Dynamic Contrast Enhanced
EPI	Echo Planar Imaging
FAIR	Flow sensitive Alternating Inversion Recovery
HASTE	Half-Fourier Acquisition Single-shot Turbo Spin Echo
m_1	First Gradient Moment
OEF	Oxygen Extraction Fraction
PASL	Pulsed Arterial Spin Labelling
pCASL	Pseudo-Continuous Arterial Spin Labelling
pO_2	Oxygen Tension
QUIXOTIC	QUantitative Imaging of eXtraction of oxygen and TIssue consumption
RF	Radio Frequency
SEEPAGE	Spin Echo Entrapped Perfusion Imaging
SNR	Signal to Noise Ratio
T_1	Spin-Lattice Relaxation Time
T_2	Spin-Spin Relaxation Time
TE	Echo Time
TI	Inflow Time
TILT	Magnetisation Transfer Insensitive Labeling Technique
TR	Repetition Time
VENC	Velocity Encoding
VSASL	Velocity Selective Arterial Spin Labeling
VSEAN	Venous Oxygenation Mapping Using Velocity-Selective Excitation and Arterial Nulling

List of Publications

Journal Articles

Meakin JA and Jezzard P. An Optimized Velocity-Selective Arterial Spin Labeling Module with Reduced Eddy Current Sensitivity for Improved Perfusion Quantification. *Magnetic Resonance in Medicine*, 2013;69(3):832-838.

Germuska M, **Meakin JA** and Bulte DP. The Influence of Noise on BOLD Mediated Vessel Size Imaging Analysis Methods. *Journal of Cerebral Blood Flow and Metabolism*. Early view DOI:10.1038/jcbfm.2013.141.

Guo J, **Meakin JA**, Jezzard P and Wong EC. VSASL Using Symmetric BIR-8 Radiofrequency and Gradient Pulses to Reduce Eddy Currents. *Under peer review.*

Conference Proceedings

Meakin JA and Jezzard P. BIR-8 Pulses for Reduction of Eddy Current Effects in Velocity Selective ASL. In *Proceedings of the 17th Scientific Meeting British Chapter ISMRM*, Manchester, UK, 2011. p. 58.

Meakin JA and Jezzard P. Impact of Eddy Currents on Quantification of Perfusion Using Velocity Selective Arterial Spin Labeling. In *Proceedings of the 20th Annual Meeting ISMRM*, Melbourne, Australia, 2012. p. 576.

Meakin JA, Little MW, Okell TW, Anthony S, Uberoi R and Jezzard P. Quantification of Skeletal Muscle Perfusion Using Velocity Selective Arterial Spin Labeling at 3T. In *Proceedings of the 20th Annual Meeting ISMRM*, Melbourne, Australia, 2012. p. 444.

Papoutsis K, **Meakin JA**, Hess A, Near J, Payne SJ, Edwards D and Jezzard P. Construction of a 4-Channel Transmit Neck Array for pCASL Tagging at 7 Tesla and Comparison with a Head Coil. In *Proceedings of the 21st Annual Meeting ISMRM*, Salt Lake City, USA, 2013. p. 4401.

Meakin JA, Voets NL, Okell TW and Jezzard P. Suppression of Free Fluid Perfu-

sion Artefacts in Velocity Selective ASL using a BIR-4 T_2-FLAIR Preparation. In *Proceedings of the 21st Annual Meeting ISMRM*, Salt Lake City, USA, 2013. p. 2148.

Meakin JA, Voets NL and Jezzard P. VS-TILT: Velocity Selective Arterial Spin Labeling without Diffusion Effects. In *Proceedings of the Postgraduate Meeting British Chapter ISMRM*, London, UK, 2013. p. 15.

Intellectual Property

Meakin JA and Jezzard P. An Optimized Velocity Selective Arterial Spin Labelling Module. US Patent, pending.

Chapter 1

Introduction

Personalisation of cancer treatment is a key focus of current research efforts in order to improve treatment outcomes and reduce the side effects of therapy. An important aspect of this is the development and validation of techniques that can report on parameters of the individuals tumour physiology which are predictive of treatment success.

In this thesis a central aim is to develop non-invasive Magnetic Resonance Imaging (MRI) techniques that can report on two parameters, perfusion and Oxygen Extraction Fraction (OEF), in tumours throughout the body. In this chapter the motivation for this work is described an and outline of the structure of the thesis is provided.

1.1 Motivation

Each year 325,000 people in the UK will be diagnosed with some form of cancer. After heart disease, cancer is the second most common cause of mortality in the UK, resulting in 157,000 deaths in 2010 (Cancer Research UK). This results in a total cost to the NHS of £4.5bn per annum (National Cancer Research Institute). The treatment for cancer takes a toll on the body, with chemotherapy and radiotherapy both damaging the surrounding healthy tissue. Through identifying non-responders

to treatment at early time points during therapy a decision could be made by the Oncologist to try an alternative approach to lessen the side-effects of an ineffective treatment. Two parameters that show promise in predicting treatment success are measuring changes in perfusion (Mayr et al., 2010) and OEF (Mineura et al., 1994).

A MRI method to measure blood flow to tissue, or perfusion, without the need for a contrast agent is Arterial Spin Labeling (ASL) (Williams et al., 1992). In this technique arterial water is labeled using a spatially selective RF pulse. The labeled bolus then travels down the vascular tree and exchanges into tissue, where the signal is acquired. In the brain, where ASL is well established, the time it takes the blood to arrive in the imaging plane from the labeling plane is generally shorter than the longitudinal relaxation time constant of blood. This transit time is known as the bolus arrival time (BAT). However, most tumours will occur in regions outside the head, where the arterial geometry and blood velocity are generally less favourable than the situation in the brain, which can result in long bolus arrival times (Wu et al., 2008).

An alternative approach to spatially selective selective ASL is to use Velocity Selective ASL (VSASL), which images spins as they decelerate from above to below a chosen cut-off velocity (Wong et al., 2006). Through choosing the cut-off velocity to be at the arteriole-capillary bed interface then the BAT can be considered to be zero (Wu and Wong, 2006). Along with measuring perfusion, this method can also be extended to measure the amount of oxygen extracted by the tissue, or OEF (Bolar et al., 2011).

If the BAT in VSASL is zero then perfusion is the only parameter that needs to be determined in the quantification, which is beneficial in areas of low contrast-to-noise. However, it is also important that the VSASL signal is free from any artefacts that bias the perfusion measurement. In this thesis a central aim is to increase the accuracy of VSASL measurements by avoiding artefacts at the time of acquisition, rather than

modelling the effects in post processing which may increase the uncertainty of the perfusion measurement.

1.2 Thesis Outline

In chapter 2, the basics of MRI will be re-enforced and an overview of the use of velocity selective pulses in the scientific literature will be presented. In chapter 3 the overestimation of perfusion due to eddy current errors will be characterised for three preparations through simulation and experiments. In chapter 4 VSASL is applied in four patients with brain tumours and the perfusion measurement is compared with pCASL. In chapter 5 the magnitude of the systematic errors in VSASL from both diffusion and bulk motion is investigated, and a novel preparation method is presented to eliminate the diffusion effects. A theoretical model is also derived for the bolus shape in different vascular and velocity distributions. In chapter 6 the diffusion insensitive methodology is applied to an Oxygen Extraction Fraction mapping method in order to increase the SNR of the technique. A kinetic model for QUIXOTIC is also presented to optimise the scan parameters. Finally, in chapter 7 some ideas for future investigations are presented.

Chapter 2

Background

In this chapter the literature on imaging tumour perfusion and hypoxia is briefly reviewed in section 2.1, with a focus on MRI methods. Fundamental MRI physics necessary for understanding the experimental chapters of this thesis is presented in section 2.2, along with an overview of Arterial Spin Labeling techniques.

2.1 Cancer

Tumours with a diameter greater than 1-2 mm cannot be supported by passive diffusion of oxygen alone (Folkman, 1996). The tumour will then activate angiogenic switches to develop a vascular network to support the high metabolic demand of the tumour. The neovascular network developed by a tumour is chaotic, characterised by variations in vessel caliber, non-perfusing vessels and increased vessel wall permeability (Munn, 2003). Angiogenesis is targeted in oncology, where drugs that inhibit the Vascular Endothelial Growth Factor are prescribed in conjunction with chemotherapy. This normalises the neovasculature to increase the drug delivery to the tumour, prolonging patient survival in rectal cancers (Los et al., 2007). The neovasculature is inefficient in delivering O_2 rich blood to the tumour, which results in areas of transient and chronic hypoxia. Two effects then combine which reduce the prognosis for

patients with hypoxic tumours. Firstly, a low Oxygen Tension (pO_2) creates a selective pressure towards a more aggressive tumour as anaerobic cells develop escape responses to control mechanisms such as apoptosis (Graeber et al., 1996). Secondly, the effectiveness of radiotherapy is reduced as O_2 must be present within the tumour in order to fix the double strand breaks in the DNA (Brown and Wilson, 2004).

Imaging biomarkers that can report on aspects of the individuals tumour microenvironment are being developed in order to improve treatment outcomes and reduce the side effects of therapy. Increases in perfusion and blood volume have been proposed as markers for angiogenesis due to the increased vessel number density. It's hypothesised that imaging techniques that are sensitive to Oxygen Extraction Fraction (OEF) are able report on tissue at risk of hypoxia either through increased local OEF, or by adaptation to hypoxic conditions with low OEF in the presence of adequate perfusion (Mineura et al., 1994).

2.1.1 Current Methods to Measure Perfusion and Hypoxia

Perfusion is the rate of delivery of blood from the arterial system to the tissue, and is measured in units of ml of blood per 100g of tissue per minute (ml/100g/min). In this section the current methods for measuring perfusion and hypoxia during therapy are discussed.

2.1.1.1 Measuring Perfusion

The current gold standard method for measuring perfusion is ^{15}O-H_2O Positron Emisson Tomography (PET) (Iida et al., 2000), but Computed Tomography (CT) perfusion or Dynamic Contrast Enhanced Magnetic Resonance Imaging (DCE-MRI) are also used.

PET

A bolus injection of ^{15}O-H_2O can be injected into the arteries of the subject and then detected once it has exchanged into tissue (Iida et al., 2000). PET detects the perfusion signal as photon pairs from annihilation of a positron emitted from the ^{15}O radioactive tracer. The method involves a radioactive dose, which may be insignificant compared to the patient's dose from radiotherapy. However, the technique is invasive, as quantification of perfusion involves determining the tracer concentration from arterial line samples, which is then deconvolved with the tissue signal.

CT

CT uses a bolus of contrast agent, usually iodine based, that can be detected through the absorption of the imaging X-Rays (Miles et al., 1991). Rapid volumetric data are acquired as the bolus is injected and then exchanges into tissue. The delivery of the bolus to the tissue, known as the Arterial Input Function (AIF), is measured in a nearby artery. The amount of contrast agent that builds up in the voxel over time will then depend on the AIF, perfusion and vessel permeability. The time course signal within each voxel can therefore be deconvolved with the AIF to return values of perfusion and vessel permeability. The downside to CT imaging is that the deconvolution requires many time points to fully sample the tissue response curve. This increases the radiation dose from the scan due to the X-Rays used in CT.

Dynamic Contrast Enhanced MRI

DCE-MRI uses the same principle as CT perfusion imaging, but a Gadolinium based contrast agent is used instead. The Gd chelate will reduce the T_1 of the tissue surrounding the molecule, so will increase signal on T_1 weighted MRI scans. DCE is commonly used to detect tumours, and changes in relative contrast enhancement are able to predict treatment response in cervical tumours (Mayr et al., 2010). Unlike

CT, the relationship between the concentration of contrast agent in the voxel and signal is non-linear, but once this has been determined the same pharmacokinetic models can be used to quantify the data (Tofts et al., 1999). K^{TRANS} is increasingly used as a biomarker for anti-angiogenic therapies but this parameter depends on both perfusion and vessel permeability (Padhani, 2002).

Quantitative DCE-MRI measurements are difficult since the relationship between signal intensity and contrast agent concentration is non-linear and depends on tissue T_1, B_1 and the choice of water exchange model, which alone can effect the measured parameters by a factor 3 (Yankeelov et al., 2005). Accurate knowledge of the Arterial Input Function (AIF) is crucial for deconvolution of the signal and can lead to large errors in the perfusion estimate. Measurements of the AIF in a feeding artery at high spatio-temporal resolution are limited by SNR and partial volume effects, and may not represent the tissue AIF due to dispersion (Henderson et al., 1998). Compromises are often made by using a population averaged AIF, but this does not take into account the individual's cardiac and renal function.

Arterial Spin Labeling MRI

Arterial Spin Labeling (ASL) is an MRI technique that magnetically tags blood water and is able to directly quantify perfusion (Williams et al., 1992). As there is no exogenously injected contrast agent used this technique is completely non-invasive, and is repeatable both within session and over time, making it more suitable for guiding therapy. The technique will be discussed in detail in section 2.3.

2.1.1.2 Measuring Hypoxia

Hypoxia is challenging to quantify with imaging. In general, contrast agents that report on a parameter are often injected and then detected where the agent accumulates. This relies on an adequate blood supply to the tissue to deliver the agent

before it is extracted by the body, or decays away. Given hypoxia in tumours arises from inadequate vasculature this can make the delivery of a contrast agent, and thus the detection of hypoxia, challenging.

O_2 Electrodes

Eppendorf polarography uses a 300 μm electrode to sample pO_2 within a tumour (Kallinowski et al., 1990). This technique is highly invasive as it requires access to the tumour, and the measurement itself consumes oxygen. Although the technique has proven useful in clinical trials, the measured values do not correlate with histological staining for hypoxia with nitroimidazoles (Olive et al., 2001).

PET

^{18}F-fluoromisonidazole (F-MISO) can be used as a PET tracer to detect regions of hypoxia and correlates with pimonidazole histology in preclinical studies (Lee et al., 2008). Only viable cells will give signal and the areas of hypoxia that can be detected are limited by the short half life of the tracer.

T_1 relaxation MRI

Non invasive MRI techniques that do not require an injection of contrast agent have recently been proposed to measure pO_2. The longitudinal relaxation time, T_1, of water depends on pO_2, which can be detected by manipulating pO_2 using a gas challenge (O'Connor et al., 2009). However, this measurement will be corrupted by changes in blood flow. To overcome this a technique that detects the change in T_1 of the lipid peak has been proposed (Jordan et al., 2012), which also has higher sensitivity due to the increased affinity of O_2 to lipids.

2.2 Fundamentals of MRI

In this thesis the development of Velocity Selective pulses for use in ASL is described. Only the MRI physics necessary for understanding the experimental chapters will be re-enforced. For a thorough introduction to MR Physics the books by Haacke et al. (1999), Bernstein et al. (2004) or Nishimura (2010), which all formed the basis of this chapter, are recommended. This section is limited to the classical picture of MRI, as the spin gymnastics contained in this thesis can be understood without considering the underlying quantum phenomena.

In this section the polarisation and behaviour of packets of spins in magnetic fields is described. This is followed with a discussion on imaging, gradients, how motion is encoded into the data and radio-frequency (RF) pulses.

2.2.1 Polarisation and Relaxation

Nuclear Magnetic Resonance is able to study the dynamics of any nuclei that have non-zero total spin by detecting its precession and relaxation in a magnetic field. Whilst nuclei such as ^{3}He, ^{13}C, ^{19}F, ^{23}Na or ^{31}P are studied, the most commonly targeted nuclei in MRI is ^{1}H on water molecules due to the high natural abundance *in vivo*.

On average, nuclei placed in a magnetic field will align parallel to the field as this is the lowest energy state. However, due to the latent thermal energy at room temperature approximately half of the nuclei will align antiparallel to the magnetic field. This difference in the population of the two energy states creates a net magnetic moment. It is this net magnetic moment of packets of nuclei that exist in similar magnetic fields, or magnetic isochromats, that are manipulated in MRI. These packets are referred to as *spins*.

The main magnetic field, B_0, will produce a torque on the magnetisation, $\vec{M}(t)$,

such that

$$\frac{d\vec{M}(t)}{dt} = \gamma\vec{M}(t) \times \vec{B}(t) \tag{2.1}$$

which results in a precession of $\vec{M}$ about the magnetic field vector, $\vec{B}$, with the characteristic Larmor frequency for the nuclei, γ. For ^{1}H nuclei the gyromagnetic ratio is 42.576 MHz T^{-1}, which results in a Larmor frequency of 128 MHz at 3.0 T. By convention, the frame of reference is defined by the main magnetic field, such that B_0 is in the $\hat{z}$ direction.

Only magnetisation in the transverse plane can be detected, as it is this time varying magnetisation at the Larmor frequency that induces an electromotive force in the receive coil. In order to excite magnetisation into the transverse plane RF pulses at the Larmor frequency are applied, which excites transitions between the two energy states and results in a rotation of $\vec{M}(t)$. The transmit magnetic field, B_1, is in the transverse plane when the pulse is on resonance. In the rotating frame the magnetisation will rotate around the B_1 vector, through a total angle of

$$\theta = \gamma \int_0^T B_1(t)dt \tag{2.2}$$

In order to localise a slice a gradient is applied in one direction, which will excite a slice of spins where Larmor frequency is within the bandwidth of the RF pulse.

Once excited, $\vec{M}(t)$ will precess about B_0 and two relaxation processes occur. The first, T_1, characterises the longitudinal relaxation of M, which is parallel to B_0. T_1 relaxation is known as the spin-lattice relaxation time, and is a result of excited nuclei dissipating magnetic potential energy back into thermal and rotational energy in the lattice field.

The second relaxation process, T_2, characterises components of M perpendicular to B_0, and is known as the spin-spin relaxation time. The T_2 time is a result of the loss of coherence between the magnetisation of the spins as they experience slightly

different magnetic perturbations from tumbling and exchanges with proteins and other nuclei. This relaxation is formed of two components such that

$$\frac{1}{T_2^*} = \frac{1}{T_2'} + \frac{1}{T_2} \tag{2.3}$$

where T_2' is the component of the magnetisation that can be refocussed using a spin echo pulse.

The relaxation terms are then incorporated into equation 2.1, which results in the Bloch equations

$$\frac{d\vec{M}_x(t)}{dt} = \gamma \left(\vec{M}(t) \times \vec{B}(t)\right)_x - \frac{M_x(t)}{T_2} \tag{2.4}$$

$$\frac{d\vec{M}_y(t)}{dt} = \gamma \left(\vec{M}(t) \times \vec{B}(t)\right)_y - \frac{M_y(t)}{T_2} \tag{2.5}$$

$$\frac{d\vec{M}_z(t)}{dt} = \gamma \left(\vec{M}(t) \times \vec{B}(t)\right)_z - \frac{M_z - M_0}{T_1} \tag{2.6}$$

which in this case are defined in the laboratory frame. To simplify the mathematics it is common to define the rotating frame of reference that observes the magnetisation at $\omega = \gamma B_0$, so that the cross products are zero.

2.2.2 Image Formation

In NMR the frequency that the spins precess at is given by

$$\omega_0 = \gamma B_0 \tag{2.7}$$

The key step in turning NMR into MRI was proposed by Lauterbur (1973), where position is encoded into the frequency of the spins by applying a time varying magnetic

gradient, $\vec{G(t)}$, which will change the total magnetic field at position r by

$$\vec{B}(\vec{r},t) = \left(B_0 + \vec{G(t)} \cdot \vec{r}\right) \hat{z} \tag{2.8}$$

where $\vec{G(t)}$ will only modify the $\hat{z}$ component of B_0 such that

$$\vec{G(t)} = \begin{pmatrix} G_x(t) \\ G_y(t) \\ G_z(t) \end{pmatrix} = \begin{pmatrix} \frac{dB_z(t)}{dx} \\ \frac{dB_z(t)}{dy} \\ \frac{dB_z(t)}{dz} \end{pmatrix} \tag{2.9}$$

and therefore the frequency is spatially dependent

$$\omega(\vec{r},t) = \gamma\left(B_0 + \vec{G(t)} \cdot \vec{r}\right) = \omega_0 + \gamma\vec{G(t)} \cdot \vec{r} \tag{2.10}$$

During a pulse sequence the total signal from a voxel at any given time is proportional to the spin density, $\rho(r)$,

$$S(t) = \iiint \rho(r) \exp\left(-i\phi(\vec{r},t)\right) d^3\vec{r} \tag{2.11}$$

where $\phi(r,t)$ is the relative phase of the voxel. The amount of accumulated phase during an imaging experiment, relative to the Larmor frequency, is given by the integral of the spin's frequency over time

$$\phi(\vec{r},t) = \int_0^t (\omega(\vec{r},t) - \omega_0)dt' = \gamma \int_0^t \vec{G}(t')dt' \cdot \vec{r} \tag{2.12}$$

where the spatial frequency, $\vec{k}(t)$, is the time integral of the gradient

$$\vec{k}(t) = \gamma \int_0^t \vec{G}(t')dt' \tag{2.13}$$

so if linear gradients are used signal $S(t)$ is the Fourier transform of the spin

density. The aim of any pulse sequence is to sample all of the spatial frequencies that are desired, to fill *k-space*. The maximum spatial frequency to be sampled determines the edge of k-space, such that $k_{MAX} = \pi/\delta$, where δ is the resolution of the image. The bandwidth of the k-space sampling must be sufficient to include signals from the entire field of view.

2.2.2.1 Gradients and Eddy Currents

Gradients are often described as driving through k-space in order to sample all the points. Another way to think of this is that the gradients are applying a spatial frequency to the object, which moves k-space, and it is the response at the Larmor frequency that is measured using the receive coils. In order to reconstruct the image from the acquired k-space points using the Fourier transform, the exact gradient trajectory must be known as this determines the spatial frequencies acquired. In practice, the gradients are non-linear, have components in the transverse plane due to concomitant fields, and do not follow the time course that the user has requested.

A large source of gradient errors are due to eddy currents. It is not possible to instantaneously switch on a gradient due to the inductance of the coil. The gradient must be ramped up to the desired amplitude, the slew rate of which depends on the gradient power amplifier. On the Siemens Verio used in this thesis the maximum rate is 180 T/m/s. From Maxwell's laws, this changing magnetic field will induce electric fields in the cold surfaces of the cryostat of the magnet, the gradient coil itself and the RF coil. These currents are known as eddy currents, and act to oppose any change in magnetic field. The eddy currents will build up during the slew of a trapezoidal gradient, and decay during the flat top of the gradient (fig. 2.1). The same effect also occurs during the ramp down of the gradient.

The biggest effects of eddy currents are seen when large gradient amplitudes are used, resulting in distortion in diffusion scans (Jezzard et al., 1998). Eddy currents

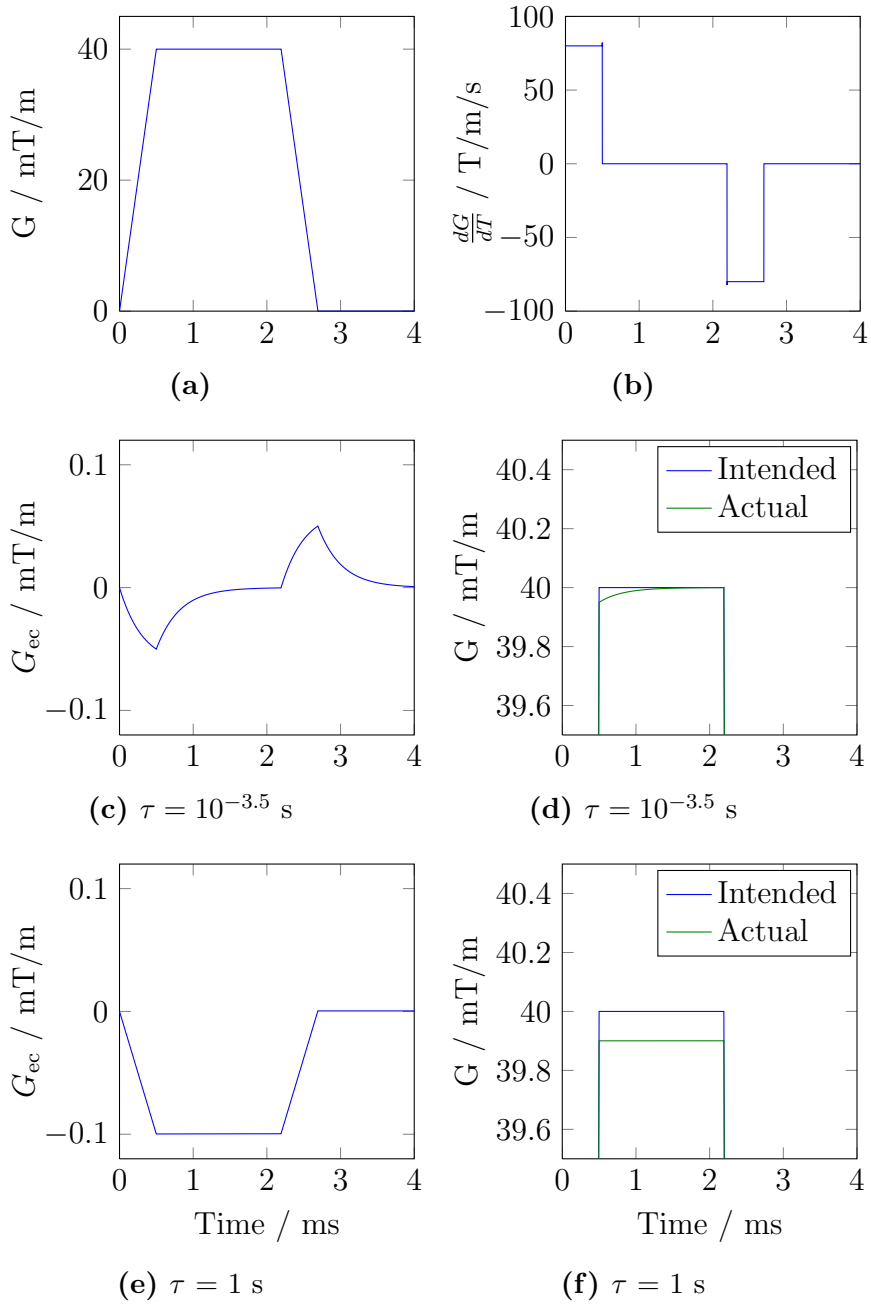


Figure 2.1: Example of eddy currents generated for the intended gradient (2.1a), the gradient slew (2.1b), the gradient eddy current for $\tau = 10^{-3.5}$ s (2.1c) and the zoomed flat top showing the actual and intended gradients for $\tau = 10^{-3.5}$ s (2.1d) with amplitude $A_n = 0.25\%$. Note that the eddy currents persist after the ramp down of the intended gradient. Long time constant eddy currents can be considered just to reduce the gradient strength, illustrated for $\tau = 1$ s (2.1e and 2.1f).

can also change the relationship between forward and reverse lines in EPI scans, which results in $N/2$ ghosts (Jesmanowicz et al., 1993). In quantitative imaging the shears in eddy currents can cause labeling errors in ASL (Jung et al., 2010), or errors in velocity measurements using phase contrast MRI (Lingamneni et al., 1995).

The eddy current response of a particular magnet can be modelled as a sum of exponentials, with time constants τ_n and amplitudes A_n (Vaals and Bergman, 1990). The gradient due to eddy currents, $G_{ec}(t)$, is then given by the convolution with the desired gradient waveform, $G(t)$,

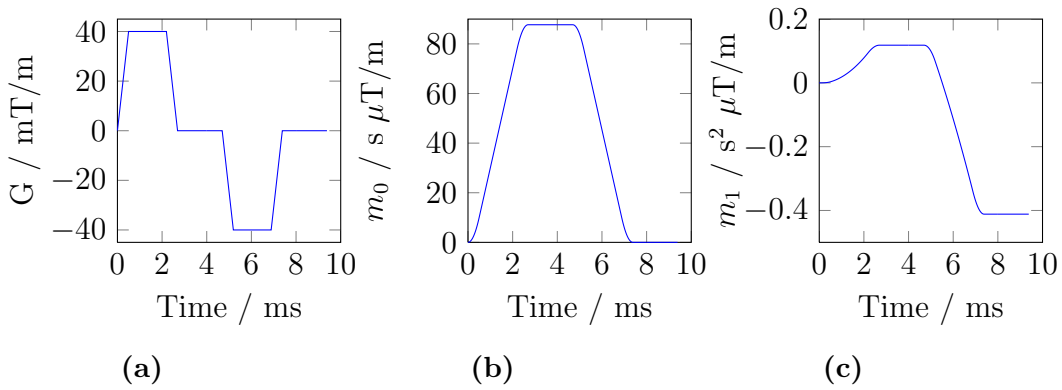
$$G_{ec}(t) = -\frac{dG(t)}{dt} * \sum_n H(t) A_n \exp(-t/\tau_n) \tag{2.14}$$

where $*$ represents convolution and $H(t)$ is the unit step function. Typical amplitudes of A_n are on the order of 0.1% on clinical scanners, and τ_n can range from microseconds to tens of seconds. The eddy currents produced are not necessarily collinear with the gradient that induced them. These are known as cross-terms, but are usually smaller than the direct terms.

Eddy currents can be reduced by applying pre-emphasis to the gradient voltage, so that the desired gradient waveform is achieved when the eddy currents are induced (Jehenson et al., 1990). However, the rate of pre-emphasis requires knowledge of the eddy current spectrum, which can be calibrated but is time variant (Spees et al., 2011). Shielded gradient coils are also used to reduce eddy current effects. These cancel the changing gradient fields outside the coil so the cold surfaces of the cryostat that generate the eddy currents are isolated.

2.2.2.2 Motion Sensitisation

Once the spins are in the transverse plane gradients can be used to impart phase, and motion sensitivity. The amount of phase accumulated by a spin from a gradient



(a) **(b)** **(c)**

Figure 2.2: Example bipolar gradient (2.2a) with zeroth gradient moment m_0 (2.2b) and first gradient moment m_1 (2.2c) as a function of time.

is given by

$$\Delta\phi = \gamma \int_0^t G(t')x(t')dt' \tag{2.15}$$

where $x(t')$ is the location of the spin along the gradient axis. The position can then be Taylor expanded to give

$$\Delta\phi = \gamma \left(m_0 x_0 + m_1 v_0 + \cdots + \frac{1}{n!} m_n \left(\frac{d^n x}{dt^n} \right)_{t=0} + \cdots \right) \tag{2.16}$$

where x_0 is the position and v_0 is the velocity along the direction of the gradient at $t = 0$. This allows us to define the gradient moment for different orders of motion

$$m_n = \int_0^t G(t')t^n dt' \tag{2.17}$$

which represents the relative amount of phase a spin will acquire from gradient $G(t)$ due to it n^{th} order of motion. An example of a bipolar blip, which has $m_0 = 0$ and finite m_1, is depicted in fig 2.2.

The phase which is accrued by a spin is proportional to its location. For a static spin, the amount of phase acquired during the negative lobe is exactly cancelled by the positive lobe. For a moving spin, the phase accrued during the first lobe is not cancelled out as the spin has moved to a different position during the bipolar blip.

This allows velocity (Pelc et al., 1991), or higher orders of motion such as acceleration (Tasu et al., 1997), to be encoded into the phase of the MR data. The bipolar blip is also used to encode diffusion data into the magnitude of the MRI signal (Le Bihan et al., 1986). The Brownian motion of spins creates a distribution of phases within a voxel, which leads to phase cancellation and a reduction of the magnitude signal.

2.2.3 RF Pulses

At the beginning of any pulse sequence will be an RF pulse to excite the magnetisation from the longitudinal to transverse planes. In the small tip angle approximation the frequency profile of an RF pulse is simply the Fourier transform of $B_1(t)$. For a top-hat shaped slice a sinc pulse would be used. However, the RF pulse must be finite, so the sinc is truncated and then windowed to improve the slice profile. However, the small tip angle approximation assumes that the magnetisation behaves linearly. At large flip angles the small tip angle approximation breaks down, and the slice profiles vastly deviate from the desired profile. The Shinnar Le-Roux algorithm, which approximates the RF as a series of small tip angle hard pulses, can be used to design pulses that take into account the non-linearities of the Bloch equations (Pauly et al., 1991).

2.2.3.1 Adiabatic RF Pulses

When using the B_1 field to manipulate the spins the total flip angle from a conventional RF pulse is given by

$$\theta = \gamma \int_0^T B_1(t)dt \tag{2.18}$$

where T is the length of the pulse. Even when using the body coil to transmit the B_1 field is not homogeneous, especially when imaging the body at 3 T due to standing

wave effects. Inhomogeneous B_1 fields lead to a spatially dependent flip angle, a variation in contrast across an image and inaccuracies in quantitative methods such as Arterial Spin Labeling. To mitigate these problems, a class of adiabatic RF pulses which do not obey equation 2.18 have been developed.

Adiabatic pulses are able to excite, invert or refocus magnetisation, and will produce the same flip angle at all locations where the local B_1 is above the adiabatic threshold. Adiabatic pulses are based on the concept of adiabatic passage. They use amplitude and frequency modulation functions that generate a slowly rotating effective field, $\vec{B}_{eff}$, that the magnetisation will follow. One of the downsides to adiabatic pulses is that they require high maximum $|B_1|$ power in order to achieve the adiabatic threshold throughout the region of interest. This leads to high specific absorption rate (SAR) as RF energy is deposited as heat in the subject, which scales with $|B_1|^2$. In this subsection the concept of the effective magnetic field and two types of adiabatic pulses: adiabatic inversion and B_1 Insensitive Rotations (BIR) are described.

The effective magnetic field

An RF pulse applied with frequency $\omega_0 + \Delta\omega_{RF}(t)$ is given by

$$B_1(t) = A(t) \exp\left(i\Delta\omega_{RF}(t)t\right) \tag{2.19}$$

where $A(t)$ is the amplitude modulation function. In the frame rotating at ω_0 this B_1 can be broken up into two components, one in the transverse and one in the longitudinal plane

$$\vec{B}_x(t) = A(t)\hat{x} \tag{2.20}$$

$$\vec{B}_z(t) = \frac{\Delta\omega_{RF}(t)}{\gamma}\hat{z} \tag{2.21}$$

and the effective field is simply the sum of these

$$\vec{B}_{eff} = A(t)\hat{x} + \frac{\Delta\omega_{RF}(t)}{\gamma}\hat{z} \tag{2.22}$$

If the RF pulse is on resonance, such as in a conventional RF pulse, $\Delta\omega_{RF}(t) = 0$ and $\vec{B}_{eff}$ is purely in the transverse plane. The magnitude of $\vec{B}_{eff}$ is $\sqrt{(A(t))^2 + (\Delta\omega_{RF}(t)/\gamma)^2}$ at an angle $\Theta = \arctan(\gamma A_0/(\Delta\omega_{RF}(t))$ to the $\hat{z}$ axis. If relaxation is neglected, the solution to the Bloch equation is a rotation about the $\vec{B}_{eff}$. If the rate of change of $\vec{B}_{eff}$ is slow relative to the rate of change of the magnetisation, then the magnetisation will follow $\vec{B}_{eff}$ as it traverses the rotating frame. This leads to the adiabatic condition

$$\left|\gamma\vec{B}_{eff}\right| > \left|\frac{d\Theta}{dt}\right| \tag{2.23}$$

When equation 2.23 is satisfied, any magnetisation that is initially aligned with $\vec{B}_{eff}$ will remain aligned throughout the adiabatic pulse. This is exploited to produce adiabatic inversions. Similarly, any magnetisation perpendicular to $\vec{B}_{eff}$ will remain perpendicular throughout the pulse, which is exploited in BIR pulses. An intuitive view when designing an adiabatic pulse is that in the ideal case, $\vec{M}$ will simply track the path of $\vec{B}_{eff}$. However, for this reason adiabatic excitations, inversions and refocussing pulses are not interchangeable.

Adiabatic Inversion

The aim of an adiabatic inversion pulse is to transform magnetisation that is aligned with $\hat{z}$ and invert it so it is aligned opposed to $\hat{z}$, such that $\vec{M}_z(T) \approx -\vec{M}_z(0)$. This is achieved adiabatically by designing a $\vec{B}_{eff}$ field that is initially aligned with $\hat{z}$ and rotates around $\hat{y}$ (say). As $\vec{M}$ is initially aligned with $\hat{z}$ this will precess about $\vec{B}_{eff}$ as it drags $\vec{M}$ through the transverse plane and finally to inversion. This is known as an adiabatic full passage.

There are a number of amplitude and frequency modulation functions that will satisfy the passage of $\vec{B}_{eff}$ for inversion (Tannús and Garwood, 1997). For some functions the trajectory may not be adiabatic throughout the pulse, but these can be optimised using numerical methods that maximize the adiabacity for a given ΔB_1 range (Ugurbil et al., 1988). A common, selective, adiabatic inversion pulse is the hyperbolic secant, or sech/tanh pair, that has modulation functions

$$A(t) = A_0 \text{sech}(\beta t) \tag{2.24}$$

$$\Delta\omega_{RF}(t) = \mu\beta \tanh(\beta t) \tag{2.25}$$

where μ and β are user tunable parameters that determine the adiabatic threshold and bandwidth of the pulse. The adiabatic condition (eq. 2.23) for this pulse is

$$A_0 > \frac{\sqrt{\mu}\beta}{\gamma} \tag{2.26}$$

where equality is the adiabatic threshold for the pulse. The bandwidth of the pulse is given by $\Delta f = \mu\beta/\pi$, and when played out with a gradient this is used to adiabatically invert a region of space. The spatial selectivity can be improved by modulating the gradient and the RF modulation functions using Frequency Offset Corrected Inversions (FOCI) (Ordidge et al., 1996). Here it is realised that the slice transition zones get inverted towards the beginning and end of the adiabatic pulse. To reduce the transition width the slice selective gradient is increased at these points. Where the gradient is modulated the amplitude and frequency offsets of the pulse are then adjusted to give the same B_1 per unit time. FOCI pulses have been further improved using analytically derived modulation functions to minimise the transition band and total RF power, known as BASSI pulses (Warnking and Pike, 2004).

In practice, the RF pulse is discretised to hard pulses on Siemens scanners with a raster time of 5 μs, which are played out with an amplitude and phase. The phase

of each hard pulse is calculated by

$$\phi_{RF}(t) = \int_0^t \Delta\omega_{RF}(t)dt \tag{2.27}$$

B_1 Insensitive Rotations

A B_1 Insensitive Rotation (BIR) pulse is able to adiabatically rotate $\vec{M}$ through arbitrary angles about an axis in the transverse plane, or a plane rotation (fig. 2.3). A BIR pulse is made up of segments of adiabatic half passage (AHP), which adiabatically transform magnetisation from $\hat{z}$ to the $\hat{x}\hat{y}$ plane, and time reversed adiabatic half passage (rAHP), which adiabatically transform magnetisation from $\hat{x}\hat{y}$ to the $\hat{z}$ plane.

A simple AHP pulse would be the hyperbolic secant discussed in the previous section. This is an adiabatic full passage, but to transform it to an AHP the pulse is stopped half way through. At this point $\Delta\omega_{RF}(t) = 0$ and $\vec{B}_{eff}$, thus $\vec{M}$, is in the transverse plane. However, an AHP would not be sufficient for plane rotations, as $\vec{M}$ must be collinear with $\vec{B}_{eff}$ at the start of the pulse and any transverse magnetisation will fan out in a plane perpendicular to $\vec{B}_{eff}$ (Garwood and Ke, 1991).

BIR pulses have been proposed with 2 and 3 segments (Ugurbil et al., 1987), but the four-segment BIR-4 pulse (Staewen et al., 1990) has been shown to be the most robust to B_0 inhomogeneity and has a lower adiabatic threshold (Garwood and Ke, 1991). The BIR-4 achieves this through reflection symmetry of the modulation function about the mid point of the composite preparation. This results in an off resonance response that is also symmetric.

The BIR-4 pulse consists of $\text{rAHP}_0 \rightarrow \text{AHP}_{\pi+\frac{\theta}{2}} \rightarrow \text{rAHP}_{\pi+\frac{\theta}{2}} \rightarrow \text{AHP}_0$ segments, where the subscript denotes the initial phase to produce a θ rotation. The BIR-4 uses

tanh/tan modulation functions, such that the first segment (rAHP_0) is given by

$$A_1(t) = A_0 \tanh\left[\zeta\left(1 - \frac{4t}{T_p}\right)\right] \tag{2.28}$$

$$\phi_1(t) = \frac{\phi_{MAX}}{4} - \frac{\Delta\omega_{MAX} T_p}{4\kappa \tan(\kappa)} \ln\left[\frac{\cos(4\kappa t/T_p)}{\cos(\kappa)}\right] \tag{2.29}$$

for $0 < t \leq \frac{T_p}{4}$, where T_p is the total pulse length, ζ, ω_{MAX} and κ are tunable parameters. For segments 2 and 3 a π phase shift is added which improves the performance at low B_1. In addition to this there is a $\frac{\theta}{2}$ phase increment, which produces the arbitrary plane rotation. The remaining segments are then for $\frac{T_p}{4} < t \leq \frac{T_p}{2}$:

$$A_2(t) = A_1\left(\frac{T_p}{2} - t\right) \tag{2.30}$$

$$\phi_2(t) = \phi_1\left(\frac{T_p}{2} - t\right) + \pi + \frac{\theta}{2} \tag{2.31}$$

for $\frac{T_p}{2} < t \leq \frac{3T_p}{4}$:

$$A_3(t) = A_1\left(t - \frac{T_p}{2}\right) \tag{2.32}$$

$$\phi_3(t) = \phi_1\left(t - \frac{T_p}{2}\right) + \pi + \frac{\theta}{2} \tag{2.33}$$

and finally, for $\frac{3T_p}{4} < t \leq T_p$:

$$A_4(t) = A_1\left(T_p - t\right) \tag{2.34}$$

$$\phi_4(t) = \phi_1\left(T_p - t\right) \tag{2.35}$$

In the case of excitation $\vec{M}$ will begin aligned with $\hat{z}$. The initial $\vec{B}_{eff}$ of the first rAHP is perpendicular to $\vec{M}$, and will remain so throughout the passage (fig. 2.3a). The result of the rAHP is to transform $M_z \rightarrow M_{xy}$ (fig. 2.3g). $\vec{M}$ is then

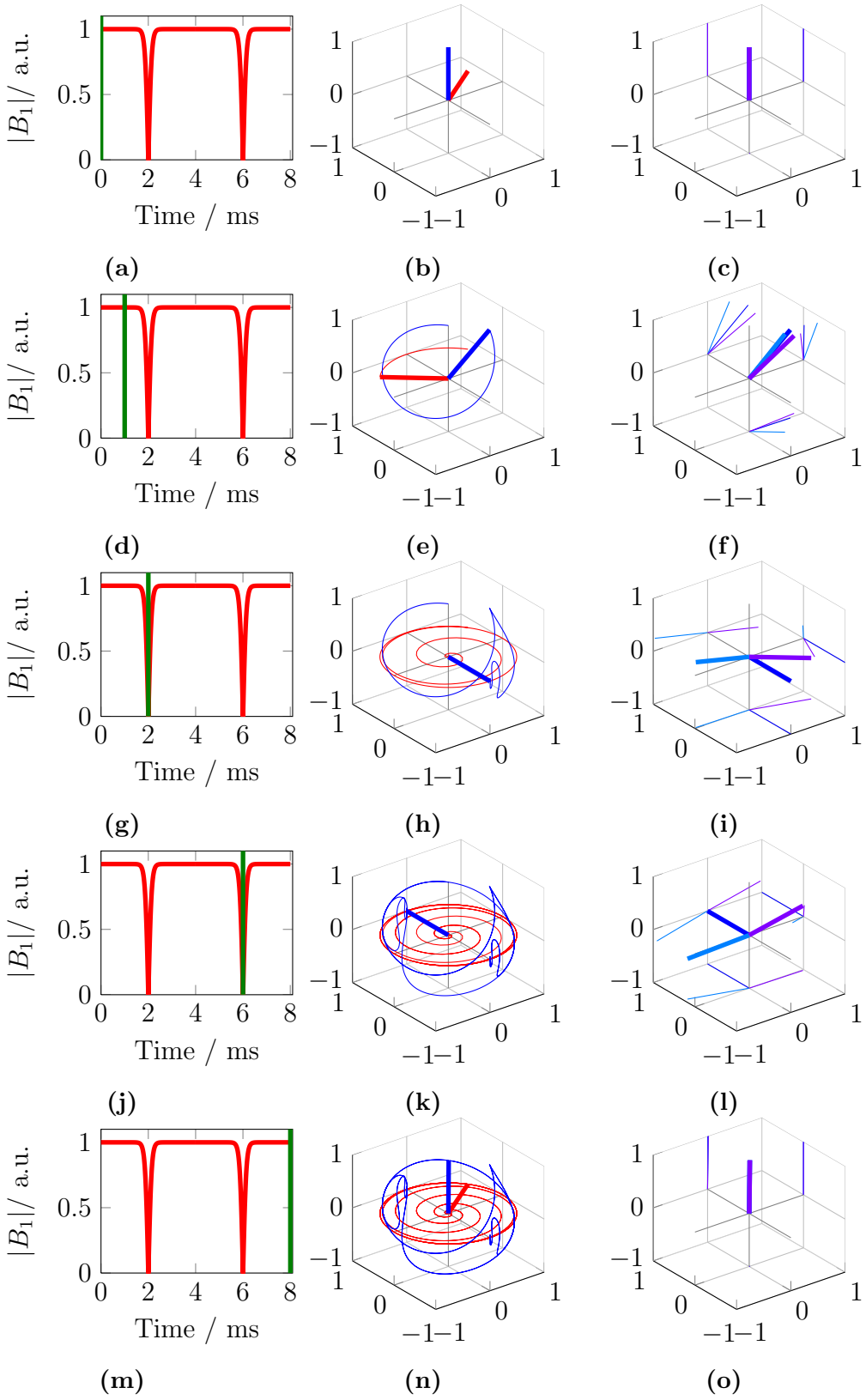


Figure 2.3: The magnetisation trajectory at 5 different time points during a zero degree BIR-4 pulse. Displayed are the B_1 (red), time (green), on resonance magnetization (blue), -200 Hz off-resonance magnetization (purple) and +200 Hz off-resonance magnetisation (turquoise). See text for details.

rotated through the arbitrary plane by the AHP and rAHP of segments 2 and 3 (fig. 2.3j), before being returned to $\hat{z}$ (fig. 2.3m). Segments 2 and 3 combine to act as an adiabatic full passage. One property of the AFP is that the resulting phase is quadratic, but this quadratic phase can be reversed by playing out a second AFP (Cano et al., 2002). In the case of off-resonance spins the BIR-4 pulse will not transform $M_z \rightarrow M_{xy}$ completely (fig. 2.3, right column). However, due to the time symmetry of the pulse the preparation is robust to these effects.

The BIR-4 pulse has found uses when using surface coils, in spectroscopy (Gruetter et al., 1998) or for vascular suppression in ASL (Schepers et al., 2003).

2.3 Arterial Spin Labeling

The concept of labeling the blood spins pre-dates Magnetic Resonance Imaging itself (Lauterbur, 1973). Morse and Singer (1970) placed the arms of volunteers in a magnetic field and labeled the venous blood with an RF coil. The spins were then detected further down the vein in a second coil, which was spatially separated from the labeling coil. However, Arterial Spin Labeling as it is known today was first developed by Williams et al. (1992), where continuous labeling of arterial blood was used to measure perfusion in the rat brain.

In healthy human grey matter the blood supply will deliver approximately 0.01 ml of arterial blood per ml of tissue per second, which is equivalent to 60 ml/100g/min. The rate of delivery of blood to the capillary bed, known as perfusion, can be directly measured with MRI by using Arterial Spin Labeling (ASL).

In ASL a bolus of blood is magnetically labeled in the arteries upstream to the tissue and a series of images are acquired after the labeled water exchanges into the capillary bed. Two image types are acquired to subtract out the static tissue signal: a tag condition where the blood is labeled, and a control condition where the blood

is left unperturbed.

The key to the success of any ASL sequence is the quality of the control condition. The perfusion signal is only on the order of a few percent of the equilibrium magnetisation so the signal in each voxel will be dominated by tissue. Any imbalance between tag and control of Magnetisation Transfer (MT), eddy currents, diffusion or RF pulse profile will cause tissue artefacts to appear in the ΔM subtraction, leading to erroneous perfusion values.

The basic ASL sequence will consist of three sequence blocks. First there is a labeling or control RF pulse. This is followed by a post label delay time to allow for passage of the labeled spins to reach the tissue bed, during which time background suppression pulses can be played out to minimise the tissue signal. Finally there is a readout module, which is usually a fast imaging technique such as 2D EPI/Spiral, or 3D GRASE with EPI/Spiral.

The method of generating the bolus divides ASL into two broad approaches: pulsed and continuous labeling. In this section several of the approaches to label and control the blood are described. Once the data are acquired, the signal is then quantified in order to extract the physiological parameters. Along with perfusion, ASL has also been extended to perform quantitative angiography (Okell et al., 2012), or to infer arterial blood volume (Petersen et al., 2006), vessel permeability (Parkes and Tofts, 2002) or oxygen extraction fraction (Bolar et al., 2011), which are also described in this section.

2.3.1 Spatially Selective Labeling

To measure perfusion the bolus of blood must be labeled in arteries upstream to the tissue of interest. Classically this has been achieved by applying a spatially selective RF pulse to saturate or invert spins before they are delivered to the organ of interest. Two different principles are used in the generation of the bolus. In Pulsed

ASL (PASL) an RF pulse will define a spatial width to the bolus. Continuous ASL (CASL) is instead based on the principle of flow-driven adiabatic inversion, which defines a labeling plane that inverts the spins as they flow through this, creating a bolus that is defined temporally. CASL is now implemented on most scanners as pseudo-Continuous ASL (pCASL) (Dai et al., 2008), which overcomes the hardware limitations of CASL.

There are a plethora of ASL methods, and acronyms, that have been developed over the past 20 years. There is now a growing consensus within the ASL community that pseudo-CASL is the technique that should be used clinically, due to its increased SNR over PASL and immunity to eddy current and MT effects. However, outside the brain the ideal ASL method is still unclear, which will be explored in this thesis, and so a discussion of the major PASL techniques is included here.

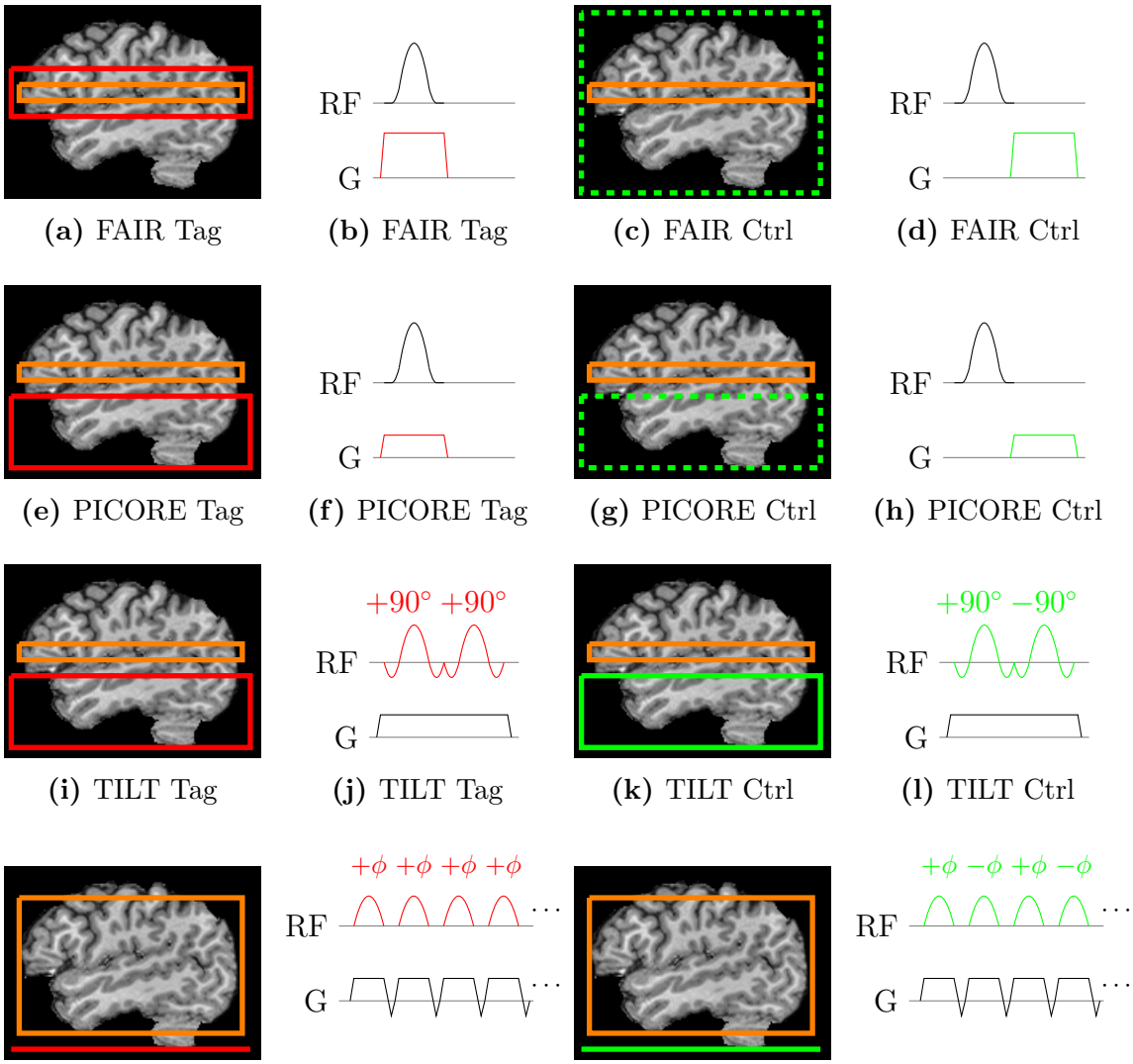
2.3.1.1 Pulsed Labeling

FAIR

In Flow-sensitive Alternating Inversion Recovery (FAIR) an inversion pulse is applied which is slice selective in the control condition and non-selective for the tag (Kim, 1995) (fig. 2.4a). In the control condition the slice selective pulse inverts a region with a slightly greater extent than the imaging region to avoid any edge effects in the transition band of the inversion pulse.

For the tag condition the RF pulse is played out at the same frequency, so that MT effects are balanced, but the slice selective gradient is turned off. The extent of the bolus in FAIR is given by the field of view of the RF coil used to play out the inversion pulse. To help mitigate eddy current effects the slice selective gradient can be played out after the RF pulse, acting as an additional spoiler.

During the inflow time blood will then flow into the slice from either side of the imaging band. As the imaging region is recovering with T_1, care must be taken



(a) FAIR Tag **(b)** FAIR Tag **(c)** FAIR Ctrl **(d)** FAIR Ctrl

(e) PICORE Tag **(f)** PICORE Tag **(g)** PICORE Ctrl **(h)** PICORE Ctrl

(i) TILT Tag **(j)** TILT Tag **(k)** TILT Ctrl **(l)** TILT Ctrl

(m) pCASL Tag **(n)** pCASL Tag **(o)** pCASL Ctrl **(p)** pCASL Ctrl

Figure 2.4: Example ASL labeling schemes showing the acquisition volume (orange), the location acted on by the RF during the tag condition (red) and the location acted on by the RF during the control condition (green). Shown are FAIR, PICORE, TILT and pCASL with a sketch of the labeling module for each condition. See the text for details.

at inflow times close to the null point of the tissue, so it is advisable to take the complex subtraction, or use the FAIRER technique (Mai et al., 1999) that saturates the imaging region after the application of the inversion.

Another issue with FAIR is that the labeling region is intrinsically linked to the imaging region. When planning the scan it is important to make sure that any arteries supplying the tissue do not meander in and out of the imaging region, as this will result in a non-contiguous labeled bolus and an underestimation of perfusion. This may limit the possible acquisition planes in the body where the arterial geometry is complex, and may not be optimal for reducing respiratory motion. However, due to the simplicity of the sequence FAIR has been used in many organs outside the brain such as kidney (Gardener and Francis, 2010), prostate (Li and Metzger, 2012) and pancreas (Schraml et al., 2008).

PICORE

Promixal Inversion with Control for Off Resonance Effects (PICORE) inverts a region with arteries proximal to the imaging slice in the tag condition (Wong et al., 1997) (fig. 2.4e). The gap between the inversion and imaging region is generally on the order of 5 - 10 mm. This must be minimised so that the bolus arrival time is minimal, but must be large enough so that the imaging region is not perturbed by any side lobes of the inversion pulse.

For the control condition the same RF pulse is played out so that the MT effects are balanced, however the slab selective gradient is turned off. As the RF pulse is largely off-resonance (≈ 5 kHz) the imaging region is unperturbed by this pulse (aside from MT). Like FAIR the slab selective gradient can be played out after the inversion pulse to help negate the mismatch in eddy current effects.

TILT

Transfer Insensitive Labeling Technique (TILT) is a technique related to PICORE (Golay et al., 1999). However, rather than using an adiabatic full passage to invert a slab, two slab selective +90° RF pulses are used to achieve a 180° inversion (fig. 2.4i). In the control condition the same gradients are played out, making the technique insensitive to eddy current effects, but π phase is added to the second pulse. In effect, this becomes a +90° -90° in the control condition, or a 0° total RF, so that the blood is unperturbed.

As the same RF is played out in both tag and control conditions MT effects are balanced. However, it is relatively difficult to achieve a slice selective, adiabatic, 90° tip. In the original implementation conventional slice selective pulses were used, but this will cause the labeling efficiency to be proportional to the local B_1, which may vary along the arterial path. A modification to the sequence was subsequently proposed where one FOCI inversion is used in the tag case, and two FOCI inversions with 50% power are used in the control (Golay et al., 2001).

Controlling the bolus shape

In PASL the bolus is defined spatially, either by the width of the inversion slab (PICORE, TILT) or by the extent of the RF coil (FAIR). Each artery will have a different length through this slab due to siphoning or changes in blood velocity. This results in a different temporal width to the labeled bolus, which must be determined for each voxel. To mitigate these effects it is possible to saturate either the leading or trailing edge of the bolus by applying saturation pulses in both tag and control conditions to the imaging or labeling region respectively (Luh et al., 1999).

2.3.1.2 Continuous Labeling

In this next section the method that is becoming the standard sequence for performing ASL, pseudo-continuous ASL (pCASL) (Dai et al., 2008), is described. Continuous labeling methods rely on the principle of flow driven adiabatic inversion, which defines a labeling plane rather than a labeling slab (Williams et al., 1992). The length of the RF pulse (or train of RF pulses) will also define the temporal bolus width, and so does not need to be determined in the quantification. Compared to PASL the leading and trailing edges of the CASL bolus will have experienced the same amount of T_1 decay, which leads to a higher perfusion SNR.

Despite this, the long RF and gradient pulses required to achieve flow driven adiabatic inversion has limited the implementation of standard CASL to specialist hardware setups. However, in recent years pCASL (Dai et al., 2008) treated the labeling pulse as a Steady State Free Precession sequence, which has reduced the demand on the hardware and has been implemented on a range of clinical systems, including 1 T open scanners (Heijtel et al., 2012).

Flow Driven Adiabatic Inversion

Flow Driven Adiabatic Inversion is achieved by applying an RF pulse with constant amplitude $|B_{1,av}|$ along with a constant gradient with amplitude G_{av}. When the RF pulse is played out with a frequency ω_{RF} and the gradient played out along the z axis, spins at a location $z_0 = \frac{\omega_{RF}}{\gamma G_{av}}$ from isocentre will be on resonance. As the pulse is played out for $1-3$ s, it will have a very narrow bandwidth and thus a very narrow labeling plane. Static spins will experience a very large flip angle as for these spins this is obviously not an adiabatic pulse.

However, spins that move through the labeling plane at z_0 will become adiabatically inverted. A moving spin will start off a finite distance away from the labeling

plane, $z(t)$, where the effective field will be given by

$$B_{eff} = \gamma B_1 \hat{x'} + (\omega - \omega_{RF})\hat{z'} \tag{2.36}$$

$$= \gamma B_{1,av} \hat{x'} + G_{av}(z(t) - z_0)\hat{z'} \tag{2.37}$$

When the spins are far away from the labeling plane the $\hat{z'}$ term dominates, and then reduces and becomes negative as the spins travel through z_0. As γB_1 is constant the B_{eff} vector seen by the moving spins will slowly rotate from $+z$, through the transverse plane and finally to $-z$. If the parameters are chosen correctly the magnetisation of the spins will rotate about B_{eff}, resulting in adiabatic inversion. The adiabatic condition is given by

$$\frac{1}{T_2} < \frac{G_{av} v}{|B_{eff}|} < \frac{\gamma |B_{eff}|}{2\pi} \tag{2.38}$$

where v is the velocity of the spins and T_2 is the T_2 of blood. This inequality can be understood as on the right hand side this is the term for the spins travelling through the labeling plane too quickly for the inversion to be adiabatic (as the B_{eff} sweep is too rapid). On the left hand side the passage is too slow as the label will decay as the spins spend time in the transverse plane and decay away with T_2.

CASL

In the original implementations of CASL the flow driven adiabatic inverstion was played out proximal to the imaging region in the tag condition. For the control condition there are two options that will move the labeling plane distal to the imaging region: either the RF frequency is modified or the gradient amplitude is reversed. The former has the problem of MT effects not being balanced as these are generally not symmetric about the center frequency, and the latter has the problem of eddy currents not being balanced.

In addition to these confounds the duration of the labeling pulse required for CASL usually exceeds the duty cycle of clinical RF amplifiers or the SAR limit. To reduce the MT effects and SAR a separate labeling coil can be used (Zaharchuk et al., 1999), which will only deposit local rather than whole body SAR, and the localised B_1 will not induce MT in the imaging region. Another approach is to amplitude modulate the RF pulse so that two labeling planes are produced in the control (Wang et al., 2005), resulting in a net 0° perturbation, but this results in a low labeling efficiency.

pCASL

Multiple receive coils have become standard on clinical systems in order to perform parallel imaging, the result of this is that the body coil transmit is increasingly the only option on clinical systems. In order for CASL to be implemented with body coil transmit the duty cycle of the labeling pulse needed to be reduced to $\approx 50\%$.

The first step is to split the continuous pulse up into a series of hard RF pulses (fig. 2.4i). The Fourier transform of this sequence will result in a series of aliased labeling planes located at $z = \frac{n}{\gamma G_{av} \cdot \Delta t}$, where n is an integer and Δt is the pulse separation. The amplitude of these labeling planes will be modulated by a broad sinc function (the fourier transform of a hard pulse).

The aliased labeling planes are then suppressed by using a Hanning windowed RF pulse, the fourier transform of which has a much sharper cutoff than the sinc. This drop off is then further enhanced by increasing the slice select gradient during the application of the pulse to G_{MAX}, and then using a refocussing lobe so that the average gradient is maintained. Aliased labeling planes will then occur at $z = \frac{n}{\gamma G_{MAX} \cdot \Delta t}$, and will be suppressed if $G_{MAX} > \frac{G_{av} \Delta t}{\delta}$, where δ is the width of an individual RF pulse.

For the tag condition the RF pulses are played out with the same phase. The spins will be perturbed by the first RF pulse, after which they free precess in the G_{av} field, acquiring $\Delta\phi_0 = \gamma G_{av} \Delta z \Delta t$ phase, where Δz is the location of the labeling plane.

In order to track the spins magnetisation throughout the pseudo-adiabatic inversion, each subsequent RF pulse must be incremented with this phase.

For the control condition the same RF and gradient pattern is played out which exactly balances any MT or eddy current effects. The only difference is that π phase is added to each subsequent RF pulse. The results in the first RF pulse perturbing the magnetisation, which is then tipped back to its original position by the subsequent pulse. The net result of this is a tagging efficiency of $\alpha = 96\%$ at 33% duty cycle (Dai et al., 2008).

One of the major limitations of pCASL is any B_0 inhomogeneity in the labeling plane. In addition to the phase acquired from the free precession in the G_{av} field, there will be an additional phase increment from off resonance which will result in a total phase increment of

$$\Delta\phi = \gamma G_{av}\Delta z\Delta t + \gamma\Delta B_0\Delta t \tag{2.39}$$

where ΔB_0 is the local off resonance. As the RF phase will only increment by $\Delta\phi_0 = \gamma G_{av}\Delta z\Delta t$, the $\gamma\Delta B_0\Delta t$ term will result in the RF not tracking the magnetisation as it is inverted, and inefficient labeling will occur. This results in the labeling efficiency being proportional to the local ΔB_0 in the artery. If $\gamma\Delta B_0\Delta t = \pi$ then tag and control will simply be swapped. This can be thought of as the labeling efficiency being negated to $-\alpha$. In between these two extremes there lies a continuum of labeling efficiencies between $\{+\alpha, -\alpha\}$. There is no analytical expression for this curve so the response must be simulated. However, the response is approximately cosinusoidal, but the transition width and flat top depends on $\delta, \Delta t$ and $|B_{1,av}|$. Obviously the worst case scenario is an intermediate off resonance, where the tagging efficiency is 0%.

Several approaches have been proposed to overcome the problem of the labeling

plane being off resonance. The simplest to implement is the multi-phase pCASL approach (Jung et al., 2010). This is where instead of incrementing the RF pulses by $\Delta\phi_0$ for the tag and $\Delta\phi_0+\pi$ for the control, the RF is incremented in four or eight steps between 0 and 2π. Then the perfusion data are not subtracted, but is fitted voxelwise to a Bloch equation simulation of the known efficiency response. If the response is assumed to be cosinusoidal, one can simply take the Fourier transform along the phase increment direction to speed up the analysis (Jung and Liu, 2010). This technique lowers the total labeling efficiency, but it is possible to generate perfusion territory information if the arteries in the labeling plane are at different off resonances.

A second approach is to change the shim in the labeling plane during the pCASL pulse train. The labeling plane is usually located close to, but outside the imaging region that the scanner will automatically shim for. By performing higher order shimming in the imaging region, the shim in the labeling plane may be degraded. Several solutions could be thought of here. The operator could manually include the labeling plane in the shim volume calculation, or turn off the linear shims during the pCASL pulse train (assuming that they are always acting detrimentally). A low resolution ASL pre scan can be used to optimise the linear gradients required during the pCASL pulse train to normalise the off resonance across all arteries supplying the tissue of interest (Dai et al., 2012). This could potentially be extended to include optimisation of the TI set for the subsequent ASL experiment (Xie et al., 2010).

Another final issue is that the tagging efficiency will be proportional to velocity. Therefore, for every application the parameters of the pCASL pulse train (δ, Δt, G_{MAX}, G_{av} and $|B_{1,av}|$) must be optimised to optimal tagging efficiency. Especially in the case of slow flow the tagging efficiency will rapidly reduce, and may be a particular problem in the case of pulsatile flow. Even in the carotids it has been shown that there is some benefit to tracking the cardiac phase with ECG triggers and adjusting the pulse train during the scan (Luh et al., 2008).

Despite these challenges a consensus is forming that pCASL should be used for clinical brain ASL (2012 ISMRM Perfusion Study Group consensus white paper, *in preparation*). Outside the brain the technique has been successfully implemented in the retina using bSSFP (Park et al., 2013) and kidneys using HASTE (Robson et al., 2009). In all these organs the arteries supplying the tissue are relatively easy to identify, have favourable non-pulsatile blood velocities, and it is possible to prescribe a labeling plane that is perpendicular to a straight arterial segment in order to maximise tagging efficiency. In addition to this the labeling plane must not bisect the artery more than once, else the blood will be inverted twice and no ASL contrast will be observed. All of these issues must be considered when implementing the pCASL labeling method for measuring perfusion in organs that are supplied by arteries of greater complexity than the carotids, vertebrals or aorta.

2.3.2 Velocity Selective Labeling

In the ASL methods described previously the perfusion contrast is generated by exploiting a spatial difference between where the arterial spins are and the tissue that the spins will perfuse into. This is achieved by instantaneously inverting a slab of spins proximal to the tissue (PASL), or continually inverting spins traversing through a plane (CASL). In both cases there is a necessary spatial gap between the labeling and imaging regions, on the order of 5 mm in PASL (Warnking and Pike, 2006), or 1-2 cm for pCASL, in addition to the coverage of the imaging volume. If the arterial supply has a low average velocity or the gap is too large the Bolus Arrival Time (BAT) between the labeling and imaging regions will be increased. An increased BAT results in increased T_1 decay of the bolus and a reduction of perfusion CNR. This may result in the ASL signal change falling below the noise floor of the experiment due to T_1 decay the bolus, resulting in an underestimation of perfusion. This is a particular problem in situations where BAT is already increased, such as in stroke

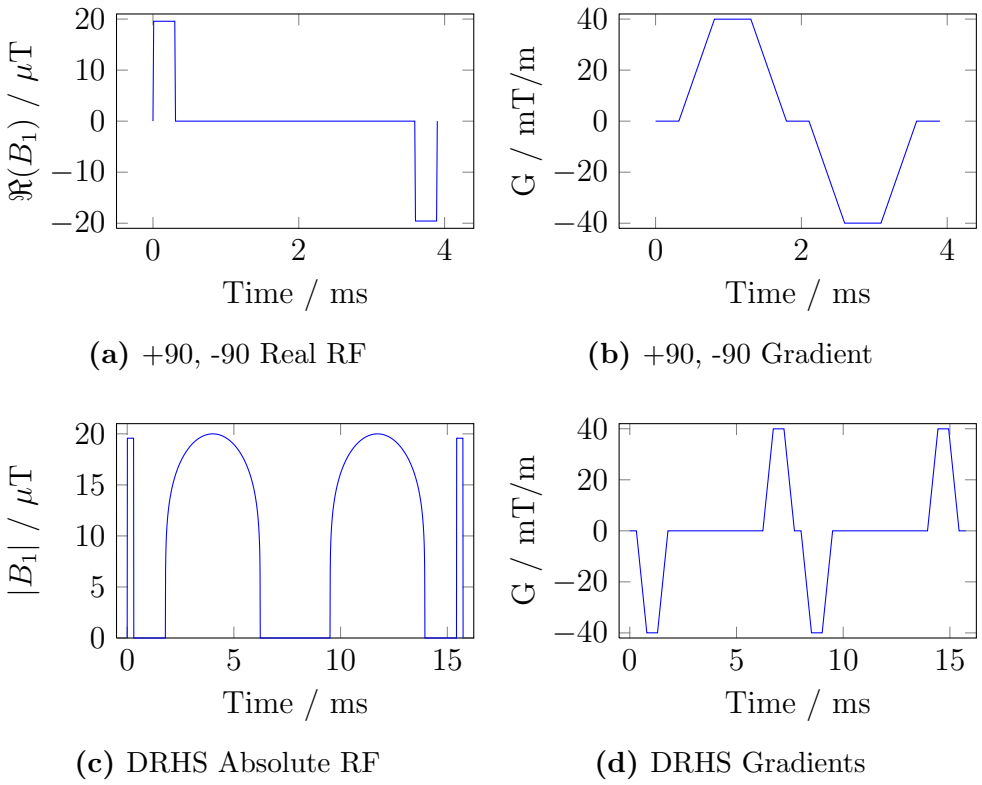
where collatoral flow may exist. One strategy to reduce BAT is to reduce the gap between labeling and imaging planes, but soon the limits of slice profile, SAR and gradient strength may be reached.

An alternative strategy is to generate the contrast based on higher orders of motion (Wong et al., 2006; Schmid et al., 2013). Instead of expoliting a difference in position, Velocity Selective ASL (VSASL) is instead based on a separation of the arterial and tissue spins by their velocity. This has the potential to generate the leading edge of the bolus closer to the capillary bed in order to reduce the BAT (Wu and Wong, 2006).

2.3.2.1 Velocity Selective RF Pulses

Generating the VSASL contrast requires an RF pulse that will modulate the longitudinal magnetization, M_z, of the spins as a function of velocity, independent of the spin's position. To eliminate errors in the final quantification of perfusion the pulse much be insensitive to B_0 and B_1 inhomogeneity, and must be within the hardware limits of clinical scanners. Ideally, the Velocity Selective RF pulse will invert spins above a characteristic velocity, leaving static spins unperturbed.

To the best of the author's knowledge, there exists no adiabatic RF pulse that can achieve the inversion required for VSASL. Recently a class of pulses have been proposed based on the Shinnar Le-Roux algorithm (Shin et al., 2012b). In the SLR algorithm a 'soft' RF pulse is designed by approximating it as a series of hard pulses, followed by free precession in the slice selective gradient given by zeroth moment $m_0 = G\Delta t$, where Δt is the hard pulse length. A velocity selective inversion can then be designed using hard pulses that are played out without spatial selection, followed by a bipolar blip with first gradient moment m_1. This has been applied in angiography (Shin et al., 2012b), inverting velocities of between zero and 50 cm/s. However, the m_1 that can be achieved on clinical systems is low relative to the velocity of the blood



(a) +90, -90 Real RF

(b) +90, -90 Gradient

(c) DRHS Absolute RF

(d) DRHS Gradients

Figure 2.5: Example velocity selective pulses.

that would be of interest for VSASL. Therefore, there is a non-negligable time between the hard pulses of the Velocity Selective SLR pulse in which extra phase is accrued due to off resonance. Hard π refocussing pulses can be added to overcome the B_0 sensitivity (Shin et al., 2012a). However, the preparation will still be sensitive to the local B_1 as the SLR algorithm fundamentally designs conventional pulses. Although an adiabatic SLR algorithm has been proposed (Balchandani et al., 2010), it is likely that the number of support points required will create a pulse that is much greater in length than the T_2 of blood, so may be limited to pre-clinical systems where the higher gradient strengths can achieve higher m_1.

Instead, Velocity Selective preparations have been designed which rely on the assumption of laminar flow and mixing within the artery to approximate a saturation above a chosen velocity (Wong et al., 2006). First, the longitudinal magnetisation is tipped down into the transverse plane. Here, gradients can be applied that will

impart phase given by the relevant gradient moments. For velocity selection a gradient pattern is applied such that $m_0 = 0$, and $m_1 \neq 0$. This magnetisation is then tipped back up into the longitudinal plane and any transverse component is spoiled using a spoiler gradient. The simplest velocity selective preparation is therefore $90_{+x} \rightarrow (+G) \rightarrow (-G) \rightarrow 90_{-x}$ (fig. 2.5a). To overcome B_0 inhomogenity a refocussing pulse can be added to give $90_{+x} \rightarrow (+G) \rightarrow 180_y \rightarrow (+G) \rightarrow 90_{-x}$. If relaxation is ignored the resulting longitudinal magnetisation after the application of the preparation is given by

$$M_z = M_0 \cos(\gamma \Delta\phi) \tag{2.40}$$

which for a velocity selective pulse is

$$M_z = M_0 \cos(\gamma m_1 v_0) \tag{2.41}$$

where M_0 is the fully relaxed longitudinal magnetisation. A vessel with laminar flow will contain a uniform distribution of velocities from 0 to V_{MAX} (twice the average velocity in the vessel). Therefore the resulting M_z in this vessel is given by

$$\begin{aligned} M_z =& M_0 \int_0^{V_{MAX}} \frac{1}{V_{MAX}} \cos(\gamma m_1 v_0) dv_0 && (2.42)\\ =& M_0 \frac{\sin(\gamma m_1 V_{MAX})}{\gamma m_1 V_{MAX}} && (2.43)\\ =& M_0 \mathrm{sinc}(\gamma m_1 V_{MAX}) && (2.44) \end{aligned}$$

This sinc function can be considered a saturation for velocities greater than the first zero point of the function, where $\gamma m_1 V_{MAX} = \pi$ (fig. 2.6). It is therefore useful to define the m_1 of the preparation as

$$m_1 = \frac{\pi}{\gamma V_{\mathrm{cut}}} \tag{2.45}$$

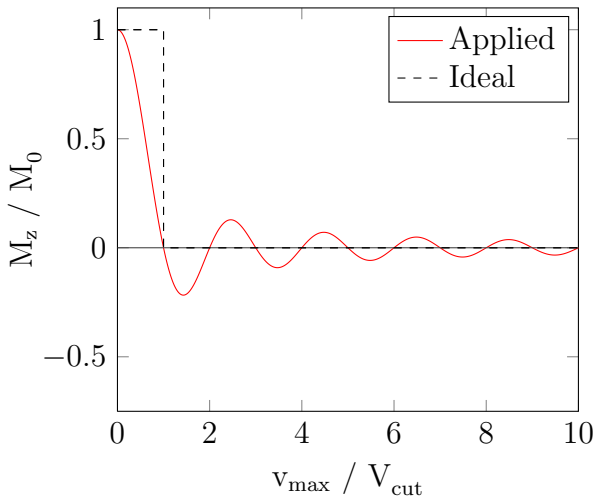


Figure 2.6: The theoretical magnetisation profile after the application of a velocity selective pulse in laminar flowing vessels with maximum velocity V_{MAX}. In VSASL it is assumed that spins are saturated for all $v > V\mathrm{cut}$.

where V_{cut} is the characteristic cutoff velocity.

The most commonly used velocity selective preparation in VSASL is the Dual Refocussed Hyperbolic Secant (DRHS) (Wong et al., 2006) (fig. 2.5d). The DRHS preparation is built up from the $90_{+x} \rightarrow (+G) \rightarrow 180_{y} \rightarrow (+G) \rightarrow 90_{-x}$ sequence. To overcome the incomplete refocussing from the hard 180 pulse this is replaced by two adiabatic hyperbolic secant pulses. Two pulses need to be added as a single adiabatic refocussing pulse will impart quadratic phase, which is reversed by using the second adiabatic pulse. The non selective adiabatic pulses can then be reduced in duration by using the VERSE algorithm (Conolly et al., 1988), but this results in an infinite frequency offset at the onset of the pulse. To overcome this Wong et al. (2006) proposed modulating the pulse into a form $\cos^{n}(t)$ with $-\pi/2 < t < \pi/2$.

The use of two refocussing pulses leads to three positions where the spins are in the transverse plane and gradients can impart phase. This allows the monopolar velocity selective gradients to be split up into bipolar gradients, which has been shown to reduce eddy current effects in diffusion imaging (Reese et al., 2003). The final DRHS preparation is therefore $90_{+x} \rightarrow (+G) \rightarrow \pi_{\mathrm{sech}} \rightarrow (-G) \rightarrow (+G) \rightarrow \pi_{\mathrm{sech}} \rightarrow (-G) \rightarrow$

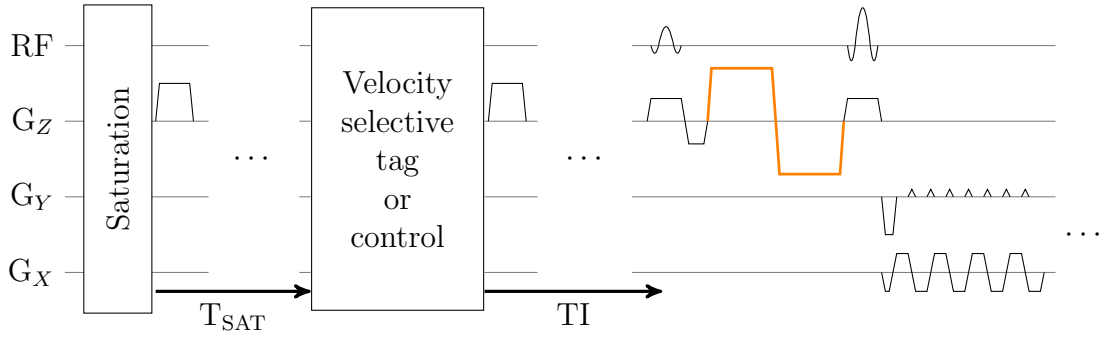


Figure 2.7: The VSASL pulse sequence.

90_{-x}.

Although the DRHS preparation is insensitive to B_1, the tagging efficiency will be proportional to the sine of the local B_1 field as hard pulses are used at the beginning and end of the preparation. To overcome this a BIR-4 pulse interspersed with velocity selective gradients (Schepers et al., 2003) was applied to VSASL (Wong and Guo, 2010). The BIR-4 is an adiabatic plane rotation pulse consisting of four units (Garwood and Ke, 1991). When there is no phase offset between the four units the pulse produces a 0° rotation. At the two zero points of the $|B_1|$ the magnetization is in the transverse plane, and gradients are inserted to impart the velocity selectivity.

Although the Velocity Selective pulses are only producing a saturation, it is possible to play multiple saturation units out to create multiple tagged boluses (Guo and Wong, 2011a). This is able to boost the SNR of VSASL to a comparable level to pCASL. However, this comes at a cost of increased SAR, especially for the high RF power required for the adiabatic velocity selective pulses.

2.3.2.2 Velocity Selective ASL Perfusion Experiment

Velocity Selective ASL is essentially a Pulsed ASL technique, the only difference being the order of the spatial moment that separates the arterial and tissue spins. Like PASL there is a tag and control image acquisition. In the tag condition the velocity selective pulse is applied to the entire RF coil field of view, without any

spatial selection. In this case the velocity selective gradients are played out with a first order moment

$$m_1^{tag} = \frac{\pi}{\gamma V_{\text{cut}}} \tag{2.46}$$

where V_{cut} is the chosen cutoff velocity. As in spatially tagged ASL, the tag acquisition will be dominated by background tissue signal that must be subtracted out from a control acquisition. In the control condition the same RF is applied, but the VS gradients are turned off so that $m_1^{control} = 0$. There is then an inflow time so as to allow the spins to travel down the arterial tree (fig. 2.7). For the readout module a 2D EPI, 2D spiral or 3D stack of GRASE spirals is typically used. In both conditions an image is acquired after inflow time (TI) where the same m_1^{tag} is applied in the readout, restricting the acquired signal to spins with velocity less than V_{cut}. The subtraction of tag from control is therefore sensitive to spins that have decelerated from above to below V_{cut} in time TI. This will eliminate signal from venous flow as this is generally accelerating out of the capillary bed (Zweifach and Lipowsky, 1977). As the velocity selective pulses act on the whole RF field of view, and the imaging will only cover a small proportion of this, a non-selective saturation pulse is used immediately after the imaging to reset the magnetisation.

Ideally the RF pulse would saturate, or invert, all spins above V_{cut}. However, the current state of the art is to apply a cosinusoidal M_z profile, which is a sinc velocity response in vessels that are laminar and are aligned with the gradient axis. This profile is non-ideal, assumes that the vessels allow mixing of the magnetisation (which may be incompatible with the assumption of laminar flow), and assumes that the vasculature is monotonically decelerating. However, by using the same V_{cut} in both tag and readout the leading and trailing edges of the bolus are defined in exactly the same way, so that the signal should be proportional to perfusion.

In theory, the V_{cut} will define both the transit time, and how far up the vascular tree the tail end of the VSASL signal will be. In order to reduce BAT the bolus must

be generated as close to the capillary bed as possible, which means that V_{cut} must be minimised. However, as V_{cut} is reduced, m_1^{tag} and the gradient duration increases, which reduces the tagging efficiency. There will also be an increased sensitivity to non-blood motion, such as CSF flow and bulk motion. There is therefore some user choice over which V_{cut} to select, and the direction that the gradients are applied in. The current consensus is that 2 cm/s is ideal for healthy grey matter, which is argued based on the lack of focal artefacts from large arteries (Wu and Wong, 2006), or that the perfusion signal is invariant with the gradient direction (Wong et al., 2006; Frank et al., 2008). It is hypothesised that this independence from gradient direction indicates that the bolus is originating from an isotropic distribution of laminar arterioles within a grey matter voxel. Although this may minimise the BAT, recent work has shown that when using a TI < 1.6 s, VSASL will overestimate perfusion using $V_{\text{cut}} = 1$ and 2 cm/s (Guo and Wong, 2012a). In addition to this, the VSASL signal actually implies a *negative* BAT when fitting using the full model (J. Guo, private communication), which is obviously non-physical.

Although the VSASL signal has been shown to be independent of gradient direction at a V_{cut} of 2 cm/s, in the healthy brain the calculated flow is higher in the z (head/foot) direction at a V_{cut} of 8 or 16 cm/s (Frank et al., 2008). This might be expected given that the flow is going to be delivered from the heart, so the extent of the labeled bolus is larger in this direction.

VSASL Applications

Recently, VSASL has started to transfer to the clinic with the method being applied in Moyamoya disease (Qiu et al., 2012), in which the large arteries collapse over a number of months and small collateral arteries form to bypass this. The authors compared VSASL to pCASL and Xenon clearance computed tomography. Those authors showed that VSASL perfusion values were less dependent on BAT compared

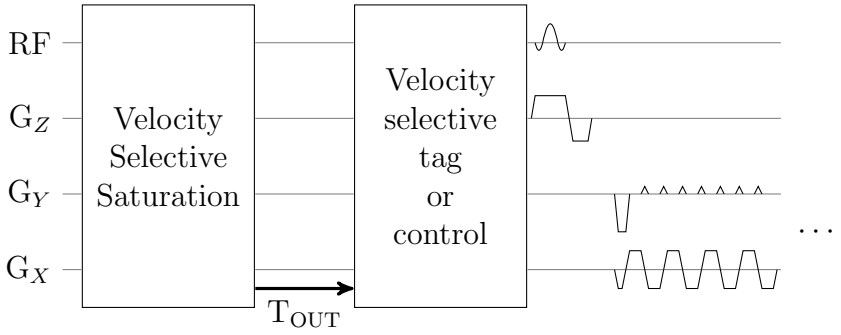


Figure 2.8: Simplified QUIXOTIC pulse diagram. First moving spins are saturated with the first velocity selective pulse. Tissue spins then flow into the venous compartment during outflow time T_{out}. The venous spins are then isolated with a velocity selective tag or control pulse immediately prior to an EPI readout. In practice an inversion pulse is applied between the two velocity selective pulses to account for relaxation of the tissue/venous spins.

to pCASL, when the BAT was defined as the time to peak on the CT scan. However, only single TI VSASL data were reported. Although multiple TI pCASL data were acquired, the authors fitted each TI to a kinetic model individually, assuming that the BAT was zero. This is potentially the source of the pCASL dependency on BAT.

VSASL has also been applied outside the brain, in the lungs (Guo and Wong, 2013) and prostate (Li and Metzger, 2013). Both these organs are challenging due to bulk motion, which may be erroneously encoded as flow. To overcome this Guo and Wong (2013) used background suppression, balanced steady state free precession to readout in the B_0 inhomogeneous lung, a timed breathing scheme and cardiac gated labeling using a long TR.

2.3.2.3 VSASL Beyond Perfusion

Along with perfusion, velocity selective pulses have been used to non-invasively isolate different compartments of the blood and measure different physiological properties including Oxygen Extraction Fraction, Venous Sources and Blood Volume.

QUIXOTIC and TRUST

Quantitative imaging of extraction of Oxygen and tissue consumption (QUIXOTIC) uses a pair of velocity selective pulses to isolate spins that accelerate out of the capillary bed and into the venous compartment (Bolar et al., 2011). Once the venous signal is isolated T_2 relaxometry is then performed. This T_2 is then converted into a measure of Oxygen Extraction Fraction (OEF) through using calibration data (Lu et al., 2012).

QUIXOTIC is essentially a voxelwise T_2 Relaxation Under Spin Tagging (TRUST) measurement (Lu and Ge, 2008). The blood is considered to be composed of erythrocytes and plasma, with water able to rapidly exchange between the two compartments. As deoxyhemoglobin has a shorter T_2 than oxyhemoglobin, which is again different from plasma, the T_2 of the composite will depend on the hematocrit and the oxygenation of the blood (van Zijl et al., 1998). The T_2 can be measured with a Carr-Purcell-Meiboom-Gill (CPMG) sequence, which is a 90_x pulse followed by a train of echos comprising a delay of $\frac{\tau_{\text{CPMG}}}{2}$, a 180_y refocussing and another $\frac{\tau_{\text{CPMG}}}{2}$ delay. Spin echos are spaced by τ_{CPMG}, at which points the T_2 decay can be sampled. As the spins are diffusing during the experiment they will sample different off resonances that may not be refocussed, so the T_2 measured will depend on the τ_{CPMG} time. Modeling the blood as diffusion of water amongst weakly magnetised spheres best fits the data using preclinical 2.35 T and 7 T systems (Gardener et al., 2010). However, several studies simply generate a calibration surface relating T_2, OEF and Hct for the field strength and pulse sequence the authors wish to use later (Lu et al., 2012). These calibration data are then fitted to a 2 compartment rapid exchange model (Luz and Meiboom, 1963). One of the key problems is extrapolation from the calibration data to disease states, and that some numbers generated for the fit to the model are non-physical, such as a negative plasma T_2 (Lu et al., 2012).

The TRUST sequence is able to report on whole brain oxygen extraction frac-

tion, if the hematocrit is known through another experiment (Lu and Ge, 2008). The signal from the saggital sinus is localised by using a PICORE ASL preparation, but with the inversion volume above the imaging slice. The signal is then T_2 mapped using a global CPMG pre-pulse consisting of 4 refocussing pulses with phases $[\pi/2, \pi/2, -\pi/2, -\pi/2]$, which is more robust to B_1 inhomogeneity, followed by an EPI readout. TRUST has not yet been validated in human venous blood, but changes in arterial oxygenation through use of a 14% O_2 gas challenge correlated with pulse oximeter measurements (Lu et al., 2012).

TRUST assumes that the venous blood being sampled is representative of the whole brain. OEF is about 40% in healthy brain, but locally increased in stroke when the perfusion supply cannot meet the metabolic demand of the tissue (Derdeyn et al., 2002). Consequently QUIXOTIC was developed to isolate the venous signal on a voxelwise basis, and then perform the same T_2 mapping in order to measure OEF.

In QUIXOTIC it is assumed that the arterial and venous spins are saturated using a velocity selective pulse (Bolar et al., 2011). Then there is a delay, where the spins flow down the vascular tree and fully relaxed spins from the tissue bed enter the venous compartment. There is then a second velocity selective pulse, where the control condition will excite all spins, and in the tag condition the velocity selective pulse saturates spins in the venous compartment. The subtraction of tag from control is an image which is proportional to the number of spins that have left the tissue compartment and entered the venous compartment in the delay time. In the original implementation a TRUST and QUIXOTIC measurement was performed, but the QUIXOTIC measurement returned a longer T_2 in the brain (86 ms) than in the saggital sinus (58 ms). The authors of the study attributed this to incomplete extraction of O_2 at the point of the QUIXOTIC measurement (Bolar et al., 2011). However, the technique has very low SNR as, unlike ASL, the signal does not build up in the venous compartment and an inversion pulse must be used in-between the velocity selective

pulses to suppress the arterial signal. This low SNR could bias the T_2 results if the noise floor is not taken into account, although as the technique is a subtraction the noise may not be rician distributed if the SNR is high (Zhao and Meyer, 2012).

VSEAN

It has been hypothesised that the mismatch between the saggital sinus and tissue T_2 in QUIXOTIC could be due to diffusion effects from partial volume of CSF (Bolar et al., 2011). As the velocity selective gradients are on in the tag condition and off in the control condition, along with there being a difference in first gradient moment m_1 there is also a difference in diffusion b-value. In VSASL this is hypothesised to be insignificant at 2 cm/s (Wong et al., 2006). Nevertheless, the Velocity Selective Excitation with Arterial Nulling (VSEAN) (Guo and Wong, 2012b) is a sequence that increases the accuracy of QUIXOTIC measurement through designing a diffusion balanced acquisition that increases SNR.

To increase SNR VSEAN removes the first velocity selective pulse in QUIXOTIC and replaces this with a PICORE inversion of the arterial spins. Then a delay time is inserted so that the arterial spins are nulled at the time of the acquisition for both tag and control cases, essentially an inflow-VASO preparation (Donahue et al., 2010). During this time spins from the tissue will enter the venous compartment, and will have a larger M_z than in QUIXOTIC as the intermediate inversion pulse is not used. The venous spins are then isolated using a pair of velocity selective pulses, but with the gradients on in both tag and control cases to balance diffusion effects. This is achieved using a velocity selective excitation to directly image the venous compartment, where the phase of the last segment of the BIR-4 is increased by $\pi/2$. Instead of producing $M_z \propto \cos(\gamma m_1 v)$, this will produce $M_z \propto \sin(\gamma m_1 v)$. If there are spins that have opposed velocites in the same voxel the signal will cancel out, so a second velocity selective preparation is applied so that $M_z \propto \sin^2(\gamma m_1 v)$ in the

control acquisition. As mentioned in the original publication, it was found that the static tissue suppression using this technique was not adequate, so a tag acquisition to determine the phase of the static tissue was added. The control acquisition is projected on to this phase, such that the imaginary signal is from the moving spins, and the real signal is from the tissue.

The VSEAN technique was successful in removing the mismatch between the sagittal sinus and tissue T_2. However, the signal will only be sensitive to velocities where $n\gamma m_1 v = \pi/2$, where n is an integer. In addition to this the phase of the static tissue is not guaranteed to be constant between repetitions, as this can drift during the EPI scan. Generation of the $\sin^2$ dependence on velocity relies on complete spoiling between the first and second velocity selective units, which may be difficult to achieve in practice.

VENTI

Venous Territory Imaging using remote sensing (VENTI) is a recently proposed technique that determines the tissue origin of venous blood in different vessels (Wong and Guo, 2013). The tissue is Fourier encoded using a preparation that spatially modulates M_z. This is immediatly followed by a velocity selective pulse to saturate spins in the veins. Then there is a delay for the tissue spins to exchange into the venous system followed by a rapid angiographic readout. Data are acquired with different spatial Fourier components so that the signal in any given particular vein can be tracked to a location in the tissue, analogous to perfusion territory imaging with ASL (Wong, 2007). This could potentially be combined with a TRUST measurement in the same veins using a phase contrast venography (Krishnamurthy et al., 2013), to return a local OEF. However, the large number of Fourier components required to spatially encode the tissue limits the VENTI spatial resolution, but the problem may be ideal for compressed sensing acceleration (Lustig et al., 2007).

accASL

Velocity selective preparations can also be extended to higher orders of motion, such as acceleration. It has been shown in periphial angiography that there is greater contrast between the arteries and veins using acceleration rather than velocity (Priest et al., 2011), due to the greater deceleration rate of arterial spins. This has been applied to ASL by inserting a single acceleration selective preparation a time TI before the acquisition (accASL) (Schmid et al., 2013). It is hypothesised that the accASL signal is more blood volume weighted, principally because the arterial signal that is crushed in VSASL is included in accASL. The crushing with the second velocity selecitve preparation in VSASL makes the technique sensitive to deceleration spins by excluding both arterial and venous signal. Depending on the cutoff acceleration used venous signal could contribute to the accASL signal. The accASL signal will also be generated at points in the arteries that are changing in velocity, which may be due to the cardiac cycle or bifurcations, and like VSASL this may not result in a contiguous bolus.

2.3.3 Background Suppression

The perfusing arterial spins will only replace on the order of 1% of the voxel's signal during the inflow time, so the signal in any tag or control acquisition will be dominated by the static background signal. Therefore any fluctuations in the background signal due to physiological noise can produce large errors in the perfusion weighted subtraction. A method to increase the temporal stability of the ASL data is to suppress the static tissue using a combination of saturation and inversion pulses prior to the acquisition, known as background suppression (Ye et al., 2000a). In spatially selective ASL this is typically achieved by pre-saturating the imaging volume by using a series of 90° pulses and spoilers (Haase et al., 1985). Then the labeling is applied before a number of background suppression inversion pulses are played out. The timing

of the pulses can be chosen to null a particular T_1. Increased numbers of T_1 species can be nulled as the number of inversion pulses is increased (Mani et al., 1997). For example, if two pulses are applied with inversion times τ_1^{BS} and τ_2^{BS} given by

$$\tau_{1,2}^{BS} = \mathrm{TI} + 2T_{1,opt} \ln \left[\left(\frac{1}{2} \pm \frac{1}{4} \right) + \left(\frac{1}{2} \mp \frac{1}{4} \right) \exp \left(- \frac{T_{1,opt} \cdot \mathrm{TI}}{2} \right) \right] \tag{2.47}$$

prior to the image acquisition, then at time TI the two T_1 species with T_1 values of $T_{1,opt}$ and $2T_{1,opt}$ will be nulled (Günther et al., 2005). With perfect inversions pulses background suppression does not reduce the perfusion SNR, as the contrast is decaying with T_1 from the time of the labeling pulse.

In 2D acquisitions different slices are being excited at different inflow times, typically from inferior to superior in the brain. During this time the background tissue will be recovering with T_1, so the effectiveness of the background suppression will vary from slice to slice. For a 3D acquisition there is only one excitation per TR, leading to uniform background suppression over the whole volume.

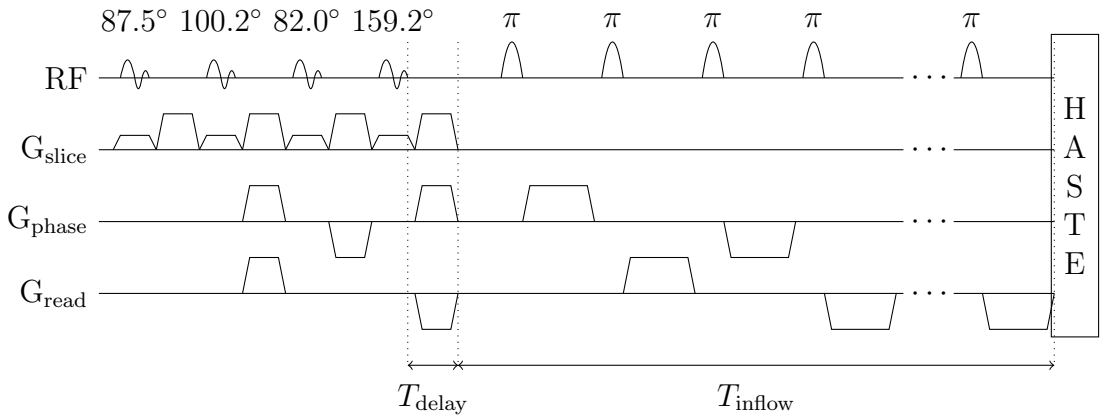
Some care must be taken when applying background suppression as if the tissue signal is exactly zero, the perfusion signal will be complex for TI less than the null time of blood, so a magnitude subtraction would underestimate perfusion. A strategy to avoid this is to set the null time of tissue to be prior to the first image acquisition so that the tissue signal is always positive, and a magnitude subtraction can be taken for the perfusion weighted data. Background suppression will also reduce the contrast of the un-subtracted data, which could introduce errors if using motion registration algorithms for perfusion reconstruction in moving organs (Gardener and Francis, 2010). Background suppression is more efficient for longer T_1 species in PASL due to the large amount of dead time between labeling and imaging, which is filled by the labeling pulse in pCASL.

SEEPAGE

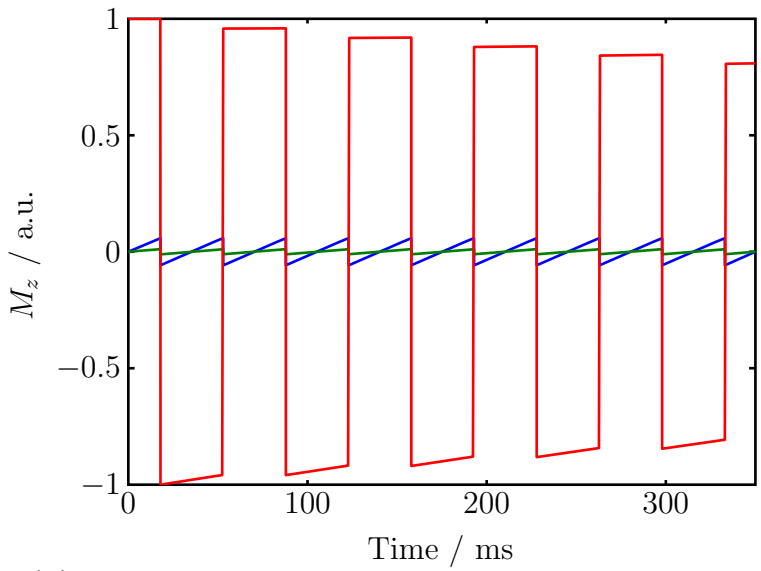
Background suppression can be taken to the limit with non-subtraction ASL, such as Spin Echo Entrapped Perfusion Imaging (SEEPAGE) (Blamire and Styles, 2000). Non-subtraction ASL excites at the null time of static tissue acquiring signal from only the inflowing spins, removing the need for a control image and subsequent subtraction (Duyn et al., 2001). As there is no subtraction SEEPAGE is potentially more robust to motion artefact, particularity when trying to measure perfusion in moving organs, such as the lungs (Fischer et al., 2008) and kidneys (Robson et al., 2009). SEEPAGE saturates the imaging region before playing out a series of equally spaced global inversion pulses, typically 10 to 20, during the inflow time (Blamire and Styles, 2000). These inversions prevent M_z recovery of the saturated imaging region, whereas the unsaturated inflowing spins will keep a component of M_z at the time of excitation (Fig. 2.9b). As there is only one null time for the static spins, the technique is limited to a single slice. Like FAIR, the SEEPAGE sequence is sensitive to flow from either side of the imaging region.

Although SEEPAGE has the potential to provide quantitative perfusion information, in practice this was found to be difficult to achieve. In standard ASL, imaging artefacts that are present in the tag condition are ideally subtracted out in a well designed control acquisition. As there is no subtraction in SEEPAGE the sequence must be carefully designed to achieve an artefact free image. The principal source of artefacts is from static tissue, which must be saturated to a level much lower than the perfusion signal at the beginning of the sequence, and then this saturation must be maintained throughout the inflow time using the inversion pulses.

Previous implementations of SEEPAGE used Chemical Shift Selective (CHESS) water suppression (Haase et al., 1985) for slice saturation, and hard inversion pulses during the TI. CHESS is a series of spatially selective 90° RF pulses followed by spoilers to saturate static tissue, however, the saturation efficiency with CHESS will



(a) SEEPAGE Pulse Diagram



(b) Magnetisation during the SEEPAGE inversion train

Figure 2.9: The pulse diagram for SEEPAGE which consists of a slice selective saturation followed by a train of inversion pulses (2.9a), which is tailored to null grey matter spins (green), whilst preserving the inflowing blood signal (red) (2.9b).

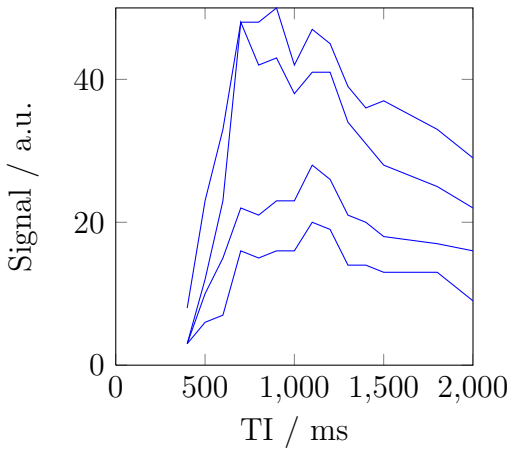


Figure 2.10: SEEPAGE Signal in four voxels located in the Internal Iliac artery in arbitrary units showing the inflow of labeled blood into the imaging region.

depend on the T_1 of tissue and local B_1. SEEPAGE was implemented on the FMRIB Verio using water suppression enhanced through T_1 relaxation (WET) (Golay et al., 2005), with adiabatic hyperbolic secant pulses for inversion. WET consists of four variable angle RF pulses which were optimised to produce a spatial saturation over a pre-determined range of T_1 and B_1.

The WET-SEEPAGE sequence was then tested in the pelvis of healthy volunteers at multiple inflow times. For each TI twenty inversion pulses were used so that T_2 and MT losses during the adiabatic pulses remained constant. The time between the pulses was altered to give a range of TI from 400 - 2000 ms. In the brain no perfusion signal was detected above the noise floor in an axial slice. The signal time course in the internal iliac artery shows the expected inflow and washout due to T_1 decay (Fig. 2.10), demonstrating that although the arterial spins are being tagged they are not being detected in the tissue.

The lack of signal could be be due to either low perfusion or a long BAT, where not enough arterial spins are reaching the tissue. It could also be due to magnetisation transfer, where the series of inversion pulses will introduce MT effects during the TI, which will then saturate any perfusing spins that have exchanged into the tissue. In addition to this the perfusion signal will be reduced by α^n, where α is the inversion

efficiency of the n adiabatic pulses, resulting in an inherently low SNR.

2.3.4 ASL Readout

The only requirement of the ASL readout is that it is principally sensitive to M_z to detect the changes from the inflow of blood. Rapid imaging is most commonly used due to the many averages of tag and control acquisitions required to sample the low SNR ASL signal. In the brain, 2D EPI is the most common readout used for ASL, sometimes with a spin-echo to refocus signal dropout due to B_0 inhomogeneity. However, 2D readouts are not optimal for background suppression and the multiple excitations result in TI varying from slice to slice.

3D readouts, where the whole imaging slab is excited and a second phase encoding in the third dimension is performed, have the advantage of increasing spatial SNR by acquiring signal from the whole volume. However, some of this increase in spatial SNR may be due to blurring in the third dimension from T_2 decay during the readout window, especially if single shot acquisitions are used. Nevertheless, it has recently been shown in the brain that 3D GRASE or 3D stack of spirals offers a two fold increase in spatial SNR compared to 2D EPI, and that background suppression increases the temporal SNR by 3 fold compared to the unsuppressed 3D sequence (Vidorreta et al., 2012).

Rapid imaging outside the brain is more of a challenge as there is increased motion and B_0/B_1 inhomogeneity. Sources of motion include not only cardiac and respiratory related movements which can be gated using bellows or a pulsed oximeter, but also stomach motion and peristalsis of the intestines and bowels. At 3 T the size of the trunk can be on the order of the wavelength of the RF excitation pulse, so standing wave artefacts can be found, similar to head imaging at 7 T. However, if 90° pulses are used the B_1 errors associated with the readout are minimised, but this may introduce large errors in small tip angle look-locker ASL (Günther et al., 2001). Compared

to the brain, there are more sources of field inhomogeneity in the body, such as air in the intestinal system, and as a larger area is generally imaged this is more difficult to shim. For these reasons EPI (or segmented EPI) is a challenge outside the brain. Some studies have had success using EPI with Spin Echos and parallel imaging to reduce the distortion (Gardener and Francis, 2010). Readouts such as Half Fourier Acquisition Single Shot Turbo Spin Echo (HASTE) (Robson et al., 2009), and balanced SSFP with magnetisation preparations (Park et al., 2013) are used as these are more robust to B_0 inhomogeneity than EPI. At 1.5 T, where B_0 inhomogeneity is less of an issue, it has been shown that 3D-GRASE FAIR using 3 shots is feasible in the kidneys (Cutajar et al., 2012).

2.3.5 Quantification of ASL

Buxton et al. (1998) proposed a general model for quantifying ASL data which has become the standard model in the literature. The model assumes that blood is being delivered by uniform plug flow and that once the arterial spins arrive in the voxel they are instantaneously extracted from the vasculature into a single tissue compartment. The tag control subtraction can then be described by

$$\Delta M(t) = 2M_{0,b}f \int_0^t c(t')r(t-t')m(t-t')dt' \tag{2.48}$$

$$= 2M_{0,b}f \left(c(t) * [r(t)m(t)]\right) \tag{2.49}$$

where the factor 2 indicates that an inversion is used to tag the blood, $M_{0,b}$ is the equilibrium magnetisation of a voxel of blood, f is perfusion and $*$ represents a convolution. The arterial delivery function, $c(t)$, represents the magnetisation being

delivered to the voxel, and is given by

$$c(t) = \begin{cases} 0 & 0 < t < \text{BAT} \quad (2.50) \\ \alpha \exp\left(-\frac{t}{T_{1,b}}\right) & \text{BAT} < t < \tau + \text{BAT (Pulsed)} \quad (2.51) \\ \alpha \exp\left(-\frac{\text{BAT}}{T_{1,b}}\right) & \text{BAT} < t < \tau + \text{BAT (Continuous)} \quad (2.52) \\ 0 & \tau + \text{BAT} < t \quad (2.53) \end{cases}$$

where α is the *inversion* efficiency, for a saturation used in VSASL this is a maximum of 0.5. For a TI less than the bolus arrival time (BAT) there is no ASL signal as the magnetisation is still in the artery. Once the bolus is labeled the contrast will decay with the T_1 of blood, $T_{1,b}$. For inflow times longer than BAT but shorter than the bolus length (τ) the magnetisation will depend on the labeling used. For pulsed labeling the leading edge of the bolus will have experienced less $T_{1,b}$ decay than the trailing edge, due to the length of the artery that is labeled. For continuous labeling the entire bolus experiences the same decay, simply the bolus arrival time from labeling plane to voxel. It is this difference that results in a higher SNR from CASL, theoretically by a factor e (Wong et al., 1998b).

The residue function, $r(t)$, represents the clearance of the bolus from the tissue to the venous compartment, assuming that the ratio of tissue to venous concentration is given by the blood water partition coefficient, λ. Additionally, $m(t)$ represents the T_1 decay of the contrast once it has exchanged into the tissue.

$$r(t) = \exp\left(-\frac{ft}{\lambda}\right) \quad (2.54)$$

$$m(t) = \exp\left(-\frac{t}{T_1}\right) \quad (2.55)$$

In order to compare values of perfusion between sessions $M_{0,b}$ needs to be determined. The data must be normalised for receive coil sensitivity, either using a body

coil acquisition or a pre-scan normalisation (Belaroussi et al., 2006). Measuring $M_{0,b}$ directly is challenging due to the low resolution of ASL data, so a calibration tissue is often used. Common approaches are to use ventricular CSF as a reference and correct for the relative relaxations of CSF and blood such that

$$M_{0,b} = R \cdot M_{0,CSF} \exp\left(\frac{TE}{T^{(*)}_{2,CSF}} - \frac{TE}{T^{(*)}_{2,b}}\right) \tag{2.56}$$

where R is the relative blood/CSF proton density. Similarly, an average of grey matter and white matter, or the segmented grey and white matter compartments can be used as a reference. There is no significant difference between mean grey matter f when calibrated with each of the methods, but the ratio of grey to white matter does depend on the method used, with the segmented tissue calibration being the most accurate (Yang et al., 2011).

The more parameters that need to be determined from the data, the more uncertainty there is in those parameters especially in the case of low SNR. The commonly assumed parameters are λ, the tissue blood partition coefficient, which represents the relative water concentrations of the labeled bolus in the blood and tissue pools, and in the brain a value of 0.9 ml/g is used (Herscovitch and Raichle, 1985a). The T_1 of tissue and blood are have been measured separately and are commonly assumed, but $T_{1,t}$ should be measured in pathology. If a multiple TI acquisition is performed it is possible to estimate $T_{1,t}$ from the decay of the perfusion signal in ΔM. Unless sequences are used to limit the maximum BAT, such as QUIPSSII (Luh et al., 1999), three parameters must be determined for a PASL experiment: BAT, τ and f. For CASL the bolus length is known, so only the BAT and f need to be determined on a voxelwise basis. In VSASL, it is typically assumed that BAT = 0, so only f needs to be determined.

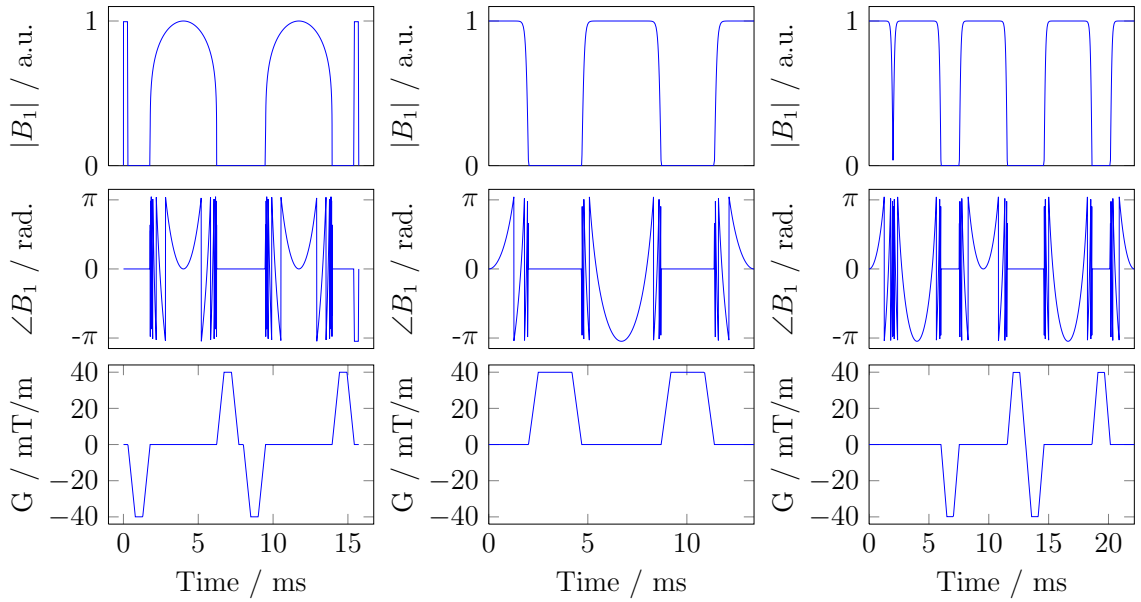
Chapter 3

Physical and Hardware Effects in VSASL

In this chapter the physical limitations of a VSASL experiment are explored. These are fundamental errors that have origins in the scanner hardware, and when the experiment is performed in the presence of inhomogeneous magnetic fields.

Inhomogeneous static (B_0) and radiofrequency (B_1) magnetic fields are known to cause an underestimation of perfusion with VSASL (Duhamel et al., 2003). Additionally, the standard VSASL sequence is not eddy current balanced, since the velocity encoding gradients played out in the tag acquisition are not played out in the control acquisition. Whilst artefacts in VSASL have been attributed to eddy currents (Wong et al., 2006), the magnitude and spatial distribution of these has not previously been studied.

The hypothesis in this chapter is that eddy currents will cause a systematic overestimation of perfusion through erroneous tagging of static tissue. Two previous velocity selective preparations are compared: a Double Refocused Hyperbolic Secant (DRHS) (Wong et al., 2006) and a four segment BIR (BIR-4) (Wong and Guo, 2010). Also introduced is an eight segment BIR preparation (BIR-8), which additionally



(a) DRHS **(b)** BIR-4 **(c)** BIR-8

Figure 3.1: Pulse diagrams for DRHS (3.1a), BIR-4 (3.1b) and BIR-8 (3.1c) with $G_{\mathrm{MAX}} = 40$ mT/m at $V_{\mathrm{cut}} = 2$ cm/s. Displayed are the absolute RF (top), RF phase (middle) and tag condition gradients (bottom). In the control condition the gradients are zero.

reduces eddy current effects whilst maintaining the B_0 and B_1 insensitivity of BIR-4.

3.1 Design of a B_1 and Eddy Current Insensitive VS Pulse

In the VSASL tag condition a velocity selective preparation will produce longitudinal magnetisation $M_z \propto \cos(\gamma m_1 v)$, where v is the velocity of the spins and m_1 is the first moment of the velocity encoding gradients. Most previous studies have used the DRHS preparation (fig. 3.1a) (Wong et al., 2006; Wu and Wong, 2006; Frank et al., 2008; Qiu et al., 2012).

The DRHS preparation first tips the magnetisation from the longitudinal to the transverse plane using a hard 90° pulse. Four velocity encoding gradients then impart phase $\phi = \gamma m_1 v$ to the transverse magnetisation component. A second hard 90° pulse

is played out with π phase, which tips the spins back up from the transverse plane to the longitudinal plane. The preparation is insensitive to ΔB_0 as between the velocity encoding gradients two adiabatic hyperbolic secant pulses are applied to cancel out any phase increments due to B_0 inhomogeneity. However, the preparation is sensitive to ΔB_1, which will result in a spatially varying tagging efficiency (Wong and Guo, 2010). This because a spatially inhomogeneous B_1 gives rise to a spatial variation in the tip angle of the hard RF pulses, which is given by $\theta = \gamma B_1 t$, where t is the length of the pulse. The velocity encoding gradients will only impart phase to the transverse component of the magnetisation, so the labeling efficiency is reduced if the tip angle is not 90°. The result is that the labeling efficiency of the DRHS is proportional to $\sin(B_1(r))$.

To overcome the spatial variation in labeling efficiency a velocity selective BIR-4 pulse was proposed (Wong and Guo, 2010). The BIR-4 pulse consists of a reversed AHP, which adiabatically tips longitudinal magnetisation down to the transverse plane, followed by an AFP that when applied with π phase rotates the transverse magnetisation in plane, and an AHP that returns the magnetisation to the longitudinal plane. The result is that BIR-4 pulses produce an adiabatic 0° tip of longitudinal magnetisation. Segmented 0° BIR-4 pulses had previously been proposed as a B_1 insensitive T_2 preparation (Nezafat et al., 2009). T_2 weighting is imparted by adding equal delays between before and after the AFP, where the spins are in the transverse plane. To impart velocity sensitivity, Wong and Guo (2010) added monopolar gradients at these points (fig. 3.1b). Velocity selective BIR-4 pulses had previously been used to crush vascular signal in a FAIR acquisition (Schepers et al., 2003), but were developed independently and applied to VSASL by Wong and Guo (2010).

In VSASL two acquisitions are made, a tag acquisition with the velocity encoding gradients on, and a control acquisition with the gradients off so that $m_1 = 0$. Eddy currents generated by the velocity selective preparation in the tag acquisition are not

present in the control. It has previously been hypothesised by Wong et al. (2006) that using bipolar gradients in the VS preparation reduces eddy current errors, similar to the approach adopted in diffusion imaging (Reese et al., 2003). To include the bipolar gradient concept to the improved B_0 and B_1 insensitive BIR preparation an eight segment "BIR-8" VS preparation is proposed here.

3.1.1 Methods

To incorporate the bipolar gradient pattern two BIR-4 pulses are applied sequentially, resulting in four zero points of the RF amplitude function, $A(t)$ (fig. 3.1c). The doubling of the number of BIR segments from four to eight maintains RF pulse symmetry about the mid point of $A(t)$, and therefore theoretically preserves the B_0 insensitivity of the preparation. Velocity encoding gradients were then inserted at the last three zero points of $A(t)$, such that the delay between the AFP pulses had a 0:1:2:1 ratio. As the AFP pulses act as a 180° plane rotation, albeit imparting quadratic phase, the phase increments from ΔB_0 inhomogeneity during the first and third delay will be cancelled out by the second and fourth (Conolly et al., 1991).

Both the BIR-4 and BIR-8 preparations were designed to be insensitive over ΔB_0 = ±250 Hz with an adiabatic threshold of 15 μT, chosen as these are typical (n = 3) worst case values in the brain on the Verio system, by optimising the tunable parameters ζ, κ and ω_{MAX} (see section 2.2.3.1) through Bloch equation simulations. A brute force search was carried out where ζ was varied from 1 to 30, $\tan(\kappa)$ was varied from 1 to 100 and ω_{MAX} was varied from 1 to 500 KHz. A static spin was simulated with off resonance from 0 to 1000 Hz at 15 μT. The parameter set with the largest bandwidth at $M_z = 0.99$ was then chosen. The segment length was set to 2 ms to minimise SAR. The DRHS preparation matched the one used in Wong et al. (2006), with hard pulse length 600 μs, and hyperbolic secant parameters $\mu = 6$, β = 800 and cosine window power 0.2.

In both the simulations and experiments the duration of the velocity encoding gradients is calculated to produce $m_1 = \frac{\pi}{\gamma V_{\text{cut}}}$. For the bipolar gradient pattern used in the DRHS and BIR-8 the first gradient moment is given by

$$m_1^{\text{bi}} = \int_0^T G(t)tdt = 4 \cdot G_{\text{MAX}} \cdot (\text{F} + \text{R}) \cdot \left(\text{F} + 2\text{R} + \frac{T_{RF}}{2}\right) \tag{3.1}$$

where G_{MAX} is the chosen maximum gradient strength, F is the flat top time of an individual gradient lobe, R is the gradient rise time which was fixed at 0.5 ms and T_{RF} is the time between gradient pulses (the duration of a hyperbolic secant, 4.4 ms, or AFP, 4 ms). For the monopolar gradient pattern used in the BIR-4 the first gradient moment is

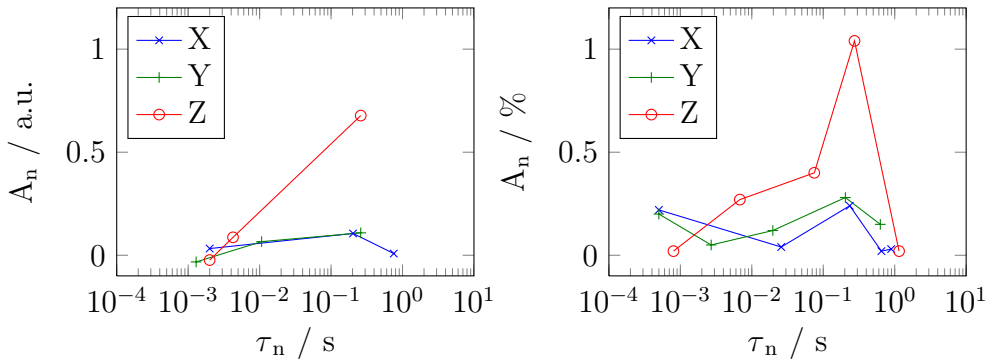
$$m_1^{\text{mono}} = G_{\text{MAX}} \cdot (\text{F} + \text{R}) \cdot (\text{F} + 2\text{R} + T_{RF}) \tag{3.2}$$

where T_{RF} is the duration of an AFP (4 ms). The gradient duration must be on the 10 μs raster time of the Siemens scanner. For each G_{MAX} and m_1 combination the flat top time was calculated and then rounded up to the nearest 10 μs. Then the applied gradient strength was reduced so that m_1 was applied exactly.

Bloch equation simulations were then used to determine the labeling efficiency, and to evaluate the response of the three preparations to ΔB_0 and ΔB_1 inhomogeneity and eddy currents. In these simulations V_{cut} was 2 cm/s and G_{MAX} was 40 mT/m. The simulation was implemented in MATLAB 2012a (The MathWorks Inc., Natick, MA, USA) and considers a rotation of the normalised magnetisation about B_{eff} followed by relaxation with a timestep of 5 μs.

Simulations: ΔB_0, ΔB_1, and Labeling Efficiency

To determine the adiabatic threshold of the three pulses moving spins were simulated with velocities -4 cm/s to 4 cm/s in 20 steps and $|B_1|$ was 0 μT to 30 μT in 20 steps.



(a) B_0 Eddy Currents **(b)** G Eddy Currents

Figure 3.2: The applied eddy current compensation for B_0 terms (3.2a) and direct linear gradient terms (3.2b) on the FMRIB Verio.

To determine the effect of off resonance $|B_1|$ was set to 20 μT and ΔB_0 ranged from -250 Hz to 250 Hz in 20 steps. In both of these simulations relaxation was ignored, and the magnetisation was initially fully relaxed.

The predicted tagging efficiency for each preparation was also determined by simulation. As adiabatic pulses are used the relaxation decay of the bolus during the preparations is a mix of T_1 and T_2 effects (Wang et al., 2012). For each preparation the response of arterial spins was simulated with $|B_1| = 20$ μT, v = 0 and 2 cm/s, assuming 3 Tesla arterial $T_1 = 1664$ ms (Lu et al., 2004) and $T_2 = 150$ ms (Zhao et al., 2007). The tagging efficiency, α, for each preparation is then given by

$$\alpha = \frac{M_z(v=0) - M_z(v=2)}{2} \tag{3.3}$$

where M_z is the longitudinal magnetization at the end of each preparation.

Simulations: Eddy Currents

For each preparation the effect of the preparation on static spins in the presence of eddy currents was also simulated. Eddy current effects are modeled as linearly independent components with eddy current amplitudes A_n and time constants τ_n (Vaals and Bergman, 1990). The additional gradient due to eddy currents ($g(t)$) is

given by

$$g(t) = -\frac{dG(t)}{dt} * \sum_n H(t) A_n \exp\left(-\frac{t}{\tau_n}\right) \tag{3.4}$$

where $*$ represents convolution with the desired gradient waveform, $G(t)$, and $H(t)$ is the unit step function. Static spins were then simulated at different positions from gradient isocentre (limits ± 25 cm). τ_n was logarithmically spaced from 10^{-4} s to 1 s in 20 steps and $A_n = 0.25$ %. This value of A_n was chosen as this is the average of the spatial eddy current pre emphasis that is applied on the FMRIB Verio scanner (fig. 3.2b). Only the presence of a single time constant τ_n was considered and relaxation was ignored. It was assumed that the eddy currents acted on the same gradient axis as the velocity encoding gradients. G_{MAX} was set to 10 mT/m and 40 mT/m.

The effect of B_0 eddy currents was simulated by adding a temporally varying $\Delta B_0(t)$ offset during the pulse given by

$$\Delta B_0(t) = -\frac{dG(t)}{dt} * \sum_n H(t) A_n \exp\left(-\frac{t}{\tau_n}\right) \tag{3.5}$$

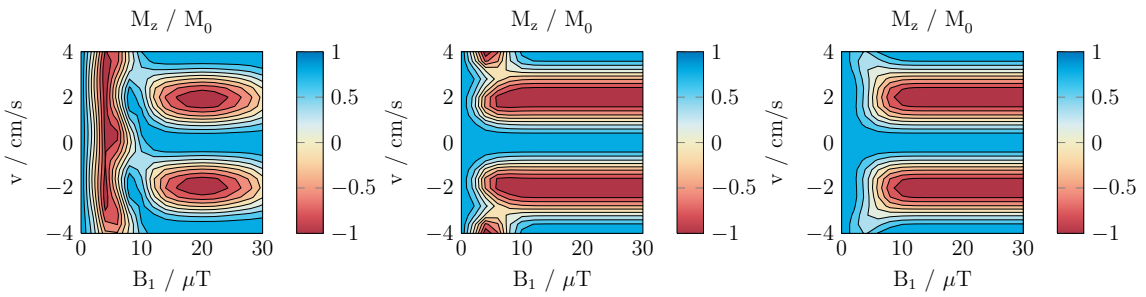
where A_n was set to 0.05%, this was chosen empirically as the conversion from the Siemens calibration amplitudes (fig. 3.2a) to frequency is not known, and τ_n was logarithmically spaced from 10^{-4} s to 1 s in 20 steps.

3.1.2 Results

Simulations: ΔB_0, ΔB_1, and Labeling Efficiency

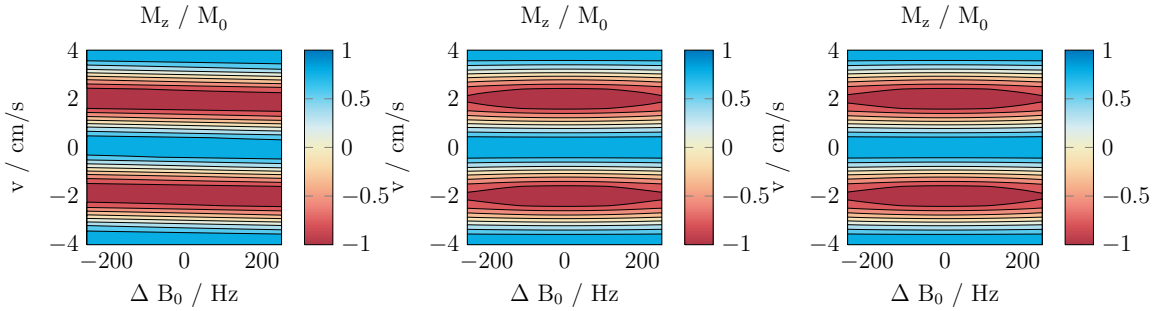
For the DRHS preparation the simulations show that the expected $M_z \propto cos(v)$ is produced when $|B_1| = 20$ μT (fig. 3.3a). However, as $|B_1|$ is either increased or decreased the tagging efficiency is reduced, and below 10 μT the response is complex as the adiabatic threshold is not reached.

For the BIR-4 (fig. 3.3b) and BIR-8 (fig. 3.3c) the dependency on $|B_1|$ is removed



(a) DRHS **(b)** BIR-4 **(c)** BIR-8

Figure 3.3: Simulations of the response of moving spins to a DRHS (3.3a), BIR-4 (3.3b) and BIR-8 (3.3c) velocity selective pulse at $V_{\text{cut}} = 2$ cm/s. Above the adiabatic threshold (10 μT) the BIR-4 and BIR-8 produce $M_z \propto \cos(v)$. The efficiency of the DRHS is maximised at 20 μT.



(a) DRHS **(b)** BIR-4 **(c)** BIR-8

Figure 3.4: Simulations of M_z after the application of a DRHS (3.4a), BIR-4 (3.4b) or BIR-8 (3.4c) velocity selective pulse for moving, off resonant spins. All pulses produce the desired cosinusoidal variation in velocity.

as the cosinusoidal response is produced for all $|B_1|$ above the adiabatic threshold at ≈ 10 μT.

At 20 μT all preparations are insensitive to ΔB_0 (fig. 3.4) due to their symmetry about $\Delta B_0 = 0$. However, it can also be observed that the modulation is slightly skewed for the DRHS preparation. The tagging efficiency reduced to 90% as ΔB_0 is increased to 250 Hz for both the BIR-4 and BIR-8, even when ignoring relaxation effects.

Although the first two segments of the BIR-8 look unnecessary, they are required to impart the B_0 insensitivity. If these are not played out the resulting magnetisation

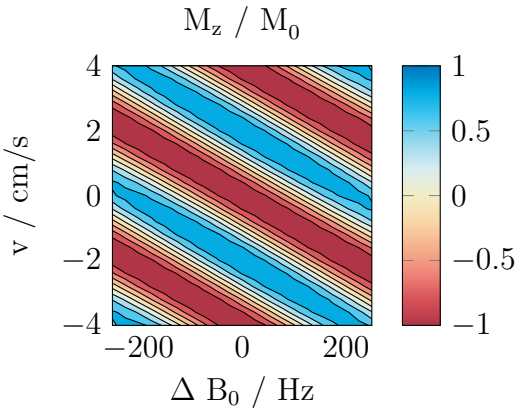


Figure 3.5: Simulation of the response to a BIR-6 pulse for moving and off resonant spins. For $\Delta B_0 = 0$ the signal is proportional to $-\cos(v)$.

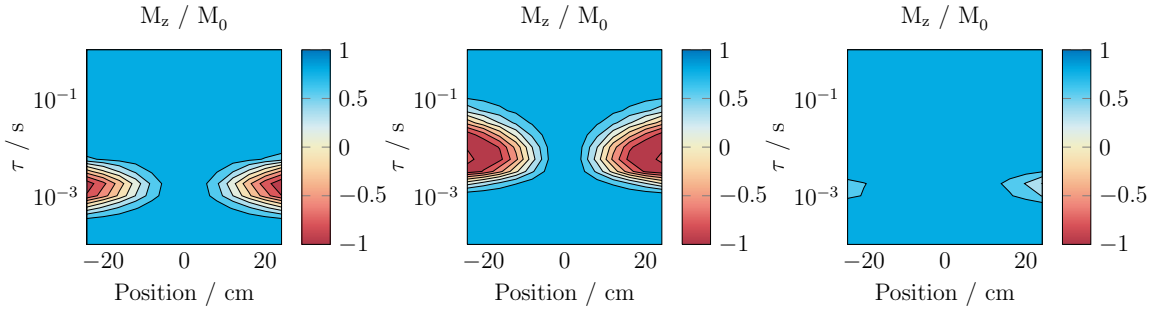
is proportional to $-\cos(v)$, and the ΔB_0 response is not symmetric (fig. 3.5).

When considering relaxation the tagging efficiency for on-resonant spins was found as $\alpha_{\text{DRHS}} = 0.92$, $\alpha_{\text{BIR-4}} = 0.93$, $\alpha_{\text{BIR-8}} = 0.89$.

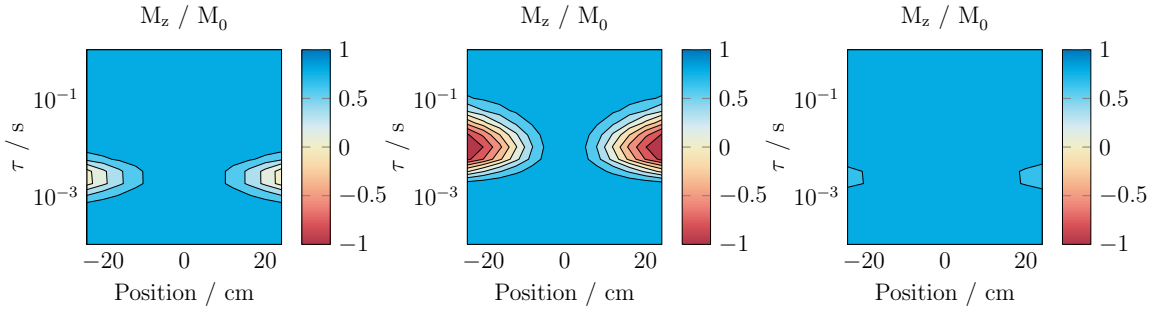
Simulations: Eddy Currents

Figure 3.6 shows the predicted response of static spins to the velocity preparations with $G_{\text{MAX}} = 10$ mT/m and 40 mT/m at $A_n = 0.25$ %. At isocentre static spins are returned to $+M_z$, as expected for a VS preparation. However, for all preparations static spins can become erroneously inverted with increased distance from isocentre. This will appear as a spatially dependent apparent hyper-perfusion in the ΔM images. Simulations show that the DRHS preparation is most sensitive to this effect for short τ_n (10^{-4} to 10^{-2} s) and that the BIR-4 preparation is most sensitive to this effect for longer τ_n (10^{-3} to 1 s), whilst the BIR-8 preparation has the least sensitivity to eddy currents. Reducing G_{MAX} does not alter the spectrum of eddy currents produced, but does reduce the maximum error for all preparations.

The effects are similar for B_0 eddy currents (fig. 3.7). However, the B_0 term will lead to a spatially independent positive artefact in the ΔM subtraction.

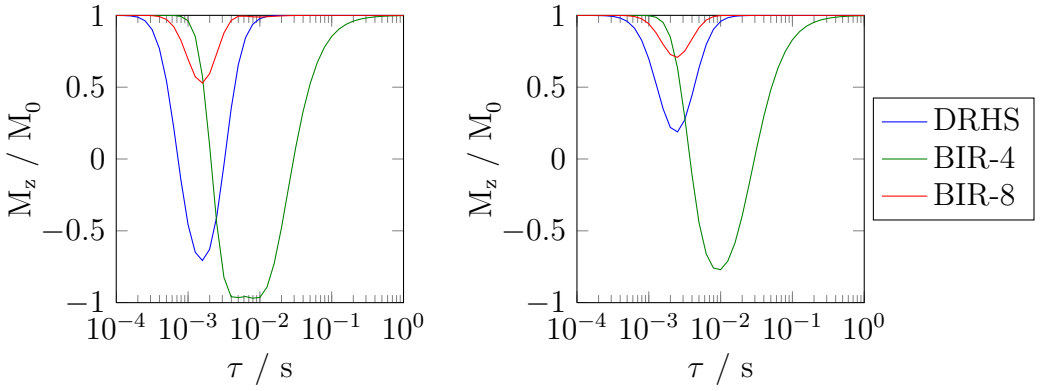


(a) DRHS 40 mT/m **(b)** BIR-4 40 mT/m **(c)** BIR-8 40 mT/m



(d) DRHS 10 mT/m **(e)** BIR-4 10 mT/m **(f)** BIR-8 10 mT/m

Figure 3.6: Simulated response of static spins to a DRHS, BIR-4 or BIR-8 velocity selective pulse in the presence of eddy currents with amplitude $A_n = 0.25$ % and time constant τ_n as a function of the spin's position from isocentre. The pulses had $V_{\text{cut}} = 2$ cm/s, top row is $G_{\text{MAX}} = 40$ mT/m and bottom row with $G_{\text{MAX}} = 10$ mT/m.



(a) $G_{\text{MAX}} = 40$ mT/m **(b)** $G_{\text{MAX}} = 10$ mT/m

Figure 3.7: Simulated response of static spins to B_0 eddy currents with amplitude $A_n = 0.05$ % and time constant τ_n when DRHS, BIR-4 and BIR-8 velocity selective pulses are applied at $V_{\text{cut}} = 2$ cm/s with $G_{\text{MAX}} = 40$ mT/m (3.7a) and $G_{\text{MAX}} = 10$ mT/m (3.7b).

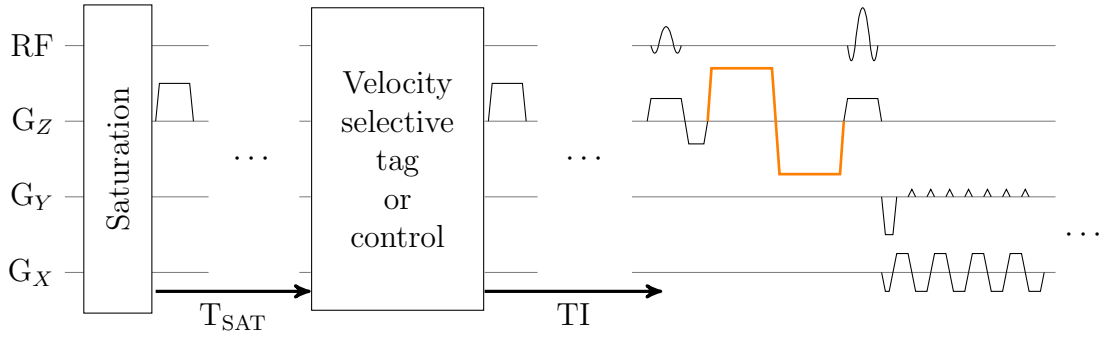


Figure 3.8: The VSASL pulse sequence.

3.2 VSASL Implementation

The VSASL pulse sequence consists of three sequence building blocks (fig. 3.8). First there is a non-selective saturation to remove any spin history effects. This is necessary for quantification as arterial spins in the imaging region would have been excited by the 90° pulses used in the EPI readout, whereas arterial spins outside the imaging region would otherwise be fully relaxed. This is followed by a saturation time, T_{SAT} to allow the arterial spins to partially recover. The velocity selective tag or control preparation, either a DRHS, BIR-4 or BIR-8, is then applied. A multi-slice spin echo EPI readout begins after inflow time TI.

The signal was limited to spins with velocity $v < V_{CUT}$ by using a bipolar pair of gradients in the readout (shown in orange). Compared to using a second velocity selective module this minimises SAR and is consistent when comparing velocity selective preparations. These crushers are on in both tag and control conditions.

To implement the VSASL sequence two non-selective saturation preparations were compared: WET, which consists of four variable angle hard pulses (88.9°, 98.7°, 82.5° and 159°) interspersed with spoilers (Ogg et al., 1994), and a 90° BIR-4 pulse followed by a spoiler (Staewen et al., 1990). The adiabatic thresholds of the BIR-4 and BIR-8 velocity selective preparations were also determined in a phantom.

3.2.1 Methods

Pre-saturation method

The WET preparation was implemented as in Golay et al. (2005), which had been optimised to saturate T_1 in the range 400 ms to 4400 ms with $\Delta B_1 = \pm$ 10%. The 600 μs hard pulses with flip angles 88.9°, 98.7°, 82.5° and 159° were separated by 10 ms. The spoiler axis was cycled to avoid stimulated echos, with spoiler moments 16 to 27.7 s mT/m. The 90° BIR-4 used $\zeta = 15$, $\tan(\kappa) = 60$, and $\omega_{\mathrm{MAX}} = 39.8$ kHz as previously optimised, and 45° of phase was added to segments 2 and 3 in order to achieve the 90° tip.

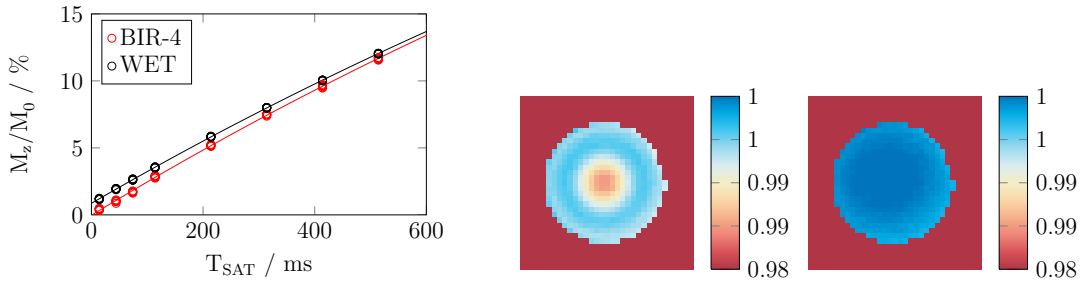
The saturation efficiency was tested in a tap water phantom. A saturation recovery experiment was performed with TR = 30 s, four averages with twelve T_{SAT} times from 14 ms to 2014 ms. Data were fitted voxelwise to

$$S = S_0 \left[1 - \mathrm{A} \exp\left(-\frac{T_{\mathrm{SAT}}}{T_1}\right)\right] \tag{3.6}$$

where A is the saturation efficiency, S_0 is the equilibrium signal.

BIR-4 and BIR-8 adiabatic threshold

In a doped water phantom the BIR-4 and BIR-8 velocity selective pulses were applied immediately prior to a single slice EPI readout. Both tag and control conditions were tested with $G_{\mathrm{MAX}} = 20$ mT/m and $V_{\mathrm{cut}} = 2$ cm/s. The TR was 30 s and TI was 14 ms to allow for crushers and a fat saturation pulse. The voltage of the BIR pulses was varied from 0 V to 908 V in 9 steps. The scanner calibrates the RF transmission power over the entire object, and will return a reference voltage, $\mathrm{V_{REF}}$, that corresponds to an average B_1 of 11.7 μT. This was then used to convert voltage to nominal B_1.



(a) Signal from central pixel and fit **(b)** WET **(c)** BIR-4

Figure 3.9: The BIR-4 and WET pre-saturation modules in a water phantom. Displayed are the raw data for the central pixel (isocentre) and fit to the data for each pre-saturation pulse (3.9a), saturation efficiency maps for WET (3.9b) and BIR-4 (3.9c). The mean efficiency over the whole mask for WET was 99.3 ± 0.3 % (mean ± SD), whilst BIR-4 was 99.96 ± 0.06 %.

3.2.2 Results

Pre-saturation method

The 90° BIR-4 (fig. 3.9c) produced a more efficient and homogeneous saturation compared to the WET preparation (fig. 3.9b). The mean value for the efficiency A was 99.96 ± 0.06 % for the BIR-4 and 99.3 ± 0.3 % for WET. The measured relaxation times were 2318 ± 16 ms for BIR-4 and 2361 ± 20 ms for WET. In WET, the saturation is less efficient in the middle of the phantom (fig. 3.9a) which is due to B_1 effects.

BIR-4 and BIR-8 adiabatic threshold

For the doped water phantom V_{REF} was 442 V. The signal from the phantom is constant when the nominal B_1 is above 16.6 μT for both the BIR-4 and BIR-8 tag and control conditions (fig. 3.10). The BIR-8 has a lower tagging efficiency due to the longer preparation, but is comparable to the BIR-4.

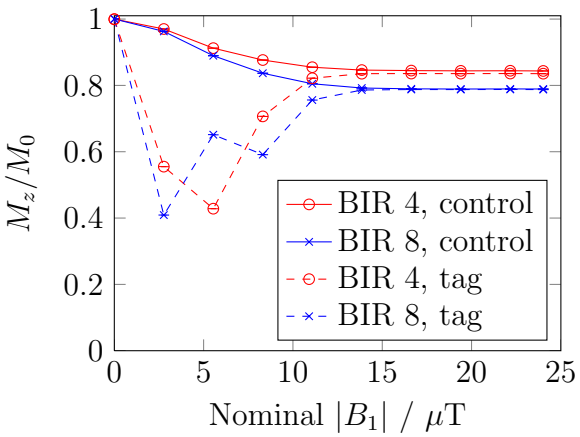


Figure 3.10: The signal from a static phantom as the maximum BIR B_1 amplitude is increased from 0 V to 908 V. With $V_{\mathrm{REF}} = 442$ V the maximum nominal $|B_1|$ was 24.0 μT, and the nominal adiabatic threshold is observed at 16.6 μT for both the BIR-4 and BIR-8. For the tag conditions $V_{\mathrm{cut}} = 2$ cm/s and $G_{\mathrm{MAX}} = 20$ mT/m.

3.2.3 Discussion

Due to the superior homogeneity of the 90° BIR-4 non-selective saturation over the WET saturation this was used in the following experiments. However, the 8 ms pulse does have higher SAR than the WET preparation but this could be reduced by using 1.5 ms segments.

The adiabatic threshold for both BIR-4 and BIR-8 was determined at a nominal B_1 of 16.6 μT. This is larger than the target design of 15 μT, and is probably due to the range of B_1 values in the phantom as only the nominal B_1 was measured. All BIR pulses in future experiments were applied at the maximum 908 V to ensure that this threshold is reached at all positions.

3.3 Eddy Current Effects in vivo

To modulate eddy currents it would have been ideal to either turn the system eddy current compensation off or to induce additional eddy currents with an extra metallic surface. Our vendor was not willing to give out the password to modify the compen-

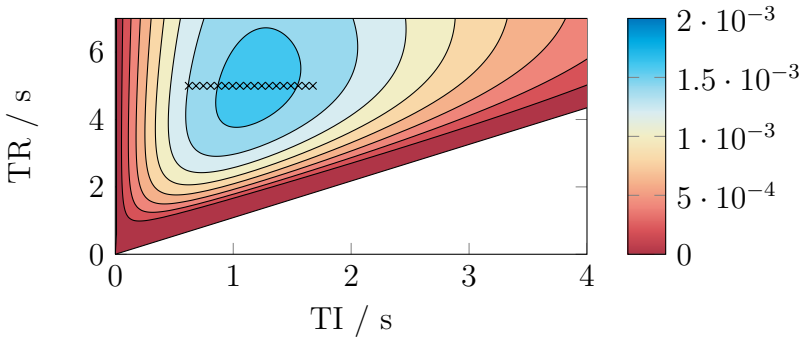


Figure 3.11: Optimisation of TR and TI for 18 slices with slice TR = 61.92 ms, and assuming $T_{1,t}$ = 1.1 s. Each 'x' represents a slice acquisition with first TI = 651 ms, TR = 5.1s.

sation terms and the latter idea was dismissed on safety grounds. The eddy currents were therefore modulated by reducing G_{MAX}, known as gradient waveform de-rating.

3.3.1 Methods

VSASL measurements with the DRHS, BIR-4 and BIR-8 preparations were performed in five healthy volunteers using a 3 Tesla Siemens Verio scanner (Siemens Healthcare, Erlangen, Germany) to assess the influence of eddy currents. All volunteers provided written consent under an institutionally agreed technical development protocol.

The VSASL pulse sequence (fig. 3.8) used $\mathrm{T_{SAT}}$ = 3.2 s and the velocity selective preparations were applied with V_{CUT} = 2 cm/s. The tagging gradients were applied on the x axis. A spin echo EPI readout is then applied after inflow time TI = 0.7 s. Other acquisition parameters were TR = 5.1 s, TE = 32 ms, 256 mm FOV, 64x64 matrix, slice thickness = 5 mm, 18 slices. The TR and TI were chosen to maximise the SNR efficiency ($\Delta M/\sqrt{\mathrm{TR}}$), where ΔM is derived below and a $T_{1,t}$ = 1.1 s was assumed (fig. 3.11).

The volunteers were moved so that the centre of the imaging slice group was at the magnet isocentre. The velocity selective preparations were played out on a whole body transmission coil at maximum amplitude (23 μT) and a 32-channel

head receive coil was used. A separate body coil receive image was acquired for coil sensitivity correction and M_0^{CSF} calibration. A double inversion recovery acquisition with inversion times designed to null white matter and CSF was used as a gray matter mask with adiabatic inversions 4150 ms and 550 ms before an identical SE-EPI readout (Redpath and Smith, 1994).

The eddy current spectrum will be different for each scanner. As A_n and τ_n are generally not known the eddy current amplitudes were modulated by varying G_{MAX}. At the end of a gradient ramp (t=R), the unwanted additional gradient due to eddy currents is given by

$$g(t = R) = -G_{\mathrm{MAX}} \sum_n \frac{A_n \tau_n}{R} \left[1 - \exp\left(-\frac{R}{\tau_n} \right) \right] \tag{3.7}$$

where G_{MAX} is the maximum amplitude of the desired trapezoidal gradient. The eddy current gradient amplitude can therefore be modulated by applying the velocity selective preparations with different G_{MAX}, keeping rise time R constant. The flat top time of the indiviual gradients are also adjusted so that m_1, thus V_{cut} remains constant. The increased duration of the gradients is then corrected for by assuming pure T_2 decay of arterial blood in the analysis. For each preparation five G_{MAX} values (equally spaced from from 10 to 40 mT/m) were applied with R = 0.5 ms. Sixteen tag-control pairs were acquired for each preparation and G_{MAX} combination. The acquisition order was randomized. Total scan time was 50 minutes.

Data were corrected for motion and registered to the M_0 scan using FLIRT (Jenkinson and Smith, 2001). Images were subtracted pairwise and then averaged to form the ΔM image. Perfusion was quantified on a voxelwise basis using a modified general

kinetic model inversion given by (Buxton et al., 1998):

$$\Delta M_b(\mathrm{TI}) = M_{0,B} \cdot \left[1 - \exp\left(-\frac{T_{SAT}}{T_{1,B}}\right)\right] \cdot \alpha \cdot f \cdot \mathrm{TI} \cdot q_p(f) \cdots \\ \cdots \exp\left(-\frac{\mathrm{TI}}{T_{1,B}}\right) \cdot \exp\left(-\frac{\mathrm{TE}}{T_{2,B}}\right) \tag{3.8}$$

where $M_{0,B}$ is the magnetization of a fully relaxed voxel of blood as determined from calculation via the M_0 scan; α is the tagging efficiency of the velocity selective preparation; f is perfusion and $q_p(f)$, given by

$$q_p(f) = \frac{\exp(k(f) \cdot \mathrm{TI}) - 1}{k(f) \cdot \mathrm{TI}} \tag{3.9}$$

where

$$k(f) = \frac{1}{T_{1,B}} - \frac{1}{T_{1,t}} - \frac{f}{\lambda} \tag{3.10}$$

and λ is the blood water partition coefficient, takes into account the different T_1 relaxation times of the bolus and the tissue. The quantification assumes that the bolus arrival time is zero and that the bolus length is equal to TI. Since reducing G_{MAX} will increase the tagging gradient duration was simulated α for each velocity selective preparation and G_{MAX}.

Mean perfusion, $f(G_{\mathrm{MAX}})$, was calculated for each preparation and G_{MAX} within the grey matter mask derived from the subjects double inversion recovery scan. The effect of eddy currents on apparent perfusion should only depend on the scanner used, the relaxation times of static tissue and the TI, but not the underlying perfusion of an individual subject. $\Delta f = f(G_{\mathrm{MAX}}) - \overline{f}(G_{\mathrm{MAX}})$ was therefore correlated where $\overline{f}(G_{\mathrm{MAX}})$ is the individual subjects perfusion, averaged over all G_{MAX} (reported in table 3.1).

As the direction of flow is principally in the z direction the three velocity selective preparations were applied on z with a sagittal readout in one further volunteer. Only

Subject	$\overline{f}$ over all G_{MAX} / ml/100g/min		
	DRHS	BIR-4	BIR-8
A	52.3 ± 8.1	86.3 ± 3.4	45.9 ± 3.1
B	65.0 ± 7.7	88.5 ± 3.1	50.0 ± 2.2
C	70.3 ± 8.6	90.4 ± 3.7	59.7 ± 2.2
D	71.8 ± 9.0	93.5 ± 4.2	58.5 ± 1.6
E	59.3 ± 6.1	98.5 ± 2.7	55.8 ± 2.2
Mean	63.8 ± 3.6	91.4 ± 2.1	53.9 ± 2.6

Table 3.1: Mean perfusion ± SEM for each subject and preparation, calculated over all G_{MAX}.

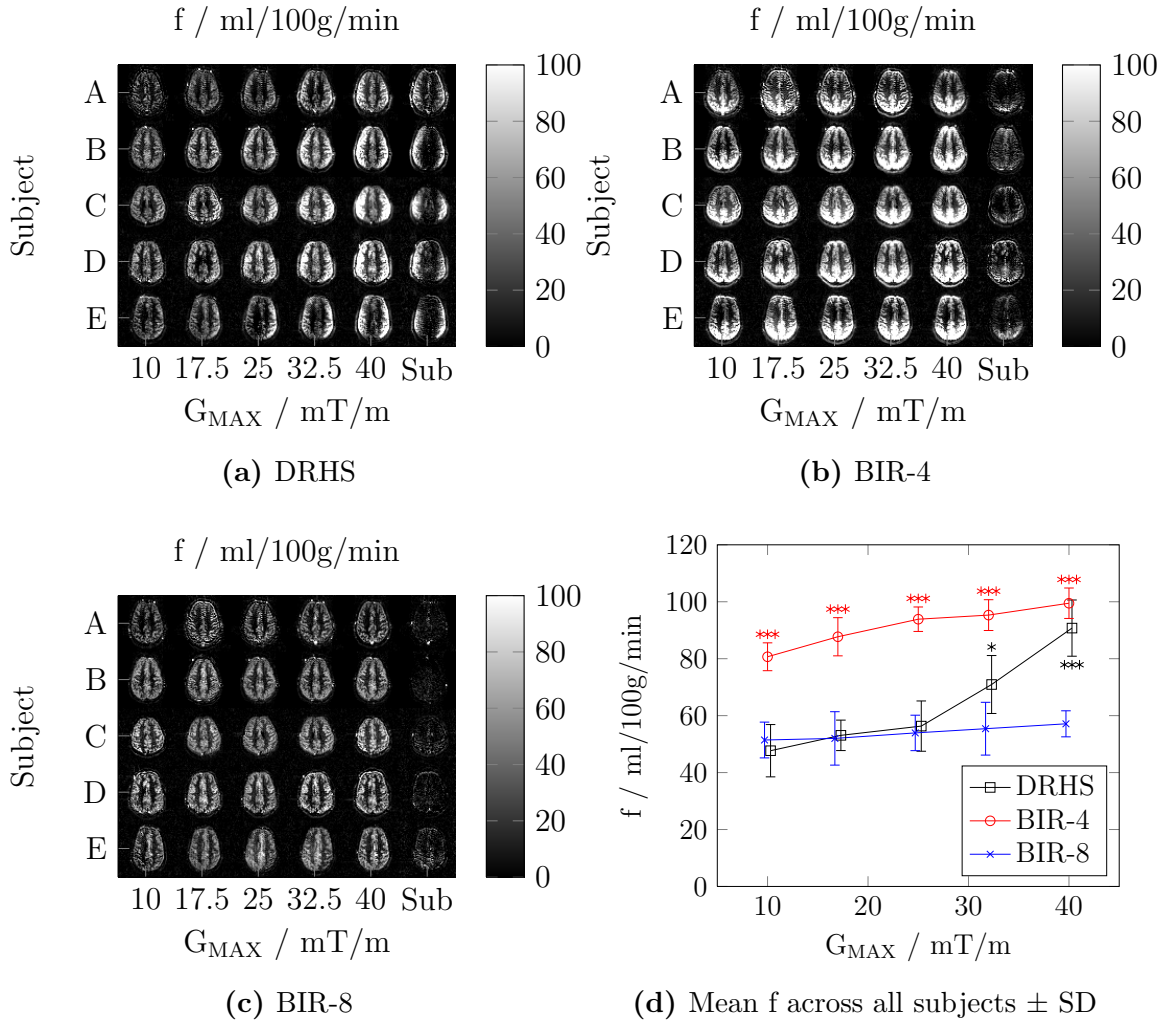
two G_{MAX} were used, 10 and 40 mT/m for this sub study.

3.3.2 Results

Mean grey matter perfusion values averaged over all G_{MAX} for each preparation are reported in table 3.1, corrected for differences in the theoretical efficiency between the preparations, and for regional receive coil sensitivity differences. The mean perfusion over all subjects using the DRHS preparation was 63.8 ± 3.6 ml/100g/min, for the BIR-4 preparation was 91.4 ± 2.1 ml/100g/min, and for the BIR-8 preparation was 53.9 ± 2.6 ml/100g/min.

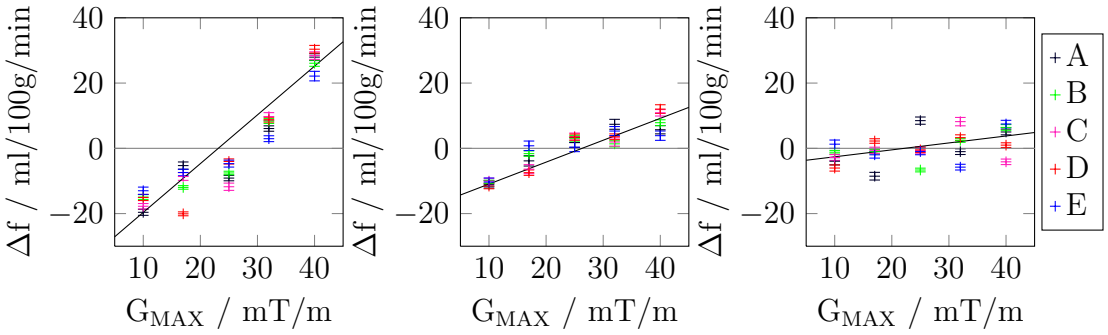
Representative perfusion maps are displayed in Figure 3.12 for $G_{MAX} = 10$ and 40 mT/m. The DRHS preparation displays the expected spatial variation in erroneous perfusion values due to eddy currents for $G_{MAX} = 40$ mT/m, but this artifact is seen to be reduced for $G_{MAX} = 10$ mT/m. The BIR-4 preparation exhibits an erroneous spatial variation of perfusion in the A-P direction, on an orthogonal axis to the applied tagging gradients. The perfusion maps based on the BIR-8 preparation display reduced eddy current artifact compared to the DRHS and BIR-4 preparations.

Analysis of the mean perfusion calculated over all subjects shows that the BIR-4 measures significantly higher perfusion than the BIR-8 for all G_{MAX} (one way ANOVA, $P < 0.001$). The DRHS only measures significantly higher perfusion than



(a) DRHS **(b)** BIR-4 **(c)** BIR-8 **(d)** Mean f across all subjects ± SD

Figure 3.12: Variation of measured perfusion vs G_{MAX} *in vivo* for all five subjects for DRHS (3.12a), BIR-4 (3.12b) and BIR-8 (3.12c). Displayed is slice 13 of 18 (z = +40 mm from isocentre, slice TI = 1.51 s). Velocity selective gradients are in the left-right direction. The averaged tag control images are shown for all G_{MAX}, and the final column is the subtraction of G_{MAX} = 10 mT/m from G_{MAX} = 40 mT/m to indicate the artefacts due to increased eddy current effects. Plotted are the mean perfusion across all subjects ± SD (3.12d). Significantly higher perfusion values for the DRHS and/or the BIR-4 vs BIR-8 are indicated (One way ANOVA, * $P < 0.05$, *** $P < 0.001$).



(a) DRHS **(b)** BIR-4 **(c)** BIR-8

Figure 3.13: Correlation of the change in perfusion from the individual subject mean perfusion with G_{MAX} for DRHS (3.13a), BIR-4 (3.13b) and BIR-8 (3.13c). R^2 was 0.8, 0.84 and 0.25 for DRHS, BIR-4 and BIR-8 respectively.

the BIR-8 for $G_{\mathrm{MAX}} = 32.5$ ($P < 0.05$) and 40 mT/m ($P < 0.001$).

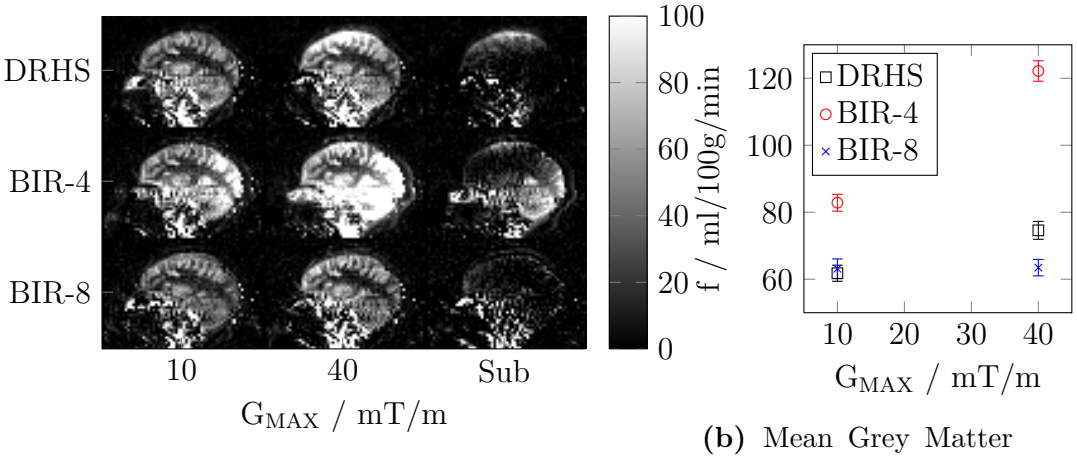
Figure 3.13 shows the variation of apparent perfusion versus G_{MAX} for each preparation. Perfusion measured by the DRHS and BIR-4 methods significantly correlate with G_{MAX} ($P < 0.001$), whilst the correlation for the BIR-8 was not significant ($P = 0.011$). The slope of $\Delta f/G_{\mathrm{MAX}}$ was 1.5 (ml/100g/min)/(mT/m) for the DHRS and 0.67 (ml/100g/min)/(mT/m) for the BIR-4, but was reduced to 0.21 (ml/100g/min)/(mT/m) for the BIR-8 preparation.

The labeling on the z axis show a similar effect (fig 3.14), although in this case the artefacts are principally in the z direction for both the DRHS and BIR-4.

3.3.3 Discussion

In this study the performance of two existing velocity selective preparations in the presence of eddy currents was evaluated. The data show that all velocity selective preparations may overestimate perfusion due to static spin contamination in the ΔM image, caused by eddy currents, but show that the new BIR-8 preparation performs the best.

For the DRHS and BIR-8 velocity selective preparations the average grey matter perfusion estimates that are calculated over all G_{MAX} values fall within expected



(a) Perfusion Maps

(b) Mean Grey Matter Perfusion

Figure 3.14: Velocity encoding gradients applied on z with a sagittal readout in a healthy volunteer (3.14a) and the mean perfusion in a grey matter mask derived from the DIR scan (3.14b). Displayed is slice 13 of 18 for $G_{\mathrm{MAX}} = 40$ and 10 mT/m. Artefacts due to eye motion and physiological noise in the neck are apparent.

normal physiological ranges. However, there is a clear artifact in the case of the BIR-4 preparation that persists over all G_{MAX} values (Figs. 3.12b), which results in an overestimation in average perfusion. For $G_{\mathrm{MAX}} = 10$ mT/m there is not a significant difference between the apparent perfusion as measured by the DRHS and BIR-8 preparations (47.7 ± 4 ml/100/min versus 51.4 ± 3 ml/100/min, respectively), but even at this low value of G_{MAX} the BIR-4 method measures an artifactually elevated perfusion (80.7 ± 2 ml/100g/min) due to the persistence of the hyper-perfused artifact in the posterior regions of the brain.

Note that the artifact in the BIR-4 data is on an orthogonal axis to the applied gradient, but this is attributed to a long τ_n eddy current cross term, since perfusion is still erroneously correlated with G_{MAX}. This cross term is supported by the eddy current compensation that is applied by the scanner hardware from the eddy currents measured independently by our vendor. Table 3.2 shows that the compensation for X-Y eddy currents is an order of magnitude larger than the other cross terms, with a time constant in the range that the BIR-4 is sensitive to.

As the mean values of perfusion for the DRHS and BIR-4 preparations agree at

Gradient Axis	Eddy Current Axis		
	X	Y	Z
X	-	-0.24 %	-0.06 %
Y	-0.08 %	-	-0.03 %
Z	n/a	-0.06 %	-

(a) Amplitudes

Gradient Axis	Eddy Current Axis		
	X	Y	Z
X	-	0.17 s	0.17 s
Y	0.18 s	-	0.43 s
Z	n/a	0.18 s	-

(b) Time Constants

Table 3.2: The applied compensation for eddy current cross terms on the FMRIB Verio. Note that there is no compensation for Z-X.

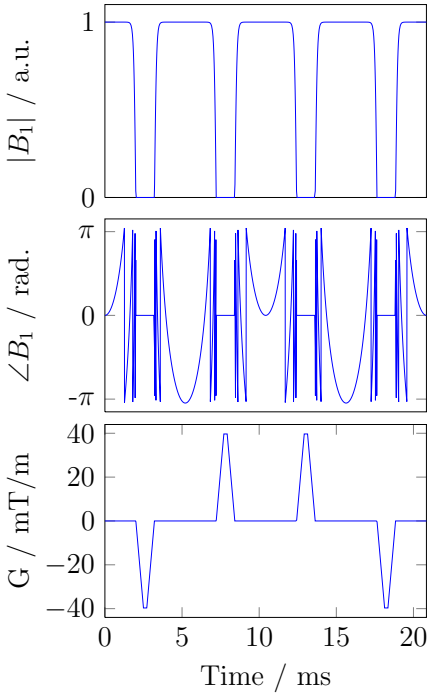
$G_{\mathrm{MAX}} = 10$ mT/m this suggests that the approach taken to simulate the tagging efficiency for these preparations is a valid one. The change in efficiency for each G_{MAX} should only depend on the T_2 of arterial blood since the spins are in the transverse plane during the application of the tagging gradients, which vary in duration depending on their G_{MAX} value. Any errors in the estimation of the efficiency would result in an apparent change in global perfusion, but this should not have any spatial dependence. However, it can be seen from the subtractions in Fig. 4 that the DRHS and BIR-4 artefacts do have a spatial distribution, indicating the confounding effects of eddy currents.

3.4 Further Eddy Current Reduction: symBIR-8

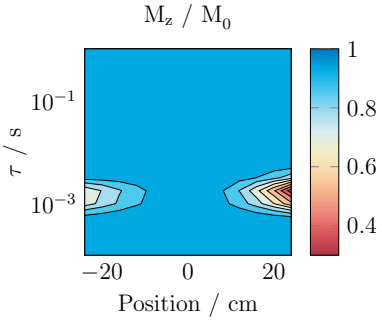
Subsequent to submission of this work for publication an improvement on the BIR-8 preparation was proposed by Guo and Wong (2012c). Here it was shown that the errors due to eddy currents can be further reduced by inserting gradient lobes at all four $|B_1| = 0$ points of the BIR-8 preparation with polarities -1:+1:+1:-1 (fig. 3.15a). This symmetric preparation, symBIR-8, was implemented on our system and compared to the BIR-4 and BIR-8 preparations previously used.

3.4.1 Methods

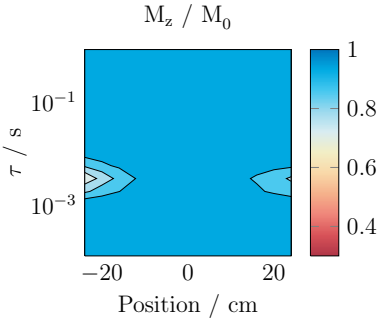
The first gradient moment of the symBIR-8 preparation is given by



(a) symBIR-8



(b) BIR-8 Eddy Current



(c) symBIR-8 Eddy Current

Figure 3.15: Symmetric BIR-8 pulse diagram (3.15a) for $V_{\text{cut}} = 2$ cm/s at $G_{\text{MAX}} = 40$ mT/m. Simulations of the eddy current response show that the errors are reduced (3.15c) compared to the BIR-8 (3.15b), which is reproduced here with a reduced scaling to visualise the errors.

$$m_1^{\text{symBIR8}} = 4 \cdot G_{\text{MAX}} \cdot (\text{F} + \text{R}) \cdot (\text{F} + 2\text{R} + T_{RF}) \tag{3.11}$$

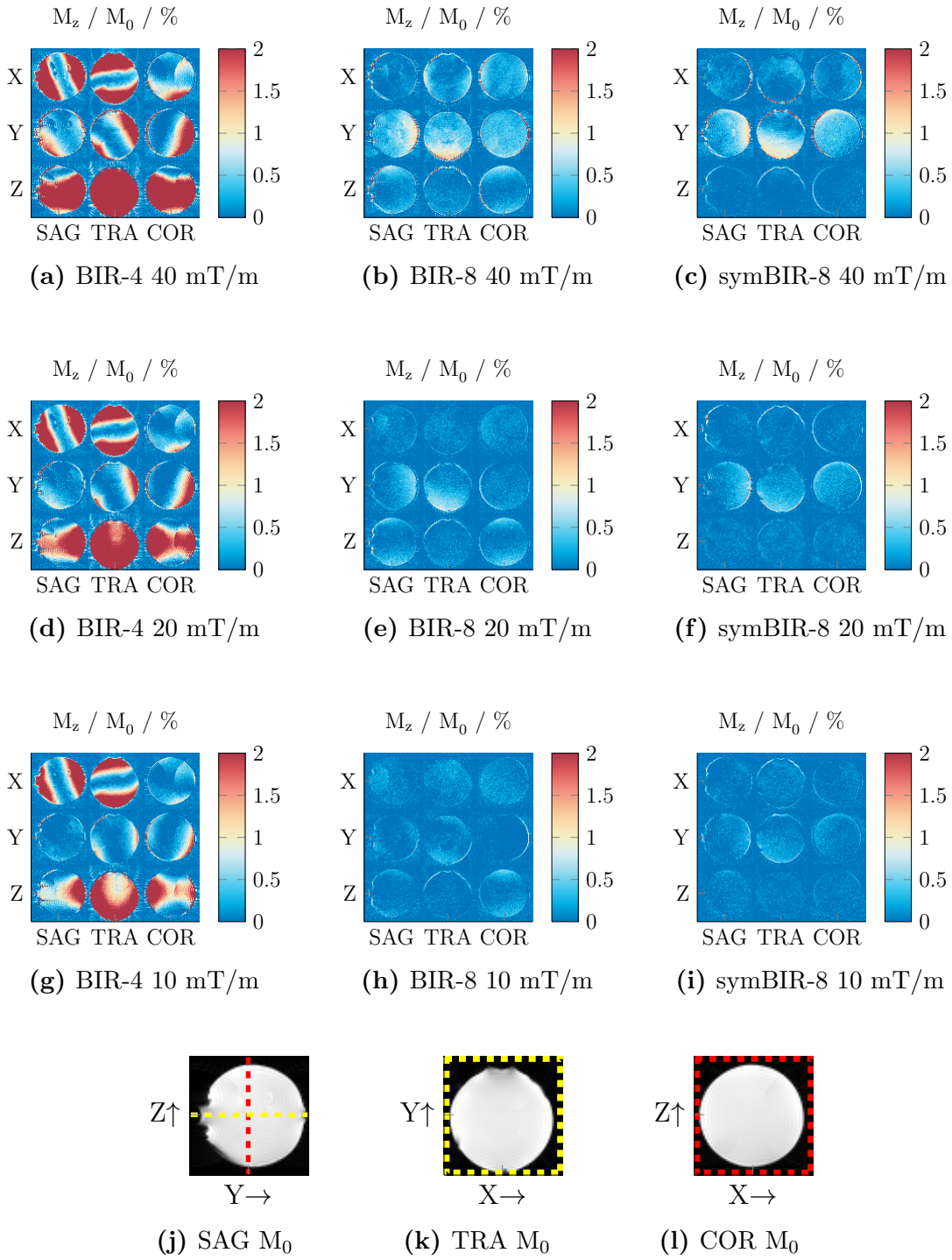
where F is the flat top time and R is the gradient rise time. The RF pulse used 2 ms BIR segments as previously implemented. The response of static spins to symBIR-8 pulse was simulated with time constants 10^{-4} s to 1 s with $A_n = 0.25$ %.

The BIR-4, BIR-8 and symBIR-8 preparations were then evaluated in a phantom. To eliminate the effects of diffusion an 18 cm spherical silicone oil phantom was used. The phantom was placed at the centre of the 12 channel head receive coil and positioned at magnet isocentre. MR safe sandbags were used to immobilise the phantom. The preparations were applied immediately prior to a spin echo EPI readout without crushers. The TE was 37 ms, FOV = 20 cm, 64 × 64 matrix and slice thickness was 8 mm. Data were normalised for receive coil sensitivity using the scanners 'prescan normalise' option. Each preparation (BIR-4, BIR-8 and symBIR-8) was applied with $V_{\text{cut}} = 2$ cm/s, with $G_{\text{MAX}} = 10$, 20 and 40 mT/m. This was repeated for each tagging direction (X, Y and Z), readout direction (sagittal, transverse and coronal). This resulted in 81 acquisitions in total, with a TR of 3 s and 16 tag and control pairs. The value for M_0 was determined from a scan without a velocity selective preparation with TR = 30 s.

3.4.2 Results

The simulations show that the symBIR-8 (fig. 3.15c) does reduce eddy current effects compared to the BIR-8 (fig. 3.15b).

The mean ΔM subtraction images for all three preparations, tagging directions, readout directions and gradient strengths are displayed in figure 3.16. The BIR-4 (left column) has the greatest amount of artefacts compared to the BIR-8 (middle) and symBIR-8 (right). When labeling on the X axis the greatest variation is in



(a) BIR-4 40 mT/m **(b)** BIR-8 40 mT/m **(c)** symBIR-8 40 mT/m

(d) BIR-4 20 mT/m **(e)** BIR-8 20 mT/m **(f)** symBIR-8 20 mT/m

(g) BIR-4 10 mT/m **(h)** BIR-8 10 mT/m **(i)** symBIR-8 10 mT/m

(j) SAG M_0 **(k)** TRA M_0 **(l)** COR M_0

Figure 3.16: Application of BIR-4 (a,d,g), BIR-8 (b,e,h) and symBIR-8 (c,f,i) in a silicone oil phantom at isocentre. The velocity selective gradients are applied on X, Y and Z and readout is in the sagittal (SAG), transverse (TRA) and coronal (COR) planes. G_{MAX} is 40 mT/m (a-c), 20 mT/m (d-f) and 10 mT/m (g-i). The images are the mean of 16 ΔM subtractions. The velocity encoding directions are indicated for each readout plane in sub-figures j-l.

the Y direction for the BIR-4, which matches the previous scans *in vivo*. Similarly, when labeling on the Y axis the variation is along X for the BIR-4. This is not the case for the BIR-8 or symBIR-8, where the spatial variation of the artefacts is along the direction of the applied gradient. All artefacts are reduced as G_{MAX} is reduced. Artefactual signal at isocentre is apparent for all preparations. The artefacts are reduced when using symBIR-8 compared to BIR-8, especially on the X and Z labeling axes.

The data in figure 3.16 were quantified by taking the average root mean square error in a mask containing the phantom, plotted in figure 3.17.

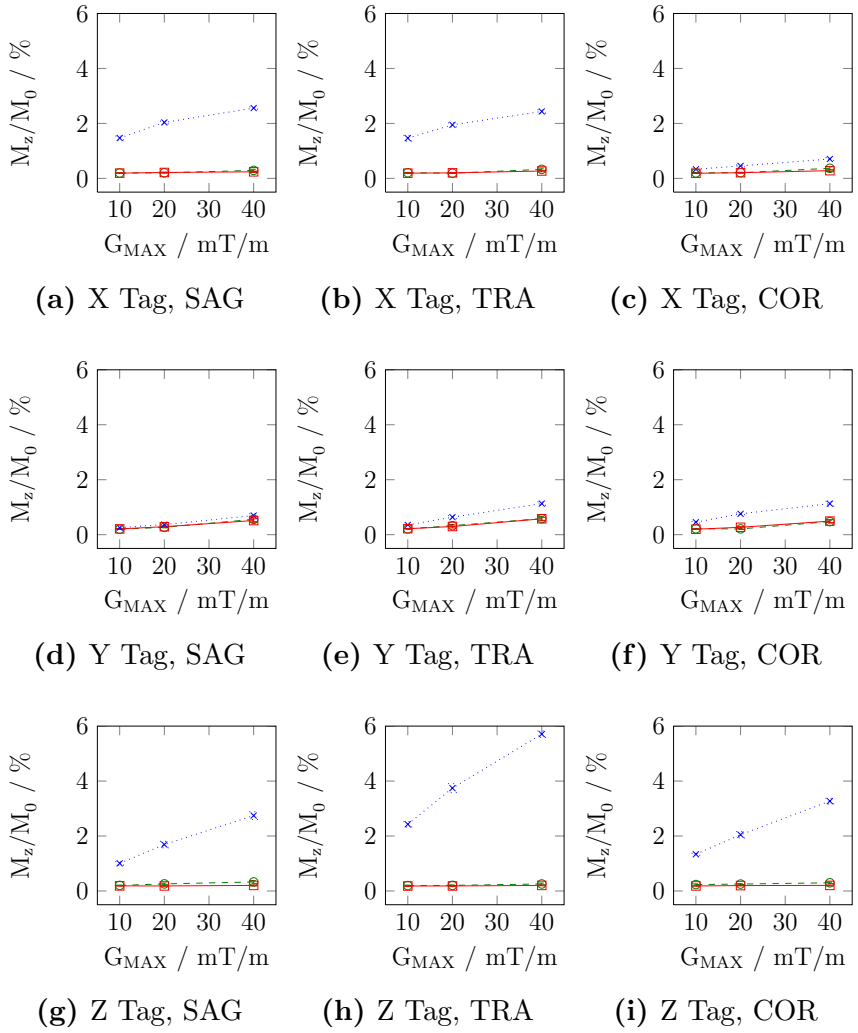
3.4.3 Discussion

This phantom experiment confirms that the symBIR-8 preparation does have reduced artefacts compared to the BIR-8, particularly on the X and Z axes. As these artefacts have a spatial distribution and reduce with G_{MAX} they are attributed to eddy currents. The artefacts are unlikely to be from diffusion as the diffusion coefficient of the silicone oil is 1 to 2 orders of magnitude lower than water and the artefacts are spatially inhomogeneous.

There was not a significant difference between the symBIR-8 at 20 mT/m to 10 mT/m, so to minimise T_2 decay during the preparation 20 mT/m was used on this scanner.

3.5 Discussion and Conclusions

In this chapter the systematic errors due to eddy currents in VSASL were quantified. A new velocity selective preparation, BIR-8, was introduced and was shown to be the most robust preparation to eddy current effects. This was further refined and it was shown that the symBIR-8 did further reduce the artifacts.



(a) X Tag, SAG **(b)** X Tag, TRA **(c)** X Tag, COR

(d) Y Tag, SAG **(e)** Y Tag, TRA **(f)** Y Tag, COR

(g) Z Tag, SAG **(h)** Z Tag, TRA **(i)** Z Tag, COR

Figure 3.17: Quantified subtraction errors in a silicone oil phantom for the BIR-4 (blue), BIR-8 (green) and symBIR-8 (red). Velocity encoding gradients are applied in X (a-c), Y (d-f) and Z (g-i) directions. Data are from masks of the images in figure 3.16. The root mean squared error is calculated for each tag control pair, data are the mean of this ± SD over the 16 tag control pairs.

In this chapter an exponential model of eddy currents was used (Vaals and Bergman, 1990). However, this may not reflect the realistic situation as mechanical vibration or capacitive coupling can produce oscillatory behaviour (Giese et al., 2012). It was also shown using a silicone oil phantom that the artefacts are not due to diffusion effects, although the b-value of the preparations will depend on G_{MAX}. Although the eddy current amplitude after the gradient rise or fall time is linearly proportional to G_{MAX}, the compensation achieved by each velocity selective preparation is non-linear. Despite these flaws, the RMSE errors in a silicone oil phantom are not significantly different from zero when using the symBIR-8 on Z at 20 mT/m.

It was previously assumed that the DRHS preparation had a low sensitivity to eddy currents (Wong et al., 2006), due to the use of bi-polar gradients, but it has been shown here that the choice of G_{MAX} can result in an overestimation of perfusion by a factor of 2. This could have implications for previous work that has serially applied the tagging gradients on different axes, as the apparent perfusion will depend on the relative position of the organ to magnet isocentre (Wong et al., 2006; Frank et al., 2008).

In conclusion, eddy currents during the velocity selective preparation cause unwanted tagging of static tissue and hence an overestimation of perfusion in VSASL. The BIR-8 preparation that is introduced in this chapter is the most robust velocity selective preparation to both eddy currents and B_1 inhomogeneity with comparable efficiency to BIR-4.

Chapter 4

VSASL Applied in Brain Tumours

Tumour vasculature is known to be chaotic and composed of leaky, tortuous vessels where the blood is less likely to be monotonically decelerating. A feasibility study was therefore conducted in patients with brain tumours, to first determine whether a significant VSASL signal is produced in tumours, and secondly to compare VSASL and pCASL techniques measures of perfusion in pathology. To the best of the authors' knowledge the only published clinical application of VSASL to date is in Moyamoya disease (Qiu et al., 2012).

A study involving 66 pre-surgery epilepsy patients has been ongoing at FMRIB since 2010. Of these patients, 30 patients had epilepsy originating from an operable tumour. The original 90 minute scan included structural imaging, BOLD fMRI, DTI and pCASL. Following the development of the BIR-8 pulse a 5 minute VSASL scan was then added in the final four tumour patients covered by the ethical protocol.

4.1 Methods

Subjects were scanned on a 3 T Siemens Verio scanner (Siemens Healthcare, Erlangen, Germany) and provided informed consent under a protocol that received favourable opinion from the London Surrey Borders Research Ethics Committee (10/H0806/23).

Patient	Tumour	Volume / cm^3
A	Probable glioma	16.9
B	Grade III glioma	120.1
C	Grade II glioma	24.6
D	Probable high grade glioblastoma multiforme	101.0

Table 4.1: The tumour types and volumes as defined on the anatomical T1 weighted image for the four patients in this study. Patients A and D are radiological grade. Patients B and C are histological grade.

Four patients were recruited between October and December 2012. The tumours the patients presented with are summarised in table 4.1. The pathology report showed that patients B and C presented with glioma, and at the time of writing patients A and D had not undergone surgery.

The pCASL sequence already being acquired in this cohort used a GRE-EPI readout without crushers, 24 slices acquired parallel to the AC-PC line, 5 mm thick slices, 0.5 mm slice gap, 64 × 64 matrix with FOV 220 mm. The pCASL labeling scheme (Okell et al., 2010) used a labeling duration of 1.4 s and six post label delays from 250 ms to 1500 ms in 250 ms steps. The TE was 13 ms, TR = 4.5 s and 7 tag-control pairs were acquired per TI. A 32 channel receive coil was used to maximise SNR in the cortex.

To maximise the SNR the VSASL sequence used a SE-EPI readout, 13 axial slices, 8 mm thick, 4 mm gap, 64 × 64 matrix with FOV 220 mm. Crushers were used in the readout so that the VSASL signal is proportional to decelerating spins. The velocity encoding was applied on the scanner's z axis as this is the principle direction of blood flow (roughly in the foot-head direction). Due to a coding limitation the crushers in during the readout module could only be applied in the slice direction, so the slices were acquired in a pure axial view. Other parameters included a cutoff velocity at 2 cm/s, a single TI of 1 s, 32 tag control pairs, TE = 37 ms and TR = 5 s.

All acquired data were normalised for the receive coil sensitivity using the scanner's prescan normalise function. To determine $M_{0,b}$ a TR = 30 s scan was used

to determine $M_{0,CSF}$. Two acquisitions were made, one with a SE-EPI readout and a second with a GRE-EPI readout, with the geometry parameters matched to the VSASL and pCASL acquisitions, respectively. This resulted in a separate determination of $M_{0,b}$ for pCASL and VSASL, due to the different geometries and acquisition contrast. Due to time limitations neither a double inversion recovery scan for masks nor T_1 maps for quantification could not be acquired. A global $T_{1,t} = 1.1$ s, $\lambda = 0.87$, $T_2 = 150$ ms, $T_2^* = 40$ ms was assumed.

To generate the masks of grey matter, white matter and CSF the subject's MPRAGE scan was automatically segmented using FAST (FMRIB Software Library, University of Oxford) assuming 3 tissue types. An experienced researcher (Dr. Natalie Voets, University of Oxford) manually segmented the subjects' lesions on the same MPRAGE scan. The three masks from FAST and the lesion mask were then combined, reassigning the voxels manually identified as tumour to give 4 tissue types. The MPRAGE scan was then registered to each ASL space, the M_0 with GRE-EPI and SE-EPI respectively, using BBR (FSL, University of Oxford). The masks for grey matter, white matter and CSF were then generated by thresholding the registered segmentations with a probability of > 80 % of the ASL voxel being a single tissue type.

The ASL timeseries were motion corrected using FLIRT (FSL, University of Oxford), registering to the respective M_0 volume. Data were quantified voxelwise using a single compartment model (Buxton et al., 1998) using a Variational Bayes approach (Chappell et al., 2009). For both pCASL and VSASL the prior on the value of perfusion was non informative (ie. uniform and unbiased), for the pCASL Bolus Arrival Time (BAT) the prior was 1.3 s and for VSASL the BAT was assumed to be zero. Perfusion values are reported as means calculated within the previously described masks, along with BAT for pCASL. The temporal SNR at was calculated voxelwise by

$$\text{SNR} = \sqrt{N}\frac{\text{mean}(f)}{\text{std}(f)} \tag{4.1}$$

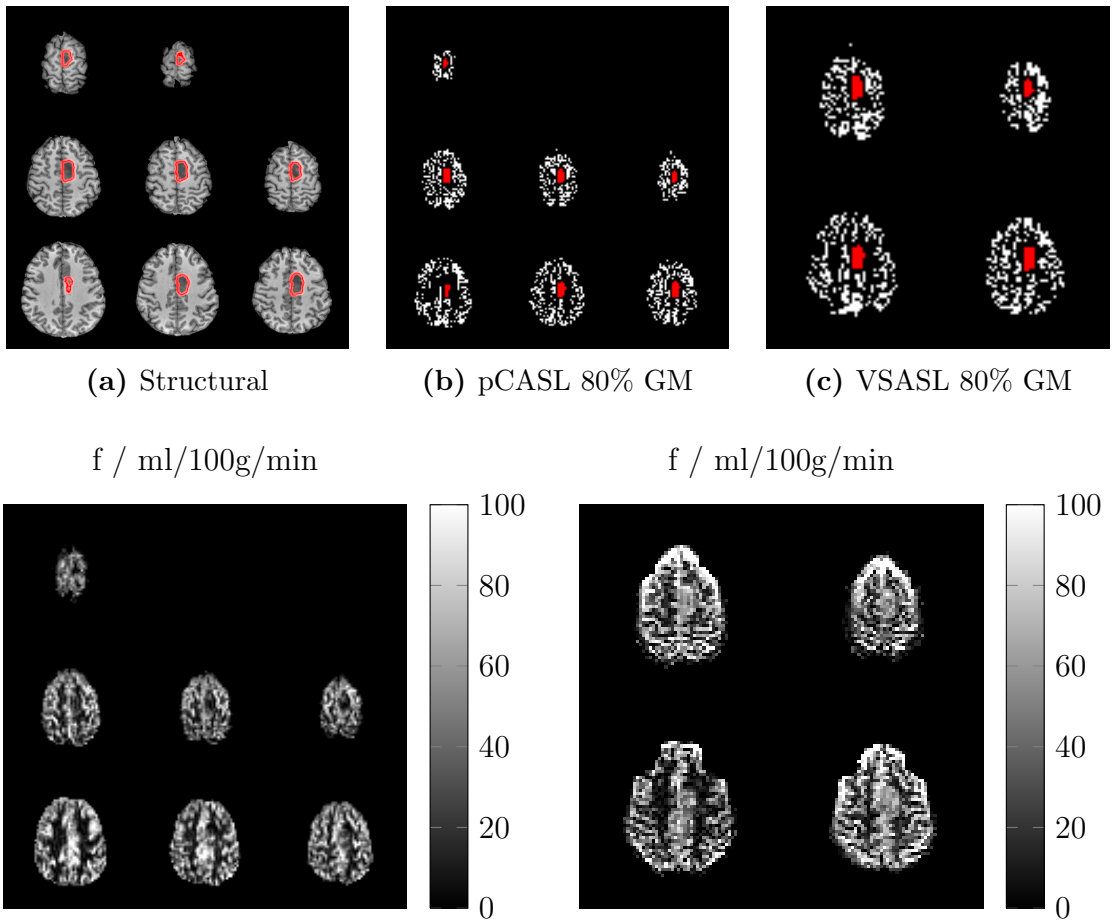
where std is the standard deviation. This was then averaged over each tumour mask for each subject. The percentage of significant tumour voxels as a function of scan time was then calculated. A voxel was defined as significantly different from zero by use of a two-sided Students t-test ($P < 0.05$). The agreement of the values of perfusion measured by pCASL (f_{pC}) and VSASL (f_{VS}) were then compared using Bland-Altman plots (Bland and Altman, 1986).

4.2 Results

Figures 4.1 to 4.4 display the data acquired for each subject. Subfigure a shows the MPRAGE scan with tumour segmentation overlaid in red. Subfigures b and c show the masks for grey matter (white) and tumour (red) in the pCASL space and VSASL space respectively. Subfigures d and e show the perfusion maps for pCASL and VSASL. Only slices with more than 10 tumour voxels are displayed, and the MPRAGE slices may not exactly correspond with the masks or perfusion maps.

The pCASL perfusion images for patient C appear to be focal, and not reflect a typical ASL map. The raw data was inspected for motion and the acquisition checked for labeling and inflow times but these appeared normal, although there is a large tag control difference for the first TI (1650 ms). The perfusion measured in patient D may be overestimated as the tumour has developed around the middle cerebral artery, which was included in the tumour masks for both sequences. The MCA is probably supplying blood to tissue superior to the tumour and not the tumour itself, biasing the measurement. However, the mask and therefore any error is consistent across both VSASL and pCASL.

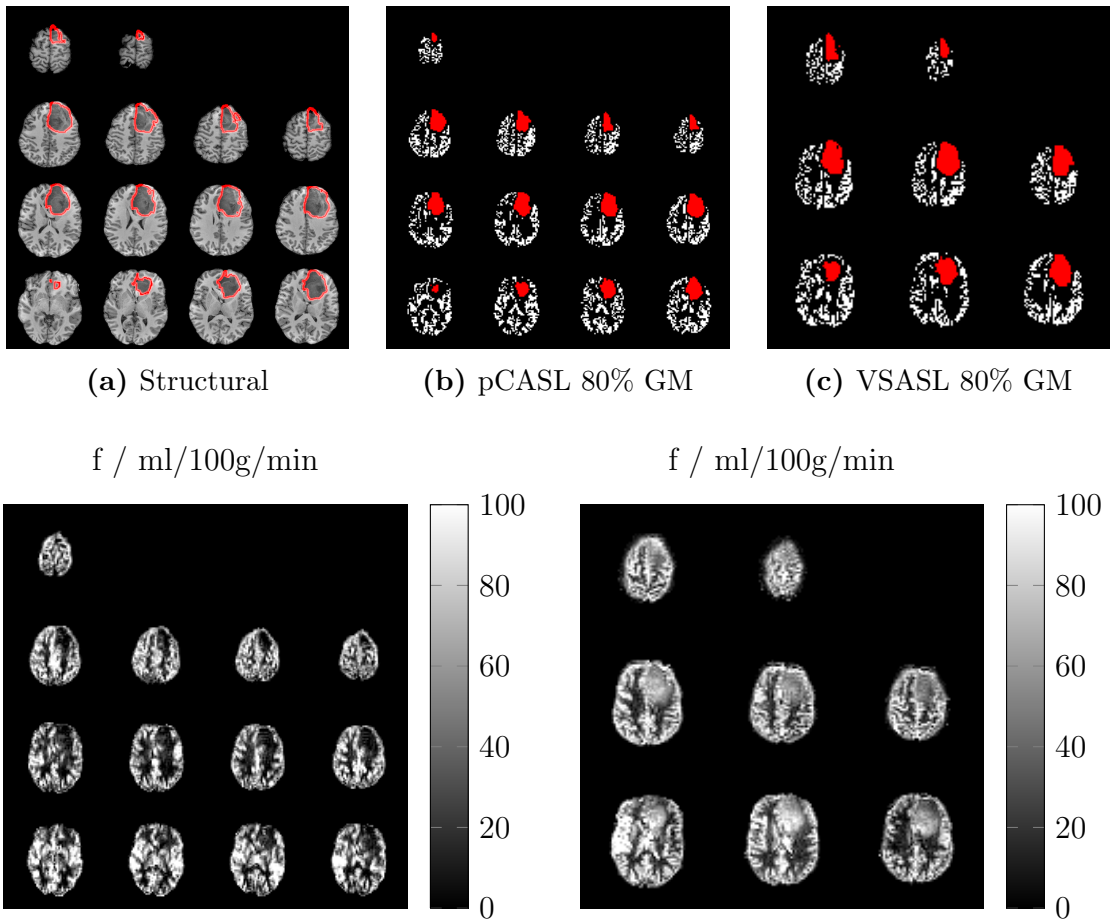
In all four patients a significant signal was found in VSASL, with tumour perfusion values ranging from 56.3 ± 16.0 ml/100g/min to 98.7 ± 101.6 ml/100g/min, summarised in table 4.2. Note that the standard deviations will include any spatial



(a) Structural **(b)** pCASL 80% GM **(c)** VSASL 80% GM

(d) pCASL **(e)** VSASL

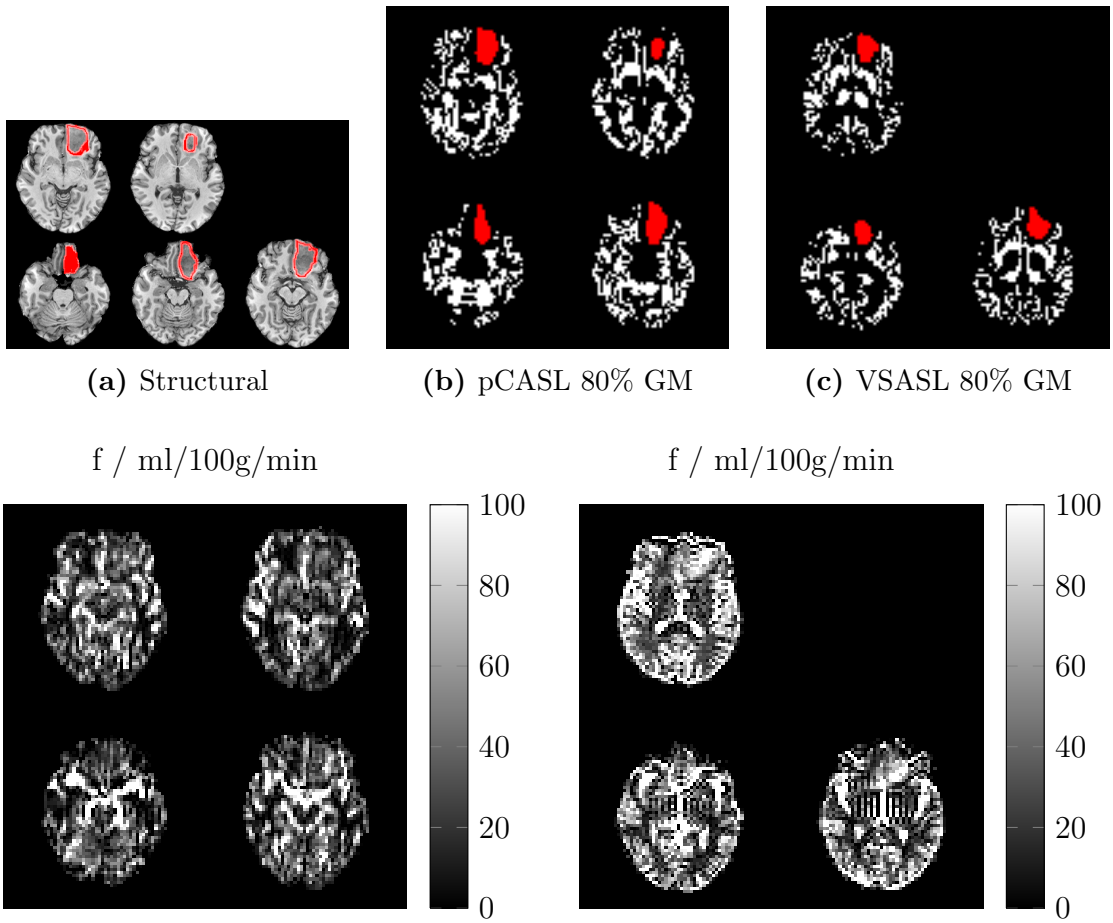
Figure 4.1: Patient A, presumed low grade glioma.



(a) Structural **(b)** pCASL 80% GM **(c)** VSASL 80% GM

(d) pCASL **(e)** VSASL

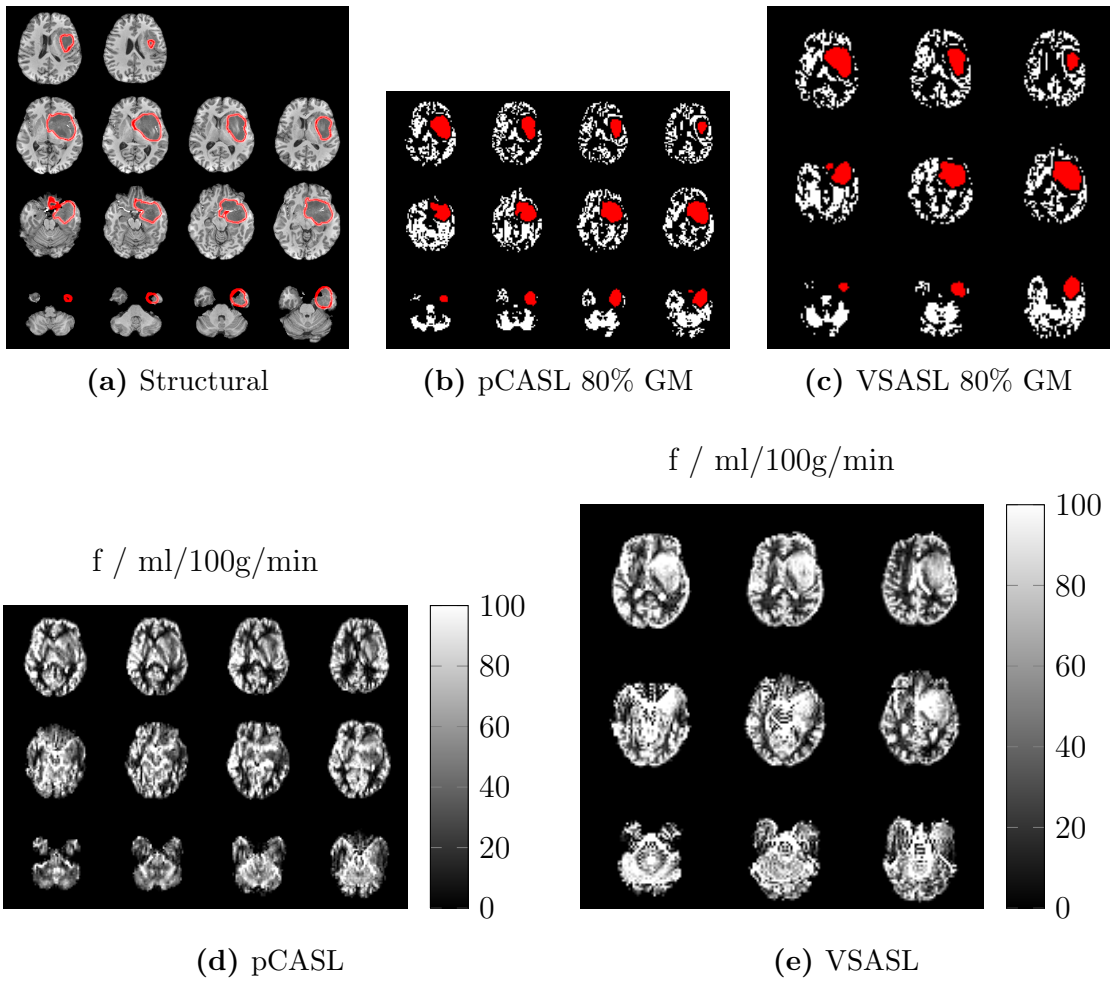
Figure 4.2: Patient B, grade III glioma.



(a) Structural **(b)** pCASL 80% GM **(c)** VSASL 80% GM

(d) pCASL **(e)** VSASL

Figure 4.3: Patient C, grade II glioma.



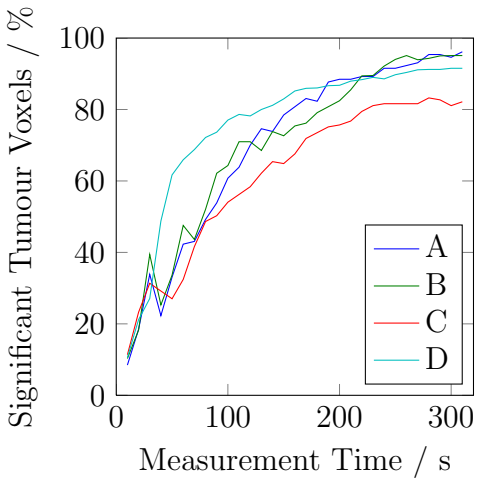
(a) Structural **(b)** pCASL 80% GM **(c)** VSASL 80% GM

(d) pCASL **(e)** VSASL

Figure 4.4: Patient D, presumed high grade glioblastoma multiforme.

Patient	Grey Matter			Tumour		
	pCASL BAT / s	f_{pC} / ml/100g/min	f_{VS} / ml/100g/min	pCASL BAT / s	f_{pC} / ml/100g/min	f_{VS} / ml/100g/min
A	1.23±0.23	44.1±32.6	46.0±49.6	1.39±0.17	35.1±25.3	56.3±16.0
B	1.23±0.27	63.7±32.5	67.9±34.7	1.33±0.19	20.7±22.0	61.5±20.2
C	1.38±0.23	33.5±24.8	45.1±35.7	1.37±0.18	34.0±22.6	80.0±73.0
D	1.22±0.25	62.5±31.0	69.7±47.2	1.17±0.18	54.6±26.9	98.7±101.6
Mean	1.27±0.08	51.0±14.7	57.2±13.5	1.32±0.10	36.1±14.0	74.1±19.3

Table 4.2: Grey Matter and Tumour pCASL and VSASL quantification. All values are mean ± SD.



(a) Significant VSASL Tumour Voxels

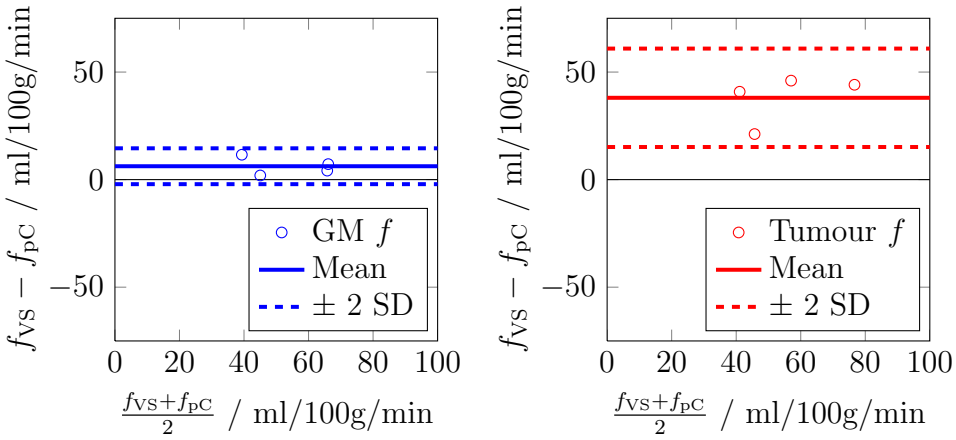
Figure 4.5: The percentage of significant VSASL voxels within each tumour (4.5a).

heterogeneity within the tumour mask itself. The percentage of significant VSASL voxels within the tumour are plotted in figure 4.5. In all tumours, more than 50% of the voxels were significant after 120 s and a plateau seems to be reached for all tumours by the end of the 5 minute scan.

The mean VSASL SNR calculated over all tumours at the end of the scan was 5.4 ± 0.9. Mean grey matter perfusion measured by VSASL was 57.2 ± 13.5 ml/100g/min (range 45.1 to 69.7). With VSASL, the mean tumour perfusion was 74.1 ± 19.3 ml/100g/min (range 56.3 to 98.7), higher than the VSASL measurement in grey matter. In all VSASL measurements there is hyper-intense signal in the ventricles.

In pCASL the BAT was elevated in the tumours compared to grey matter, but this difference was not significant ($P > 0.05$). Mean grey matter perfusion measured by pCASL was 51.1 ± 14.7 ml/100g/min (range 33.5 to 63.7). Mean tumour perfusion measured by pCASL was 36.1 ± 14.0 ml/100g/min (range 20.7 to 54.6), lower than the pCASL measurement in grey matter.

Although only four patients are available for analysis, using Bland-Altman plots it can be seen that the perfusion values measured in grey matter agree between VSASL and pCASL (fig. 4.6). There is a bias of +6.2 ± 4.2 ml/100g/min towards VSASL,



(a) Grey Matter **(b)** Tumour

Figure 4.6: Agreement between the perfusion value measured by pCASL and the perfusion value measured by VSASL in each patients grey matter mask (4.6a) and tumour mask (4.6b).

but this is not significant with only 4 subjects. In the tumour masks VSASL is shown to measure significantly higher perfusion than pCASL, with a bias of +38.0 ± 11.4 ml/100g/min.

4.3 Discussion and Conclusions

The primary aim of this study was to determine the feasibility of performing VSASL measurements in patients with tumours. In all four subjects there was significant signal within the tumours in a clinically feasible scan time of 5 minutes, indicating that VSASL does yield a signal in a clinically realistic time.

A secondary aim was to compare the perfusion values measured by pCASL with the values measured with VSASL. These results appear to show that although there is a good agreement in perfusion estimate between pCASL and VSASL in grey matter, there is poor agreement in tumour. As such, it is concluded that VSASL is not validated in tumours. In spatially labelled ASL in the brain the labeling can simply be applied inferior and superior to the slice to validate the perfusion signal, as blood

will generally be delivered to the tissue only from the inferior side. However, in VSASL it is more difficult to control for all non-perfusion related phenomena that confound the signal.

Despite this apparant lack of validation of the VSASL measurement, the comparison between the VSASL and pCASL techniques in this feasibility study has several flaws. The first is the difference in the acquisition and analysis of the data (readout, crushing, number of inflow times and correction for transverse decay rates). As the study was ongoing the pCASL sequence could not be altered. As only 5 minutes were available for the VSASL scan compromises were made to maximise SNR, since VSASL theoretically has $0.5e$ lower SNR than pCASL (Wong et al., 1998a). The pCASL labeling efficiency was not measured or corrected for velocity. Additionally, T_1 and λ were assumed to be constant across the whole brain, whereas they will probably differ in tumour. Finally, this is only a small cohort of four patients where the VSASL cutoff velocity has not been optimised.

Nevertheless, the perfusion values in grey matter agreed between VSASL and pCASL. However, the perfusion signal in tumours measured with VSASL is significantly higher than tumour perfusion measured by pCASL. This may be due to two possible reasons: either the bolus arrival time in pCASL is longer than the maximum TI, or VSASL is overestimating perfusion some a systematic bias related to the tumour physiology.

It seems unlikely that the bolus arrival time in tumours for the pCASL labeling plane used is greater than the longest TI of 2.9 s. Acquisitions at longer TIs, with longer labeling durations, could be used to test this hypothesis. Literature values suggest that low grade glioma perfusion is on the order of white matter perfusion, and rises with tumour grade (Hakyemez et al., 2005). The pCASL sequence measured a lower perfusion in the tumours compared to grey matter (36.1 $\pm$ 14.0 ml/100g/min and 51.0 $\pm$ 14.7 ml/100g/min, respectively), which supports this expected trend in

perfusion measurement. Conversely, VSASL measured a significantly higher perfusion in tumours (74.1 ± 19.3 ml/100g/min) than grey matter (57.2 ± 13.5 ml/100g/min) (P = 0.019, two sided t-test), contrary to what would be expected from previous studies.

The second possibility is that VSASL is overestimating tumour perfusion due to a systematic bias. The VSASL perfusion maps exhibit artefacts in the ventricles, which could be due to CSF flow and motion. In and around tumours oedema can form and there is high interstitial fluid pressure (Lunt et al., 2008). Both these effects would increase the apparent diffusion coefficient of the tumour, which could be mistaken for perfusion when using the VSASL sequence. This artefact in the ventricles, along with the suggestions from the literature that these tumours are more likely to have lower perfusion than grey matter, led to the hypothesis that the most likely explanation of these results is that standard VSASL measurements are systematically biased by a sensitivity to bulk motion and water diffusion. This led to the development of a diffusion insensitive VSASL sequence that is discussed in Chapter 5.

Chapter 5

Physiological Effects in VSASL

In chapter 3 the hardware and physical sources of error when using velocity selective pulses were studied, and it was concluded that eddy currents can contribute to a significant overestimation of perfusion measured with VSASL. In this chapter the magnitude of the physiological sources of error when using velocity selective pulses are determined. Two effects that are not balanced between the tag and control condition of current VSASL sequences will be studied: bulk motion and diffusion. The hypothesis is that both effects cause an overestimation of perfusion in VSASL.

The chapter will begin with a derivation of the magnitude of the two effects using the standard model (Buxton et al., 1998). A novel labeling scheme in then developed to eliminate the confounds of diffusion effects, Velocity Selective Transfer Insensitive Perfusion Technique (VS-TILT). Finally, expressions for the bolus shape from non-laminar, non-isotropic vascular networks are derived.

5.1 Simulation of Motion and Diffusion Effects

In this section an equation is derived that expresses the systematic perfusion errors due to the diffusion and bulk motion of background tissue. This is then simulated using literature values of tissue properties.

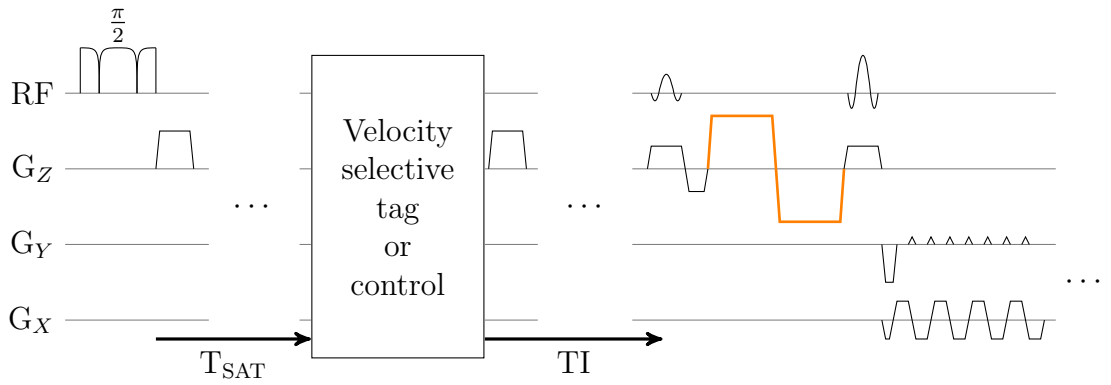


Figure 5.1: The VSASL pulse sequence used in this chapter consists of three sequence building blocks. First there is a global pre-saturation using a non-selective $\pi/2$ BIR-4 pulse to remove any spin history effects. This is followed by a saturation delay T_{SAT} and the velocity selective preparation in either the tag or control condition. This is followed by the inflow time delay, TI, and a spin echo EPI readout for each slice. The crusher gradients (orange) have VENC $= V_{cut}$ in both tag and control conditions, and is applied on the same axis as the velocity encoding gradients.

5.1.1 Theory

Physiological noise due to fluctuations of the large fraction of static tissue in the acquired voxel reduces the sensitivity of ASL data. These fluctuations can be reduced with background suppression (Ye et al., 2000b) and/or cardiac RETROICOR (Wu et al., 2009). In this chapter the additional physiological effects during the velocity selective pulse itself are considered. The hypothesis is that these could generate additional systematic errors beyond the physiological noise in spatially labeled ASL, since in VSASL the labeling pulse is applied to the entire RF field of view. In this work only the velocity selective pulse is considered as only this is modified between tag and control, potentially resulting in a systematic bias in the perfusion weighted subtraction. All other pulses and crushers are identical between tag and control, so will not lead to a systematic bias.

Consider a voxel that has tissue with equilibrium magnetisation $M_{0,t}$ and relaxation times $T_{1,t}$ and $T_{2,t}$. At the start of the VSASL pulse sequence the magnetisation is reset by the pre-saturation pulse (fig. 5.1). At the time of the velocity selective

pulse (T_{SAT}) the tissue magnetisation is given by

$$M_t(T_{SAT}) = M_{0,t} \cdot \left[1 - \exp\left(-\frac{T_{SAT}}{T_{1,t}}\right)\right] \tag{5.1}$$

The velocity selective pulse with saturation efficiency α is then applied. If there are any differences in the velocity selective pulse between tag and control the difference in tissue M_z will be given by

$$\Delta M_t(T_{SAT}) = M_{0,t} \cdot \left[1 - \exp\left(-\frac{T_{SAT}}{T_{1,t}}\right)\right] \cdot \alpha \cdot (1 - \Delta\beta) \tag{5.2}$$

where $\Delta\beta$ is a factor that accounts for these perturbations. Ideally, the background tissue is not perturbed by the velocity selective pulse and $\Delta\beta = 1$. However, in VSASL the contrast is fundamentally generated by a difference in first gradient moment, m_1, of the velocity selective pulse. For the tag condition $m_1 = \frac{\pi}{\gamma V_{\text{cut}}}$ and for the control $m_1 = 0$. This results in a cosinusodial variation with velocity in M_z in the tag condition, but M_z is constant for all velocities in the control condition. For this difference in m_1, $\Delta\beta$ is given by

$$\Delta\beta_v = \cos(\gamma \cdot m_1 \cdot v) = \cos\left(\pi \cdot \frac{v_t}{V_{\text{cut}}}\right) \tag{5.3}$$

where v_t is the velocity of the tissue projected along the direction of the velocity selective gradient.

In current VSASL implementations the difference in m_1 is achieved by playing out the velocity selective gradients in the tag condition but turning them off in the control condition (Wong et al., 2006; Duhamel et al., 2003). Along with a difference in m_1 between tag and control there is also a difference in the diffusion b-value. For

diffusion effects, the $\Delta\beta$ term is

$$\Delta\beta_D = \exp\left(-b(V_{\text{cut}}) \cdot ADC_t\right) \tag{5.4}$$

where ADC_t is the apparent diffusion coefficient of the tissue and $b(V_{\text{cut}})$ is the difference in b-value for the chosen V_{cut}.

The difference in tissue M_z at the time of the acquisition is then given by

$$\Delta M_t(\text{TI}) = M_{0,t} \cdot \left[1 - \exp\left(-\frac{T_{SAT}}{T_{1,t}}\right)\right] \cdot \alpha \cdot (1 - \Delta\beta) \cdot \exp\left(-\frac{\text{TI}}{T_{1,t}}\right) \cdot \exp\left(-\frac{\text{TE}}{T_{2,t}}\right) \tag{5.5}$$

where TI is the inflow time and TE is the echo time. Equation 5.5 shows that the difference in m_1 and b lead to a positive contribution from tissue in the perfusion weighted subtraction as $\Delta\beta < +1$ in both cases.

The bolus arrival time in VSASL is assumed to be zero (Wu and Wong, 2006), so the standard PASL model (Buxton et al., 1998) describes the contribution from blood as

$$\begin{aligned}\Delta M_b(\text{TI}) = M_{0,B} \cdot \left[1 - \exp\left(-\frac{T_{SAT}}{T_{1,B}}\right)\right] \cdot \alpha \cdot f \cdot \text{TI} \cdot q_p(f) \cdots \\ \cdots \exp\left(-\frac{\text{TI}}{T_{1,B}}\right) \cdot \exp\left(-\frac{\text{TE}}{T_{2,B}}\right)\end{aligned} \tag{5.6}$$

where the B subscripts indicate blood, f is perfusion and $q_p(f)$ takes into account the difference in relaxation rates between blood and tissue, as defined by equation 3.9.

Consider a voxel where the true perfusion is zero and the only signal in the VSASL experiment is from tissue. If perfusion were to be quantified using equation 5.6 the erroneous perfusion signal from tissue, Δf, would be given by equating equations 5.6 and 5.5:

$$\Delta M_t(\text{TI}) = \Delta M_B(\text{TI}) \tag{5.7}$$

Tissue	T_1 / s	T_2 / s	ADC / mm^2/s	$M_{0,t}/M_{0,CSF}$
CSF	3.7[A]	1.30[C]	2.7×10^{-3} [F]	1.00[G]
Grey Matter	1.1[A]	0.11[D]	0.9×10^{-3} [F]	0.89[G]
White Matter	0.8[A]	0.08[D]	0.7×10^{-3} [F]	0.73[G]
Blood	1.6[B]	0.15[E]	-	0.87[G]

Table 5.1: Table of tissue properties used in the simulation. Data are from Clare and Jezzard (2001) (A), Lu et al. (2004) (B), Guo and Wong (2011b) (C), Wansapura et al. (1999) (D), Lu et al. (2012) (E), Helenius et al. (2002) (F) and Herscovitch and Raichle (1985b) (G).

such that

$$\Delta f = \frac{M_{0,t} \cdot \left[1 - \exp\left(-\frac{T_{SAT}}{T_{1,t}}\right)\right] \cdot (1 - \Delta\beta) \cdot \exp\left(-\frac{\mathrm{TI}}{T_{1,t}}\right) \cdot \exp\left(-\frac{\mathrm{TE}}{T_{2,t}}\right)}{M_{0,B} \cdot \left[1 - \exp\left(-\frac{T_{SAT}}{T_{1,B}}\right)\right] \cdot \mathrm{TI} \cdot q_p(f) \cdot \exp\left(-\frac{\mathrm{TI}}{T_{1,B}}\right) \cdot \exp\left(-\frac{\mathrm{TE}}{T_{2,B}}\right)} \tag{5.8}$$

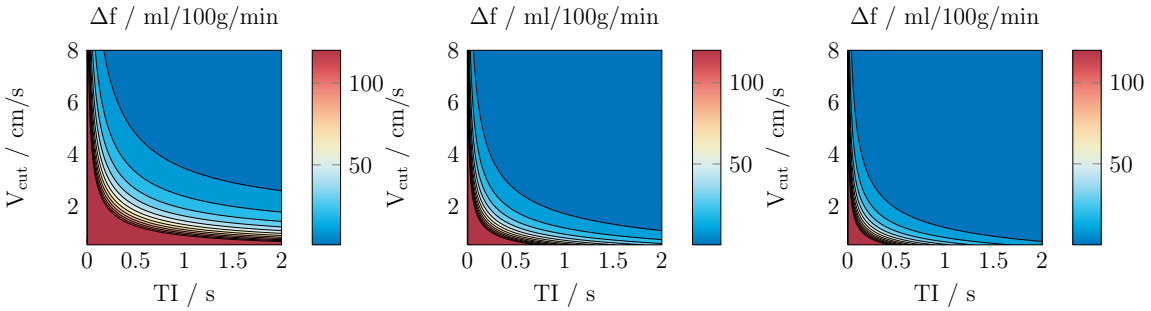
For simplicity, the value of perfusion used in $q_p(f)$ was 0.01 ml/ml/s.

5.1.2 Methods

The systematic perfusion overestimation (eq. 5.8) was then simulated using MATLAB r2012a (The Mathworks, Natick, MA, USA). Three example tissue types were considered: Grey Matter, White Matter and Cerebrospinal fluid (CSF) with tissue properties summarised in table 5.1.

A VSASL acquisition was simulated with $\mathrm{T_{SAT}} = 3$ s and TE = 30 ms. The diffusion b-value was calculated for a BIR-8 VSASL preparation with maximum gradient strength 20 mT/m, rise time 0.5 ms, and V_{cut} from 0.5 cm/s to 8 cm/s in steps of 0.05 cm/s. The TI was varied from 1 ms to 2 s and Δf from equation 5.8, with $\Delta\beta$ from equation 5.4, was calculated for CSF, Grey Matter and White Matter.

The effect of tissue motion was simulated using equation 5.8, with $\Delta\beta$ from equation 5.3. This simulation is independent of the velocity selective pulse used, and only depends on the m_1 imparted in the tag condition relative to the control condition. The diffusion b-value for the tissue motion simulation was assumed to be zero. Pa-



(a) CSF **(b)** Grey Matter **(c)** White Matter

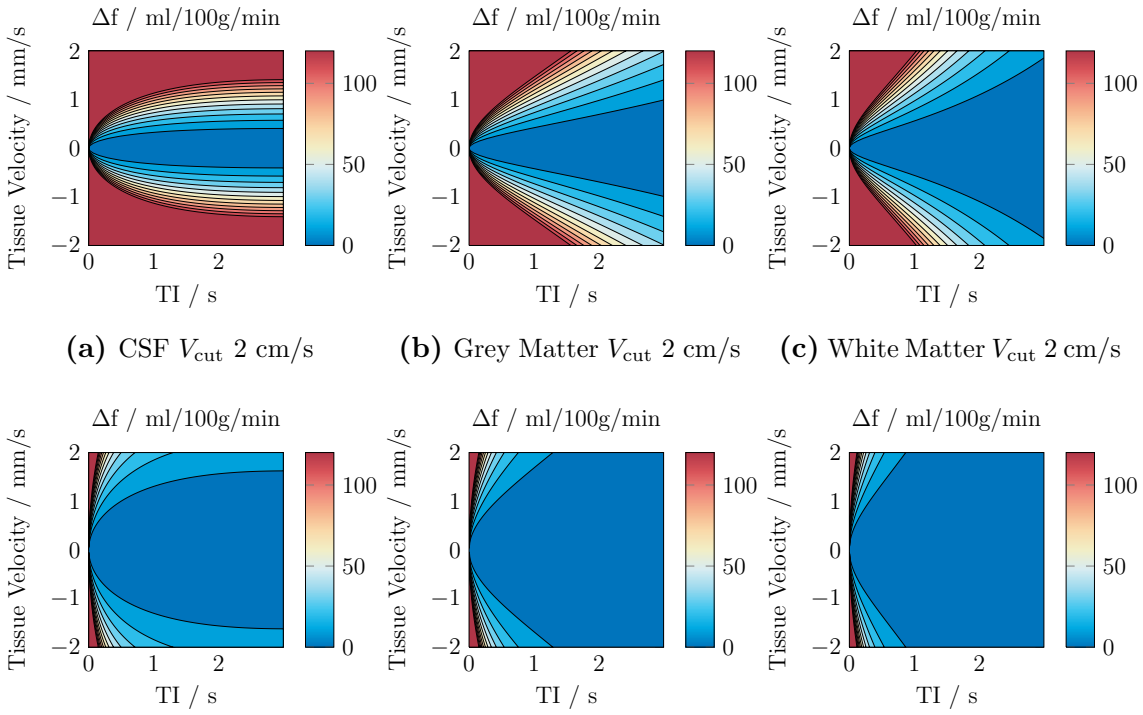
Figure 5.2: Perfusion overestimation according to eq. 5.8 due to tissue diffusion when using BIR-8 VSASL for CSF (fig. 5.2a), grey matter (fig. 5.2b) and white matter (fig. 5.2c).

rameters used were T_{SAT} = 3 s, TE = 30 ms, TI was varied from 1 ms to 3 s in steps of 1 ms and the velocity of the tissue varied from -2 mm/s to +2 mm/s in steps of 1 μm/s.

5.1.3 Results

The perfusion overestimation values due to tissue diffusion in BIR-8 VSASL are displayed in figure 5.2. It can be see that the overestimation is highest for CSF, as CSF has a greater ADC than grey matter or white matter. The overestimation increases as V_{cut} decreases, due to the increasing b-value of the velocity selective pulse. The error reduces as TI increases, as the tissue signal will decay with $T_{1,t}$. For TI = 1 s at V_{cut} = 2 cm/s the overestimation in a voxel of CSF will be +32.0 ml/100g/min, grey matter will be +6.4 ml/100g/min and white matter will be +2.8 ml/100g/min.

The results for the simulation of tissue motion at V_{cut} = 2 cm/s and 8 cm/s are displayed in figure 5.3. The errors are again largest for CSF, due to the long T_1 of the tissue. At V_{cut} = 2 cm/s and TI = 1 s, CSF that has velocity of ±1 mm/s will cause an overestimation of perfusion of +93.8 ml/100g/min, grey matter at ±1 mm/s will cause an overestimation of +53.7 ml/100g/min and white matter at ±1 mm/s an overestimation of +31.8 ml/100g/min. These overestimations are reduced when using



(a) CSF V_{cut} 2 cm/s **(b)** Grey Matter V_{cut} 2 cm/s **(c)** White Matter V_{cut} 2 cm/s

(d) CSF V_{cut} 8 cm/s **(e)** Grey Matter V_{cut} 8 cm/s **(f)** White Matter V_{cut} 8 cm/s

Figure 5.3: Perfusion overestimation according to eq. 5.8 due to tissue motion for CSF (fig. 5.3a), grey matter (fig. 5.3b) and white matter (fig. 5.3c) at $V_{\text{cut}} = 2$ cm/s. The errors are reduced when using $V_{\text{cut}} = 8$ cm/s for CSF (fig. 5.3d), grey matter (fig. 5.3e) and white matter (fig. 5.3f).

V_{cut} = 8 cm/s to +5.9 ml/100g/min for CSF, +3.4 ml/100g/min for grey matter and 2.0 ml/100g/min for white matter, respectively.

5.1.4 Discussion

Although the tissue velocity and ADC may be small, the errors are on the order of the expected *in vivo* perfusion signal, especially for tissue motion of ±1 mm/s at V_{cut} = 2 cm/s. Whilst the diffusion error could be eliminated by creating a diffusion insensitive labeling scheme, the errors due to motion are a fundamental bi-product of the blood-tissue contrast generation in VSASL.

The derivations show that physiological noise due to bulk motion is rectified in VSASL, and will always contribute to a perfusion overestimation. Depending on the tissue type, even a small velocity of motion during the labeling pulse can cause artefacts on the order of the genuine perfusion signal. The error increases as V_{cut} is reduced or as short TI values are used. Due to the cosinusoidal variation in velocity produced in the tag condition both positive and negative tissue velocities will result in an overestimation of perfusion. As the signal compartment of the background tissue is large, only a small velocity during the pulse (for example, 1 mm/s results in a displacement of 20 μm during the BIR-8 pulse) will result in significant perfusion overestimation.

It is important to note that these systematic errors will not be reduced when using traditional background suppression approaches. In traditional background suppression two inversion pulses are applied during the inflow time, between the labeling pulse and the readout excitation (Ye et al., 2000b). This reduces the magnetisation of the background tissue at the time of signal readout so that any fluctuations from physiological variation are minimised, but the difference between the tagged and controlled blood magnetisation is preserved. It follows that any magnetisation difference between tag and control states caused by the labeling pulse will be preserved when

using traditional background suppression techniques. As the diffusion and bulk motion errors are being generated during the labeling pulse, they will not be reduced when using inversion pulses during the inflow time.

However, the background suppression principle can be used to minimise the bulk motion errors in VSASL. The difference is that the background suppression must be played out *before* the velocity selective pulse (Wong, 2004). This results in the magnetisation of the background tissue being ≈ 0 at the time of the velocity selective pulse, so that it cannot be erroneously tagged.

In these simulations quantification using only a single TI is considered. Alternatively, it is possible to add eq. 5.8 as another signal component when fitting multi-TI data. However, the approach taken in this chapter is to remove these artefacts at the time of acquisition rather than in post processing, since if the BAT in VSASL can be approximated as being zero only a single TI needs to be acquired.

In this section it has been shown that diffusion effects will contribute to a overestimation of perfusion when using VSASL, with tissues with long T_1 and high b-value contributing the largest artefacts. As large voxels are used in VSASL in order to overcome the low SNR of the technique partial volume with CSF is inevitable. To eliminate this systematic error a diffusion insensitive VSASL preparation is developed in the next section.

5.2 Elimination of Diffusion Effects

In section 5.1 it was shown that diffusion effects can cause an overestimation of perfusion in VSASL. This is because the velocity selective preparation has a higher diffusion b-value in the tag condition than in the control condition, as the gradients that impart the velocity sensitivity in the tag condition are simply turned off for the control condition.

Velocity selective preparations have also been used to isolate the venous blood compartment to determine OEF in QUIXOTIC (Bolar et al., 2011). However, it was found in that study that the measured venous T_2 in grey matter was longer than the value in the sagittal sinus, indicating that the venous T_2 in grey matter was not being measured correctly. Guo and Wong (2012b) used a diffusion balanced velocity selective preparation (VSEAN) that eliminated the mis-match between the grey matter and sagittal sinus T_2. Those authors hypothesised that long T_2 components such as CSF were contaminating the QUIXOTIC measurement as they were likely to contribute erroneous signal through the diffusion effects mentioned above.

The velocity selective labeling scheme used in VSEAN requires complete spoiling of signal half way through the preparation, and a phase projection step. The VSEAN preparation is not directly applicable to VSASL as the resulting longitudinal magnetisation is proportional to $\sin^2\left(\pi\frac{v}{V_{\text{cut}}}\right)$. For a comparison with current VSASL techniques $M_z \propto \cos\left(\pi\frac{v}{V_{\text{cut}}}\right)$ is required.

In this section a new diffusion balanced velocity selective preparation is proposed that is able to produce $M_z \propto \cos\left(\pi\frac{v}{V_{\text{cut}}}\right)$, and is referred to as VS-TILT. The VS-TILT preparation is evaluated for robustness to eddy currents and ΔB_0, and is applied *in vivo* to determine empirically the magnitude of diffusion contamination in VSASL.

5.2.1 VS-TILT Design

5.2.1.1 Theory

In the VSASL tag condition the velocity selective preparation is applied with first gradient moment $m_1^{\text{tag}} = \frac{\pi}{\gamma V_{\text{cut}}}$, and in the control condition $m_1^{\text{ctrl}} = 0$. In standard VSASL the gradients are turned off in the control condition, which results in a difference in diffusion b-value compared to the tag condition. To balance the diffusion effects a preparation with the same magnitude gradient pattern is desired whilst still achieving the desired difference in m_1. This is achieved by playing out two veloc-

ity selective pulses, VS-A and VS-B, sequentially without any spoiling between the pulses. The total first gradient moment after the application of VS-A and VS-B is simply

$$m_1 = m_{1,A} + m_{1,B} \tag{5.9}$$

In the tag condition the velocity selective pulses are applied with

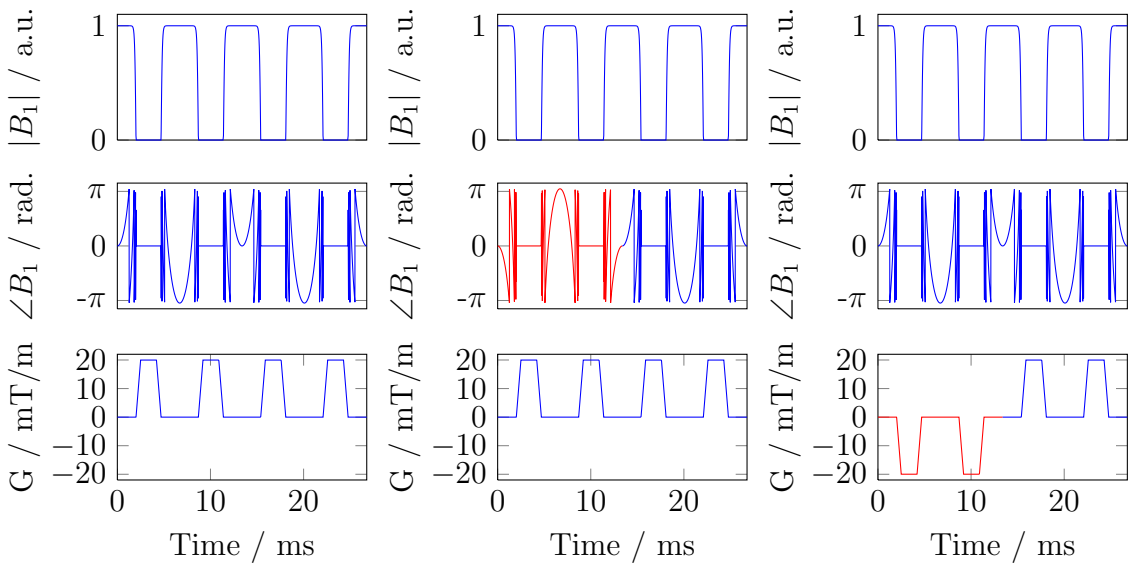
$$m_{1,A}^{\text{tag}} = m_{1,B}^{\text{tag}} = \frac{\pi}{2\gamma V_{\text{cut}}} \tag{5.10}$$

so that the total first gradient moment is $m_1^{\text{tag}} = \frac{\pi}{\gamma V_{\text{cut}}}$. In the control condition VS-A and VS-B are played out with one of the first gradient moments negated

$$-m_{1,A}^{\text{ctrl}} = m_{1,B}^{\text{ctrl}} = \frac{\pi}{2\gamma V_{\text{cut}}} \tag{5.11}$$

so that the total first gradient moment is $m_1^{\text{ctrl}} = 0$. This is analogous to the Magnetisation Transfer Insensitive Labeling Technique (TILT) used in spatially selective PASL (Golay et al., 1999). In the TILT tag condition two +90° RF pulses are played out to produce a spatially selective 180° inversion, and in the control condition a +90° -90° RF pattern leaves the blood unperturbed but balances magnetisation transfer effects. Due to the conceptual similarity with TILT, albeit with the different goal of balancing diffusion effects, the novel velocity selective labeling scheme developed here is referred to as Velocity Selective TILT (VS-TILT).

Any velocity selective pulse can be inserted for VS-A and VS-B, and there is also some freedom in how to negate the m_1 of either VS-A or VS-B in the control condition. Due to the robustness to B_1 inhomogeneity the BIR-4 (fig. 5.4) and sym-BIR-8 (fig. 5.5) pulses are used as the base velocity selective pulse in this work. To negate the m_1 of VS-A for the control condition either the gradient polarity can be negated (figs. 5.4c and 5.5c), or the frequency sweep of the adiabatic pulse can be negated (figs.

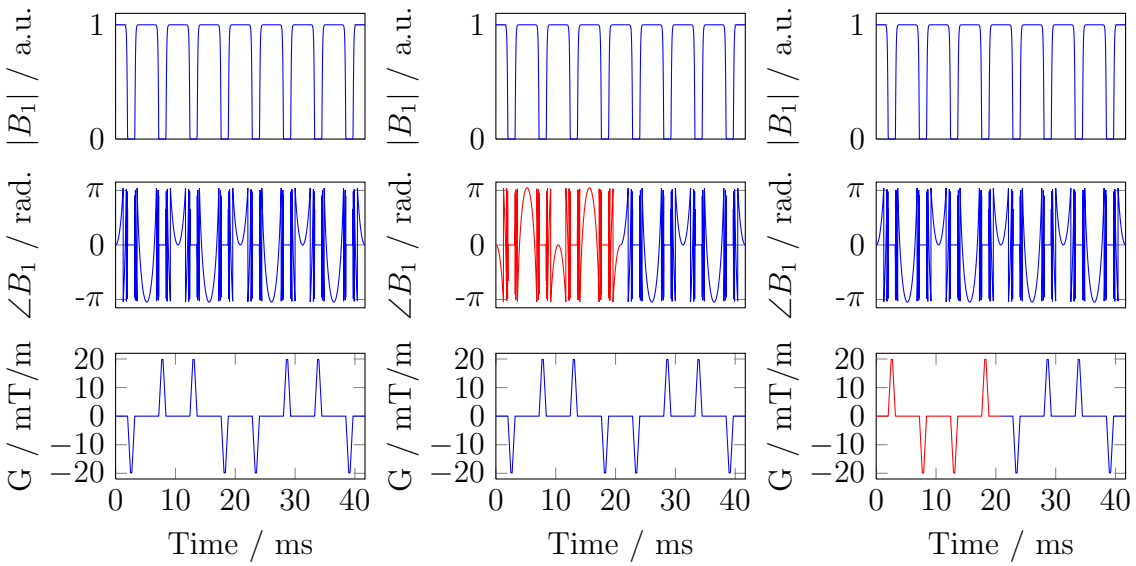


(a) BIR-4 tag condition

(b) Control condition negating frequency sweep

(c) Control condition negating gradients

Figure 5.4: BIR-4 VS-TILT pulse diagram showing normalised RF power (top), RF phase (middle) and velocity selective gradient (bottom). The changes between the tag condition and two control conditions are highlighted in red. In the tag condition two velocity selective BIR-4 pulses are inserted for VS-A and VS-B (5.4a). The control condition can be achieved in two ways: by negating the frequency sweep of VS-A (5.4b), or by negating the gradient polarities in VS-A (5.4c).



(a) BIR-8 tag condition

(b) Control condition negating frequency sweep

(c) Control condition negating gradients

Figure 5.5: BIR-8 VS-TILT pulse diagram showing normalised RF power (top), RF phase (middle) and velocity selective gradient (bottom). The changes between the tag condition and two control conditions are highlighted in red. Displayed are the tag condition with two sequential BIR-8 pulses (5.5a), the control condition can be achieved either by negating the frequency sweep (5.5b) or by negating the gradient polarities (5.5c).

5.4b and 5.5b). Neither method will alter the b-value of the composite pulse as this is proportional to the time integral of the gradient squared

$$b = \gamma^2 \int_0^{TE} \left[\int_0^t G(t')dt' \right]^2 dt \tag{5.12}$$

whereas the m_1 is linearly proportional to the applied gradient

$$m_1 = \int_0^t G(t')t'dt' \tag{5.13}$$

Since it is possible that negating the gradient polarities for the control condition may be sensitive to eddy current effects, this was simulated and tested experimentally. In the next section the four permutations of velocity selective pulse (BIR-4 or BIR-8)

and m_1 negation method (gradient or frequency sweep negating) are simulated.

5.2.1.2 Simulation Methods

Bloch equation simulations were performed using MATLAB 2012a (The MathWorks Inc., Natick, MA, USA). The simulation considers rotations of the normalised magnetisation about B_{eff} with a time step of 5 μs. For these simulations relaxation times were ignored and the magnetisation was initially fully relaxed in the $\hat{z}$ direction.

For each simulation two VS-TILT pulses were used (BIR-4 and BIR-8), and for each pulse type three conditions were simulated: the tag condition with $m_1 = \frac{\pi}{\gamma V_{\text{cut}}}$, the control condition by negating the frequency sweep of VS-A, and the control condition by negating the gradient polarities of VS-A.

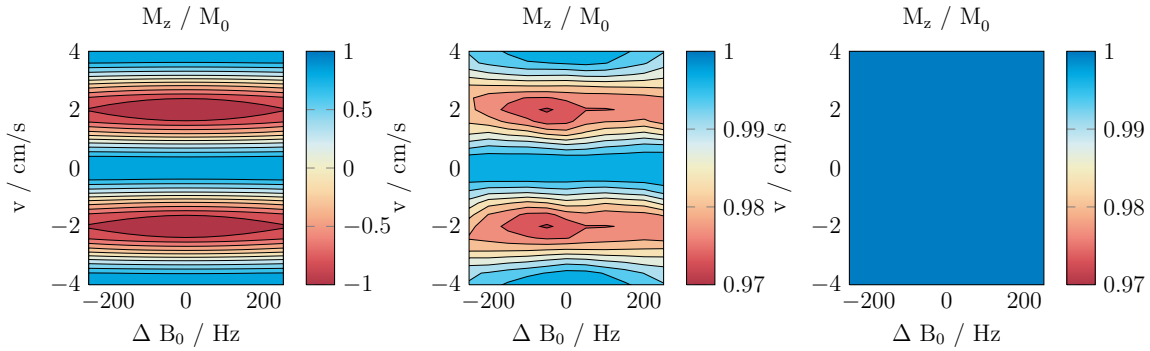
For all simulations $V_{\text{cut}} = 2$ cm/s, the maximum gradient strength was 20 mT/m with a rise time of 0.5 ms and the maximum $|B_1|$ was 20 μT unless otherwise specified. The BIR-4 and BIR-8 pulses used parameters $\zeta = 15$, $\tan(\kappa) = 60$, and $\omega_{\text{MAX}} = 39.8$ kHz as optimised in chapter 3. The BIR-8 pulse used the +1:-1:-1:+1 gradient pattern to minimise eddy current effects.

ΔB_0 Simulation

The effect of B_0 inhomogeneity on the tagging efficiency was simulated with ΔB_0 offset from -250 Hz to +250 Hz in steps of 50 Hz and the velocity of the spin packet from -4 cm/s to 4 cm/s in steps of 0.4 cm/s.

Eddy Currents Simulation

The effect of eddy currents on static spins was simulated by convolving the desired gradient waveform with an eddy current of amplitude 0.25% (eq 2.14). The eddy current time constants, τ, were logarithmically spaced from 10^{-4} s to 1 s in 9 steps, and the position of the static spins from gradient isocentre ranged from -24 cm to +



(a) BIR-4 tag condition **(b)** Control condition negating frequency sweep **(c)** Control condition negating gradients

Figure 5.6: BIR-4 VS-TILT off-resonance response for moving spins for the tag condition (5.6a), frequency sweep negation control condition (5.6b) and gradient polarity negation (5.6c). Note that figures 5.6b and 5.6c have a reduced colour scale.

24 cm in steps of 4 cm.

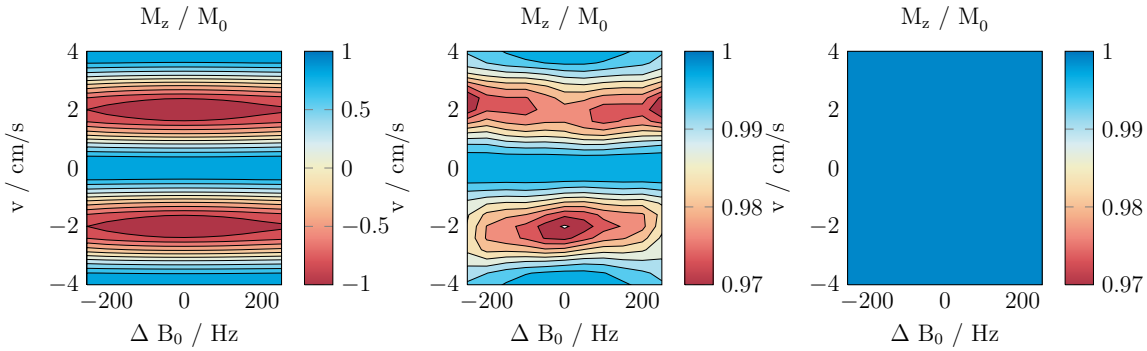
5.2.1.3 Results

ΔB_0 Simulation

Displayed are the final M_z for moving spins after the application of the BIR-4 VS-TILT preparations (fig. 5.6) and BIR-8 VS-TILT preparation (fig. 5.7). For both tag conditions the VS-TILT preparation imparts the desired cosinusodial variation in velocity (figs. 5.6a and 5.7a). When ignoring relaxation the labeling efficiency of both BIR-4 VS-TILT and BIR-8 VS-TILT is reduced to 90% as off resonance is increased to 250 Hz.

After the application of the velocity selective control preparation M_z/M_0 is ideally 1 for all velocities. Both the BIR-4 and BIR-8 control conditions when negating the frequency sweep produce an inadequate control condition for moving spins (figs. 5.6b and 5.7b) in the presence of off-resonance. The minimum M_z/M_0 when negating the frequency sweep is 97.3% for BIR-4 VS-TILT and 97.0% for BIR-8 VS-TILT.

When negating the gradient polarities of VS-A for the control condition both the BIR-4 and BIR-8 produce more homogeneous control conditions (figs. 5.6c and 5.7c).



(a) BIR-8 tag condition **(b)** Control condition negating frequency sweep **(c)** Control condition negating gradient

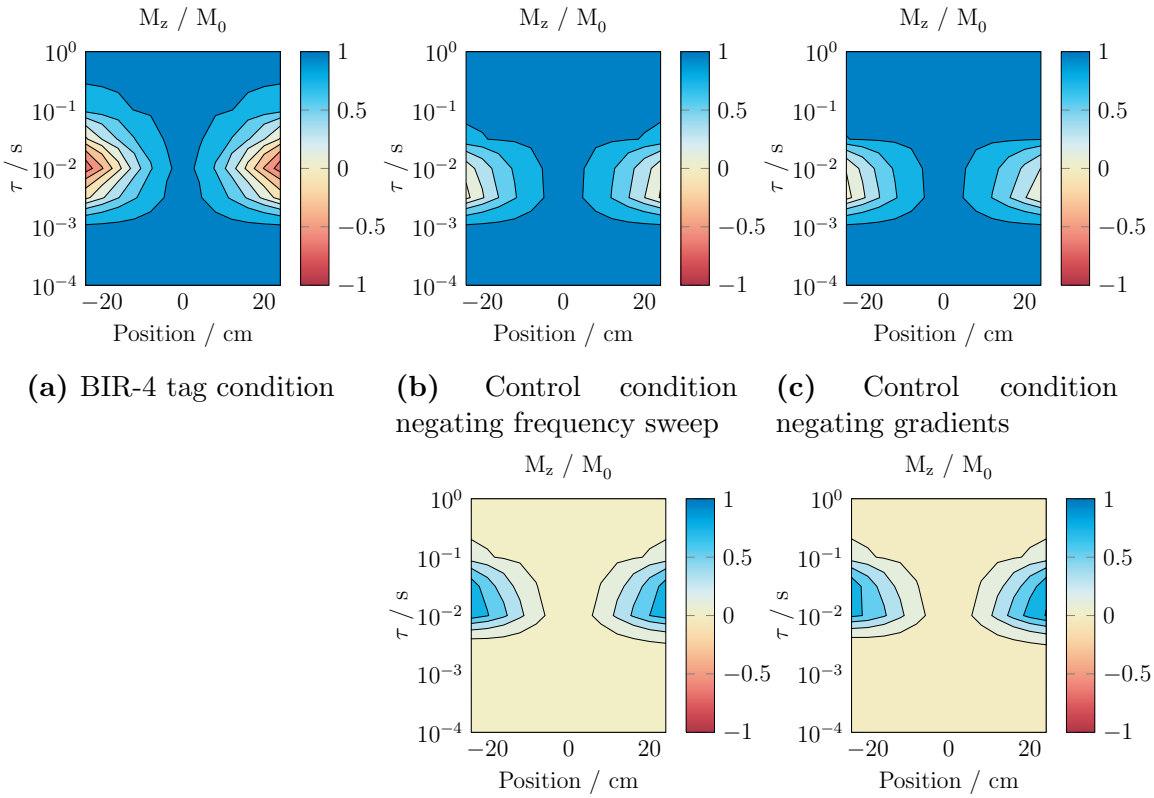
Figure 5.7: BIR-8 VS-TILT off resonance response for moving spins for the tag condition (5.7a), frequency sweep negation control condition (5.7b) and gradient polarity negation (5.7c). Note that figures 5.7b and 5.7c have a reduced colour scale.

In this case the minimum M_z/M_0 when negating the frequency sweep is 99.9% for both BIR-4 VS-TILT and BIR-8 VS-TILT.

Eddy Currents Simulation

The final M_z/M_0 plots for static spins after the application of the VS-TILT preparation in the presence of eddy currents are displayed for BIR-4 VS-TILT (fig. 5.8) and BIR-8 VS-TILT (fig. 5.9). After the application of the preparation M_z/M_0 is ideally 1 for all static spins at all positions from isocentre. In the tag condition the BIR-4 VS-TILT is sensitive to eddy currents in the range 10^{-3} s to 10^{-1} s, with minimum $M_z/M_0 = -66.0\%$ (fig. 5.8a). The eddy current sensitivity is reduced using BIR-8 VS-TILT, with minimum $M_z/M_0 = 92.2\%$ (fig. 5.9a).

Eddy currents effects are not eliminated in the tag condition for either BIR-4 or BIR-8. Thus, in order that eddy currents do not produce artefacts, the control condition must produce the same eddy current spectrum such that the subtraction ($|\Delta M_z|/M_0$) is 0. Both BIR-4 VS-TILT control conditions have a different eddy current response to the BIR-4 VS-TILT tag condition (fig. 5.8b and 5.8c). The $|\Delta M_z|/M_0$ subtraction shows that the difference in the eddy current response would



(a) BIR-4 tag condition

(b) Control condition negating frequency sweep

(c) Control condition negating gradients

(d) ΔM subtraction when negating frequency sweep

(e) ΔM subtraction when negating gradients

Figure 5.8: M_z of static spins after a BIR-4 VS-TILT preparation (fig. 5.4) in the presence of eddy currents with time constants τ as a function of distance from isocentre. Displayed are the tag condition (5.8a), the control condition when negating the frequency sweep of VS-A (5.8b) and the control condition when negating the gradient polarity of VS-A (5.8c). The ΔM subtraction for the frequency sweep negation (5.8d) and gradient polarity negation (5.8e) indicates that eddy currents would result in positive signal from static spins in the BIR-4 VS-TILT ΔM.

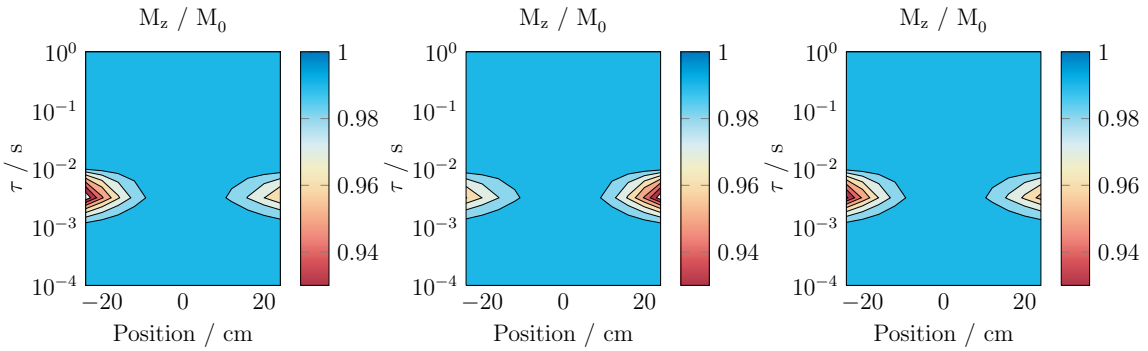
produce positive M_z/M_0 from static spins in the perfusion weighted image (fig. 5.8d and fig. 5.8e). The overall effect is that the BIR-4 VS-TILT is most sensitive to eddy current time constants in the range 10^{-2} s to 10^{-1} s, with maximum $|\Delta M_z|/M_0 = 96.0\%$.

For the BIR-8 VS-TILT control condition the reversed frequency sweep of VS-A produces an eddy current response that is spatially negated compared to the tag condition (fig. 5.9b). The ΔM subtraction of this control condition indicates that eddy currents would produce both positive and negative artefacts (fig. 5.9d), with maximum $|\Delta M_z|/M_0 = 3.7\%$ for eddy current time constants on the order of 10^{-3} s. This error is reduced by using the BIR-8 VS-TILT gradient negation control condition (fig. 5.9c), which has a similar eddy current response to the BIR-8 tag condition. In this case the maximum $|\Delta M_z|/M_0 = 0.6\%$ (fig. 5.9e).

5.2.1.4 Discussion

The simulations suggest that the frequency sweep negation approach does not produce an adequate control condition for moving spins. This could be due to the switch from the negative frequency sweep to positive frequency sweep at the interface of VS-A and VS-B violating the adiabatic condition. The effect is not present when simulating the pulse at $|B_1| = 40$ μT (data not shown), suggesting that the frequency sweep reversal control condition would have a higher adiabatic threshold than the 20 μT used in the simulations and the minimum $|B_1|(r)$ that is achieved with body coil transmit.

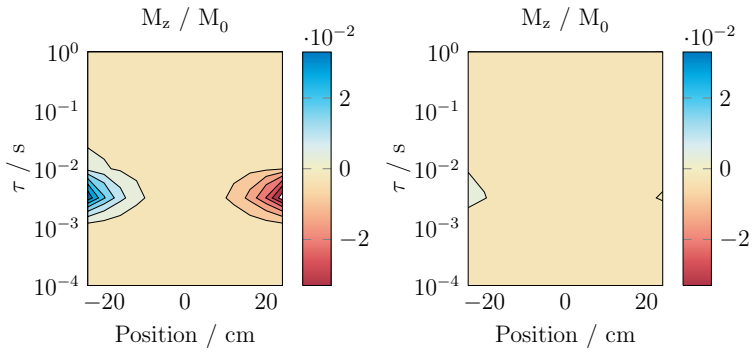
The alternative to frequency sweep negation is to negate the gradient polarities for VS-A. The eddy current simulations suggest that both the BIR-4 VS-TILT control schemes will be more sensitive to eddy current effects than BIR-8 VS-TILT. The simulations also suggest that the BIR-8 VS-TILT with negated gradient polarities will be the least sensitive to eddy currents, and produce the optimal control condition for moving spins at the achievable $|B_1|(r)$.



(a) BIR-8 tag condition

(b) Control condition negating frequency sweep

(c) Control condition negating gradients



(d) ΔM subtraction when negating frequency sweep

(e) ΔM subtraction when negating gradients

Figure 5.9: M_z of static spins after a BIR-8 VS-TILT preparation (fig. 5.5) in the presence of eddy currents. Note that the scale is reduced compared to 5.8 as the eddy current effects are smaller. Displayed are the tag condition (5.9a), the control condition when negating the frequency sweep of VS-A (5.9b) and the control condition when negating the gradient polarity of VS-A (5.9c). Also shown is the ΔM subtraction for the frequency sweep negation (5.9d) and gradient polarity negation (5.9e). Note that the colour scale for subfigures 5.9d and 5.9e is on the order of $10^{-2}M_0$. This indicates that static tissue contamination from eddy currents would be reduced when using the BIR-8 in VS-TILT versus the BIR-4 preparation, and will be almost eliminated when negating the gradients (5.9e).

5.2.2 Implementation of VS-TILT

Following the simulations in section 5.2.1 the BIR-4 and BIR-8 VS-TILT preparations with gradient negation of VS-A were implemented in Siemens IDEA. Experiments were performed to determine the eddy current and diffusion errors by varying the V_{cut} and the labeling gradient axis in a static phantom. The tagging efficiency of BIR-8 VS-TILT was measured by varying the velocity of spins in a flow phantom using a single V_{cut} which was then compared to the BIR-8 VSASL preparation.

5.2.2.1 Methods

Static Phantom

All experiments were performed on a 3 tesla Verio scanner (Siemens Healthcare, Erlangen, Germany) using a spin echo EPI readout. Four preparations, BIR-4 and BIR-8 for both VSASL and VS-TILT labeling schemes, were evaluated for diffusion and eddy current effects. The subtraction errors were measured in a doped water phantom with ADC = 2.7 $\times 10^{-3}$ mm^2/s, T_1 = 100 ms and T_2 = 70 ms. To minimise any potential motion artefact the phantom was packed into the 32 channel receive coil using MR safe sandbags. For each preparation V_{cut} = 1, 2, 4, 8 and 16 cm/s was used, and the experiments were repeated for each logical tagging gradient axis ($\hat{x}, \hat{y}$ and $\hat{z}$). A TR of 4 s allowed full relaxation of the spins prior to the application of the velocity selective pulse. Two dummy TRs were used followed by 4 tag/control pairs for each of the four preparations, five V_{cut} values and three labeling gradient directions.

The preparations used a maximum gradient strength of 20 mT/m, with the RF applied at the system maximum (nominal 24 μT). The preparations were applied TI = 10 ms prior to acquisition of a single 5 mm axial slice. The readout incorporated crushers with VENC = V_{cut}, TE = 28 ms with 7/8$^{\text{th}}$ partial Fourier acquisition.

The magnitude of the ΔM subtraction is then reported in a manually defined mask generated by thresholding an M_0 acquisition.

Flow Phantom

To evaluate the tagging efficiency the BIR-8 pulse was used in VS-TILT and VSASL labeling schemes and the response of spins in a flowing tube was measured. A peristaltic pump was set up in the control room to pump tap water through a 4 mm diameter tube which was fed through a waveguide in the RF screen. The tube was fed through the scanner bore, and looped around so that positive and negative velocities could be measured simultaneously. The two legs of the tube were taped to a board positioned so that the flow was along the $\hat{z}$ direction.

A 10 mm coronal slice was prescribed with the readout in the $\hat{z}$ direction. To avoid phase correction errors and minimise flow artefact a flyback spin echo EPI readout without crushers was used (Pat et al., 1997). The resolution in the phase encode direction was 6 mm to ensure that the voxel contained a laminar distribution of velocities. The two velocity selective preparations used $V_{\text{cut}} = 2$ cm/s, maximum gradient strength of 20 mT/m and were applied TI = 10 ms proir to the readout. A TR of 10 s was used along with a non-selective pre-saturation pulse to remove any spin history effects. Two dummy TRs were used followed by 4 tag/control pairs which were averaged.

The velocity of the spins in the tube was varied by adjusting a power index (v_i) on the pump from 0 to 10 in steps of 1 unit. The volume flow rate has previously been calibrated that relates the power index to V_{max} in cm/s by

$$V_{\text{max}} = (2.48 \pm 0.04) \times v_i \tag{5.14}$$

assuming laminar flow (calibration data courtesy of Dr. Thomas Okell, FMRIB).

However, the peristaltic pump has three rotating contact points with the tube and at power indices less than 5 some retrograde flow was observed due to inadequate contact. The data were therefore analysed without converting the flow to cm/s. For each power index the saturation efficiency, $\alpha(v_i)$, was calculated voxelwise as

$$\alpha(v_i) = \frac{\overline{m^{\text{ctrl}}}(v_i) - \overline{m^{\text{tag}}}(v_i)}{M_0(v_i)} \tag{5.15}$$

where $\overline{m^{\text{ctrl}}}(v_i)$ is the average control magnetisation, $\overline{m^{\text{tag}}}(v_i)$ is the average tag magnetisation and $M_0(v_i)$ is an acquisition at power index v_i without a velocity selective preparation applied. This was then averaged for each tube to get a measurement at $+v_i$ and $-v_i$. The mask was defined by a manual threshold at 10% signal of an M_0 acquisition.

5.2.2.2 Results

Static Phantom

In the static phantom the VSASL BIR-4 produced the highest root mean squared subtraction error (RMSE) on all three axes (fig. 5.10a). The error increased as V_{cut} was reduced due to the increase in both the diffusion b-value and eddy current effects. As shown in the previous chapter, the VSASL BIR-8 reduced the spatially dependent eddy current errors, but there is still residual signal due to diffusion (fig. 5.10b). The RMSE values are reduced when using VS-TILT BIR-4 (fig. 5.10c), but there is some negative signal when using X or Y labeling.

This residual signal is almost eliminated when using VS-TILT BIR-8 (fig. 5.10d). However there are still some subtraction errors on the edges of the phantom at $V_{\text{cut}} =$ 1 cm/s. On all three labeling axes and for all V_{cut} the VS-TILT BIR-8 has the lowest RMSE value.

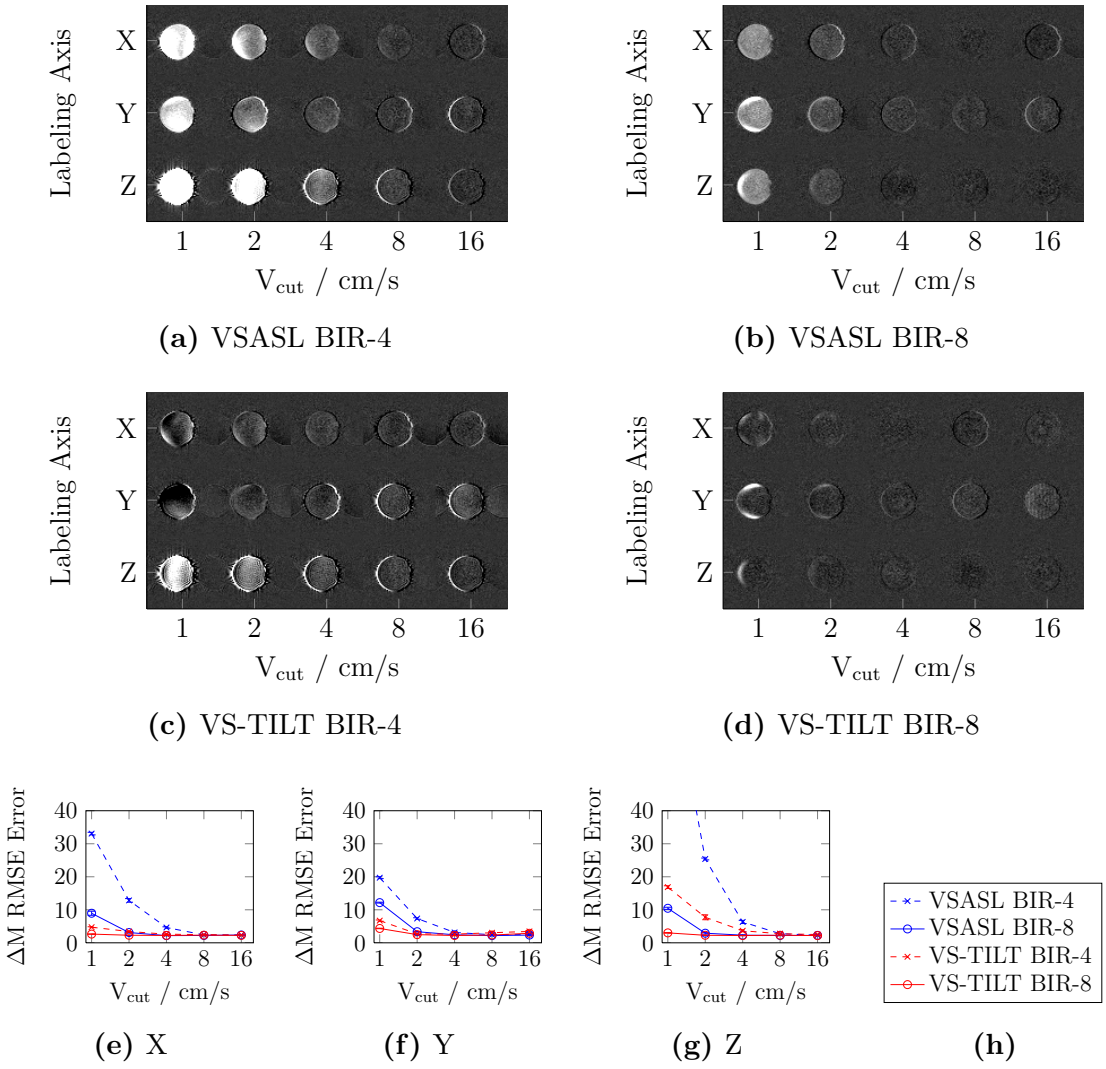
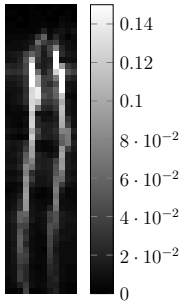
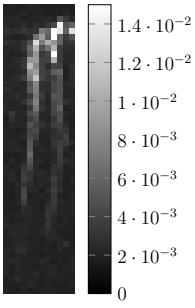


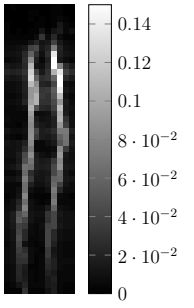
Figure 5.10: ΔM subtraction errors in a static phantom. All images are on the same colour scale. The RMSE values show that the BIR-8 VS-TILT has the lowest residual error for all three labeling axes and cut-off velocities.



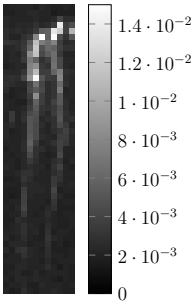
(a) VSASL Ctrl



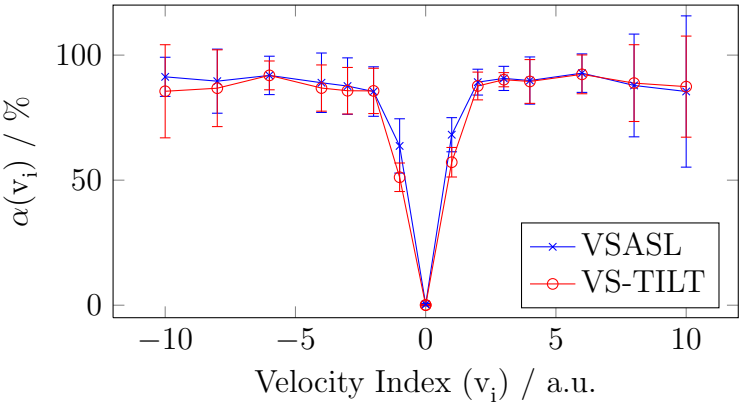
(b) VSASL Tag



(c) VS-TILT Ctrl



(d) VS-TILT Tag



(e) Saturation Efficiency

Figure 5.11: Saturation efficiency in flowing tap water using BIR-8 as the velocity selective pulse for both the VSASL and VS-TILT labeling schemes. Note that the tag acquisitions are on a reduced colour scale compared to the control acquisitions.

Flow Phantom

The BIR-8 VSASL and BIR-8 VS-TILT both produced saturations in flowing tap water. The efficiency of both preparations was comparable (fig. 5.11e). For $|v_i| > 2$ the average efficiency was $\alpha = 89.2 \pm 2.3$ % for VSASL and $\alpha = 88.2 \pm 2.4$ % for VS-TILT.

5.2.2.3 Discussion

These phantom experiments have shown that VS-TILT eliminates the diffusion error in a static phantom. Although the eddy currents are reduced when using VS-TILT compared to VSASL, the errors when using the BIR-4 pulse are larger than when using

the BIR-8. However, the negative ΔM residual signal when using the BIR-4 was not predicted by the simulations. Potential reasons for this are an overcompensated eddy current term, or table vibration (Gallichan et al., 2009). Nevertheless, due to the reduced error in the static phantom for all V_{cut} the BIR-8 was used in the remainder of this work.

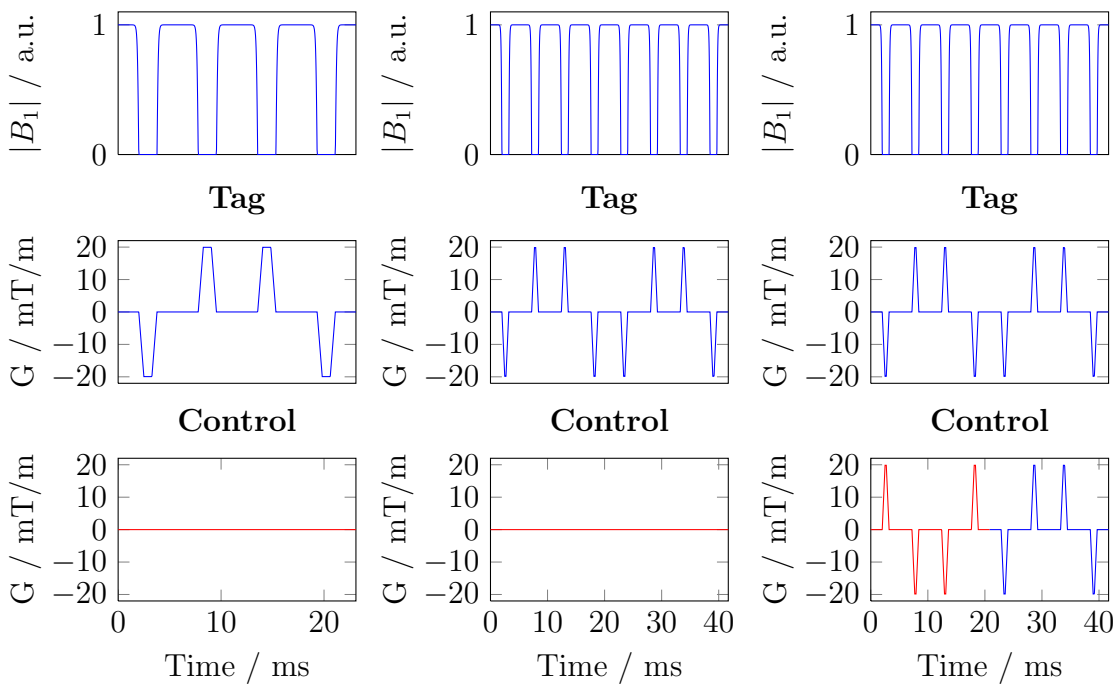
The BIR-8 VSASL and BIR-8 VS-TILT were then tested in a flow phantom and found to produce silimar saturation efficiencies. Due to the observed unstable flow at low velocity indices, and the lack of a phase contrast velocity measurement, the precise V_{cut} was not determined. To test this in the future a rotating phantom may be more accurate (Guo and Wong, 2011a). However, the absolute velocity of the spins in the flow phantom is not important. The key finding is that the BIR-8 VSASL and BIR-8 VS-TILT produce comparable labeling and control of flowing spins at a nominal $V_{\text{cut}} = 2$ cm/s. The efficiency of the pulses (≈89%) in tap water might not be the same *in vivo*, due to the shorter T_1 and T_2 of arterial blood.

5.2.3 Diffusion Effects in VSASL

To investigate the diffusion effects in VSASL the BIR-8 VS-TILT preparation was compared to BIR-8 VSASL *in vivo*. It has been shown that the perfusion overestimation measured by VSASL increases as V_{cut} is reduced from 2 cm/s to 1 cm/s (Guo and Wong, 2012a). Our hypothesis is that this is caused by diffusion effects as the b-value difference of the VSASL preparation increases as V_{cut} is reduced. Three preparations were therefore implemented to determine at which V_{cut} diffusion effects become significant.

5.2.3.1 Methods

The three velocity selective preparations used in this experiment are plotted in figure 5.12, all of which use BIR-8 as the basic velocity selective pulse. The VSASL (fig.



(a) VSASL **(b)** VSASL-II **(c)** VS-TILT

Figure 5.12: The velocity selective preparations used in the *in vivo* data for $V_{\text{cut}} = 2$ cm/s.

5.12a) and VS-TILT (fig. 5.12c) preparations have previously been described. As the VS-TILT preparation is almost double the duration of the VSASL preparation this could result in decreased labeling efficiency. To match the labeling efficiency exactly a third preparation is used, named VSASL-II. The VSASL-II preparation uses the VS-TILT tag preparation, but for the control acquisition the velocity encoding gradients are turned off (fig. 5.12b). The VSASL-II and VS-TILT will therefore have the same labeling efficiency, and the VSASL-II and VSASL will have similar b-value differences between the tag and control acquisitions.

Four healthy volunteers (two female, aged 23 to 33) were scanned having provided written consent under an institutionally agreed technical development protocol. For each of the three preparations values of $V_{\text{cut}} = 1$, 2, 4, 8, 16 and 32 cm/s were acquired. The maximum gradient strength used was 20 mT/m and the ramp time was fixed at 0.5 ms. The diffusion b-values for each tag preparation are summarised

V_{cut} / cm/s	Diffusion b-value / s/mm^2		
	VSASL	VSASL-II	VS-TILT
1	5.32	3.12	3.12
2	1.56	0.872	0.872
4	0.436	0.228	0.228
8	0.114	0.0569	0.0569
16	0.0285	0.0142	0.0142
32	0.00712	0.00356	0.00356

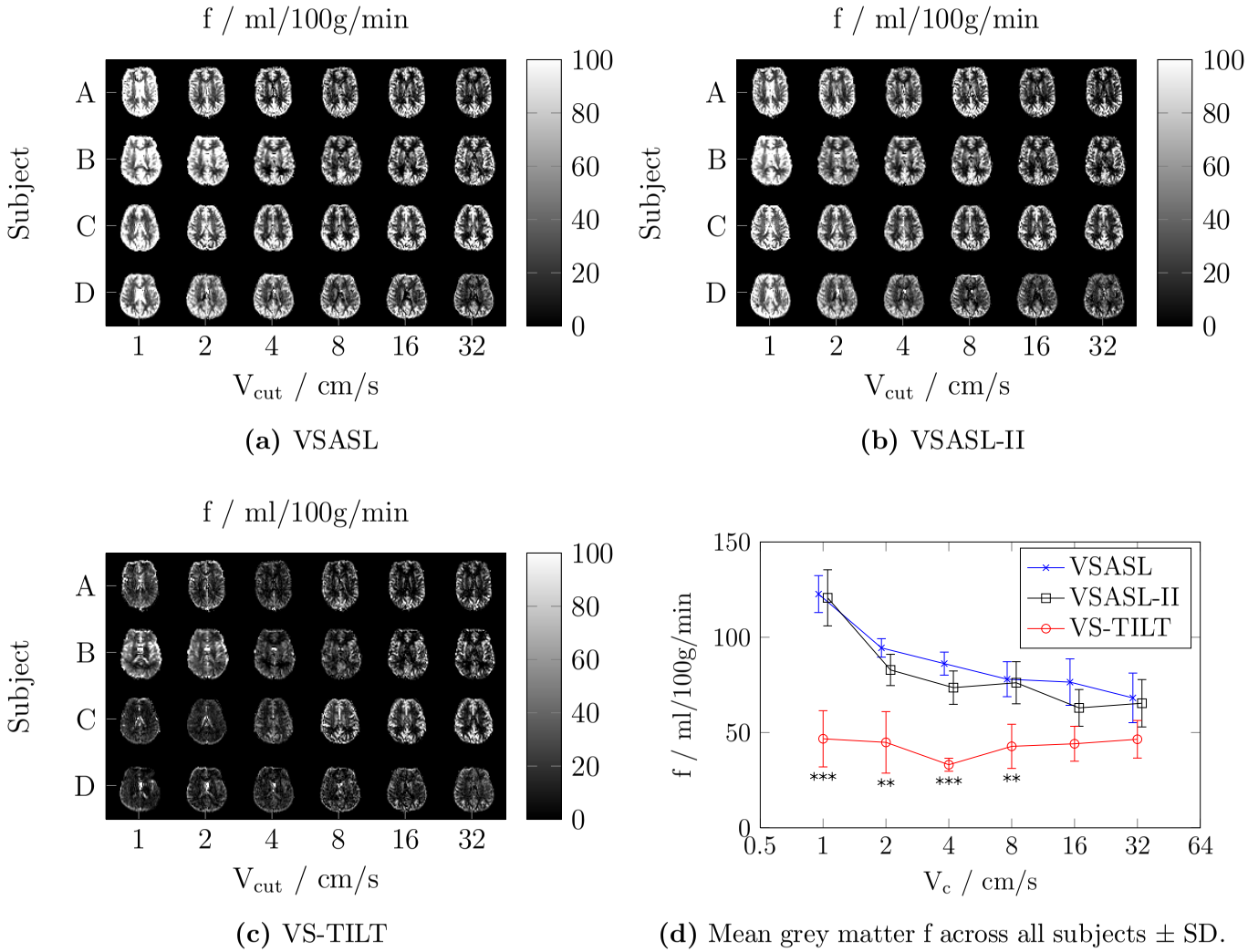
Table 5.2: Diffusion b-values for VSASL, VSASL II and VS-TILT.

in table 5.2. The scan parameters were optimised in a preliminary pilot study, with the slice thickness increased to 10 mm to increase SNR. A spin echo EPI readout was used with 16 tag control pairs for each preparation and V_{cut} combination. Other parameters were TI = 1 s, TR = 4 s, TE = 36 ms and 7 slices which resulted in a T_{sat} = 2.4 s. A DIR sequence was acquired and thresholded for use as grey matter mask. An M_0 acquisition without crushing gradients was segmented to obtain the CSF reference value.

Data were corrected for motion by registering to the M_0 image. Perfusion was then quantified voxelwise using the standard model (eq. 5.6). The same labeling efficiency was assumed for each pulse, with $\alpha = 0.89$. A grey matter mask was created by applying a manual threshold to the DIR acquisition. Mean grey matter perfusion values were calculated for each subject and preparation/V_{cut} combination by averaging over the grey matter mask. The grey matter perfusion values were then averaged over all subjects. Differences between the mean group perfusion for each preparation/V_{cut} combination were then evaluated using one-way ANOVA.

5.2.3.2 Results

The quantified perfusion maps for a single slice containing the ventricles are displayed for VSASL (fig. 5.13a), VSASL-II (fig. 5.13b) and VS-TILT (fig. 5.13c) for all subjects. It is observed that as V_{cut} is reduced there is increased signal in the ventricles



(a) VSASL

(b) VSASL-II

(c) VS-TILT

(d) Mean grey matter f across all subjects ± SD.

Figure 5.13: Perfusion maps in a slice containing the ventricles for all subjects for VSASL (5.13a), VSASL-II (5.13b) and VS-TILT (5.13c) and mean f (5.13d). 128 seconds acquisition time per image. Significant difference in apparent grey matter perfusion between VS-TILT and both VSASL and VSASLII (One way ANOVA, ** $P < 0.01$, *** $P < 0.001$).

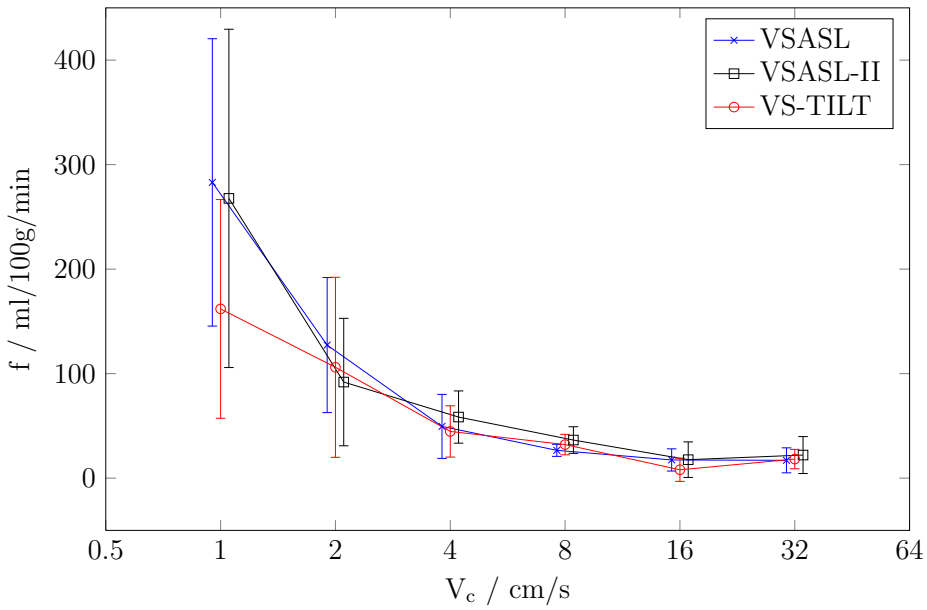


Figure 5.14: f measured in the CSF masks for VSASL, VSASL-II and VS-TILT.

for VSASL and VSASL-II. However, the grey-white matter contrast reduces when using VS-TILT.

The group mean perfusion for each preparation and V_{cut} is plotted in figure 5.13d. There are no significant differences between VSASL and VSASL-II at any V_{cut}. There are significant differences between VS-TILT and both VSASL and VSASL-II for V_{cut} = 1 ($P < 0.001$), 2 ($P < 0.01$), 4 ($P < 0.001$) and 8 ($P < 0.01$) cm/s. At 2 cm/s, the mean perfusion measured by VSASL-II was 82.9 ± 8.2 ml/100g/min and VS-TILT was 44.9 ± 16.1 ml/100g/min.

The mean f within the CSF masks is plotted in fig. 5.14. The difference in the measured f within these masks is not significant ($P>0.05$, one way ANOVA) for any cutoff velocity, however, the signal is lower when using VS-TILT at 1 cm/s due to the elimination of diffusion effects, but CSF flow still contributes a large positive signal.

5.2.3.3 Discussion

The reduction in perfusion at the previously recommended V_{cut} = 2 cm/s from 82.9 ± 8.2 ml/100g/min to 44.9 ± 16.1 ml/100g/min was not predicted by the simulations

using physiological values for tissue ADC and relaxation time. Some potential reasons for this loss of signal include a reduction in labeling efficiency of VS-TILT, a reduction in the acceleration effects in VS-TILT, or that intravoxel incoherent motion could contribute significant signal to VSASL at $V_{\text{cut}} = 2$ cm/s.

The labeling efficiency of VS-TILT is reduced compared to VSASL and was not corrected for in the quantification of the data. However, the labeling efficiency was exactly matched to the VS-TILT preparation by using the VSASL-II preparation. Although there was no significant difference between VSASL and VSASL-II perfusion measures, the values of apparant perfusion were consistently lower when using VSASL-II, suggesting there is a small difference in labeling efficiency. Although the VSASL-II and VS-TILT preparations are over 40 ms long the decay during the adiabatic pulse is not purely T_2, so the signal is preserved by T_1 decay. One problem with doubling the number of segments is that SAR is increased, although at TR = 4 s the acquisition was not SAR limited.

Although the VS-TILT preparation is designed to be insensitive to diffusion, there is still some residual signal in the ventricles, that increases as V_{cut} is reduced. The hypothesis here is that this is due to the flow of CSF.

It has recently been shown that the acceleration moment can contribute a significant signal in the brain (Schmid et al., 2013). In the control acquisition for VSASL and VSASL-II the gradients are turned off, so the acceleration moment, m_2, is zero. For VS-TILT there will be a finite m_2 in the control. As with the first gradient moment, the variation in phase caused by m_2 will be tipped up to M_z at the end of the velocity selective pulse. The difference in m_2 would therefore contribute positive signal in the ΔM subtraction. The values for m_1 and m_2 are summarised in table 5.3. The calculated values suggest that the m_2 difference in VSASL-II is almost twice that of VSASL. However, the signal in VSASL-II is consistently lower than VSASL. For VS-TILT, the magnitude subtraction of the m_2, taken as m_2 is projected on to

the $\hat{z}$ axis, suggests that the acceleration contribution will be similar between VSASL and VS-TILT. In addition to this, m_2 is two orders of magnitude lower than m_1 so is an unlikely source of the difference between VS-TILT and VSASL-II. It would be possible to extend the TILT labeling scheme to study acceleration, by using acceleration selective pulses ($m_0 = m_1 = 0$) at VS-A and VS-B, albeit with a further increase in preparation duration and SAR.

The difference between VS-TILT and VSASL-II is potentially explained by the increased ADC measured at b-values < 200 s/mm^2 in Intravoxel Incoherent Motion (IVIM) experiments (Le Bihan et al., 1986). In IVIM it is hypothesised that incoherent flow produces a distribution of phase within a voxel that result in a reduction of magnitude of the signal. This is the same process as diffusion, but on a larger scale. Consequently, two apparent diffusion coefficients are fitted with a bi-exponential model, one that corresponds to fast diffusion (ADC*), another to slow diffusion (ADC). These are attributed to 'perfusion' and 'tissue' respectively. However, the fact that the data are well described by a bi-exponential model does not mean that there are two compartments in the data. For free water at 37° C the ADC is 3 $\times 10^{-3}$ mm^2/s, whereas the measured ADC* in the brain is on the order of 7 $\times 10^{-3}$ mm^2/s (Federau et al., 2012). To investigate this an IVIM experiment was performed to determine the ADC of tissue in the grey matter mask used in VSASL.

5.2.4 Measurement of ADC

The increased ADC when using b-values < 200 s/mm^2 has been previously observed. However, in the human brain IVIM techniques have not been validated as a measure of perfusion, and it has been argued that IVIM cannot provide a measure of classical perfusion as it is sensitive to all incoherent flow in the voxel (Henkelman, 1990). In liver tumours IVIM has been shown to correlate with histological staining for necrosis, not viable tissue (Chiaradia et al., 2013). In animal models the fast component

V_{cut} / cm/s	m_1^{tag} / $\mathrm{s^2T/m}$	VSASL		VSASL-II		VS-TILT		
		m_2^{tag} / $\mathrm{s^3T/m}$	m_2^{ctrl} / $\mathrm{s^3T/m}$	m_2^{tag} / $\mathrm{s^3T/m}$	m_2^{ctrl} / $\mathrm{s^3T/m}$	m_2^{tag} / $\mathrm{s^3T/m}$	m_2^{ctrl} / $\mathrm{s^3T/m}$	$\lvert m_2^{\mathrm{ctrl}}\rvert - \lvert m_2^{\mathrm{tag}}\rvert$ / $\mathrm{s^3T/m}$
1	1.17×10^{-6}	3.15×10^{-8}	0	5.43×10^{-8}	0	5.43×10^{-8}	-2.71×10^{-8}	2.72×10^{-8}
2	5.87×10^{-7}	1.36×10^{-8}	0	2.45×10^{-8}	0	2.45×10^{-8}	-1.22×10^{-8}	1.23×10^{-8}
4	2.94×10^{-7}	6.12×10^{-9}	0	1.17×10^{-8}	0	1.17×10^{-8}	-5.87×10^{-9}	5.83×10^{-9}
8	1.47×10^{-7}	2.94×10^{-9}	0	5.87×10^{-9}	0	5.87×10^{-9}	-2.94×10^{-9}	2.93×10^{-9}
16	7.34×10^{-8}	1.47×10^{-9}	0	2.94×10^{-9}	0	2.94×10^{-9}	-1.47×10^{-9}	1.47×10^{-9}
32	3.67×10^{-8}	7.34×10^{-10}	0	1.47×10^{-9}	0	1.47×10^{-9}	-7.34×10^{-10}	7.36×10^{-10}

Table 5.3: Table of acceleration moments for VSASL, VSASL-II and VS-TILT.

correlated with interstitial fluid pressure (Kim et al., 2012). It has also been shown that the IVIM fast component is reduced when using a FLAIR pulse, suggesting that the origin in the healthy brain is from CSF (Kwong et al., 1991). In VSASL, the aim is to report on classical perfusion, or the rate of delivery of blood from the arterial system to the capillary bed. If the VSASL signal is contaminated from IVIM effects, which do not report only on classical perfusion, then the true perfusion will be overestimated.

In this experiment a multiple b-value experiment was performed to measure the ADC of the tissue used in the grey matter masks in VSASL experiments. To determine if the fast compartment of IVIM reported on the motion of blood the experiment was repeated with a FLAIR preparation to exclude the CSF compartment (Hajnal et al., 2001), and a VASO preparation to exclude the (arterial) blood compartment (Lu et al., 2003).

5.2.4.1 Methods

The experiment was performed in one healthy volunteer (33 M) who had taken part in the previous VS-TILT study. Written consent was provided under an institutionally agreed technical development protocol. A single axial 10 mm slice was prescribed through the ventricles. Monopolar Stejkal-Tanner diffusion encoding gradients were applied in the $\hat{z}$ direction with b-values 0 s/mm^2 to 100 s/mm^2 in steps of 10 s/mm^2; 100 s/mm^2 to 200 s/mm^2 in steps of 20 s/mm^2; 200 s/mm^2 to 500 s/mm^2 in steps of 50 s/mm^2; and 500 s/mm^2 to 1000 s/mm^2 in steps of 100 s/mm^2. The acquisition was a spin echo EPI with 96 x 96 matrix, 230 mm FOV, partial fourier 6/8$^{\text{th}}$, TE 80 ms to account for the time needed to achieve high b-values, TR 4 s. Four averages of each b-value were made. Following the readout was a non-selective saturation pulse to remove spin history effects.

The experiment was repeated with a VASO preparation, where a non-selective

BASSI inversion was applied 1009.4 ms prior to the readout to null arterial blood species with $T_1 = 1.664$ s at the time of acquisition. For the FLAIR preparation the non-selective BASSI inversion was applied 1483.9 ms prior to the excitation, to null CSF species with $T_1 = 3.7$ s. A DIR acquisition was also acquired for a grey matter mask.

The data were registered using 2D FLIRT (FSL, University of Oxford). The grey matter mask was generated by applying a manual threshold to the DIR image, as in the VS-TILT experiment. For each b-value the data were averaged within the mask across all repetitions. For each preparation (IVIM, VASO-IVIM and FLAIR-IVIM) the data were first quantified to a mono-exponential model

$$S = S_0 \exp(-b \cdot \mathrm{ADC}) \tag{5.16}$$

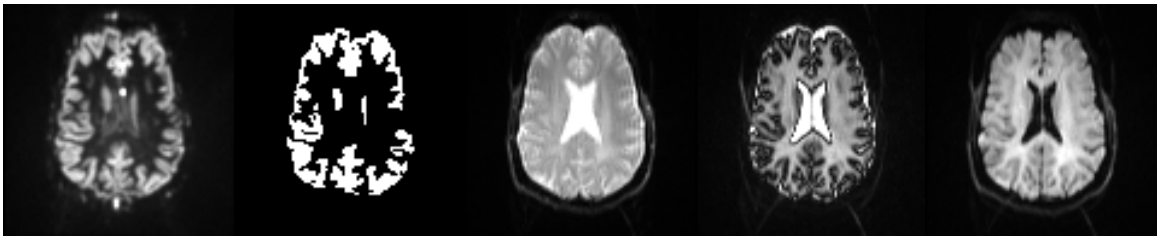
which was then used as a starting guess for a non-linear least squares fit to a bi-exponential model using the MATLAB trust region reflective algorithm, bound to restrict f^* to between 0 and 1

$$S = S_0 \cdot ([1 - f^*] \cdot \exp[-b \cdot \mathrm{ADC}_{BI}] + f^* \cdot \exp[-b \cdot \mathrm{ADC}^*]) \tag{5.17}$$

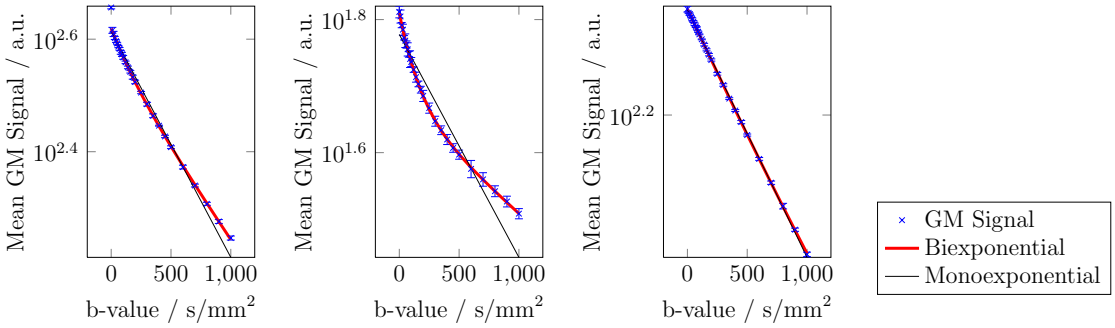
where f^* is the fast component fraction, ADC* is the fast diffusion coefficient and ADC_{BI} is the slow diffusion coefficient. To determine if the bi-exponential model is overfitting by introducing two new degrees of freedom a Bayesian Information Criterion (BIC) was used, given by

$$\mathrm{BIC} = n \cdot \ln\left[\frac{1}{n}\sum_{i=1}^{n}(x_i - \hat{x}_i)^2\right] + k \cdot \ln(n) \tag{5.18}$$

where n is the number of data points, x_i are the data, $\hat{x}_i$ are the model's estimate of the data and k is the number of degrees of freedom in the model. The model with



(a) DIR **(b)** GM Mask **(c)** IVIM **(d)** VASO-IVIM **(e)** FLAIR-IVIM



(f) IVIM **(g)** VASO-IVIM **(h)** FLAIR-IVIM **(i)**

Figure 5.15: VIM, VASO-IVIM and FLAIR-IVIM in vivo. Data are mean ± SD.

the lowest BIC is then selected, so the bi-exponential model is only chosen if the data support the extra degrees of freedom.

5.2.4.2 Results

The acquired b = 0 images are displayed in figure 5.15. The mask in figure 5.15b is generated by manually setting the threshold of the DIR image (fig. 5.15a), which has been normalised for receive coil sensitivity. The data averaged over the mask for IVIM, VASO-IVIM and FLAIR-IVIM (fig. 5.15c-e) are displayed in figures 5.15f-h respectively. For IVIM and VASO-IVIM the BIC was lower for the bi-exponential model than the mono-exponential model. However, for FLAIR-IVIM the BIC was lower for the mono-exponential fit.

The values of apparent diffusion coefficients are reported in table 5.4. For the fast diffusion coefficient, ADC*, a value of (4.6 ± 10.9) $\times 10^{-3}$ mm^2/s was measured with IVIM and a value of (6.4 ± 11.8) $\times 10^{-3}$ mm^2/s was measured with VASO-IVIM. The

fractional signal size of the fast compartment, f^*, was 0.13 ± 0.01 and 0.27 ± 0.01 respectively.

5.2.4.3 Discussion

The voxelwise fits to the IVIM data were not significant, so a common approach is to average over the whole brain (Federau et al., 2012). The mask used in this experiment is the same as the one used in the VSASL data when taking an average over the perfusion values calculated voxelwise. The data show that a fast ADC is observed in the case of the IVIM experiment for low b-values, which is on the order of (4.6 ± 10.9) $\times 10^{-3}$ mm^2/s. The elevated ADC also was observed when T_1 species of 1.664 ms (arterial blood) were nulled using a VASO pulse. However, the BIC indicated that that the data for FLAIR-IVIM was best described by a mono-exponential fit, so the fast component is not measurable when nulling T_1 species of 3700 ms. Note that the data point at b = 0 for IVIM is an outlier for both models (fig. 5.15f).

It is possible that the CSF or blood spins are not completely nulled by the BASSI pulse due to inefficiencies in the inversion, differences from the assumed T_1 or the delivered blood being outside the RF field of view when the magnetisation reset pulse is applied. In the VASO-IVIM data there may still be some capillary and venous blood present, as the T_1 is reduced as Oxygen is extracted (Lu et al., 2004). The size of each signal compartment in this experiment will not be the same as in VSASL, as a longer T_2 needs to be used in order to play out the diffusion encoding gradients in IVIM.

Nevertheless, these data show that for low b-values the ADC is elevated compared to literature values of tissue diffusion. The hyper-ADC is observed even with a blood null pulse, but is absent when a FLAIR pulse is used. This suggests that the origin of the hyper-ADC is spins with long T_1, such as CSF. The elevated ADC is too large to be Brownian motion diffusion, but could be due to CSF flows in the subarachnoid

Sequence	Mono	Bi-exponential			$BIC_{BI} < BIC_M$?
	ADC / $\times 10^{-3}$ mm^2/s	ADC_{BI} / $\times 10^{-3}$ mm^2/s	ADC* / $\times 10^{-3}$ mm^2/s	f^* / f_0	
IVIM	0.92 ± 0.01	0.72 ± 0.01	4.6 ± 10.9	0.13 ± 0.01	Yes
VASO-IVIM	0.77 ± 0.02	0.38 ± 0.02	6.4 ± 11.8	0.27 ± 0.01	Yes
FLAIR-IVIM	0.68 ± 0.01	(0.27 ± 0.82)	(0.87 ± 821.01)	(0.74 ± 0.01)	**No**

Table 5.4: IVIM, VASO-IVIM and FLAIR-IVIM in vivo results. Values in brackets are not used as the BIC does not support the bi-exponential model over the monoexponential

spaces (Henry-Feugeas et al., 1993).

5.2.5 Discussion: Diffusion in VSASL

In this chapter it has been shown that diffusion effects contribute significant positive signal to the ΔM subtraction for $V_{\text{cut}} < 8$ cm/s. This was not predicted using literature values of tissue properties. However, at low b-values the ADC is increased, even when the arterial blood signal is nulled. The likely source for this signal is from long T_1 species such as CSF. If a voxel of pure CSF had an ADC of 4.6 $\times 10^{-3}$ mm^2/s, the error for TI = 1 s is +54.5 ml/100g/min for BIR-8 VSASL at V_{cut}, and for an ADC of 6.4 $\times 10^{-3}$ mm^2/s the overestimation would be 74.5 ml/100g/min. However, even with a partial volume of 20%, this would not completely explain the measured difference of 38 $\pm$ 18 ml/100g/min between VSASL-II and VS-TILT. It is possible that the ADC is even higher, as the first point in the IVIM is an outlier in the data. If only the b = 0 s/mm^2 and b = 10 s/mm^2 are taken into account the monoexponential ADC is 53.8 $\times 10^{-3}$ mm^2/s, which would describe the VS-TILT data.

Even using the conservative ADC*, there would still be significant contribution from the 'fast' spins in the VSASL measurement, which could be CSF. IVIM ADC* has been shown to report on tumour necrosis and interstitial fluid pressure, so it would be ideal to avoid these effects when interpreting data in the clinic. Although VS-TILT will have lower SNR than VSASL, the measurement will not be systematically biased from effects that are not related to classical perfusion.

This work raises the question of what value of V_{cut} to use. There is still no adequate method of calibrating VSASL for this. As the effects of diffusion, motion and eddy currents are all increased as V_{cut} is reduced, there seems to be no benefit to reducing V_{cut} below 8 cm/s in the healthy brain. The choice of $V_{\text{cut}} = 2$ cm/s has previously been argued by there being less evidence of "large vessel trees" and "grey matter is better depicted [at lower V_{cut} than higher V_{cut}]" (Wu and Wong, 2006). However,

the reduction in artefacts may also be explained as being due to the fact that when the V_{cut} is reduced, the b-value difference is increased. This may introduce signal subtraction errors from the CSF in the voxel, acting as a blurring of the image and making the images appear less focal.

5.3 What Is the Bolus Shape in VSASL?

It has previously been assumed that the VSASL bolus is generated in a laminar flowing artery that is aligned with the gradient axis. In the next section some of these assumptions are relaxed in order to determine the bolus shape in the presence of plug flow and under conditions of different distributions of arteries.

In VSASL it is assumed that the blood in the arteries is anisotropic coherent, in that the artery is aligned with the gradient axis and has a laminar distribution of velocities. It has been hypothesised that the VSASL tag cannot generate signal at the level of the capillaries due to the lack of laminar flow (Schmid et al., 2013). However, the shape of the labeled bolus will depend not only on the velocity profile within the vessel, but also the distribution of the vessels. In this derivation isotropic distributions of vessels are considered, where the orientations are uniformly distributed within the voxel (He and Yablonskiy, 2007).

5.3.1 Theory

The magnetisation profile after the application of a velocity selective pulse can be calculated from integrating over the distribution of vessels and their velocity profiles. The longitudinal magnetisation after a velocity selective pulse is given by

$$M_z(v) = M_0\alpha \cdot \cos\left[\gamma m_1 \cdot v \cdot \cos(\theta)\right] \tag{5.19}$$

where M_0 is the magnetisation prior to the velocity selective pulse, v is the velocity

of the spins and θ is the angle between the velocity and the direction of the applied gradient pulse. In VSASL the first moment of the gradients is chosen to be

$$m_1 = \frac{\pi}{\gamma V_{\text{cut}}} \tag{5.20}$$

which results in the longitudinal magnetisation after the application of a velocity selective pulse as

$$M_z(v) = M_0\alpha \cdot \cos\left[\pi \frac{v}{V_{\text{cut}}} \cos(\theta)\right] \tag{5.21}$$

A laminar vessel has a uniform distribution of velocities between 0 and v_{MAX}. The normalised magnetisation within the vessel after the application of the pulse will therefore be given by the integral over the distribution of velocities present

$$M_z^{\text{ANISO, LAM}} = \frac{\int_0^{v_{MAX}} M_z(v)dv}{\int_0^{v_{MAX}} dv} \tag{5.22}$$

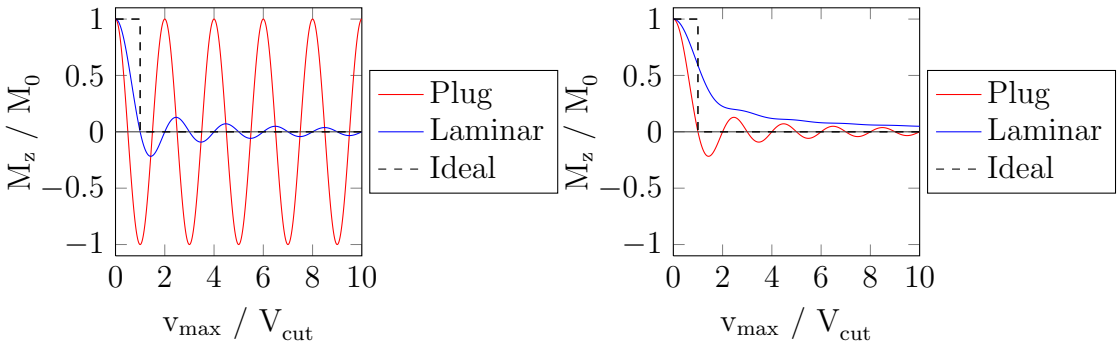
$$= \frac{\int_0^{v_{MAX}} M_0\alpha \cdot \cos\left[\pi \frac{v}{V_{\text{cut}}} \cos(\theta)\right] dv}{\int_0^{v_{MAX}} dv} \tag{5.23}$$

$$= M_0\alpha \cdot \text{sinc}\left[\pi \frac{v_{\text{MAX}}}{V_{\text{cut}}} \cos(\theta)\right] \tag{5.24}$$

This sinc function is considered a saturation for laminar vessels aligned with the gradient axis ($\theta = 0$). If the vessel does not have laminar flow, but is instead plug flow with velocity v_{MAX}, the normalised magnetisation after the application of the pulse is simply

$$M_z^{\text{ANISO, PLUG}} = M_0\alpha \cdot \cos\left[\pi \frac{v_{MAX}}{V_{\text{cut}}} \cos(\theta)\right] \tag{5.25}$$

Whilst the cosine variation in M_z will produce positive contrast in the ΔM subtraction, this cannot be considered a saturation so the tagging efficiency would be unclear. These bolus shapes for anisotropic laminar and plus vessels are plotted in figure 5.16a.



(a) Anisotropic vessel distribution **(b)** Isotropic vessel distribution

Figure 5.16: Theoretical M_z after the application of a cosinusoidal velocity selective pulse for vessels with plug and laminar velocity distributions, when considering an anisotropic (5.16a) or isotropic (5.16b) vessel distribution . The ideal function is a saturation of vessels with $v > V_{\text{cut}}$.

The Bolus Shape from an Isotropic Distribution

Consider a vessel that is not aligned with the velocity encoding axis. In this derivation spherical co-ordinates (r, θ, ϕ) with radial distance r, polar angle θ and azimuthal angle ϕ are used. For simplicity the tagging gradients are applied along the z axis. The bolus shape for an isotropic distribution of vessels is given by the integral over all the magnetisation in the individually distributed vessels

$$M_z^{\text{ISO}} = \frac{\iint M_z(\theta)\sin(\theta)d\theta d\phi}{\iint \sin(\theta)d\theta d\phi} \tag{5.26}$$

For an isotropic distribution of laminar vessels equation 5.24 can be substituted into 5.26 to yield:

$$M_z^{\text{ISO, LAM}} = \frac{\iint M_0\alpha \cdot \text{sinc}\left[\pi\frac{v_{\text{MAX}}}{V_{\text{cut}}}\cos(\theta)\right]\sin(\theta)d\theta d\phi}{\iint \sin(\theta)d\theta d\phi} \tag{5.27}$$

$$= \frac{M_0\alpha}{\pi\frac{v_{\text{MAX}}}{V_{\text{cut}}}} \cdot \text{Si}\left(\pi\frac{v_{\text{MAX}}}{V_{\text{cut}}}\right) \tag{5.28}$$

Vessel Velocity Distribution	Vessel Spatial Distribution	
	Anisotropic	Isotropic
Plug	$M_0\alpha \cdot \cos\left(\pi \frac{v_{MAX}}{V_{\text{cut}}} \cos(\theta)\right)$	$M_0\alpha \cdot \text{sinc}\left(\pi \frac{v_{MAX}}{V_{\text{cut}}}\right)$
Laminar	$M_0\alpha \cdot \text{sinc}\left(\pi \frac{v_{\text{MAX}}}{V_{\text{cut}}} \cos(\theta)\right)$	$M_0\alpha \cdot \frac{\text{Si}\left(\pi \frac{v_{\text{MAX}}}{V_{\text{cut}}}\right)}{\pi \frac{v_{\text{MAX}}}{V_{\text{cut}}}}$

Table 5.5: Bolus shape in VSASL for different distributions of vessel velocities and orientations. For the anisotripic distribution the vessel is at an angle θ to the velocity selective gradient.

where Si(x) is the sine integral defined by

$$\text{Si}(x) = \int_0^x \frac{\sin(t')}{t'} dt' \tag{5.29}$$

Due to rotational symmetry of the network this will hold for any tagging gradient direction. If an isotropic distribution of plug vessels is present the bolus shape will be given by substituting equation 5.25 into 5.26

$$M_z^{\text{ISO, PLUG}} = \frac{\iint M_0\alpha \cdot \cos\left[\pi \frac{v_{MAX}}{V_{\text{cut}}} \cos(\theta)\right] \sin(\theta) d\theta d\phi}{\iint \sin(\theta) d\theta d\phi} \tag{5.30}$$

$$= M_0\alpha \cdot \text{sinc}\left(\pi \frac{v_{\text{MAX}}}{V_{\text{cut}}}\right) \tag{5.31}$$

This result is interesting as an isotropic distribution of plug flowing vessels will produce a saturation. The bolus shape for the isotropic distribution of plug vessels is the same as a laminar vessel aligned along the labeling gradient axis.

The bolus shapes are summarised in table 5.5 and plotted in figure 5.16. This derivation shows that when the vessel network is taken into account both plug flow and laminar flow produce a bolus that can be considered a saturation.

A 'Well Mixed Vessel'?

There is an apparent paradox with two assumptions of the labeling process in VSASL. Firstly, it is assumed that labeling will occur in a vessel with a laminar distribution

of velocities (Wong et al., 2006). Secondly, after labeling the blood then mixes. The magnetisation delivered to the voxel is then proportional to $\text{sinc}\left(\frac{\pi v_{max}}{V_{\text{cut}}}\right)$, which is considered saturation for vessel velocities $v_{max} > V_{\text{cut}}$.

The second assumption is incompatible with the first as in laminar flow there is no macroscopic mixing of fluid between layers (Fox and McDonald, 1985). Instead, consider the magnetisation and volume of each velocity laminar that exit the vessel per unit time. Intuitively, a greater number of spins from the center of the vessel are going to be delivered as these have a higher velocity. The velocity of the laminar at radius r of the vessel is

$$v(r) = v_{max}\left(1 - \frac{r^2}{R^2}\right) \tag{5.32}$$

where R is the radius of the vessel. The volume flow rate from the vessel is given by

$$F = \iint v(r)dA = \int_0^R v(r)dr \int_0^{2\pi} d\phi \tag{5.33}$$

where ϕ is the azimuth angle within the vessel. The total magnetisation that exits the vessel per unit time is given by

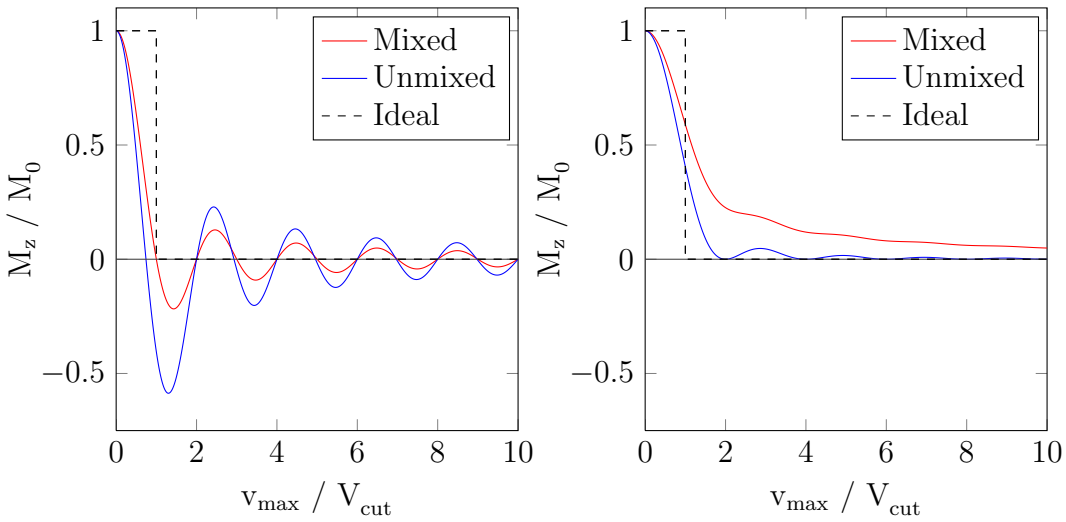
$$M_z^{\text{ANISO, UNMIXED}} = \frac{\iint M_z(r)v(r)dA}{F} = \frac{\int_0^R M_z(r)v(r)dr \int_0^{2\pi} d\phi}{\int_0^R v(r)dr \int_0^{2\pi} d\phi} \tag{5.34}$$

After the application of the velocity selective pulse the magnetisation of the laminar at r is

$$M_z(r,\theta) = \cos\left[\pi\frac{v_{max}}{V_{\text{cut}}}\cos(\theta)\left(1 - \frac{r^2}{R^2}\right)\right] \tag{5.35}$$

where θ is the angle between the vessel and the velocity selective gradient. Substituting equation 5.35 and equation 5.32 into equation 5.34 leads to the total magnetization delivered from a single laminar vessel

$$M_z^{\text{ANISO, UNMIXED}} = 2 \cdot \text{sinc}\left[\pi\frac{v_{max}}{V_{\text{cut}}}\cos(\theta)\right] - \text{sinc}^2\left[\pi\frac{v_{max}}{2V_{\text{cut}}}\cos(\theta)\right] \tag{5.36}$$



(a) Anisotropic vessel distribution **(b)** Isotropic vessel distribution

Figure 5.17: Theoretical bolus shapes for laminar flowing vessel networks. The response to a velocity selective pulse of an anisotropic distribution, or a single vessel, that is aligned with the velocity selective gradient where $\theta = 0$ (5.17a) and the response of an isotropic distribution of laminar vessels (5.17b).

This equation shows that at large v_{max}/V_{cut} the sinc term will dominate, but there will be some differences from the well-mixed case at low values of v_{max}/V_{cut}. This function, along with the mixed bolus shape (eq. 5.24) is plotted in figure 5.17a.

This can be extended to consider an isotropic distribution of vessels as in the previous section. Here the total magnetization delivered is given by

$$M_z^{\text{ISO, UNMIXED}} = \frac{\iiint M_z(r,\theta)v(r)dS}{F} = \frac{\int_0^{\pi}\int_0^{R} M_z(r,\theta)v(r)\sin(\theta)drd\theta\int_0^{2\pi}d\phi}{\int_0^{R}v(r)dr\int_0^{2\pi}d\phi\int_0^{\pi}\sin(\theta)d\theta} \tag{5.37}$$

which after a substitution and some algebra leads to

$$M_z^{\text{ISO, UNMIXED}} = \text{sinc}^2\left(\pi\frac{v_{max}}{2V_{\text{cut}}}\right) \tag{5.38}$$

This elegant solution suggests that an isotropic distribution of laminar vessels where the magnetization does not mix will result in the most efficient saturation. However, the first point at which this function is zero is when $v_{max} = 2V_{\text{cut}}$, which is

twice the assumed cutoff velocity with an anisotropic laminar vessel. This function, along with the mixed bolus shape (eq. 5.28) is plotted in figure 5.17b.

5.3.2 Discussion

It is concluded from this derivation that even if the magnetization within the vessel does not mix, the total magnetisation that leaves the vessel will result in a saturation. In the case of an anisotropic laminar vessel the saturation efficiency would be higher if the spins mix. However, in the case of an isotropic network of laminar vessels the saturation efficiency is higher if the spins do not mix. In realistic blood flows the Reynolds Number is between 1 in arterioles to 4000 at peak systole in the aorta (Ku, 1997). Therefore, some mixing and flattening of the velocity profile may occur, so the true solution will be somewhere between the two extremes derived in this section that both result in saturation when the distribution of vessels is taken into account.

Although VS-TILT will exclude vascular networks that have incoherent flows, the technique is still theoretically generating a saturation in the capillary and arterioles.

This derivation suggests that untangling the vascular distribution from the velocity distribution is difficult in VSASL. However, it is possible to apply a velocity selective pulse that results in $M_z \propto \pm\sin(v)$ by adding phase to alternate AHPs in the BIR preparations. In this case, opposed velocities in an isotropic distribution of vessels will cancel out, leaving only the contributions from anisotropic vessels along the direction of the velocity selective gradient. By eliminating the isotropic contributions the technique will have lower SNR, but it could potentially be useful to study this geometry distribution during vascular normalisation in anti-angiogenic treatment.

5.4 Conclusions

In this chapter expressions for the magnitude of the perfusion error due to tissue diffusion and bulk motion effects have been derived. A novel labeling scheme was then developed to eliminate diffusion effects, and it was shown that diffusion contributes an error of $+38 \pm 18$ ml/100g/min in the grey matter masks for the conditions used in the simulation. Expressions for the bolus shape from non-laminar, non-isotropic vascular networks were then derived, demonstrating that a saturation is still produced when considering vascular networks for both plug and laminar flow. Finally, a paradox in two assumptions about the labeling process and delivery of blood from laminar vessels was then solved, and shown to produce the most efficient saturation in an isotropic vascular network.

Chapter 6

Measurement of Oxygen Extraction Fraction

In this chapter the VS-TILT method is applied to QUIXOTIC in an attempt to non-invasively measure Oxygen Extraction Fraction (OEF) using T_2 Relaxation Under Spin Tagging (TRUST) principles. In a TRUST measurement of whole brain OEF the venous compartment is isolated through spatial tagging of the sagittal sinus (Lu and Ge, 2008). The T_2 of this signal is then measured in the sagittal sinus, and converted to venous oxygenation (Y_v) through use of a calibration curve. The venous oxygenation is then converted to OEF by

$$\text{OEF} = \frac{Y_a - Y_v}{Y_a} \tag{6.1}$$

where Y_a is the arterial oxygenation. Y_a can be obtained from a pulse oximeter or a second TRUST measurement in an artery supplying the organ of interest. The TRUST method only returns an average OEF for the whole organ as the signal is localised in a major draining vein. The aim of QUIXOTIC is to produce a map of local OEF by isolating the venous compartment on a voxelwise basis through use of a velocity selective preparation (Bolar et al., 2011).

In this chapter TRUST is implemented on the FMRIB Verio scanner to establish a baseline venous T_2, as this will depend on the RF pulse shape and timing in the preparation (Lu et al., 2012), which is then used to optimise the QUIXOTIC acquisition. The TRUST sequence was also validated using an Oxygen breathing challenge in a collaboration with Michael Germuska (FMRIB, University of Oxford), who had ethics to perform such a challenge. In this chapter the pulse sequence was implemented and the data for this chapter were analysed by myself, however the subjects were scanned by MG. In order to optimise the QUIXOTIC acquisition a kinetic model is derived. The VS-TILT method is then applied to QUIXOTIC in order to reduce diffusion and eddy current errors that may otherwise be present.

6.1 TRUST

In this section TRUST is implemented by adding an MLEV preparation to the FMRIB pCASL sequence and is shown to be able to detect a change in venous oxygenation when using a 100% O_2 breathing challenge relative to air breathing.

6.1.1 Methods

In TRUST spins are labeled in a volume superior to the acquisition slice, and then detected whilst still in a large draining vein after a short inflow time. In this experiment 5 subjects (4 men and 1 woman, mean age 34) were scanned on a 3T Verio system (Siemens Healthcare, Erlangen, Germany). In this implementation the venous spins were labeled using a 1.4 s pCASL pulse train located 4 cm superior to the imaging slice and angled to be perpendicular to the sagittal sinus. This was followed by an inflow time of 150 ms to allow the application of a T_2 preparation module. So as to exactly match the T_2 to Y_v calibration data in Lu et al. (2012) a Malcom-Levitt T_2 preparation with composite RF pulses was used with a 10 ms τ_{CP}. This resulted in

effective TEs of 0, 40, 80, and 120 ms, with four tag-control pairs acquired for each preparation time, interleaved over the duration of the experiment. As the preparation was non-selective the delay between the end of the pCASL labeling train and start of T_2 preparation was reduced so as to maintain TR and TI. Total acquisition time was 2.2 minutes. Subjects were scanned during air breathing delivered through a non-rebreathing mask (Flexicare Medical, Mountain Ash, UK) at 15 L/min and under a 3 minute block of 100% O_2 breathing delivered through the same mask.

For each subject data were motion corrected using FLIRT and complex subtracted after coil combination using adaptive combine. The most intense pixel on the effective TE = 0 ms subtraction during air breathing was then used as a mask for fitting T_2 for both the air and O_2 block.

Venous Oxygenation (Y_v) is then estimated from a calibration curve from TRUST data (Lu et al., 2012). The T_2 of the venous compartment is described by

$$\frac{1}{T_{2,V}} = A + B \cdot (1 - Y) + C \cdot (1 - Y)^2 \tag{6.2}$$

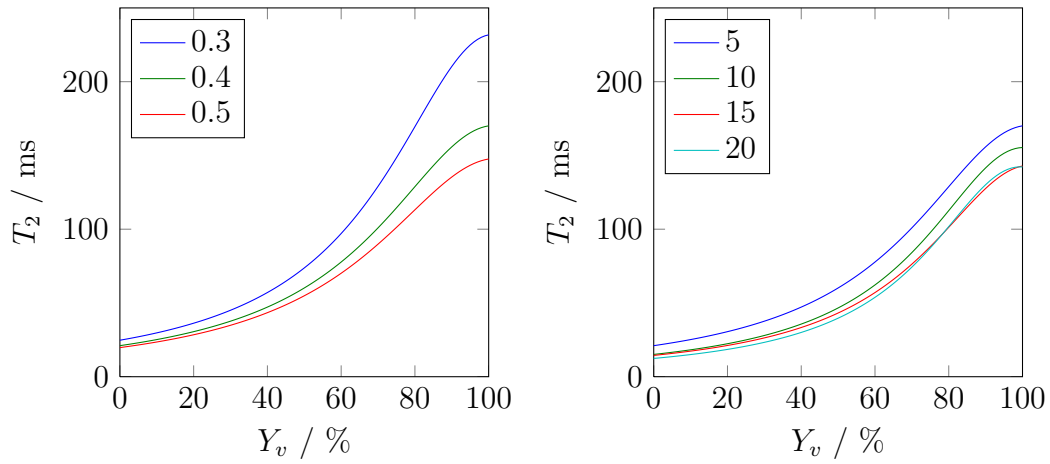
where A, B and C are experimentally determined constants that very with τ_{CP} and Hct given by

$$A = a_1 + a_2 \cdot Hct + a_3 \cdot Hct^2 \tag{6.3}$$

$$B = b_1 \cdot Hct + b_2 \cdot Hct^2 \tag{6.4}$$

$$C = c_1 \cdot Hct \cdot (1 - Hct) \tag{6.5}$$

Assumed values were a_1 = -13.5, a_2 = 80.2, a_3 = -75.9, b_1 = -0.5, b_2 = 3.4 and c_1 = 247.4, which were calibrated for 10 ms τ_{CP} as reported in Lu et al. (2012). The calibration curves for different values of hematocrit and τ_{CP} are displayed in figure 6.1.



(a) Calibration at 10 ms τ_{CP}, varying Hct

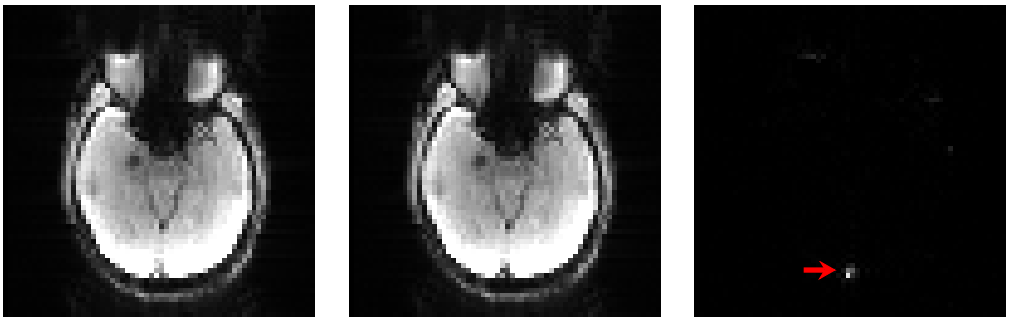
(b) Calibration at 0.4 Hct, varying τ_{CP}

Figure 6.1: The calibration curves for TRUST and QUIXOTIC data, relating blood T_2 to oxygenation, Y. Data are from the a, b and c coefficients given in Lu et al. (2012), table 1, for the composite RF pulse MLEV T_2 preparation. Figure 6.1a shows the calibration curve for τ_{CP} = 10 ms, with three values of hematocrit from 0.3 to 0.5. Figure 6.1b shows the calibration curve for hematocrit 0.4, where τ_{CP} is 5, 10, 15 and 20 ms.

Due to a lack of pulse oximeter in this work Y_v was not converted to OEF and Hct was assumed to be 0.4 for all subjects. Y_v was then averaged over all subjects.

6.1.2 Results

An example of a tag acquisition, control acquisition and subtraction is displayed in figure 6.2. The temporal SNR in the sagittal sinus averaged over all subjects was 21.3 ± 3.9. During air breathing the average T_2 over all subjects was 64.1 ± 2.6 ms, which increased to 75.2 ± 6.1 ms during Oxygen breathing. This resulted in an increase in estimated Y_v from 60.9 ± 2.8 % to 65.8 ± 5.3 % (fig. 6.3). The change in Y_v was therefore +4.9 ± 6.0 percentage points, p = 0.046 (two tailed t-test).



(a) Control **(b)** Tag **(c)** Subtraction

Figure 6.2: A representative tag (6.2a) and control acquisition (6.2b) with effective TE = 0 ms and averaged absolute subtraction over the four tag-control pairs (6.2c). The red arrow indicates the localisation of the signal from the sagittal sinus. All images are on the same colour scale.

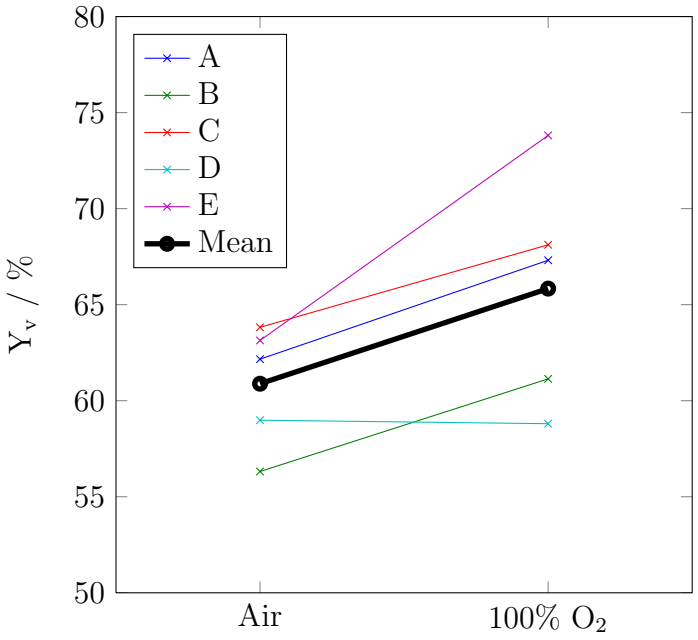


Figure 6.3: Venous oxgenation in all 5 subjects (A-E) as measured with pCASL-TRUST. The mean change in Y_v was +4.9±6.0 percentage points (p = 0.046).

6.1.3 Discussion and Conclusions

These data show that when adding the MLEV T_2 preparation to the pCASL pulse sequence an estimate of Y_v falls within the expected physiological range, and a significant change in venous oxygenation can be measured with a 100% O_2 challenge. The baseline venous T_2 was measured as 64.1 $\pm$ 2.6 ms using this implementation of the TRUST sequence.

A potential issue with this pulse sequence is that the Oxygen challenge will induce a susceptibility change in the venous blood, which will change the labeling efficiency of the pCASL pulse train. This may reduce the signal-to-noise of the data in the 100% O_2 block but this would not be a confound in measuring T_2 as multiple effective TEs are used. Indeed, it can be seen from the example acquisition images in figure 6.2 that the labeling in the sagittal sinus is approximately 50% efficient as the magnetisation is not fully inverted, possibly due to the velocity or susceptibility of the venous spins.

In a conventional TRUST experiment the venous spins are typically isolated using a PICORE tag-control scheme, with the labeling region superior to the imaging slice (Lu and Ge, 2008). In this sequence pCASL was used to label the blood within the sagittal sinus instead. This is primarily due to the pCASL sequence building block being available at the time of performing the experiments, so was used in the interests of speed of implementation. The main aim of this sequence was to determine the baseline venous T_2 for the optimisation of QUIXOTIC, and demonstrate that a change in Oxygenation could be detected using the MLEV preparation implemented. A version was later programmed using BASSI pulses in a PICORE labeling scheme, but was not tested with an O_2 challenge.

It is possible that spins in smaller veins that drain into the sagittal sinus will be labeled as they traverse the pCASL labeling plane in the foot-head direction. These spins will probably not be included in the imaging region due to the short post label delay used. However, due to the long labeling duration they could pass through the

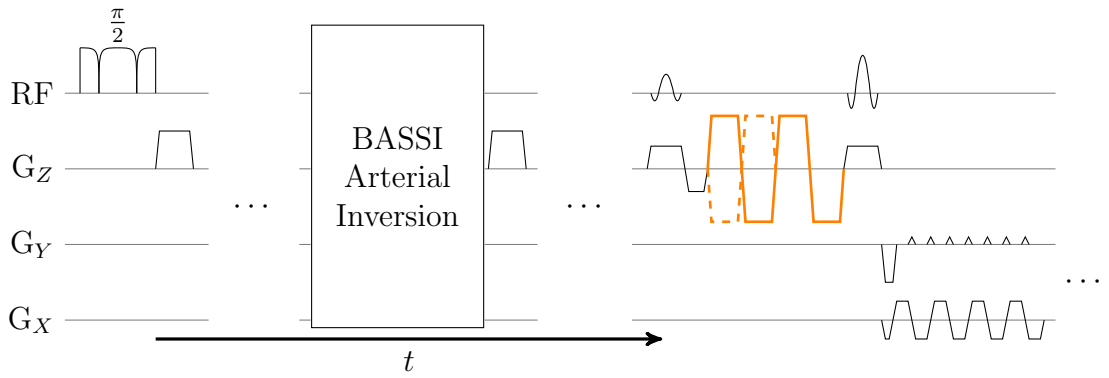


Figure 6.4: The iVASO-QUIXOTIC-TILT pulse sequence to isolate venous spins, using a spatially selective BASSI pulse to exclude arterial signal. The TILT gradients are depicted in orange with a solid line for the tag condition and a dashed line for the control condition.

labeling plane twice as they enter the sagittal sinus and traverse the pCASL labeling plane in the head-foot direction. In this case they would still be absent from the image as these spins are inverted twice in the tag condition. It is therefore hypothesised that the pCASL-TRUST signal will mostly come from the sagittal sinus, whereas a PICORE-TRUST sequence would include spins from both the sagittal sinus and veins further upstream.

6.2 QUIXOTIC

QUIXOTIC is a method that performs a voxelwise T_2 fit and converts this value to OEF using the TRUST calibration. However, this method is not currently clinically feasible as the low SNR results in a scan time of up to 20 minutes (Bolar et al., 2011). In this section a kinetic model is derived for QUIXOTIC in order to maximise SNR.

6.2.1 A Kinetic Model for QUIXOTIC

The sequence consists of first a magnetisation reset (a global saturation), then a delay, t, before a velocity selective saturation is either played out in the control or

tag condition to isolate the venous spins (fig. 6.4). Like VSASL, the signal difference is a subtraction of two scans, a control with $m_1 = 0$, and a tag with $m_1 = \frac{\pi}{\gamma V_{\mathrm{CUT}}}$. Arterial spins are excluded through the use of an inflow VASO pulse to null the arterial magnetisation at the time of slice excitation.

To incorporate the VS-TILT preparation into QUIXOTIC either the two BIR-8 pulses can be performed immediately before slice excitation, or the TILT gradients can be incorporated into the readout train itself. The TILT gradients consist of two velocity selective bipolar blips that have the same polarity in the tag condition, and the opposed polarity in the control condition. The acquisition is essentially a flow compensated diffusion sequence in the control condition and a flow spoiled diffusion sequence in the tag condition.

Here the kinetics of the venous signal are treated in a similar way to ASL (Buxton et al., 1998). The available venous magnetisation for T_2 mapping, ΔM, is given by

$$\Delta M(t, \mathrm{TE}) = \alpha \cdot c(t) \cdot m(t, \mathrm{TE}) \tag{6.6}$$

where $c(t)$ is the concentration of labeled blood in the venous pool within the voxel, and $m(t)$ is the magnetisation of the venous blood, and α is the efficiency of the VS preparation. The magnetisation of blood in the acquired image is described by a saturation recovery curve, followed by decay during the echo time

$$m(t, \mathrm{TE}) = M_{0,B} \cdot \left(1 - \exp\left[\frac{-t}{T_{1,V}}\right]\right) \cdot \exp\left(\frac{-\mathrm{TE}}{T_{2,V}}\right) \tag{6.7}$$

where $M_{0,B}$ is the equlibrium magnetisation of blood and $T_{1,V}$ is the T_1 of venous blood.

The concentration of venous blood within the voxel will linearly build up during time t as spins are delivered by perfusion. This will reach a maximum at $t = \frac{\eta_v}{f}$, where η_v is the volume of the venous pool (ml/ml) and f is the perfusion of the voxel

(ml/ml/s). The spins will flow out of the venous pool at the same rate, so that when $t > \frac{\eta_v}{f}$ the volume of venous blood within the voxel is constant. The concentration of venous blood is then given by

$$c(t) = \begin{cases} f \cdot t & 0 \leqslant t \leqslant \frac{\eta_v}{f} \\ \eta_v & t > \frac{\eta_v}{f} \end{cases} \tag{6.8}$$

The signal difference at each echo time is then given by

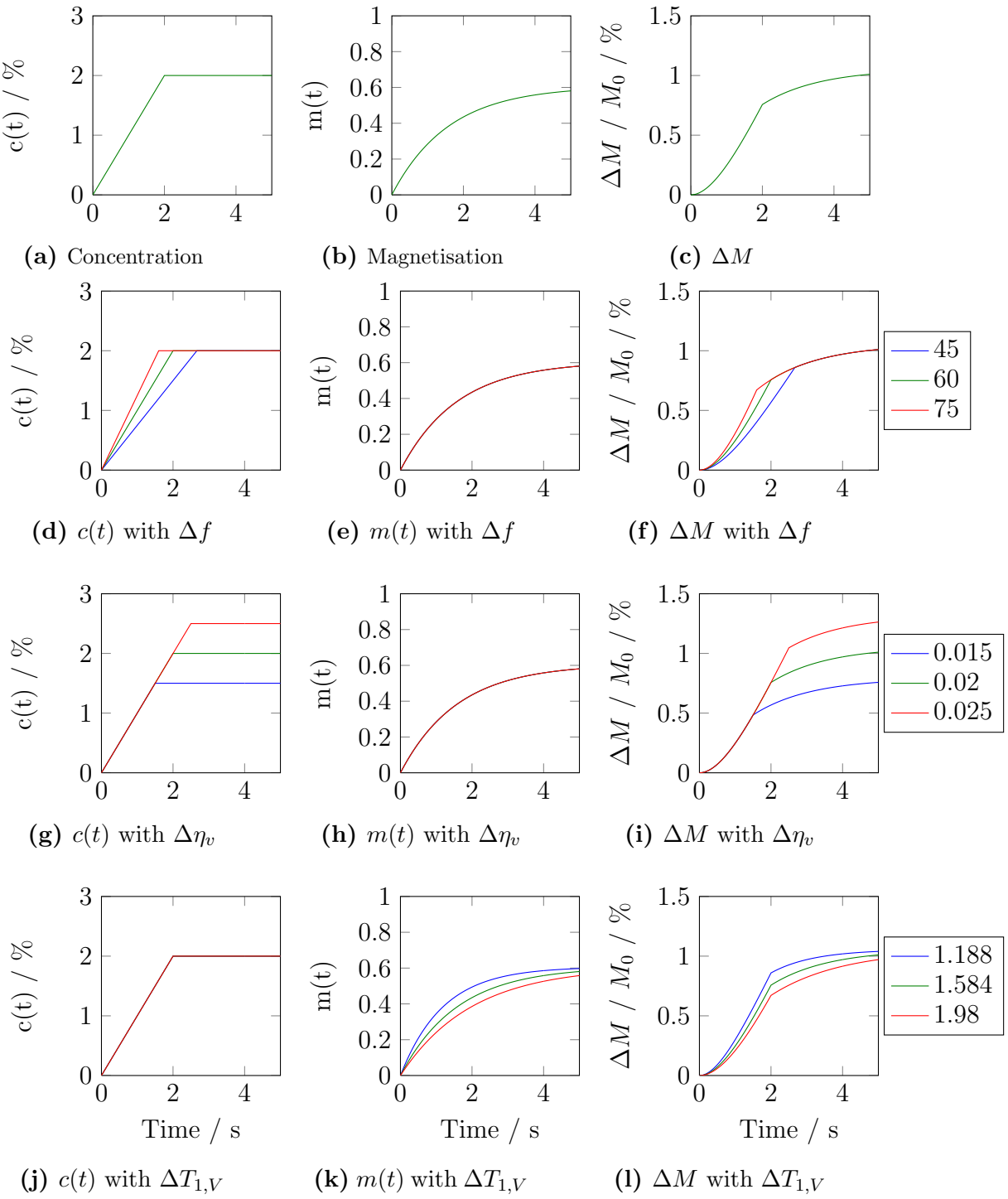
$$\Delta M(t, \mathrm{TE}) = \begin{cases} \alpha \cdot M_{0,B} \cdot \left(1 - \exp\left[\frac{-t}{T_{1,V}}\right]\right) \cdot \exp\left(\frac{-\mathrm{TE}}{T_{2,V}}\right) \cdot f \cdot t & 0 \leqslant t \leqslant \frac{\eta_v}{f} \\ \alpha \cdot M_{0,B} \cdot \left(1 - \exp\left[\frac{-t}{T_{1,V}}\right]\right) \cdot \exp\left(\frac{-\mathrm{TE}}{T_{2,V}}\right) \cdot \eta_v & t > \frac{\eta_v}{f} \end{cases} \tag{6.9}$$

The theoretical concentration of venous blood within the voxel ($c(t)$), the magnetisation of the venous blood ($m(t)$) and the QUIXOTIC subtraction signal (ΔM) are plotted in figure 6.5. In this figure it is assumed that the baseline voxel perfusion is $f = 0.01$ ml/ml/s (corresponding to 60 ml/100g/min), and venous blood volume is $\eta_v = 0.02$ ml/ml (An and Lin, 2002) and $T_{1,V}$ is 1.584 s (Lu et al., 2004). The minimum echo time of the readout was assumed to be 30 ms for EPI, but this could be reduced with a spiral acquisition. The concentration curve increases with flow until the venous compartment in the voxel is full, then the only increase in signal beyond this point is due to the relaxation of the venous spins. The magnitude signal is directly proportional to venous blood volume once this point is reached.

It should be noted that the signal change predicted by this model is on the order of the ASL signal change as $\Delta M / M_{0,b} \approx 1\%$. The acquisition can then be optimised by finding the maximum of

$$\frac{\Delta M(t, \mathrm{TE})}{\sqrt{\mathrm{TR}}} \tag{6.10}$$

which will return the maximum CNR per unit time. Assuming that the time for



(a) Concentration **(b)** Magnetisation **(c)** ΔM

(d) $c(t)$ with Δf **(e)** $m(t)$ with Δf **(f)** ΔM with Δf

(g) $c(t)$ with $\Delta \eta_v$ **(h)** $m(t)$ with $\Delta \eta_v$ **(i)** ΔM with $\Delta \eta_v$

(j) $c(t)$ with $\Delta T_{1,V}$ **(k)** $m(t)$ with $\Delta T_{1,V}$ **(l)** ΔM with $\Delta T_{1,V}$

Figure 6.5: QUIXOTIC Signal Model showing the venous concentration (left), magnetisation (middle) and tag control subtraction (right) as a function of time from the pre-saturation pulse. The top row (a-c) is the initial state assuming $f = 0.01$ ml/ml/min = 60 ml/100g/min, $\eta_v = 0.02$ ml/ml and $T_{1,V} = 1.584$ s. The next three rows vary individual parameters by ±25 %, showing a change in f (d-f), a change in η_v (g-i) and a change in $T_{1,V}$ (j-l).

reading out the slice is negligible compared to the TR (ie, $t = \text{TR}$), this function will have a maximum at $\text{TR} = \frac{\eta_v}{f}$. For grey matter this results in an optimal TR of 2 s for $f = 0.01$ ml/ml/s and $\eta_v = 0.02$ ml/ml. Note that this time must be long enough for the arterial spins nulled with the iVASO pulse to enter the voxels of interest. With an outflow time of 2 s the iVASO inversion would be applied 1034 ms prior to readout, which has previously been found to be sufficient for nulling the arterial compartment in healthy grey matter (Donahue et al., 2010).

6.2.2 The SNR Requirements for QUIXOTIC

Once the venous spins are isolated the $T_{2,V}$ is then measured in order to obtain a value of Y_v, via the calibration given in Lu et al. (2012) (fig. 6.1). Typically, three (Guo and Wong, 2012b) or five (Bolar et al., 2011) effective TEs are acquired. To correctly apply the calibration from Lu et al. (2012), the MLEV T_2 preparation should be applied with 10 ms τ_{CP} with 0 to $(n-1)$ MLEV units to give n effective TEs. As four RF pulses make up an individual MLEV unit (to compensate for B_1 inhomogeneity), the effective echo times will increase from 0 in steps of $4\tau_{CP}$, resulting in samples of the T_2 decay at 0 ms, 40 ms, 80 ms, 120 ms and so on. These later echo times will have much lower SNR than the first point as a result of the extra T_2 decay. It is possible that the low SNR points can bias the T_2 measurement (Raya et al., 2010), which may result in a systematic error in the determined Y_v. As QUIXOTIC has much lower SNR than TRUST, a Monte Carlo simulation was performed to determine the precision and accuracy of the QUIXOTIC measurement at different Y_v with respect to the SNR of the first effective TE.

6.2.2.1 Methods

QUIXOTIC experiments were simulated where Y_v ranged from 0 to 100 % in steps of 5 %. Four different τ_{CP} values (5, 10, 15 and 20 ms) were then simulated. For

each Y_v level the true T_2 was found using the calibration data for each τ_{CP} as given in Lu et al. (2012) using equation 6.2 and assuming a hematocrit of 0.4. Normalised synthetic data was then generated using four effective TEs (0 to $12\tau_{CP}$ in steps of $4\tau_{CP}$) such that

$$\Delta M = \exp\left(-\frac{\mathrm{TE}}{T_2}\right) \tag{6.11}$$

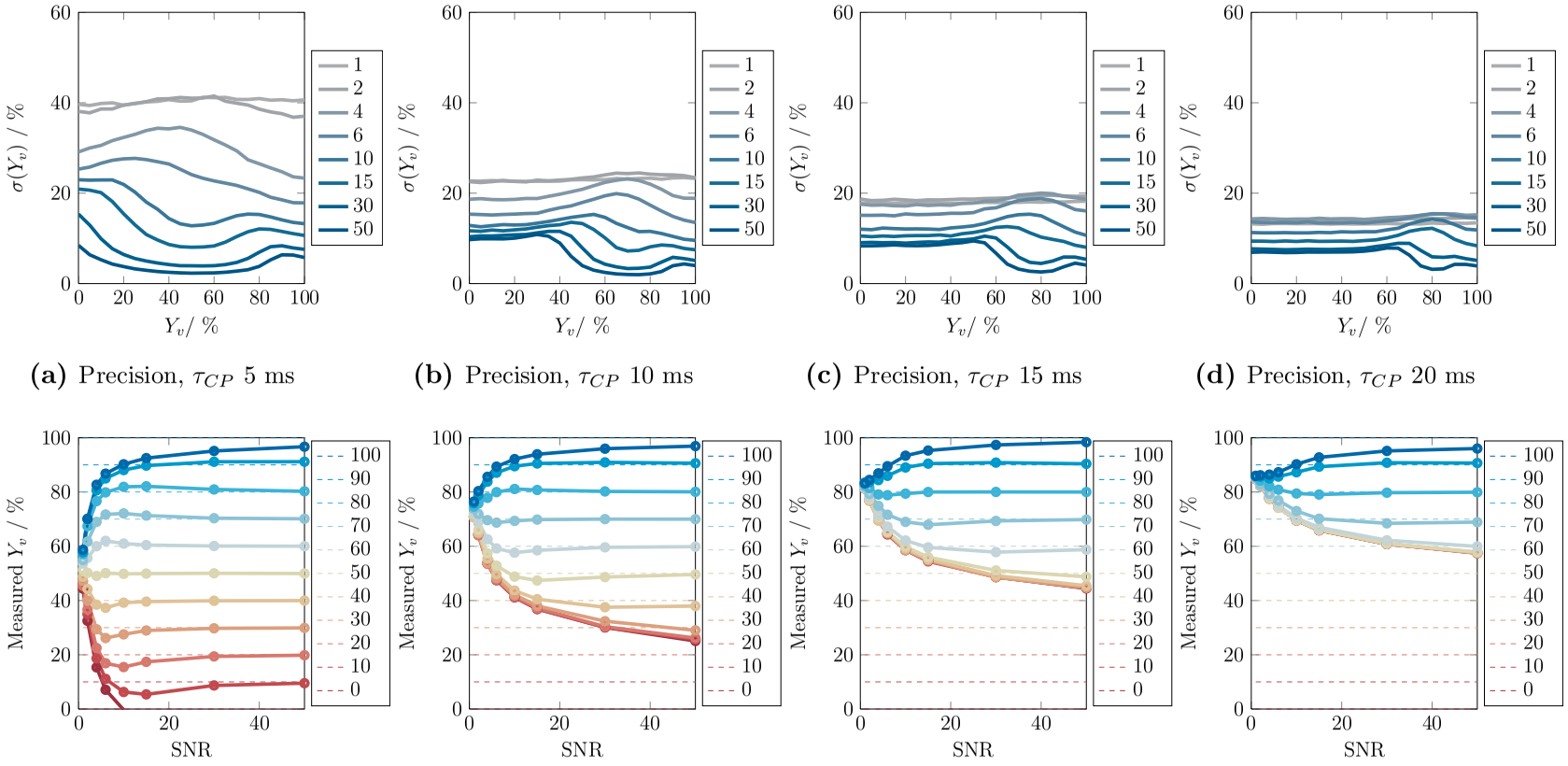
which is normalised. Zero mean random noise, generated using MATLAB's `randn` function, was then added to the ΔM signal. As the QUIXOTIC data is a subtraction of two magnitude images it was assumed that the noise on ΔM was Gaussian distributed with standard deviation $1/\mathrm{SNR}_0$. Eight values of SNR_0 were used: 1, 2, 4, 6, 10, 15, 30 and 50. The logarithm of the noisy ΔM signal was then taken and the measured T_2 was then determined by ordinary least squares regression. The measured T_2 was then converted to measured Y_v using the same calibration. This was repeated 10,000 times for each true Y_v, τ_{CP} and SNR_0.

The precision of the QUIXOTIC measurement for each τ_{CP} and SNR_0 was then determined by calculating the standard deviation of the measured Y_v values. The accuracy of the measurement was determined for each SNR_0 level by comparing the mean of the measured Y_v values to the true Y_v values.

6.2.2.2 Results

The results of the simulations to determine the precision and accuracy as a function of SNR_0 are plotted in figure 6.6. In all cases as SNR_0 increased the precision of the QUIXOTIC measurement of Y_v also increased (seen as a reduction in the standard deviation of the measured Y_v, $\sigma(Y_v)$). The precision also increased at certain points of true Y_v, due to the shape of the calibration curves that determine T_2 from Y_v.

The overall precision increased as τ_{CP} increased. However, the accuracy of the measurement is reduced as τ_{CP} is increased. In this case the measurement will tend



(a) Precision, τ_{CP} 5 ms **(b)** Precision, τ_{CP} 10 ms **(c)** Precision, τ_{CP} 15 ms **(d)** Precision, τ_{CP} 20 ms

(e) Accuracy, τ_{CP} 5 ms **(f)** Accuracy, τ_{CP} 10 ms **(g)** Accuracy, τ_{CP} 15 ms **(h)** Accuracy, τ_{CP} 20 ms

Figure 6.6: The precision and accuracy of a QUIXOTIC measurement as determined by Monte Carlo simulations plotted as a function of true Y_v (top row for precision) and SNR (bottom row for accuracy). In the precision plots the colours represent SNR and a reduction in the standard deviation of the measured Y_v ($\sigma(Y_v)$) indicates a more precise measurement. In the accuracy plots the colours represent the measured Y_v (solid lines) and the true Y_v (dotted lines) as a function of SNR.

to overestimate Y_v as a longer T_2 value than truth is measured due to the signal falling below the noise floor at the long echo times. In all cases, the accuracy of the measurement increased as SNR_0 increased. At the lowest SNR of 1, the measurement is biased towards a certain Y_v, for instance when using a 10 ms τ_{CP} the value of the measured Y_v will tend to 64.4 % with a range from 61.0 to 70.0 % for true Y_v of 0 and 100 %, respectively. Even with an SNR of 50 the complete dynamic range is not recovered for any τ_{CP}, but $\tau_{CP} = 5$ ms is the most accurate, especially at low SNR.

6.2.2.3 Discussion and Conclusions

The simulations seem to suggest that the SNR of the QUIXOTIC measurement must be at least 10 to achieve a reasonable balance of accuracy and precision in the measurement of Y_v when using four echos and fitting using the ordinary least squares method. Short τ_{CP} should be used in order to maximise accuracy, at the expense of a reduced precision.

At the shortest τ_{CP} calibrated an SNR of 30 is required to achieve a standard deviation of the measured Y_v of less than 10 percentage points over the entire range of true Y_v. The true precision of the measurement could be determined in a future study using the Cramer-Rao lower bound (Raya et al., 2010), if the underlying noise distribution is known. In this work it was assumed that the noise on ΔM is gaussian, which seems a reasonable assumption given the high SNR in the raw tag and control images.

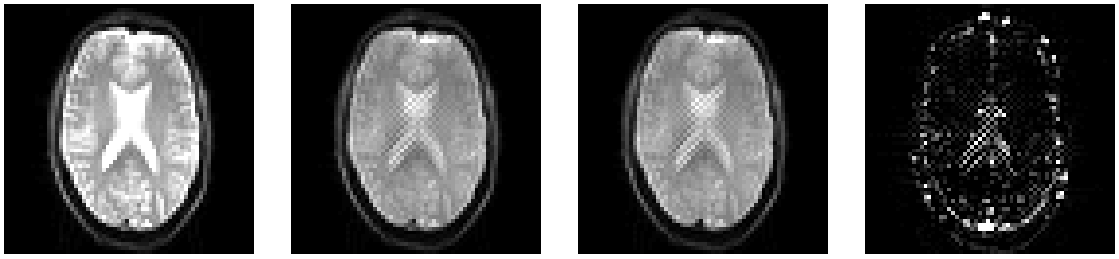
The measurement of Y_v was also shown to be biased to a particular value at low values of SNR. At 10 ms τ_{CP}, which is used in TRUST measurements (Lu et al., 2012), this value tends to 64.4 % which is in the same range as one would expect in healthy grey matter. This should not affect the results from the TRUST section previously, where the SNR was above 20 in the sagittal sinus. However, in QUIXOTIC the SNR is expected to be lower.

The accuracy is also compromised as the noise is not considered in the fit of the data. However, this would require many more effective TEs to be acquired, increasing the scan time as with the MLEV preparation only one effective TE can be acquired per two TRs (one tag-control pair). A solution to this limitation may be to acquire multiple TEs per preparation. However, the relationship between apparent T_2 and Y_v would need to be calibrated, and it would be technically challenging to acquire complete images in this time as a short ΔTE is required for the most accurate measurements.

6.2.3 Implementation of QUIXOTIC-TILT

To determine the baseline SNR of QUIXOTIC, the sequence was implemented as in figure 6.4. For the presaturation the same 90° BIR-4 pulse was used as in the previous chapters. This was followed by an inferior inversion of arterial spins, inverting a 20 cm volume with a 5 mm gap prior to a single slice spin echo EPI readout. The readout used a 64 square matrix, slice thickness 10 mm, TE = 37 ms to allow for the TILT gradients and spin echo pulse and V_{CUT} was initially applied at 2 and 8 cm/s. Since in a full QUIXOTIC experiment at least three echo times are required to calculate T_2 and roughly a 6 - 10 minute scan time is considered to be clinically feasible, the acquisition of this first effective TE which will have the highest SNR was limited to 2 minutes, resulting in 32 tag control pairs per scan.

However, in the initial tests with $V_{\mathrm{CUT}} = 2$ cm/s there was a chequerboard artefact in the data, particularly around the ventricles (fig. 6.7). When turning the TILT gradients off, or by compiling the sequence as a gradient echo EPI, this artefact was removed. This could be due to eddy currents interfering with the slice selection of the refocussing pulse or the combination of the spin echo pulse and gradients refocussing a particular coherence pathway. Attempts were made to increase the spoiler amplitude around the spin echo pulse, and to use a non-selective hard pulse refocussing, but a



(a) M_0 **(b)** Control **(c)** Tag **(d)** ΔM

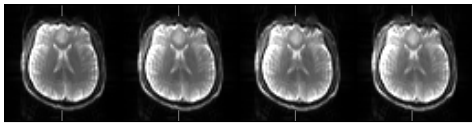
Figure 6.7: i-VASO-QUIXOTIC-TILT Images. Note the chequerboard artefact images in the tag and control acquisitions that is absent when the TILT gradients are turned off in the M_0 acquisition.

solution could not be found in the time available.

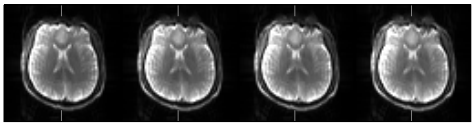
Instead, the sequence was compiled as a spin echo EPI, the gradients were removed from the readout and a BIR-8 VS-TILT preparation was inserted immediately before the EPI excitation pulse. As a separate velocity selective pulse needed to be used the TR was limited to 4 s, which resulted in the acquisition of 20 tag control pairs. By removing the the TILT gradients in the readout the echo time reduced to 30 ms. The sequence was performed with $V_{\mathrm{CUT}} = 2$, 4, 8 and 16 cm/s in one volunteer. Two experiments were performed, one with the iVASO pulse on, and a second with the iVASO pulse off. The temporal SNR ($\sqrt{N}\overline{\Delta M}/\sigma$), where N is the number of tag-control pairs, was calculated voxelwise and then averaged over the grey and white matter within the acquired slice.

6.2.4 Results

The averaged magnitude subtractions are displayed in figure 6.8. It can be seen that the sequence is able to isolate the signal in the sagittal sinus and superficial veins at all cutoff velocities. As V_{CUT} is reduced the signal in the ventricles increases, as in the VS-TILT experiments. There is some signal in the penumbra when the iVASO pulse is switched off (fig 6.8c), which is reduced when turning the iVASO pulse on (fig 6.8d).



(a) QUIXOTIC TILT Control



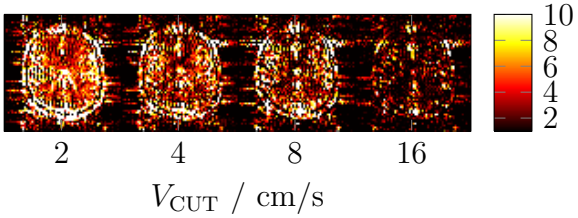
(b) iVASO QUIXOTIC TILT Control



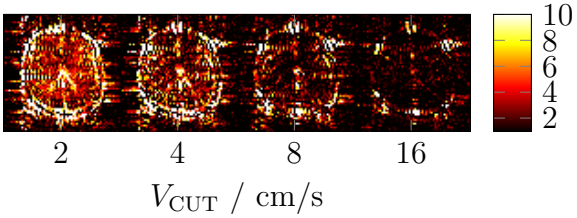
(c) QUIXOTIC TILT ΔM



(d) iVASO QUIXOTIC TILT ΔM



(e) QUIXOTIC TILT tSNR



(f) iVASO QUIXOTIC TILT tSNR

Figure 6.8: An example un-normalised control image (top), average Δ M subtraction (middle) and temporal SNR (bottom) of the QUIXOTIC-TILT (left) and iVASO-QUIXOTIC-TILT (right) sequences with effective TE of 0.

V_{CUT}	QUIXOTIC TILT	iVASO QUIXOTIC TILT
2	6.1 ± 7.1	4.5 ± 5.5
4	4.4 ± 4.8	3.3 ± 6.0
8	3.8 ± 6.0	1.8 ± 4.3
16	1.6 ± 3.6	0.5 ± 3.1

Table 6.1: Temporal SNR ± S.D. of the QUIXOTIC-TILT sequences averaged over the whole brain within the acquired slice, excluding the ventricles.

The temporal SNR averaged over the whole brain is reported in table 6.1. Temporal SNR increased as V_{CUT} was reduced, with a maximum temporal SNR of 6.1 ± 7.1 for QUIXOTIC-TILT, which reduced to 4.5 ± 5.5 with addition of the iVASO preparation.

Using the average tag-control difference the venous blood volume, η_v, was calculated. Assuming that the labeling efficiency was 80% and that TR $> \frac{\eta_v}{f}$, the average η_v in the iVASO-QUIXOTIC-TILT sequence was 0.009 ± 0.02 ml/ml at $V_{\mathrm{CUT}} = 2$ cm/s, and $(8 \pm 52) \times 10^{-4}$ ml/ml at $V_{\mathrm{CUT}} = 16$ cm/s.

6.2.5 Discussion and Conclusions

Despite optimisation of the sequence using a kinetic model the SNR of the first echo was on average 4.5 ± 5.5 after 2 minutes in iVASO-QUIXOTIC-TILT at $V_{CUT} = 2$ cm/s. Based on the results from the previous section, this SNR would not be sufficient for accurately determining Y_v. It was estimated that the raw SNR would need to be 10 for the QUIXOTIC-TILT measurement to be feasible, which would result in a scan time of approximately 8 minutes per effective TE and a minimum scan time of 24 minutes. This could be reduced by further optimisation of the sequence, such as acquiring multiple echos per preparation, reducing the TR and possibly increasing the temporal SNR using background suppression or RETROICOR.

It is possible that the effective echo time, 30 ms plus the time for the velocity selective preparation, is too long relative to the T_2 of venous blood to still maintain a

measurable transverse magnetisation. However, this hypothesis seems unlikely as the $T_{2,V}$ when breathing air was measured as 64.1 ± 2.6 ms in the previous section. The effective echo time could be reduced by using a spin echo spiral out acquisition. An optimal TR was also not achieved in this experiment as the chequerboard artefact resulted in the velocity selective pulses being used prior to the readout.

Nevertheless, the model predicted that the signal should be on the order of an ASL experiment. Assuming that the labeling efficiency was 80% and that TR $> \frac{\eta_v}{f}$, the average η_v in the iVASO-QUIXOTIC-TILT sequence was 0.009 ± 0.02 ml/ml at $V_{\mathrm{CUT}} = 2$ cm/s, and $(8 \pm 52) \times 10^{-4}$ ml/ml at $V_{\mathrm{CUT}} = 16$ cm/s, which is much lower than the expected value of 0.02 ml/ml. However, it should be noted that bulk motion will cause an overestimation of η_v as V_{CUT} is reduced, as explored in the previous chapter. This underestimation of η_v could be due to the lack of flow compensation in the acquisition, or that the velocity selective preparations do not isolate the venous pool.

However, at $V_{\mathrm{CUT}} = 16$ cm/s the iVASO-QUIXOTIC-TILT sequence is able to isolate the sagittal sinus with little contamination in the penumbra and a temporal SNR of 24, so could potentially be used for a TRUST measurement which was shown to be able to measure changes in Y_v in the first part of this chapter. This may be useful in vessels where the pCASL or PICORE labeling efficiency is low, for instance in the presence of pulsatile and retrograde flow.

Chapter 7

Thesis Summary and Future Work

In this thesis systematic errors when using velocity selective preparation have been corrected in order to improve the accuracy of perfusion quantification with Velocity Selective Arterial Spin Labeling. In chapter 2, the basics of MRI were re-enforced and an overview of the use of velocity selective pulses in the scientific literature was presented. The most widely used application of velocity selective pulses is VSASL (Wong et al., 2006), but they are also crucial for QUIXOTIC (Bolar et al., 2011), V-SEAN (Guo and Wong, 2012b), VENTI (Wong and Guo, 2013) and are related to the pulses used in accASL (Schmid et al., 2013).

In chapter 3 the overestimation of perfusion due to eddy current errors was characterised for three preparations through simulation and experiments. A novel velocity selective pulse, 'BIR-8', which combined the B_1 insensitivity of the BIR-4 with reduced eddy current errors from the DRHS gradient pattern, was shown to have the least systematic error. A proposed BIR-8 with symmetric gradients, symBIR-8, was shown to further improve on the original implementation.

In chapter 4 VSASL with BIR-8 preparations were applied clinically for the first time in four patients with CNS tumours, and was shown to produce significant signal in tumours in less than 5 minutes. In a comparison with pCASL it was found that

the tumour perfusion measured by VSASL was overestimated, despite the perfusion values in grey matter agreeing between the two methods.

In chapter 5 the magnitude of the systematic errors in VSASL from both diffusion and bulk motion was derived. A novel preparation method, VS-TILT, was then presented to eliminate the diffusion effects. It was found that diffusion effects cause a bias of $+38 \pm 18$ ml/100g/min in healthy grey matter for the VSASL parameters used. Expressions for the bolus shape when considering isotropic distributions of vessel networks were derived, and an assumption paradox was solved to derive an expression for the bolus shape in true laminar flow.

In chapter 6 the VS-TILT methodology was applied to an Oxygen Extraction Fraction mapping method, QUIXOTIC, in order to increase the SNR of the technique. A kinetic model for QUIXOTIC was presented to optimise the scan parameters. It was then shown that the quantification of OEF is biased in areas of low SNR, and that a QUIXOTIC-TILT measurement would not be possible in a clinically relevant time.

7.1 Future Work

In the remainder of this chapter several ideas for further investigations arising from this thesis are outlined.

Clinical Study

Led by the Department of Oncology an ethics application was submitted and has been approved by the Oxford A Research Ethics Committee in order to apply VSASL, VS-TILT and QUIXOTIC in 45 patients with either Grade IV Glioma, Cervical Cancer or Sarcoma over 12 months. This would have allowed a thorough investigation into the V_{cut} and a comparison with pCASL with matched readout in the Glioma cohort, and a

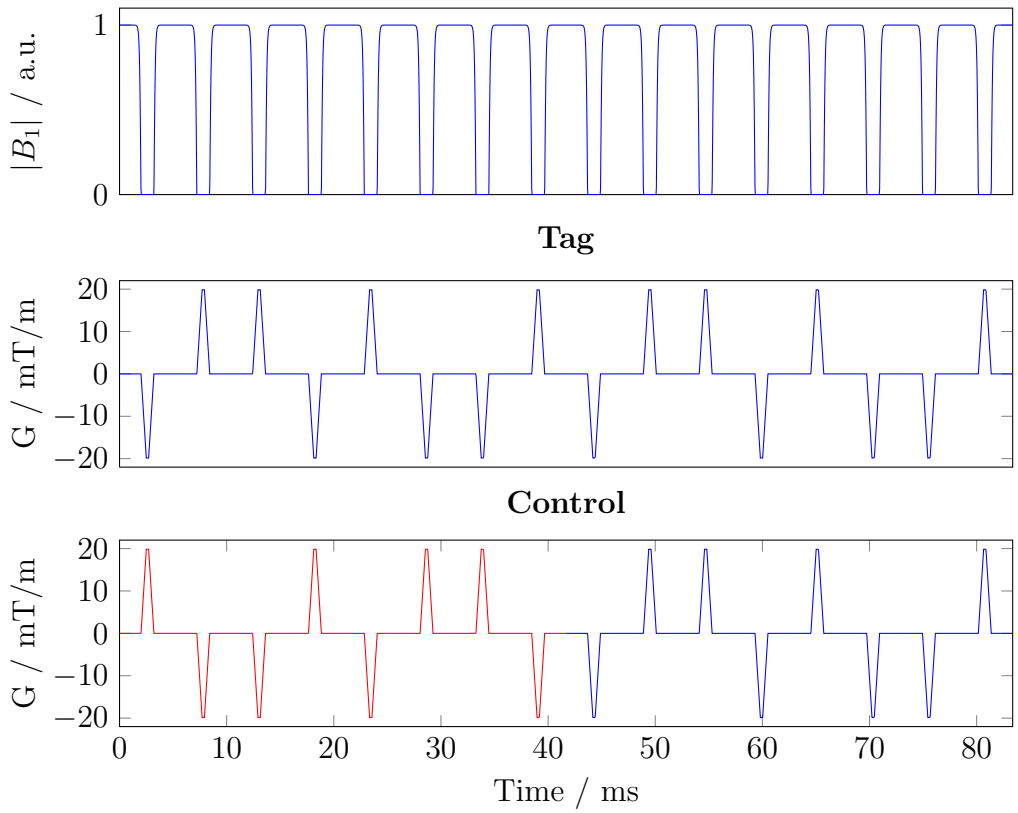


Figure 7.1: accASL-TILT tag and control preparations using BIR-8 preparations for the base velocity selective pulse.

feasibility study into performing VS-TILT or QUIXOTIC in the Cervical or Sarcoma cohorts. Unfortunately, at the time of writing no patients had been recruited.

Application of TILT to accASL

It would be relatively trivial to extend the VS-TILT approach to acceleration selective ASL by playing out four BIR-8 pulses with total $m_2 = 0$ in the control condition and $m_2 = \frac{\pi}{\gamma A_{\text{cut}}}$ in the tag condition, where A_{cut} is the cutoff acceleration (fig. 7.1). Compared to the original implementation with gradient toggled DRHS pulses (Schmid et al., 2013) this may reduce both the eddy current and diffusion effects to further determine the origin of the contrast in this technique.

Sine Velocity Profile for Vascular Distribution

In chapter 5 the velocity profile for isotropic vascular networks was described. This theory could be investigated by applying a velocity selective pulse with $M_z \propto \pm\sin(v)$, which would exclude the contributions from isotropic networks but retain the contributions from anisotropic networks.

Determine the True Bolus Arrival Time in VS-TILT

The true Bolus Arrival Time in VSASL and VS-TILT is subject to some debate, with a negative BAT being measured and T_1 decay components being reported by other groups. Most of the data in this thesis have been single inflow time due to time limitations, assuming that BAT is zero. More detailed, multi-TI studies are needed to determine if this is a safe assumption, particularly when the vasculature is disrupted in pathology.

A (Continuous) Velocity Selective Inversion?

VSASL and VS-TILT are still based on a saturation of arterial spins rather than an inversion, which limits the SNR of the technique. A Velocity Selective Inversion that is insensitive to ΔB_0, ΔB_1, eddy currents and diffusion is still the 'holy grail' of this technique. In addition to this, one could further boost SNR by moving to continuous rather than pulsed labeling. For example, an analogy can be drawn with (p)CASL, which inverts spins that move through a labeling plane defined by spatial RF pulses, to inverting spins that move through a velocity plane defined by velocity selective pulses. Like pCASL, the subpulses would not have to be adiabatic to produce this 'Acceleration Driven Adiabatic Inversion', so the SLR algorithm with m_1 blips may be useful in this case (Shin et al., 2012b).

References

An, H. and Lin, W. (2002). Cerebral oxygen extraction fraction and cerebral venous blood volume measurements using MRI: effects of magnetic field variation. *Magnetic resonance in medicine : official journal of the Society of Magnetic Resonance in Medicine / Society of Magnetic Resonance in Medicine*, 47(5):958–66.

Balchandani, P., Pauly, J., and Spielman, D. (2010). Designing adiabatic radio frequency pulses using the Shinnar-Le Roux algorithm. *Magn Reson Med*, 64(3):843–851.

Belaroussi, B., Milles, J., Carme, S., Zhu, Y. M., and Benoit-Cattin, H. (2006). Intensity non-uniformity correction in MRI: existing methods and their validation. *Medical image analysis*, 10(2):234–46.

Bernstein, M. A., King, K. F., and Zhou, X. J. (2004). *Handbook of MRI Pulse Sequences*. Elsevier.

Blamire, A. M. and Styles, P. (2000). Spin echo entrapped perfusion image (SEEPAGE). A nonsubtraction method for direct imaging of perfusion. *Magn Reson Med*, 43(5):701–704.

Bland, J. M. and Altman, D. G. (1986). Statistical methods for assessing agreement between two methods of clinical measurement. *Lancet*, 1(8476):307–10.

Bolar, D. S., Rosen, B. R., Sorensen, a. G., and Adalsteinsson, E. (2011). QUantitative Imaging of eXtraction of oxygen and TIssue consumption (QUIXOTIC) using venular-targeted velocity-selective spin labeling. *Magnetic resonance in medicine : official journal of the Society of Magnetic Resonance in Medicine / Society of Magnetic Resonance in Medicine*, 66(6):1550–62.

Brown, J. M. and Wilson, W. R. (2004). Exploiting tumour hypoxia in cancer treatment. *Nat Rev Cancer*, 4(6):437–447.

Buxton, R. B., Frank, L. R., Wong, E. C., Siewert, B., Warach, S., and Edelman, R. R. (1998). A general kinetic model for quantitative perfusion imaging with arterial spin labeling. *Magnetic resonance in medicine : official journal of the Society of Magnetic Resonance in Medicine / Society of Magnetic Resonance in Medicine*, 40(3):383–96.

Cano, K. E., Smith, M. A., and Shaka, A. J. (2002). Adjustable, broadband, selective excitation with uniform phase. *Journal of magnetic resonance (San Diego, Calif. : 1997)*, 155(1):131–9.

Chappell, M., a.R. Groves, Whitcher, B., and Woolrich, M. (2009). Variational Bayesian Inference for a Nonlinear Forward Model. *IEEE Transactions on Signal Processing*, 57(1):223–236.

Chiaradia, M., Baranes, L., Van Nhieu, J. T., Vignaud, A., Laurent, A., Decaens, T., Charles-Nelson, A., Brugières, P., Katsahian, S., Djabbari, M., Deux, J.-F., Sobhani, I., Karoui, M., Rahmouni, A., and Luciani, A. (2013). Intravoxel incoherent motion (IVIM) MR imaging of colorectal liver metastases: Are we only looking at tumor necrosis? *Journal of magnetic resonance imaging : JMRI*, doi:10.100.

Clare, S. and Jezzard, P. (2001). Rapid T(1) mapping using multislice echo planar imaging. *Magnetic resonance in medicine : official journal of the Society of Magnetic Resonance in Medicine / Society of Magnetic Resonance in Medicine*, 45(4):630–4.

Conolly, S., Glover, G., Nishimura, D., and Macovski, a. (1991). A reduced power selective adiabatic spin-echo pulse sequence. *Magnetic resonance in medicine : official journal of the Society of Magnetic Resonance in Medicine / Society of Magnetic Resonance in Medicine*, 18(1):28–38.

Conolly, S., Nishimura, D., Macovski, A., and Glover, G. (1988). Variable-rate selective excitation. *Journal of Magnetic Resonance (1969)*, 78(3):440–458.

Cutajar, M., Thomas, D. L., Banks, T., Clark, C. a., Golay, X., and Gordon, I. (2012). Repeatability of renal arterial spin labelling MRI in healthy subjects. *Magma (New York, N.Y.)*, 25(2):145–53.

Dai, W., Garcia, D., de Bazelaire, C., and Alsop, D. C. (2008). Continuous flow-driven inversion for arterial spin labeling using pulsed radio frequency and gradient fields. *Magn Reson Med*, 60(6):1488–1497.

Dai, W., Robson, P. M., Shankaranarayanan, A., and Alsop, D. C. (2012). Reduced resolution transit delay prescan for quantitative continuous arterial spin labeling perfusion imaging. *Magnetic resonance in medicine : official journal of the Society of Magnetic Resonance in Medicine / Society of Magnetic Resonance in Medicine*, 67(5):1252–65.

Derdeyn, C. P., Videen, T. O., Yundt, K. D., Fritsch, S. M., Carpenter, D. A., Grubb, R. L., and Powers, W. J. (2002). Variability of cerebral blood volume and oxygen extraction: stages of cerebral haemodynamic impairment revisited. *Brain*, 125(3):595–607.

Donahue, M. J., Sideso, E., MacIntosh, B. J., Kennedy, J., Handa, A., and Jezzard, P. (2010). Absolute arterial cerebral blood volume quantification using inflow vascular-space-occupancy with dynamic subtraction magnetic resonance imaging. *Journal of cerebral blood flow and metabolism : official journal of the International Society of Cerebral Blood Flow and Metabolism*, 30(7):1329–42.

Duhamel, G., de Bazelaire, C., and Alsop, D. C. (2003). Evaluation of systematic quantification errors in velocity-selective arterial spin labeling of the brain. *Magn Reson Med*, 50(1):145–153.

Duyn, J. H., Tan, C. X., van Gelderen, P., and Yongbi, M. N. (2001). High-sensitivity single-shot perfusion-weighted fMRI. *Magnetic resonance in medicine*, 46(1):88–94.

Federau, C., Eth, D. P., Maeder, P., Brien, K. O., and Browaeys, P. (2012). Brain Perfusion with intravoxel incoherent Motion Mr imaging. *Radiology*, 265(3).

Fischer, A., Pracht, E. D., Arnold, J. F. T., Kotas, M., Flentje, M., and Jakob, P. M. (2008). Assessment of pulmonary perfusion in a single shot using SEEPAGE. *J Magn Reson Imaging*, 27(1):63–70.

Folkman, J. (1996). New perspectives in clinical oncology from angiogenesis research. *Eur J Cancer*, 32A(14):2534–2539.

Fox, R. W. and McDonald, A. T. (1985). *Introduction to fluid mechanics*. Wiley.

Frank, L. R., Lu, K., and Wong, E. C. (2008). Perfusion tensor imaging. *Magn Reson Med*, 60(6):1284–1291.

Gallichan, D., Robson, M. D., Bartsch, A., and Miller, K. L. (2009). TREMR: Table-resonance elastography with MR. *Magnetic resonance in medicine : official journal of the Society of Magnetic Resonance in Medicine / Society of Magnetic Resonance in Medicine*, 62(3):815–21.

Gardener, A. G. and Francis, S. T. (2010). Multislice perfusion of the kidneys using parallel imaging: image acquisition and analysis strategies. *Magn Reson Med*, 63(6):1627–1636.

Gardener, A. G., Francis, S. T., Prior, M., Peters, A., and Gowland, P. a. (2010). Dependence of blood R2 relaxivity on CPMG echo-spacing at 2.35 and 7 T. *Magnetic resonance in medicine : official journal of the Society of Magnetic Resonance in Medicine / Society of Magnetic Resonance in Medicine*, 64(4):967–74.

Garwood, M. and Ke, Y. (1991). Symmetric pulses to induce arbitrary flip angles with compensation for rf inhomogeneity and resonance offsets. *Journal of Magnetic Resonance (1969)*, 94(3):511–525.

Giese, D., Haeberlin, M., Barmet, C., Pruessmann, K. P., Schaeffter, T., and Kozerke, S. (2012). Analysis and correction of background velocity offsets in phase-contrast flow measurements using magnetic field monitoring. *Magnetic resonance*

in medicine : official journal of the Society of Magnetic Resonance in Medicine / Society of Magnetic Resonance in Medicine, 67(5):1294–302.

Golay, X., Petersen, E. T., and Hui, F. (2005). Pulsed Star Labeling of Arterial Regions ({PULSAR}): A robust regional perfusion technique for high field imaging. *Magn Reson Med*, 53(1):15–21.

Golay, X., Silvennoinen, M. J., Zhou, J., Clingman, C. S., Kauppinen, R. A., Pekar, J. J., and van Zij, P. C. (2001). Measurement of tissue oxygen extraction ratios from venous blood T(2): increased precision and validation of principle. *Magn Reson Med*, 46(2):282–291.

Golay, X., Stuber, M., Pruessmann, K. P., Meier, D., and Boesiger, P. (1999). Transfer insensitive labeling technique (TILT): application to multislice functional perfusion imaging. *Journal of magnetic resonance imaging : JMRI*, 9(3):454–61.

Graeber, T. G., Osmanian, C., Jacks, T., Housman, D. E., Koch, C. J., Lowe, S. W., and Giaccia, A. J. (1996). Hypoxia-mediated selection of cells with diminished apoptotic potential in solid tumours. *Nature*, 379(6560):88–91.

Gruetter, R., Seaquist, E. R., Kim, S., and U&gcaron;urbil, K. (1998). Localized in vivo ¡sup¿13¡/sup¿C-NMR of Glutamate Metabolism in the Human Brain: Initial Results at 4 Tesla. *Developmental Neuroscience*, 20(4-5):380–388.

Günther, M., Bock, M., and Schad, L. R. (2001). Arterial spin labeling in combination with a look-locker sampling strategy: inflow turbo-sampling EPI-FAIR (ITS-FAIR). *Magnetic resonance in medicine : official journal of the Society of Magnetic Resonance in Medicine / Society of Magnetic Resonance in Medicine*, 46(5):974–84.

Günther, M., Oshio, K., and Feinberg, D. a. (2005). Single-shot 3D imaging techniques improve arterial spin labeling perfusion measurements. *Magnetic resonance in medicine : official journal of the Society of Magnetic Resonance in Medicine / Society of Magnetic Resonance in Medicine*, 54(2):491–8.

Guo, J. and Wong, E. C. (2011a). Increased Tagging Efficiency in Velocity Selective ASL using Multiple Velocity Selective Saturation Modules. In *Proc. Intl. Soc. Mag. Reson. Med. 19*, page 296.

Guo, J. and Wong, E. C. (2011b). Removal of CSF Contamination in VSASL and QUIXOTIC using a long TE CSF Scan. In *Proc. Intl. Soc. Mag. Reson. Med. 19*, page 2116.

Guo, J. and Wong, E. C. (2012a). Observations on the tagging time and velocity cutoff dependence in velocity selective ASL. In *Proc. Intl. Soc. Mag. Reson. Med. 20*, page 2004.

Guo, J. and Wong, E. C. (2012b). Venous oxygenation mapping using velocity-selective excitation and arterial nulling. *Magnetic resonance in medicine : official journal of the Society of Magnetic Resonance in Medicine / Society of Magnetic Resonance in Medicine*, 68(5):1458–1471.

Guo, J. and Wong, E. C. (2012c). VSASL using symmetric BIR-8 RF and gradient pulses to reduce eddy currents. In *ISMRM Workshop on Perfusion MRI*, page 2096.

Guo, J. and Wong, E. C. (2013). Pulmonary Blood Flow Measurement using Velocity-Selective Arterial Spin Labeling at 3.0T. In *Proc. Intl. Soc. Mag. Reson. Med. 21*, page 2149.

Haacke, M., Brown, R., Thompson, M., and Venkatesan, R. (1999). *Magnetic Resonance Imaging: Physical Principles and Sequence Design*. Wiley-Blackwell.

Haase, A., Frahm, J., Hanicke, W., and Matthaei, D. (1985). 1H NMR chemical shift selective (CHESS) imaging. *Physics in medicine and biology*, 30(4):341–344.

Hajnal, J. V., Oatridge, a., Herlihy, a. H., and Bydder, G. M. (2001). Reduction of CSF artifacts on FLAIR images by using adiabatic inversion pulses. *AJNR. American journal of neuroradiology*, 22(2):317–22.

Hakyemez, B., Erdogan, C., Ercan, I., Ergin, N., Uysal, S., and Atahan, S. (2005). High-grade and low-grade gliomas: Differentiation by using perfusion MR imaging. *Clinical Radiology*, 60(4):493–502.

He, X. and Yablonskiy, D. A. (2007). Quantitative {BOLD}: mapping of human cerebral deoxygenated blood volume and oxygen extraction fraction: default state. *Magn Reson Med*, 57(1):115–126.

Heijtel, D. F., van Osch, M. J., Caan, M. W., Majoie, C. B., VanBavel, E., and Nederveen, A. J. (2012). Feasibility of arterial spin labeling on a 1T open MRI scanner. *Journal of Magnetic Resonance Imaging*, 000:n/a–n/a.

Helenius, J., Soinne, L., Perkio, J., Salonen, O., Kangasmaki, A., Kaste, M., Carano, R. A. D., Aronen, H. J., and Tatlisumak, T. (2002). Diffusion-Weighted MR Imaging in Normal Human Brains in Various Age Groups. *AJNR Am. J. Neuroradiol.*, 23(2):194–199.

Henderson, E., Rutt, B. K., and Lee, T. Y. (1998). TEMPORAL SAMPLING REQUIREMENTS FOR THE TRACER KINETICS MODELING OF BREAST DISEASE. *Magnetic resonance imaging*, 16(9):1057–1073.

Henkelman, R. M. (1990). Does IVIM measure classical perfusion? *Magnetic resonance in medicine : official journal of the Society of Magnetic Resonance in Medicine / Society of Magnetic Resonance in Medicine*, 16(3):470–5.

Henry-Feugeas, M. C., Idy-Peretti, I., Blanchet, B., Hassine, D., Zannoli, G., and Schouman-Claeys, E. (1993). Temporal and spatial assessment of normal cerebrospinal fluid dynamics with MR imaging. *Magnetic resonance imaging*, 11(8):1107–18.

Herscovitch, P. and Raichle, M. E. (1985a). What is the correct value for the brain–blood partition coefficient for water? *Journal of cerebral blood flow and metabolism : official journal of the International Society of Cerebral Blood Flow and Metabolism*, 5(1):65–9.

Herscovitch, P. and Raichle, M. E. (1985b). What is the correct value for the brain–blood partition coefficient for water? *Journal of cerebral blood flow and metabolism : official journal of the International Society of Cerebral Blood Flow and Metabolism*, 5(1):65–9.

Iida, H., Law, I., Pakkenberg, B., Krarup-Hansen, A., Eberl, S., Holm, S., Hansen, A. K., Gundersen, H. J., Thomsen, C., Svarer, C., Ring, P., Friberg, L., and Paulson, O. B. (2000). Quantitation of regional cerebral blood flow corrected for partial volume effect using O-15 water and PET: I. Theory, error analysis, and stereologic comparison. *Journal of cerebral blood flow and metabolism : official journal of the International Society of Cerebral Blood Flow and Metabolism*, 20(8):1237–51.

Jehenson, P., Westphal, M., and Schuff, N. (1990). Analytical method for the compensation of eddy-current effects induced by pulsed magnetic field gradients in NMR systems. *Journal of Magnetic Resonance (1969)*, 90(2):264–278.

Jenkinson, M. and Smith, S. M. (2001). A global optimisation method for robust affine registration of brain images. *Medical image analysis*, 5(2):143–156.

Jesmanowicz, A., Wong, E., and Hyde, J. (1993). Phase correction for EPI using internal reference lines. In *Proceedings 12th Scientific Meeting, International Society for Magnetic Resonance in Medicine, New York*, page 1239.

Jezzard, P., Barnett, a. S., and Pierpaoli, C. (1998). Characterization of and correction for eddy current artifacts in echo planar diffusion imaging. *Magnetic resonance in medicine : official journal of the Society of Magnetic Resonance in Medicine / Society of Magnetic Resonance in Medicine*, 39(5):801–12.

Jordan, F., Magat, J., Colliez, F., Ozel, E., Fruytier, A.-c., Mignion, L., Bouzin, C., Cani, P. D., Vandeputte, C., Feron, O., Delzenne, N., Himmelreich, U., Denolin, V., Duprez, T., and Gallez, B. (2012). Mapping of Oxygen by Imaging Lipids Relaxation Enhancement : A Potential Sensitive Endogenous MRI Contrast to Map Variations in Tissue Oxygenation.

Jung, Y. and Liu, T. T. (2010). Fast CBF Estimation in Multi-Phase Pseudo-Continuous Arterial Spin Labeling (MP-PCASL) Using Signal Demodulation. In *Proc. Intl. Soc. Mag. Reson. Med. 18*, page 1739.

Jung, Y., Wong, E. C., and Liu, T. T. (2010). Multiphase pseudocontinuous arterial spin labeling (MP-PCASL) for robust quantification of cerebral blood flow. *Magnetic resonance in medicine : official journal of the Society of Magnetic Resonance in Medicine / Society of Magnetic Resonance in Medicine*, 64(3):799–810.

Kallinowski, F., Zander, R., Hoeckel, M., and Vaupel, P. (1990). Tumor tissue oxygenation as evaluated by computerized-pO2-histography. *International journal of radiation oncology, biology, physics*, 19(4):953–61.

Kim, S., Decarlo, L., Cho, G. Y., Jensen, J. H., Sodickson, D. K., Moy, L., Formenti, S., Schneider, R. J., Goldberg, J. D., and Sigmund, E. E. (2012). Interstitial fluid pressure correlates with intravoxel incoherent motion imaging metrics in a mouse mammary carcinoma model. *NMR in biomedicine*, 25(5):787–94.

Kim, S. G. (1995). Quantification of relative cerebral blood flow change by flow-sensitive alternating inversion recovery (FAIR) technique: application to functional mapping. *Magnetic resonance in medicine : official journal of the Society of Magnetic Resonance in Medicine / Society of Magnetic Resonance in Medicine*, 34(3):293–301.

Krishnamurthy, L. C., Liu, P., Ge, Y., and Lu, H. (2013). Vessel-specific quantification of blood oxygenation with T 2 -relaxation-under-phase-contrast MRI. *Magnetic Resonance in Medicine*, doi: 10.10.

Ku, D. N. (1997). Blood Flow in Arteries. *Annual Review of Fluid Mechanics*, 29(1):399–434.

Kwong, K. K., Mckinstry, R. C., Chien, D., Crawley, A. P., Pearlman, D., Rosen, B. R., and Bihan, L. (1991). CSF-Suppressed Quantitative Single-Shot Diffusion Imaging. *Magnetic Resonance in Medicine*, 21:157–163.

Lauterbur, P. C. (1973). Image Formation by Induced Local Interactions: Examples Employing Nuclear Magnetic Resonance. *Nature*, 242:190–191.

Le Bihan, D., Breton, E., Lallemand, D., Grenier, P., Cabanis, E., and Laval-Jeantet, M. (1986). MR imaging of intravoxel incoherent motions: application to diffusion and perfusion in neurologic disorders. *Radiology*, 161(2):401–7.

Lee, N. Y., Mechalakos, J. G., Nehmeh, S., Lin, Z., Squire, O. D., Cai, S., Chan, K., Zanzonico, P. B., Greco, C., Ling, C. C., Humm, J. L., and Schöder, H. (2008). Fluorine-18-labeled fluoromisonidazole positron emission and computed tomography-guided intensity-modulated radiotherapy for head and neck cancer: a feasibility study. *International journal of radiation oncology, biology, physics*, 70(1):2–13.

Li, X. and Metzger, G. J. (2012). Feasibility of measuring prostate perfusion with arterial spin labeling. *NMR in biomedicine*, (October 2011).

Li, X. and Metzger, G. J. (2013). Prostate Perfusion Imaging usin Velocity Selective ASL. In *Proc. Intl. Soc. Mag. Reson. Med. 21*, page 3402.

Lingamneni, A., Hardy, P. A., Powell, K. A., Pelc, N. J., and White, R. D. (1995). Validation of cine phase-contrast MR imaging for motion analysis. *Journal of Magnetic Resonance Imaging*, 5(3):331–338.

Los, M., Roodhart, J. M. L., and Voest, E. E. (2007). Target practice: lessons from phase III trials with bevacizumab and vatalanib in the treatment of advanced colorectal cancer. *The oncologist*, 12(4):443–50.

Lu, H., Clingman, C., Golay, X., and van Zijl, P. C. M. (2004). Determining the longitudinal relaxation time (T1) of blood at 3.0 Tesla. *Magnetic resonance in medicine : official journal of the Society of Magnetic Resonance in Medicine / Society of Magnetic Resonance in Medicine*, 52(3):679–82.

Lu, H. and Ge, Y. (2008). Quantitative evaluation of oxygenation in venous vessels using T2-Relaxation-Under-Spin-Tagging MRI. *Magn Reson Med*, 60(2):357–363.

Lu, H., Golay, X., Pekar, J. J., and Van Zijl, P. C. M. (2003). Functional magnetic resonance imaging based on changes in vascular space occupancy. *Magnetic resonance in medicine : official journal of the Society of Magnetic Resonance in Medicine / Society of Magnetic Resonance in Medicine*, 50(2):263–74.

Lu, H., Xu, F., Grgac, K., Liu, P., Qin, Q., and van Zijl, P. (2012). Calibration and validation of TRUST MRI for the estimation of cerebral blood oxygenation. *Magnetic resonance in medicine : official journal of the Society of Magnetic Resonance in Medicine / Society of Magnetic Resonance in Medicine*, 67(1):42–9.

Luh, W. M., Wong, E. C., Bandettini, P. A., and Hyde, J. S. (1999). QUIPSS II with thin-slice TI1 periodic saturation: a method for improving accuracy of quantitative perfusion imaging using pulsed arterial spin labeling. *Magnetic resonance in medicine : official journal of the Society of Magnetic Resonance in Medicine / Society of Magnetic Resonance in Medicine*, 41(6):1246–54.

Luh, W. M., Wong, E. C., Talagala, S. L., and Bandettini, P. a. (2008). Tagging Efficiency Improvement Using Velocity-matched Pseudo-continuous Arterial Spin Labeling and VERSE. In *Proc. Intl. Soc. Mag. Reson. Med. 16*, page 3341.

Lunt, S. J., Fyles, A., Hill, R. P., and Milosevic, M. (2008). Interstitial fluid pressure in tumors: therapeutic barrier and biomarker of angiogenesis. *Future Oncology*, 4(6):793–802.

Lustig, M., Donoho, D., and Pauly, J. M. (2007). Sparse MRI: The application of compressed sensing for rapid MR imaging. *Magnetic resonance in medicine : official journal of the Society of Magnetic Resonance in Medicine / Society of Magnetic Resonance in Medicine*, 58(6):1182–95.

Luz, Z. and Meiboom, S. (1963). Nuclear Magnetic Resonance Study of the Protolysis of Trimethylammonium Ion in Aqueous SolutionOrder of the Reaction with Respect to Solvent. *The Journal of Chemical Physics*, 39(2):366.

Mai, V. M., Hagspiel, K. D., Christopher, J. M., Do, H. M., Altes, T., Knight-Scott, J., Stith, A. L., Maier, T., and Berr, S. S. (1999). Perfusion Imaging Of The Human Lung Using Flow-Sensitive Alternating Inversion Recovery With An Extra Radiofrequency Pulse (FAIRER). *Magnetic resonance imaging*, 17(3):355–361.

Mani, S., Pauly, J., Conolly, S., Meyer, C., and Nishimura, D. (1997). Background suppression with multiple inversion recovery nulling: applications to projective angiography. *Magnetic resonance in medicine : official journal of the Society of Magnetic Resonance in Medicine / Society of Magnetic Resonance in Medicine*, 37(6):898–905.

Mayr, N. A., Wang, J. Z., Zhang, D., Grecula, J. C., Lo, S. S., Jaroura, D., Montebello, J., Zhang, H., Li, K., Lu, L., Huang, Z., Fowler, J. M., Wu, D. H., Knopp, M. V., and Yuh, W. T. C. (2010). Longitudinal changes in tumor perfusion pattern during the radiation therapy course and its clinical impact in cervical cancer. *Int J Radiat Oncol Biol Phys*, 77(2):502–508.

Miles, K. A., Hayball, M., and Dixon, A. K. (1991). Colour perfusion imaging: a new application of computed tomography. *Lancet*, 337(8742):643–5.

Mineura, K., Sasajima, T., Kowada, M., Ogawa, T., Hatazawa, J., Shishido, F., and Uemura, K. (1994). Perfusion and metabolism in predicting the survival of patients with cerebral gliomas. *Cancer*, 73(9):2386–94.

Morse, O. and Singer, J. (1970). Blood velocity measurements in intact subjects. *Science*, 170(3956):440–441.

Munn, L. L. (2003). Aberrant vascular architecture in tumors and its importance in drug-based therapies. *Drug discovery today*, 8(9):396–403.

Nezafat, R., Ouwerkerk, R., Derbyshire, A. J., Stuber, M., and McVeigh, E. R. (2009). Spectrally selective B1-insensitive T2 magnetization preparation sequence. *Magnetic resonance in medicine : official journal of the Society of Magnetic Resonance in Medicine / Society of Magnetic Resonance in Medicine*, 61(6):1326–35.

Nishimura, D. (2010). *Principles of Magnetic Resonance Imaging*. Self Published.

O'Connor, J., Naish, J., Parker, G. J. M., Waterton, J., Watson, Y., Jayson, G. C., Buonaccorsi, G. A., Cheung, S., Buckley, D. L., M.McGrath, D., West, C. M., Davidcon, S. E., Roberts, C., Mills, S. J., Mitchell, C. L., Hope, L., Ton, C., and Jackson, A. (2009). Preliminary Study of Oxygen-Enhanced Longitudinal Relaxation in MRI: A Potential Novel Biomarker of Oxygenation Changes in Solid Tumors. *International journal of radiation oncology, biology, physics*, 75(4):1209–1215.

Ogg, R. J., Kingsley, P. B., Taylor, J. S., and Ogg R J (1994). WET, a T1- and B1-Insensitive Water-Suppression Method for in Vivo Localized 1H NMR Spectroscopy. *Journal of magnetic resonance. Series B*, 104(1):1–10.

Okell, T. W., Chappell, M. A., Schulz, U. G., and Jezzard, P. (2012). A kinetic model for vessel-encoded dynamic angiography with arterial spin labeling. *Magnetic resonance in medicine : official journal of the Society of Magnetic Resonance in Medicine / Society of Magnetic Resonance in Medicine*, 68(3):969–79.

Okell, T. W., Chappell, M. A., Woolrich, M. W., Günther, M., Feinberg, D. A., and Jezzard, P. (2010). Vessel-encoded dynamic magnetic resonance angiography using arterial spin labeling. *Magn Reson Med*, 64(2):430–438.

Olive, P. L., Banáth, J. P., and Aquino-Parsons, C. (2001). Measuring hypoxia in solid tumours–is there a gold standard? *Acta oncologica (Stockholm, Sweden)*, 40(8):917–23.

Ordidge, R. J., Wylezinska, M., Hugg, J. W., Butterworth, E., and Franconi, F. (1996). Frequency offset corrected inversion (FOCI) pulses for use in localized spectroscopy. *Magnetic resonance in medicine : official journal of the Society of Magnetic Resonance in Medicine / Society of Magnetic Resonance in Medicine*, 36(4):562–6.

Padhani, A. R. (2002). Dynamic contrast-enhanced MRI in clinical oncology: current status and future directions. *J Magn Reson Imaging*, 16(4):407–422.

Park, S.-H., Wang, D. J. J., and Duong, T. Q. (2013). Balanced steady state free precession for arterial spin labeling MRI: Initial experience for blood flow mapping in human brain, retina, and kidney. *Magnetic resonance imaging*.

Parkes, L. M. and Tofts, P. S. (2002). Improved accuracy of human cerebral blood perfusion measurements using arterial spin labeling: accounting for capillary water permeability. *Magn Reson Med*, 48(1):27–41.

Pat, G. T. L., Meyer, C. H., Pauly, J. M., and Nishimura, D. G. (1997). Reducing flow artifacts in echo-planar imaging. *Magnetic Resonance in Medicine*, 37(3):436–447.

Pauly, J., Le Roux, P., Nishimura, D., and Macovski, a. (1991). Parameter relations for the Shinnar-Le Roux selective excitation pulse design algorithm [NMR imaging]. *IEEE transactions on medical imaging*, 10(1):53–65.

Pelc, N. J., Herfkens, R. J., Shimakawa, A., and Enzmann, D. R. (1991). Phase contrast cine magnetic resonance imaging. *Magnetic resonance quarterly*, 7(4):229–54.

Petersen, E. T., Lim, T., and Golay, X. (2006). Model-free arterial spin labeling quantification approach for perfusion MRI. *Magnetic resonance in medicine : official journal of the Society of Magnetic Resonance in Medicine / Society of Magnetic Resonance in Medicine*, 55(2):219–32.

Priest, A. N., Graves, M. J., and Lomas, D. J. (2011). Acceleration dependent vascular anatomy for non-contrast-enhanced-MRA. In *Proc. Intl. Sot. Mag. Reson. Med. 19*, page 90.

Qiu, D., Straka, M., Zun, Z., Bammer, R., Moseley, M. E., and Zaharchuk, G. (2012). CBF measurements using multidelay pseudocontinuous and velocity-selective arterial spin labeling in patients with long arterial transit delays: Comparison with xenon CT CBF. *Journal of magnetic resonance imaging : JMRI*, 36(1):110–9.

Raya, J. G., Dietrich, O., Horng, A., Weber, J., Reiser, M. F., and Glaser, C. (2010). T2 measurement in articular cartilage: impact of the fitting method on accuracy and precision at low SNR. *Magnetic resonance in medicine : official journal of the Society of Magnetic Resonance in Medicine / Society of Magnetic Resonance in Medicine*, 63(1):181–93.

Redpath, T. W. and Smith, F. W. (1994). Technical note: use of a double inversion recovery pulse sequence to image selectively grey or white brain matter. *The British journal of radiology*, 67(804):1258–63.

Reese, T. G., Heid, O., Weisskoff, R. M., and Wedeen, V. J. (2003). Reduction of eddy-current-induced distortion in diffusion MRI using a twice-refocused spin echo. *Magn Reson Med*, 49(1):177–182.

Robson, P. M., Madhuranthakam, A. J., Dai, W., Pedrosa, I., Rofsky, N. M., and Alsop, D. C. (2009). Strategies for reducing respiratory motion artifacts in renal perfusion imaging with arterial spin labeling. *Magnetic resonance in medicine : official journal of the Society of Magnetic Resonance in Medicine / Society of Magnetic Resonance in Medicine*, 61(6):1374–87.

Schepers, J., Van Osch, M. J. P., and Nicolay, K. (2003). Effect of vascular crushing on FAIR perfusion kinetics, using a BIR-4 pulse in a magnetization prepared FLASH sequence. *Magnetic resonance in medicine : official journal of the Society of Magnetic Resonance in Medicine / Society of Magnetic Resonance in Medicine*, 50(3):608–13.

Schmid, S., Ghariq, E., Teeuwisse, W. M., Webb, A., and van Osch, M. J. P. (2013). Acceleration-selective arterial spin labeling. *Magnetic resonance in medicine : official journal of the Society of Magnetic Resonance in Medicine / Society of Magnetic Resonance in Medicine*, page doi: 10.1002/mrm.24650.

Schraml, C., Schwenzer, N. F., Martirosian, P., Claussen, C. D., and Schick, F. (2008). Perfusion imaging of the pancreas using an arterial spin labeling technique. *Journal of Magnetic Resonance Imaging*, 28(6):1459–1465.

Shin, T., Hu, B. S., and Nishimura, D. G. (2012a). Off-Resonance-Robust Velocity-Selective Magnetization Preparation for Non-Contrast-Enhanced Peripheral MR Angiography. 000:1–12.

Shin, T., Worters, P. W., Hu, B. S., and Nishimura, D. G. (2012b). Non-contrast-enhanced renal and abdominal MR angiography using velocity-selective inversion preparation. *Magnetic resonance in medicine : official journal of the Society of Magnetic Resonance in Medicine / Society of Magnetic Resonance in Medicine*, 69(5):1268–1275.

Spees, W. M., Buhl, N., Sun, P., Ackerman, J. J. H., Neil, J. J., and Garbow, J. R. (2011). Quantification and compensation of eddy-current-induced magnetic-field gradients. *Journal of magnetic resonance (San Diego, Calif. : 1997)*, 212(1):116–23.

Staewen, R., Johnson, A., and Ross, B. (1990). 3-D FLASH Imaging Using a Single Surface Coil and a New Adiabatic Pulse, BIR-4. *Investigative Radiology*, 25(5):559–567.

Tannús, a. and Garwood, M. (1997). Adiabatic pulses. *NMR in biomedicine*, 10(8):423–34.

Tasu, J. P., Jolivet, O., Mousseaux, E., Delouche, A., Diebold, B., and Bittoun, J. (1997). Acceleration mapping by Fourier acceleration-encoding: in vitro study and initial results in the great thoracic vessels. *Magnetic resonance in medicine : official journal of the Society of Magnetic Resonance in Medicine / Society of Magnetic Resonance in Medicine*, 38(1):110–6.

Tofts, P. S., Brix, G., Buckley, D. L., Evelhoch, J. L., Henderson, E., Knopp, M. V., Larsson, H. B., Lee, T. Y., Mayr, N. A., Parker, G. J., Port, R. E., Taylor, J., and Weisskoff, R. M. (1999). Estimating Kinetic Parameters From Dynamic Contrast-Enhanced T1-Weighted MRI of a Diffusable Tracer: Standardized Quantities and Symbols. *Journal of Magnetic Resonance Resonance Imaging*, 232(3):223–232.

Ugurbil, K., Garwood, M., and Rath, A. (1988). Optimization of Modulation Functions to Improve Insensitivity of Adiabatic Pulses to Variations in B, Magnitude. *Journal of Magnetic Resonance (1969)*, 469(3):448–469.

Ugurbil, K., Garwood, M., and Robinbendall, A. (1987). Amplitude- and Frequency-Modulated Pulses to Achieve 90 Plane Rotations with Inhomogeneous B1 Fields. 85:177–185.

Vaals, J. J. V. and Bergman, A. H. (1990). Optimization of eddy-current compensation. *Journal of Magnetic Resonance*, 90(1):52–70.

van Zijl, P., Eleff, S., and Ulatowski, J. (1998). Quantitative assessment of blood flow, blood volume and blood oxygenation effects in functional magnetic resonance imaging. *Nature medicine*.

Vidorreta, M., Wang, Z., Rodríguez, I., Pastor, M. A., Detre, J. A., and Fernández-Seara, M. A. (2012). Comparison of 2D and 3D single-shot ASL perfusion fMRI sequences. *NeuroImage*, 66C:662–671.

Wang, G., El-Sharkawy, A. M., Edelstein, W. A., Schär, M., and Bottomley, P. A. (2012). Measuring T and T, and imaging T without spin echoes. *Journal of magnetic resonance (San Diego, Calif. : 1997)*, 214(1):273–80.

Wang, J., Zhang, Y., Wolf, R. L., Roc, A. C., Alsop, D. C., and Detre, J. A. (2005). Amplitude-modulated Continuous Arterial Spin-labeling 3.0-T Perfusion MR Imaging with a Single Coil: Feasibility Study1. *Radiology*, 235(1):218–228.

Wansapura, J. P., Holland, S. K., Dunn, R. S., and Ball, W. S. (1999). NMR relaxation times in the human brain at 3.0 tesla. *Journal of magnetic resonance imaging : JMRI*, 9(4):531–8.

Warnking, J. M. and Pike, G. B. (2004). Bandwidth-modulated adiabatic RF pulses for uniform selective saturation and inversion. *Magnetic resonance in medicine : official journal of the Society of Magnetic Resonance in Medicine / Society of Magnetic Resonance in Medicine*, 52(5):1190–9.

Warnking, J. M. and Pike, G. B. (2006). Reducing contamination while closing the gap: BASSI RF pulses in PASL. *Magnetic resonance in medicine : official journal of the Society of Magnetic Resonance in Medicine / Society of Magnetic Resonance in Medicine*, 55(4):865–73.

Williams, D. S., Detre, J. A., Leigh, J. S., and Koretsky, A. P. (1992). Magnetic resonance imaging of perfusion using spin inversion of arterial water. *Proc Natl Acad Sci USA*, 89(1):212–216.

Wong, E. C. (2004). Time Efficient CSF Suppressed Velocity Selective ASL using a T2 -FLAIR Preparation. In *Proc. Intl. Soc. Mag. Reson. Med. 11*, page 711.

Wong, E. C. (2007). Vessel-encoded arterial spin-labeling using pseudocontinuous tagging. *Magnetic resonance in medicine : official journal of the Society of Magnetic Resonance in Medicine / Society of Magnetic Resonance in Medicine*, 58(6):1086–91.

Wong, E. C., Buxton, R. B., and Frank, L. R. (1997). Implementation of quantitative perfusion imaging techniques for functional brain mapping using pulsed arterial spin labeling. *NMR in biomedicine*, 10(4-5):237–49.

Wong, E. C., Buxton, R. B., and Frank, L. R. (1998a). A theoretical and experimental comparison of continuous and pulsed arterial spin labeling techniques for quantitative perfusion imaging. *Magnetic resonance in medicine : official journal of the Society of Magnetic Resonance in Medicine / Society of Magnetic Resonance in Medicine*, 40(3):348–55.

Wong, E. C., Buxton, R. B., and Frank, L. R. (1998b). Quantitative imaging of perfusion using a single subtraction (QUIPSS and QUIPSS II). *Magnetic resonance in medicine : official journal of the Society of Magnetic Resonance in Medicine / Society of Magnetic Resonance in Medicine*, 39(5):702–8.

Wong, E. C., Cronin, M., Wu, W.-C., Inglis, B., Frank, L. R., and Liu, T. T. (2006). Velocity-selective arterial spin labeling. *Magnetic Resonance in Medicine*, 55(6):1334–1341.

Wong, E. C. and Guo, J. (2010). BIR-4 based B1 and B0 insensitive velocity selective pulse trains. In *Proceedings of the 18th Annual Meeting ISMRM, Stockholm, Sweden*, page 2853.

Wong, E. C. and Guo, J. (2013). VENTI: Venous Territory Imaging using Remote Sensing. In *Proc. Intl. Soc. Mag. Reson. Med. 21*, page 103.

Wu, W.-C., Edlow, B. L., Elliot, M. a., Wang, J., and Detre, J. a. (2009). Physiological modulations in arterial spin labeling perfusion magnetic resonance imaging. *IEEE transactions on medical imaging*, 28(5):703–9.

Wu, W.-C., Wang, J., Detre, J. a., Ratcliffe, S. J., and Floyd, T. F. (2008). Transit delay and flow quantification in muscle with continuous arterial spin labeling perfusion-MRI. *Journal of magnetic resonance imaging : JMRI*, 28(2):445–52.

Wu, W.-C. and Wong, E. C. (2006). Intravascular effect in velocity-selective arterial spin labeling: the choice of inflow time and cutoff velocity. *Neuroimage*, 32(1):122–128.

Xie, J., Clare, S., Gallichan, D., Gunn, R. N., and Jezzard, P. (2010). Real-time adaptive sequential design for optimal acquisition of arterial spin labeling MRI data. *Magnetic resonance in medicine : official journal of the Society of Magnetic Resonance in Medicine / Society of Magnetic Resonance in Medicine*, 64(1):203–10.

Yang, C., Wang, Z., and Detre, J. A. (2011). Impact of equilibrium magnetization of blood on ASL quantification. 19(1):2011.

Yankeelov, T. E., Rooney, W. D., Huang, W., Dyke, J. P., Li, X., Tudorica, A., Lee, J.-H., Koutcher, J. A., and Springer Jr, C. S. (2005). Evidence for shutter-speed variation in CR bolus-tracking studies of human pathology. *NMR Biomed*, 18(3):173–185.

Ye, F. Q., Frank, J. A., Weinberger, D. R., and McLaughlin, A. C. (2000a). Noise reduction in 3D perfusion imaging by attenuating the static signal in arterial spin tagging (ASSIST). *Magnetic resonance in medicine : official journal of the Society of Magnetic Resonance in Medicine / Society of Magnetic Resonance in Medicine*, 44(1):92–100.

Ye, F. Q., Frank, J. A., Weinberger, D. R., and McLaughlin, A. C. (2000b). Noise reduction in 3D perfusion imaging by attenuating the static signal in arterial spin tagging (ASSIST). *Magn Reson Med*, 44(1):92–100.

Zaharchuk, G., Ledden, P. J., Kwong, K. K., Reese, T. G., Rosen, B. R., and Wald, L. L. (1999). Multislice perfusion and perfusion territory imaging in humans with separate label and image coils. *Magnetic Resonance in Medicine*, 41(6):1093–1098.

Zhao, J. M., Clingman, C. S., Närväinen, M. J., Kauppinen, R. a., and van Zijl, P. C. M. (2007). Oxygenation and hematocrit dependence of transverse relaxation rates of blood at 3T. *Magnetic resonance in medicine : official journal of the Society of Magnetic Resonance in Medicine / Society of Magnetic Resonance in Medicine*, 58(3):592–7.

Zhao, L. and Meyer, C. (2012). Optimal kinetic PASL design and CBF estimation with low SNR and Rician noise. In *Proc. Intl. Soc. Mag. Reson. Med. 20*, page 3494.

Zweifach, B. W. and Lipowsky, H. H. (1977). Quantitative studies of microcirculatory structure and function. III. Microvascular hemodynamics of cat mesentery and rabbit omentum. *Circulation research*, 41(3):380–90.